UNIVERSIDAD COMPLUTENSE DE MADRID

FACULTAD DE CIENCIAS QUÍMICAS

TESIS DOCTORAL

Propiedades interfaciales de fluidos complejos

Interfacial properties of complex fluids

MEMORIA PARA OPTAR AL GRADO DE DOCTOR

PRESENTADA POR

Carlo Carbone

DIRIGIDA POR

Francisco Ortega Gómez

Eduardo Guzmán Solís

UNIVERSIDAD COMPLUTENSE DE MADRID

FACULTAD DE CIENCIAS QUÍMICAS

TESIS DOCTORAL
PROGRAMA DE DOCTORADO EN QUÍMICA AVANZADA

Propiedades interfaciales de fluidos complejos

Interfacial properties of complex fluids

MEMORIA PARA OPTAR AL GRADO DE DOCTOR

PRESENTADA POR

Carlo Carbone

DIRECTORES

Francisco Ortega Gómez
Eduardo Guzmán Solís

Madrid, 2024

Agradecimientos

Gracias a todas aquellas personas que han compartido conmigo este trozo de vida, que ha sido una etapa clave de mi camino de crecimiento académico y personal.

Empiezo con dar las gracias a mis directores de tesis, Eduardo Guzmán Solís y Francisco Ortega Gómez, que me han apoyado (y aguantado!) a lo largo de esos años, a pesar de mi pesimismo y derrotismo. Agradezco además el prof. Ramón González Rubio, que me ha ofrecido su soporte en los primeros meses y ha contribuido en la concepción del proyecto de tesis.

Agradezco a todos los miembros del proyecto de NanoPaint, en particular a los que pertenecen a las instituciones que han contribuido en la actividad de investigación relacionada con la tesis: Tatiana Gambaryan-Roisman and Seforah Carolina Marques Silva (TU Darmstadt), Joachim Venzmer (Evonik Operations GmbH), Julia Maldonado Valderrama (Universidad de Granada), Iván Navarro Arrebola, Libero Liggieri, Eva Santini y Francesca Ravera (CNR Genova).

This project has received funding from the European Union's Horizon 2020 research and innovation programme under the Marie Skłodowska-Curie grant agreement No 955612 (NanoPaInt).

No puedo evitar dar las gracias a todas las personas que se han presentado durante el camino: para mencionarlas todas, hay que escribir una tesis doctoral aparte. He encontrado muchas personas que han completado mi vida, enriqueciéndola y haciéndome vivir experiencias fantásticas, ayudándome a crecer como persona: hay que agradecer a los de Hakuna, del Bocadillo Solidario de Caritas Universitaria, de la Parroquia de Buen Suceso, los Hogares de Santa María, Aluni, las personas que he encontrado tocando en Madrid, Duc In Altum, Los GuayWay, y a todas las personas que por causalidad (o providencia) se me han presentado.

Agradezco a mis padres que a pesar de que no les gustara el hecho de que yo estuviese tan lejos y que siga en el mundo de la investigación, han respetado y apoyado mi elección.

Por último, un gracias enorme a un amigo que vive tan lejos, y que en esos últimos años se me acercó más, y que varias veces me lanzó una cuerda auxiliar para que no me ahogara.

Dedico esta página a la cuerda auxiliar, al ácido ascórbico, al árbol que camina, y sobre todo....a ti que estás leyendo ahora! Será un placer acompañarte en explorar el mundo de los fluidos complejos, para explicarte cómo fluyen! De hecho, como decía Heráclito, “PANTA REI”, ¡o sea “TODO FLUYE”! Por lo tanto, te lo digo a ti también: deja que fluya!

Con respecto a los sistemas complejos, os dejo una frase de Bruno Munari:

"Complicare è facile, semplificare è difficile"

"Complicar es fácil, simplificar es difícil"

Acknowledgments

Many thanks to all those who have shared with me this piece of life, which has been a key stage in my academic and personal growth.

I begin by acknowledging my advisors, Eduardo Guzmán Solís and Francisco Ortega Gómez, who have supported me (and put up with me!) throughout these years, despite my pessimism and defeatism. I am also grateful to Prof. Ramón González Rubio, who offered me his support during the first few months and contributed to the conception of the thesis project.

I acknowledge all of the members of the NanoPaint project, in particular those belonging to the institutions that have contributed to the research activity related to the thesis: Tatiana Gambaryan-Roisman and Seforah Carolina Marques Silva (TU Darmstadt), Joachim Venzmer (Evonik Operations GmbH), Julia Maldonado Valderrama (University of Granada), Iván Navarro Arrebola, Libero Liggieri, Eva Santini and Francesca Ravera (CNR Genova).

This project has received funding from the European Union's Horizon 2020 research and innovation programme under the Marie Skłodowska-Curie grant agreement No 955612 (NanoPaInt).

I can't help but thank all the people that I met along the way: to mention them all would require a separate doctoral thesis. I have met many people who have completed my life, enriching it and making me live fantastic experiences, helping me to grow as a person: I have to thank those from Hakuna, from the Bocadillo Solidario (Caritas Universitaria), from the Buen Suceso Parish, Hogares de Santa Maria, Aluni, the people I have met while busking in the bars of Madrid, Duc In Altum, Los GuayWay, and all the people I met by chance (or providence).

I thank my parents who have supported me, and, although they did not like the fact that I moved so far away and that I am still in the world of research, they have respected and supported my choice.

Finally, a big thank you to a friend who lives so far away, although in those last years became closer to me, and who several times threw me an auxiliary rope so that I would not drown.

I dedicate this page to the auxiliary rope, to ascorbic acid, to the walking tree, and above all.... to you who are reading now! It will be a pleasure to accompany you in exploring the world of complex fluids, to explain how they flow! In fact, as Heraclitus said, “PANTA REI”, that is “EVERYTHING FLOWS”! So, I say it to you too: let it flow!

Regarding complex systems, I will give you a quote by Bruno Munari:

"Complicare è facile, semplificare è difficile"

"Complicating is easy, simplifying is difficult"

Table of Contents

Abstract (English)

This PhD thesis is focused on providing a comprehensive investigation of the interfacial properties of complex fluids - systems that exhibit multifaceted behaviors due to their inherent structural and compositional diversity. Complex fluids encompass a broad range of substances, including those that exhibit the coexistence of multiple phases, such as foams, emulsions and dispersions; those with intricate microstructures, such as polymeric solutions; and those that involve dynamic bulk-interface mass transfer, such as surfactant solutions. By exploring these systems, this research aims to elucidate the underlying mechanisms governing interfacial phenomena, thereby contributing to a deeper understanding of how these fluids behave under various conditions and informing potential applications across industries.

In complex fluids, the interface between two phases is a critical region where distinct physical and chemical behaviors emerge, predominantly due to the presence of a monolayer of surface-active molecules. These interfacial monolayers can be classified into two types: Langmuir monolayers, which are formed by the deposition of molecules onto the surface, and Gibbs monolayers, which arise through the adsorption of molecules from the bulk phase. The study of the equilibrium properties of an interface, such as interfacial tension, is of paramount importance to understand the fundamental characteristics of these interfaces. However, equilibrium properties alone do not provide a complete framework of this type of system. To fully comprehend the behavior of complex fluid interfaces, it is also crucial to investigate their response to external perturbations—hence the importance of interfacial rheology. The rheological properties of fluid/fluid interfaces are key to controlling and optimizing the stability of emulsions and foams, which are pivotal in numerous industrial and biological processes. For instance, the ability to modulate interfacial rheology is central to applications ranging from the performance of lung surfactants and the stability of the tear film in the eye, to aerosol formation, encapsulation techniques, enhanced oil recovery, and remote sensing. Moreover, industries such as cosmetics, food processing, and pharmaceuticals rely heavily on the control of interfacial properties to ensure product stability, efficacy, and quality. Through a detailed examination of both equilibrium and dynamic interfacial phenomena, this thesis contributes to the advancement of knowledge in these critical areas, offering insights that could lead to improved design and control strategies for various industrial applications [1-10]. This PhD Thesis includes a comprehensive analysis of the interfacial properties of different complex fluids. For this purpose, the manuscript has been divides into several Sections that includes chapters that are organized according to the similarity in the aims explored in each case.

Section 1 (Chapter I-II) includes two chapters, providing a theoretical background which provides the foundations for the development of the studies developed in the following sections. In Chapter I, a brief overview on rheology and interfacial properties of complex fluids is provided, explaining their relevance and importance. In particular, the chapter introduces the theoretical foundations and the mathematical models, highlighting shear bulk rheology and interfacial dilational rheology. In Chapter II, a deep description of the experimental techniques used to characterize the interfacial rheology and/or surface tension (Langmuir trough with oscillating barriers, Pendant drop tensiometer, Electro-Capillary Waves), the bulk

rheology (flow rheometers and Diffusing Wave Spectroscopy) and other ancillary techniques (Dynamic Light Scattering, electrophoretic mobility measurement, contact angle and spreading dynamics characterization) is given. The theoretical background as well as the working principle of each apparatus will be described, with particular emphasis on the Electro-Capillary Waves (ECW) technique, which will be discussed in deeper details, focusing on the experimental set-up, the hydrodynamic models that relate the dilational interfacial response to the propagation parameters of capillary waves, and their limitations.

The experimental part of this thesis is focused as was above mentioned on the investigation of the interfacial properties (i.e., the surface tension and the surface dilational rheology) of diverse interfacial systems. These can be classified into 4 main categories: surfactant solutions, monolayers in presence of high ionic strength, dispersions of polymer-capped nanoparticles, and concentrated polymeric solutions. The goal is to try to solve several open questions remaining in the literature. This are related to the dilational surface rheology and the interfacial behavior of those systems, with particular emphasis on the interfacial dilational rheology measured by ECW technique. In particular, these studies are focused on shed light on the theoretical and experimental limits of the ECW measurements. The aim of this type of study are essential to reach a better understanding on the performance of the technique that offers a window to the improvement.

In Section 2 (Chapter III-IV), the behavior of two water-surfactant solutions will be studied. In such systems, surfactant molecules undergo a fast adsorption to the liquid/vapor interface, forming Gibbs monolayers. In this case, the rheological response of the interface can appear coupled with adsorption-desorption phenomena. Chapter III is focused on the interfacial rheology of alkyl polyglucoside (APG, a non-ionic glucosidic surfactant) aqueous solutions, focusing on the equilibrium surface tension of APG Gibbs monolayers and the dilational interfacial rheology measured by ECW technique. The existence of a local minimum in the surface tension isotherm suggests that the surfactant is not pure, consisting of molecules with diverse hydrocarbon chain length. The elastic response of the interface, depending on APG concentration and frequency, is guided by different regimes, including adsorption-desorption mechanism or intrinsic elasticity of the monolayer. The non-monotonic trend of the elastic modulus with frequency suggests the necessity to deepen on the analysis of the rheological behaviour of this system. The second chapter of this Section (Chapter IV) is aimed at studying the interfacial properties of trisiloxane solutions, comparing a superspreader surfactant (S240) with a non-superspreader one (S233). The aim of this study is to try to relate interfacial rheological response as was determined by ECW technique to the spreading kinetics. Moreover, this study will allow comparing the oscillation parameters (i.e., frequency and damping) of sessile drops on PET substrates with the propagation parameters of capillary waves determined by ECW technique (wavelength, frequency, damping). Based on the results of the surface tension isotherms, S240 shows higher hydrophobicity and slightly lower value of the equilibrium surface tension as corresponds to its superspreader character. On the other hand, the dilational interfacial response of the two surfactants was found to be very similar, and the presence of huge error bars in their results is related to the fact that resonance condition is not fulfilled. No relationship between interfacial elasticity and spreading kinetics was observed, but S240, above critical aggregation concentration, undergoes a faster

spreading than S233. The oscillation frequency of spreading sessile drops increases with surface tension, but the models that are currently available in literature are not accurate to predict this trend. Since drop oscillation parameters are comparable to the ones determined by ECW technique, drop oscillation seems to be mainly ruled by capillarity.

Section 3 (Chapter V-VI) deals with the study of interfacial properties of monolayers onto subphases with high ionic strength. The necessity to obtain a deep understanding of the effect of ionic strength comes from the fact that several studies on dilational surface rheology (by means of oscillating barriers, ECW and SQELS technique), in presence of solutions with high ionic strength, reported non-physical values of dilational moduli (such as negative storage modulus, negative loss modulus…) [11-18]. In Chapter V, the impact of NaCl on interfacial tension and dilational surface rheology of Pluronic F-68 (an amphiphilic triblock copolymer) Gibbs monolayers at both low frequency (with oscillating barriers and pendant drop, 10^{-3}-10^{-1} Hz) and high frequency (by means of ECW, 80-400 Hz) was explored. The salting-out phenomenon occurring as a consequence of the presence of salt reduces the solubility of the hydrophilic blocks of the copolymer in the aqueous phase, enhancing its adsorption at the air/solution interface and decreasing surface tension. At low frequency, ionic strength has only a reduced effect in the modification of the relaxation processes, modifying the characteristic frequencies. However, at high frequency, the rheological response can be modified in presence of high ionic strength solutions, especially at high Pluronic F-68 concentrations. The chapter points out some of the technical and theoretical limitations for obtaining reliable dilational rheological data within ECW frequency range, due to the lack of fulfillment of the resonance condition, especially at high ionic strength. Chapter VI has a similar purpose to the previous chapter, but in this case, the study is focused on the interfacial properties of a Langmuir monolayer of poly(tert-butylacrylate) (PtBA, a water insoluble polymer). In particular, the surface tension and the dilational surface rheology of PtBA monolayers, with dissolved NaCl in the aqueous subphase, were investigated. Neither surface pressure nor dilational interfacial rheology are affected by ionic strength, which leads to the conclusion that NaCl does not interact with PtBA monolayers. In this system, due to the high values of elastic modulus, the resonance condition is never accomplished, which leads to huge error bars in the elasticity.

Section 4 (including Chapter VII-VII) is dedicated to the study of the interfacial properties of polymer-capped particles aqueous dispersions to provide a deep understanding on the interaction between particles and surface active molecules, which allows assessing the influence of this nanocomposite dispersion on the liquid/vapor interface stability and properties. The Chapter VII is aimed at investigating the effect of Pluronic F-127 (an amphiphilic triblock copolymer) on silica nanoparticles adsorption at water/vapor interfaces, as well as on the interfacial rheology (at low frequency, 10^{-3}-10^{-1} Hz) of the formed layers. The interaction between Pluronic F-127 and silica nanoparticles drives the formation of copolymer-decorated particles with increased coating density and hydrodynamic diameter, and with reduced effective charge as the copolymer concentration increases. The adsorption of copolymer-decorated nanoparticles at the interface does not lead to noticeable differences from the interfacial properties of pure Pluronic F-127, only a shift of surface tension isotherm is found, depending on the particle concentration. This suggests that the presence of particles

limits the space available for Pluronic F-127 molecules to reorganize at the interface, which is also confirmed by the dilational elasticity results. Anyway, at high surfactant concentration, the interfacial behavior of pure surfactant and decorated silica nanoparticles is similar. Chapter VIII has the purpose of evaluating the interaction between chitosan (a positively charged polyelectrolyte) and negatively charged silica nanoparticles, and the stability of the resulting water dispersions at different pH and concentration conditions. Optimal conditions for the formation of stable dispersions were determined, highlighting that chitosan adsorption on silica nanoparticles, as occurs for solubility, is enhanced in acid medium (pH=4.5). Electrophoretic mobility measurements confirmed the positive zeta potential of chitosan-capped particles, indicating charge inversion due to chitosan adsorption on negatively charged silica surfaces. The presence of chitosan adsorbed on silica nanoparticles reduces the interfacial tension, with a synergistic effect observed between chitosan and silica. Capillary wave experiments demonstrated the formation of viscoelastic layers with the dilatational elastic modulus of the nanocomposite layers exceeding their viscous modulus. The frequency dependence of the interfacial dilational moduli showed that increasing particle concentration enhanced the viscoelastic properties of the interface. These results suggest potential applications in the stabilization of liquid and solid foams, and stress on the importance of chitosan-capped particles in modifying water/air interface properties and improving the rheological behavior of particle-laden interfaces.

Section 5, consisting in a single chapter (Chapter IX), is focused on the dilational interfacial response of a system exhibiting a non-negligible shear bulk viscoelasticity in the subphase. This issue is not taken into account by the classical hydrodynamic models used to determine the dilational interfacial modulus by surface wave damping propagation parameters. For the aim of this study, Poly(vinyl alcohol) (PVA, a water-soluble polymer) was mixed with a crosslinker (BORAX). PVA/BORAX solutions were chosen as potential candidates for this study, because they exhibit bulk viscoelasticity within ECW frequency range, and their bulk shear viscosity does not exceed ECW operative limits. The presence of BORAX increments both shear elasticity and viscosity of PVA, and, above a threshold PVA concentration (> 9 g/l), also increases the surface tension and the dilational interfacial modulus (both the real and the imaginary part), while in all of the other samples both storage and viscous interfacial moduli are zero. This leads to think that BORAX increases the stiffness of the interface, creating also surface crosslinks. Dilational elastic and viscous moduli calculated by means of Wang dispersion equation [19], which also takes into account the presence of viscoelasticity in the bulk, are higher than those calculated by classical hydrodynamic models (such as Lucassen dispersion equation [20]).

In summary, this PhD thesis makes a significant contribution to the understanding of the interfacial properties of a wide range of complex fluid systems, with a particular emphasis on utilizing interfacial dilational rheology as a powerful tool to probe their behavior. The research presented here not only advances our knowledge of how these fluids respond to mechanical perturbations at interfaces but also critically evaluates the current hydrodynamic models that are employed to interpret dilational interfacial responses. By identifying the limitations and gaps in these existing models, this work lays the groundwork for future improvements, offering pathways to develop more accurate and comprehensive theoretical frameworks.

These advancements could enhance the predictive capabilities of hydrodynamic models, ultimately leading to better control and manipulation of interfacial phenomena in both industrial and biological contexts. This thesis, therefore, not only deepens our understanding of interfacial rheology but also paves the way for future innovations in the study and application of complex fluids.

References Abstract

1. Rawate, H.; Goswami, A. Importance of Interfacial Rheology and its Applications - Review of the Interfacial Rheology. *JETIR* **2018**, *5*, 312.
2. Guzmán, E. Fluid Films as Models for Understanding the Impact of Inhaled Particles in Lung Surfactant Layers. *Coatings* **2022**, *12*, 277, doi:10.3390/coatings12020277.
3. Wei, Y.; Xie, Y.; Cai, Z.; Guo, Y.; Zhang, H. Interfacial rheology, emulsifying property and emulsion stability of glyceryl monooleate-modified corn fiber gum. *Food Chem* **2021**, *343*, 128416, doi:10.1016/j.foodchem.2020.128416.
4. Wang, H.; Wei, X.; Du, Y.; Wang, D. Experimental investigation on the dilatational interfacial rheology of dust-suppressing foam and its effect on foam performance. *Process Safety and Environmental Protection* **2019**, *123*, 351-357, doi:10.1016/j.psep.2019.01.027.
5. Thai, L.P.A.; Mousseau, F.; Oikonomou, E.K.; Berret, J.F. On the rheology of pulmonary surfactant: Effects of concentration and consequences for the surfactant replacement therapy. *Colloids Surf B Biointerfaces* **2019**, *178*, 337-345, doi:10.1016/j.colsurfb.2019.03.020.
6. Haslbeck, K.; Schwarz, K.; Hohlfeld, J.M.; Seume, J.R.; Koch, W. Submicron droplet formation in the human lung. *Journal of Aerosol Science* **2010**, *41*, 429-438, doi:10.1016/j.jaerosci.2010.02.010.
7. Svitova, T.F.; Lin, M.C. Tear lipids interfacial rheology: effect of lysozyme and lens care solutions. *Optom Vis Sci* **2010**, *87*, 10-20, doi:10.1097/OPX.0b013e3181c07908.
8. Zhang, H.; Lamnawar, K.; Maazouz, A. Fundamental studies of interfacial rheology at multilayered model polymers for coextrusion process. **2015**, *1664*, 100008, doi:10.1063/1.4918475.
9. Sun, H.-Q.; Zhang, L.; Li, Z.-Q.; Zhang, L.; Luo, L.; Zhao, S. Interfacial dilational rheology related to enhance oil recovery. *Soft Matter* **2011**, *7*, 7601, doi:10.1039/c1sm05234a.
10. Gade, M.; Byfield, V.; Ermakov, S.; Lavrova, O.; Mitnik, L. Slicks as Indicators for Marine Processes. *Oceanography* **2013**, *26*, doi:10.5670/oceanog.2013.39.
11. Safouane, M.; Langevin, D. Surface viscoelasticity of concentrated salt solutions: specific ion effects. *Chemphyschem* **2009**, *10*, 222-225, doi:10.1002/cphc.200800527.
12. Monroy, F.; Giermanska Kahn, J.; Langevin, D. Dilational viscoelasticity of surfactant monolayers. *Colloids and Surfaces A: Physicochemical and Engineering Aspects* **1998**, *143*, 251-260, doi:10.1016/s0927-7757(98)00373-2.
13. Monroy, F.; Giermanska-Kahn, J.; Langevin, D. Anomalous Damping of Capillary Waves With Surfactant Solutions. *Journal of Non-Equilibrium Thermodynamics* **2001**, *25*, doi:10.1515/jnetdy.2000.019.
14. Stenvot, C.; Langevin, D. Study of viscoelasticity of soluble monolayers using analysis of propagation of excited capillary waves. *Langmuir* **2002**, *4*, 1179-1183, doi:10.1021/la00083a022.
15. Earnshaw, J.C.; McCoo, E. Surface Light-Scattering Studies of Surfactant Solutions. *Langmuir* **2002**, *11*, 1087-1100, doi:10.1021/la00004a011.

16. Sharpe, D.; Eastoe, J. Properties of Surfactant Monolayers Studied by Surface Light Scattering. *Langmuir* **1996**, *12*, 2303-2307, doi:10.1021/la951078+.
17. Monroy, F.; Muñoz, M.G.; Rubio, J.E.F.; Ortega, F.; Rubio, R.G. Capillary Waves in Ionic Surfactant Solutions: Effects of the Electrostatic Adsorption Barrier and Analysis in Terms of a New Dispersion Equation. *The Journal of Physical Chemistry B* **2002**, *106*, 5636-5644, doi:10.1021/jp012044f.
18. Cuenca, V.E.; Ferna Ndez Leyes, M.; Falcone, R.D.O.; Correa, N.M.; Langevin, D.; Ritacco, H.N. Interfacial Dynamics and Its Relations with ?Negative? Surface Viscosities Measured at Water?Air Interfaces Covered with a Cationic Surfactant. *Langmuir* **2019**, *35*, 8333-8343, doi:10.1021/acs.langmuir.9b00534.
19. Wang, C.H.; Huang, Q.R. Hydrodynamic surface waves in concentrated polymer solutions in the presence of surface adsorption. *J. Chem. Phys.* **1997**, *107*, 5898–5906 doi:doi.org/10.1063/1.474315.
20. Lucassen-Reynders, E.H.; Lucassen, J. Properties of capillary waves. *Advances in Colloid and Interface Science* **1970**, *2*, 347-395, doi:10.1016/0001-8686(70)80001-x.

Resumen (Castellano)

Esta Tesis Doctoral presenta una investigación detallada de las propiedades interfaciales de fluidos complejos (sistemas que exhiben una gran diversidad de comportamientos como resultado de su diversidad estructural y composicional). Los fluidos complejos abarcan una amplia gama de sustancias, incluyendo aquellas que exhiben la coexistencia de múltiples fases, como espumas, emulsiones y dispersiones; sistemas con microestructuras complejas, como es el caso de las soluciones poliméricas; y aquellas que implican una transferencia de masa entre el seno de la disolución/dispersión (bulk) y la interfase que separa dos fases de distinta naturales, como es el caso de las soluciones de tensioactivos. Mediante el estudio de este tipo sistemas, este trabajo pretende arrojar luz sobre los mecanismos subyacentes que rigen los fenómenos interfaciales, contribuyendo así a una comprensión más profunda de cómo se comportan los fluidos complejos bajo diversas condiciones, lo que contribuirá a obtener información relativa a las posibles aplicaciones de este tipo de sistemas en diversos sectores.

En los fluidos complejos, la interfase entre dos fases es una región crítica en la que aparecen comportamientos físicos y químicos distintos, debidos predominantemente a la presencia de una monocapa de moléculas adsorbidas. Estas monocapas pueden clasificarse en dos tipos: Las monocapas de Langmuir, que se forman por la deposición de moléculas directamente en la superficie, y las monocapas de Gibbs, que surgen por la adsorción de moléculas desde la disolución/dispersión a la interfase. El estudio de las propiedades de equilibrio de una interfase, como la tensión interfacial, presenta suma importancia para la comprensión de las características fundamentales de este tipo de sistemas. Sin embargo, las propiedades de equilibrio por sí solas no proporcionan una descripción completa de este tipo de sistemas. Para comprender el comportamiento de interfases fluidas complejas, es crucial realizar un estudio sistemático de su respuesta a las perturbaciones externas, de ahí la importancia de la reología interfacial. Las propiedades reológicas de las interfaces fluido/fluido son fundamentales para controlar y optimizar la estabilidad de emulsiones y espumas, que son fundamentales en numerosos procesos industriales y biológicos. Por ejemplo, la capacidad de modular la reología interfacial es fundamental para aplicaciones que van desde la función fisiológica del tensioactivo pulmonar y la estabilidad de la película lagrimal en el ojo, hasta la formación de aerosoles, la fabricación de plataformas de encapsulación, la recuperación mejorada de petróleo y la teledetección. Además, industrias como la cosmética, la alimentaria y la farmacéutica dependen en gran medida del control de las propiedades interfaciales para garantizar la estabilidad, eficacia y calidad de sus productos. Mediante un estudio detallado de los fenómenos interfaciales tanto dinámicos como de equilibrio, esta Tesis pretende contribuir al avance del conocimiento en estas áreas críticas, ofreciendo perspectivas que podrían conducir a la mejora de las estrategias de diseño y control para diversas aplicaciones industriales [1-10]. Esta Tesis Doctoral incluye un análisis exhaustivo de las propiedades interfaciales de diferentes fluidos complejos. Para ello, el manuscrito se ha dividido en varias Secciones que incluyen capítulos que se organizan en función de la similitud en los objetivos explorados en cada caso.

La Sección 1 (Capítulos I-II) incluye dos capítulos, en los que se proporciona una base teórica que sirve de fundamento para los estudios que se desarrollan en las siguientes secciones. En el Capítulo I, se proporciona una visión general sobre reología y propiedades interfaciales de fluidos complejos, explicando su relevancia e importancia. En particular, el capítulo introduce fundamentos teóricos y modelos matemáticos, haciendo énfasis en la reología de cizalla en bulk y la reología dilacional en interfases. En el Capítulo II, se describen en profundidad las técnicas experimentales utilizadas para caracterizar la reología interfacial y/o la tensión superficial (balanza de Langmuir con barreras oscilantes, tensiómetro de gota colgante, ondas electrocapilares), la reología de bulk (reómetros de flujo y espectroscopia de bulk) y otras técnicas auxiliares (dispersión dinámica de la luz, medida de la movilidad electroforética, caracterización del ángulo de contacto y de la dinámica de extensión de gotas). En este capítulo, se describirán los antecedentes teóricos, así como el principio de funcionamiento de cada aparato, con especial énfasis en la técnica de ondas electrocapilares (ECW), que se analizará con mayor detalle, centrándose en el montaje experimental, los modelos hidrodinámicos que relacionan la respuesta interfacial dilacional con los parámetros de propagación de las ondas capilares, y sus limitaciones.

La parte experimental de esta tesis se centra, como ya se ha mencionado, en la investigación de las propiedades interfaciales (es decir, la tensión superficial y la reología de dilatación superficial) de diversos sistemas. Éstos pueden clasificarse en 4 categorías principales: disoluciones de tensioactivos, monocapas en presencia de alta fuerza iónica, dispersiones de nanopartículas recubiertas de polímeros y soluciones poliméricas concentradas. El objetivo de esta serie de capítulos es tratar de resolver varias cuestiones pendientes en la bibliografía. Éstas están relacionadas con la reología dilacional superficial y el comportamiento interfacial de dichos sistemas, con especial énfasis en la caracterización de la reología dilacional interfacial mediante la técnica ECW. En particular, estos estudios se centran en aportar luz sobre los límites teóricos y experimentales de las medidas ECW. El objetivo de este tipo de estudios es alcanzar una mejor comprensión sobre el rendimiento de la técnica y ofrecer una ventana a su mejora.

En la Sección 2 (Capítulos III-IV), se estudiará el comportamiento de dos disoluciones acuosas de tensioactivos. En estos sistemas, las moléculas de tensioactivo experimentan una rápida adsorción en la interfase líquido/vapor, formando monocapas de Gibbs. Esto conduce a que la respuesta reológica de la interfase puede aparecer acoplada a fenómenos de adsorción-desorción. El capítulo III se centra en la reología interfacial de soluciones acuosas de alquilpoliglucósido (APG, un tensioactivo glucosídico no iónico), centrándose en la tensión superficial de equilibrio de las monocapas de Gibbs de APG y en la reología interfacial dilacional medida mediante la técnica ECW. La existencia de un mínimo local en la isoterma de tensión superficial de este sistema sugiere que el tensioactivo no es puro, estando formado por moléculas con diversas longitudes de cadena hidrocarbonadas. La respuesta elástica de la interfaz, en función de la concentración de APG y de la frecuencia, está controlada por diferentes regímenes, incluido el mecanismo de adsorción-desorción o la elasticidad intrínseca de la monocapa. La tendencia no monotónica del módulo elástico con la frecuencia sugiere la necesidad de profundizar en el análisis del comportamiento reológico de este sistema. El segundo capítulo de esta sección (Capítulo IV) está dirigido al estudio de las propiedades

interfaciales de las soluciones de trisiloxano, comparando un tensioactivo superspreader (S240) con otro no superspreader (S233). El objetivo de este estudio es intentar relacionar la respuesta reológica interfacial determinada mediante la técnica ECW con la cinética de extensión de las gotas. Además, este estudio permitirá comparar los parámetros de oscilación (es decir, frecuencia y amortiguación) de las gotas sésiles sobre sustratos de PET con los parámetros de propagación de las ondas capilares determinados mediante la técnica ECW (longitud de onda, frecuencia, amortiguación). A partir de los resultados de las isotermas de tensión superficial, el S240 muestra una mayor hidrofobicidad y un valor ligeramente inferior de la tensión superficial de equilibrio, como corresponde a su carácter de superspreader. Por otra parte, se observó que la respuesta interfacial dilatacional de los dos tensioactivos era muy similar, y la presencia de grandes barras de error en los resultados se encuentra relacionada con el hecho de que no se cumple la condición de resonancia. No se observó ninguna relación entre la elasticidad interfacial y la cinética de extensión de las gotas, pero el S240, por encima de la concentración crítica de agregación, experimenta una propagación más rápida que el S233. La frecuencia de oscilación de las gotas sésiles en extensión aumenta con la tensión superficial, pero los modelos disponibles actualmente en la bibliografía no son precisos para predecir esta tendencia. Dado que los parámetros de oscilación de las gotas son comparables a los determinados mediante la técnica ECW, la oscilación de las gotas parece regirse principalmente por la capilaridad.

La Sección 3 (Capítulos V-VI) estudia las propiedades interfaciales de monocapas sobre subfases con elevada fuerza iónica. La necesidad de obtener una comprensión profunda del efecto de la fuerza iónica proviene del hecho de que varios estudios sobre reología superficial dilatacional (mediante barreras oscilantes, ECW y técnica SQELS), en presencia de disoluciones con alta fuerza iónica, condujeron a valores sin sentido físico de los módulos dilacionales (como módulo de almacenamiento negativo, módulo de pérdida negativo...) [11-18]. En el Capítulo V, se analiza el impacto del NaCl sobre la tensión interfacial y la reología superficial dilacional de monocapas de Gibbs de Pluronic F-68 (un copolímero tribloque anfifílico) tanto a baja frecuencia (con barreras oscilantes y gota colgante, 10^{-3}-10^{-1} Hz) como a alta frecuencia (mediante ECW, 80-400 Hz). El fenómeno de salting-out que se produce como consecuencia de la presencia de sal reduce la solubilidad de los bloques hidrofílicos del copolímero en la fase acuosa, potenciando su adsorción en la interfase aire/disolución y disminuyendo la tensión superficial. A baja frecuencia, la fuerza iónica sólo tiene un efecto reducido en la modificación de los procesos de relajación, modificando las frecuencias características. Sin embargo, a alta frecuencia, la respuesta reológica puede modificarse en presencia de disoluciones de alta fuerza iónica, especialmente a altas concentraciones de Pluronic F-68. El capítulo señala algunas de las limitaciones técnicas y teóricas para la obtención de datos reológicos dilacionales fiables dentro del rango de frecuencias ECW, debido a la falta de cumplimiento de la condición de resonancia, especialmente a alta fuerza iónica. El Capítulo VI tiene un propósito similar al anterior, pero en este caso, el estudio se centra en las propiedades interfaciales de monocapas de Langmuir de poli(tert-butilacrilato) (PtBA, un polímero insoluble en agua). En particular, se investigaron la tensión superficial y la reología superficial dilatacional de monocapas de PtBA, con NaCl disuelto en la subfase acuosa. Ni la tensión superficial ni la reología interfacial dilatacional se ven afectadas por la fuerza iónica, lo que lleva a la conclusión de que el NaCl no interactúa con las monocapas de PtBA. En este sistema, debido a los

elevados valores del módulo elástico, nunca se cumple la condición de resonancia, lo que da lugar a enormes barras de error en la elasticidad.

La Sección 4 (que incluye los Capítulos VII-VIII) está dedicada al estudio de las propiedades interfaciales de dispersiones acuosas de partículas recubiertas de polímeros para proporcionar un conocimiento profundo de la interacción entre las partículas y las moléculas superficialmente activas, lo que permite evaluar la influencia de esta nanodispersión sobre la estabilidad y las propiedades de la interfase líquido/vapor. El capítulo VII tiene por objeto investigar el efecto del Pluronic F-127 (un copolímero tribloque anfifílico) sobre la adsorción de nanopartículas de sílice en la interfase dispersión/vapor, así como sobre la reología interfacial (a baja frecuencia, 10^{-3}-10^{-1} Hz) de las capas formadas. La interacción entre Pluronic F-127 y las nanopartículas de sílice impulsa la formación de partículas decoradas con copolímero con una mayor densidad de recubrimiento y diámetro hidrodinámico, y con una carga efectiva reducida a medida que aumenta la concentración de copolímero. La adsorción de nanopartículas decoradas con copolímeros en la interfase no da lugar a diferencias notables con respecto a las propiedades interfaciales del Pluronic F-127 puro, encontrándose únicamente un desplazamiento de la isoterma de tensión superficial, en función de la concentración de partículas. Esto sugiere que la presencia de partículas limita el espacio disponible para que las moléculas de Pluronic F-127 se reorganicen en la interfase, lo que también confirman los resultados de elasticidad dilacional. De todos modos, a altas concentraciones de tensioactivo, el comportamiento interfacial del tensioactivo puro y de las nanopartículas de sílice decoradas es similar. El capítulo VIII tiene por objeto evaluar la interacción entre el quitosano (un polielectrolito cargado positivamente) y las nanopartículas de sílice cargadas negativamente, así como la estabilidad de las dispersiones acuosas resultantes en diferentes condiciones de pH y concentración. Se determinaron las condiciones óptimas para la formación de dispersiones estables, destacando que la adsorción del quitosano sobre las nanopartículas de sílice, al igual que ocurre con la solubilidad, se potencia en medio ácido (pH=4,5). Las medidas de movilidad electroforética confirmaron el potencial zeta positivo de las partículas recubiertas de quitosano, lo que indica una inversión de carga debida a la adsorción de quitosano sobre superficies de sílice cargadas negativamente. La presencia de quitosano adsorbido en nanopartículas de sílice reduce la tensión interfacial, observándose un efecto sinérgico entre el quitosano y la sílice. Los experimentos de ondas capilares demostraron la formación de capas viscoelásticas con un módulo elástico dilacional de las capas superior a su módulo viscoso. La dependencia de la frecuencia de los módulos dilatacionales interfaciales mostró que el aumento de la concentración de partículas mejoraba las propiedades viscoelásticas de la interfase. Estos resultados sugieren potenciales aplicaciones en la estabilización de espumas líquidas y sólidas, y subrayan la importancia de las partículas recubiertas de quitosano para modificar las propiedades de la interfase agua/aire y mejorar el comportamiento reológico de las interfaces cargadas de partículas.

La sección 5, que consta de un único capítulo (capítulo IX), se centra en la respuesta interfacial dilacional de un sistema que presenta una viscoelasticidad de cizalla no despreciable en la subfase. Esta cuestión no es tenida en cuenta por los modelos hidrodinámicos clásicos utilizados para determinar el módulo interfacial dilacional mediante los parámetros de propagación de ondas superficiales. Para el objetivo de este estudio, se mezcló poli(alcohol

vinílico) (PVA, un polímero hidrosoluble) con un reticulante (BORAX). Las soluciones de PVA/BORAX se eligieron como posibles candidatas para este estudio, ya que presentan viscoelasticidad aparente dentro del rango de frecuencias de ECW, y su viscosidad de cizalla aparente no supera los límites operativos de ECW. La presencia de BORAX aumenta tanto la elasticidad como la viscosidad del PVA y, por encima de un umbral de concentración de PVA (> 9 g/l), también aumenta la tensión superficial y el módulo interfacial de dilatación (tanto la parte real como la imaginaria), mientras que en todas las demás muestras tanto el módulo de almacenamiento como el módulo viscoso interfacial son nulos. Esto lleva a pensar que el BORAX aumenta la rigidez de la interfase, creando también entrecruzamiento superficial. Los resultados muestran que los módulos elástico y viscoso dilacionales calculados mediante la ecuación de dispersión de Wang [19] que también tiene en cuenta la presencia de viscoelasticidad en el bulk, son superiores a los calculados mediante modelos hidrodinámicos clásicos (como la ecuación de dispersión de Lucassen [20])

En resumen, esta tesis doctoral contribuye significativamente a la comprensión de las propiedades interfaciales de una amplia gama de fluidos complejos, con especial énfasis en la utilización de la reología dilacional interfacial como una poderosa herramienta para evaluar su comportamiento. La investigación que aquí se presenta no sólo avanza en nuestro conocimiento de cómo responden estos fluidos a las perturbaciones mecánicas en las interfases, sino que también evalúa críticamente los modelos hidrodinámicos actuales que se emplean para interpretar las respuestas interfaciales dilacionales. Al identificar las limitaciones y lagunas de los modelos existentes, este trabajo sienta las bases para futuras mejoras, ofreciendo vías para desarrollar marcos teóricos más precisos y completos. Estos avances podrían mejorar la capacidad predictiva de los modelos hidrodinámicos y, en última instancia, conducir a un mejor control y manipulación de los fenómenos interfaciales tanto en contextos industriales como biológicos. Esta tesis, por tanto, no sólo profundiza en nuestra comprensión de la reología interfacial, sino que también allana el camino para futuras innovaciones en el estudio y la aplicación de fluidos complejos.

Bibliografía resumen

1. Rawate, H.; Goswami, A. Importance of Interfacial Rheology and its Applications - Review of the Interfacial Rheology. *JETIR* **2018**, *5*, 312.
2. Guzmán, E. Fluid Films as Models for Understanding the Impact of Inhaled Particles in Lung Surfactant Layers. *Coatings* **2022**, *12*, 277, doi:10.3390/coatings12020277.
3. Wei, Y.; Xie, Y.; Cai, Z.; Guo, Y.; Zhang, H. Interfacial rheology, emulsifying property and emulsion stability of glyceryl monooleate-modified corn fiber gum. *Food Chem* **2021**, *343*, 128416, doi:10.1016/j.foodchem.2020.128416.
4. Wang, H.; Wei, X.; Du, Y.; Wang, D. Experimental investigation on the dilatational interfacial rheology of dust-suppressing foam and its effect on foam performance. *Process Safety and Environmental Protection* **2019**, *123*, 351-357, doi:10.1016/j.psep.2019.01.027.
5. Thai, L.P.A.; Mousseau, F.; Oikonomou, E.K.; Berret, J.F. On the rheology of pulmonary surfactant: Effects of concentration and consequences for the surfactant replacement therapy. *Colloids Surf B Biointerfaces* **2019**, *178*, 337-345, doi:10.1016/j.colsurfb.2019.03.020.

6. Haslbeck, K.; Schwarz, K.; Hohlfeld, J.M.; Seume, J.R.; Koch, W. Submicron droplet formation in the human lung. *Journal of Aerosol Science* **2010**, *41*, 429-438, doi:10.1016/j.jaerosci.2010.02.010.
7. Svitova, T.F.; Lin, M.C. Tear lipids interfacial rheology: effect of lysozyme and lens care solutions. *Optom Vis Sci* **2010**, *87*, 10-20, doi:10.1097/OPX.0b013e3181c07908.
8. Zhang, H.; Lamnawar, K.; Maazouz, A. Fundamental studies of interfacial rheology at multilayered model polymers for coextrusion process. **2015**, *1664*, 100008, doi:10.1063/1.4918475.
9. Sun, H.-Q.; Zhang, L.; Li, Z.-Q.; Zhang, L.; Luo, L.; Zhao, S. Interfacial dilational rheology related to enhance oil recovery. *Soft Matter* **2011**, *7*, 7601, doi:10.1039/c1sm05234a.
10. Gade, M.; Byfield, V.; Ermakov, S.; Lavrova, O.; Mitnik, L. Slicks as Indicators for Marine Processes. *Oceanography* **2013**, *26*, doi:10.5670/oceanog.2013.39.
11. Safouane, M.; Langevin, D. Surface viscoelasticity of concentrated salt solutions: specific ion effects. *Chemphyschem* **2009**, *10*, 222-225, doi:10.1002/cphc.200800527.
12. Monroy, F.; Giermanska Kahn, J.; Langevin, D. Dilational viscoelasticity of surfactant monolayers. *Colloids and Surfaces A: Physicochemical and Engineering Aspects* **1998**, *143*, 251-260, doi:10.1016/s0927-7757(98)00373-2.
13. Monroy, F.; Giermanska-Kahn, J.; Langevin, D. Anomalous Damping of Capillary Waves With Surfactant Solutions. *Journal of Non-Equilibrium Thermodynamics* **2001**, *25*, doi:10.1515/jnetdy.2000.019.
14. Stenvot, C.; Langevin, D. Study of viscoelasticity of soluble monolayers using analysis of propagation of excited capillary waves. *Langmuir* **2002**, *4*, 1179-1183, doi:10.1021/la00083a022.
15. Earnshaw, J.C.; McCoo, E. Surface Light-Scattering Studies of Surfactant Solutions. *Langmuir* **2002**, *11*, 1087-1100, doi:10.1021/la00004a011.
16. Sharpe, D.; Eastoe, J. Properties of Surfactant Monolayers Studied by Surface Light Scattering. *Langmuir* **1996**, *12*, 2303-2307, doi:10.1021/la951078+.
17. Monroy, F.; Muñoz, M.G.; Rubio, J.E.F.; Ortega, F.; Rubio, R.G. Capillary Waves in Ionic Surfactant Solutions: Effects of the Electrostatic Adsorption Barrier and Analysis in Terms of a New Dispersion Equation. *The Journal of Physical Chemistry B* **2002**, *106*, 5636-5644, doi:10.1021/jp012044f.
18. Cuenca, V.E.; Ferna Ndez Leyes, M.; Falcone, R.D.O.; Correa, N.M.; Langevin, D.; Ritacco, H.N. Interfacial Dynamics and Its Relations with ?Negative? Surface Viscosities Measured at Water?Air Interfaces Covered with a Cationic Surfactant. *Langmuir* **2019**, *35*, 8333-8343, doi:10.1021/acs.langmuir.9b00534.
19. Wang, C.H.; Huang, Q.R. Hydrodynamic surface waves in concentrated polymer solutions in the presence of surface adsorption. *J. Chem. Phys.* **1997**, *107*, 5898–5906 doi:doi.org/10.1063/1.474315.
20. Lucassen-Reynders, E.H.; Lucassen, J. Properties of capillary waves. *Advances in Colloid and Interface Science* **1970**, *2*, 347-395, doi:10.1016/0001-8686(70)80001-x.

Section 1 Introduction

This section includes two chapters, providing a theoretical background about the foundations for the development of the studies developed in the following sections. It is divided into two chapters:

- *Chapter I: Foundations of Rheology, with special emphasis on Interfacial Rheology*

This chapter includes a brief overview on rheology and interfacial properties of complex fluids, explaining their relevance and importance. In particular, the chapter introduces the theoretical foundations and the mathematical models, highlighting on shear bulk rheology and interfacial dilational rheology.

- *Chapter II: Experimental methods*

In this chapter, a deep description of the experimental techniques used to characterize the interfacial rheology and/or surface tension (Langmuir trough with oscillating barriers, Pendant drop tensiometer, Electro-Capillary Waves), the bulk rheology (flow rheometers and Diffusing Wave Spectroscopy) and other ancillary techniques (Dynamic Light Scattering, electrophoretic mobility measurement, contact angle and spreading dynamics characterization) is given. The theoretical background as well as the working principle of each apparatus will be described, with particular emphasis on the Electro-Capillary Waves (ECW) technique, which will be discussed in deeper details, focusing on the experimental set-up, the hydrodynamic models that relate the dilational interfacial response to the propagation parameters of capillary waves, and their limitations.

Chapter I: Foundations of Rheology, with special emphasis on Interfacial Rheology[†]

1.1. Introduction: Rheology foundations

The term rheology (from Greek "ῥέω" ("rhéō") which means flow, and "λογία" ("logia") which means "study of") is referred to the science that studies the flow of matter and its mechanical response to an applied deformation or stress. This concept was initially introduced by E.C. Bingham and M. Reiner in the late 20s of the XX century [1], taking inspiration from a quote from Heraclitus of Ephesus: "πάντα ῥεῖ" ("Panta rhei", "everything flows") [2].

The study of flow and deformation of matter may concern different states of aggregation: fluids as well as soft solids. Special consideration should be paid to the study of rheology of complex fluids, which are commonly characterized by the coexistence of multiple phases: liquid-gas (foams), liquid-liquid (emulsions), liquid-solid (suspensions, dispersions). They also include fluids with complex microstructure, like polymeric solutions, nanosuspensions, but also fluids that are subjected to mass transfer from the volume to the surface, as observed in water solutions with surface active molecules (surfactants). Complex fluids are found in many fields: cosmetics, food industry, pharmaceutical industry, biological fluids, oil industry and oil derivates, water recover plants, paintings, polymer industry, and many other. The study of rheology also plays a key role in understanding the mechanical behavior of soft solids, like thermoplastic and thermoset polymers, gels, rubbers, because such systems present a complex microstructure and peculiar response when subjected to deformation. The focus of this PhD Thesis will be the study of the rheology of complex fluids rather than that of soft solids, with particular focus on the interfacial rheological behavior of surfactant solutions, polymer solutions and nanosuspensions.

Rheological properties of matter vary according to the direction and orientation of the applied stimulus, making it essential to distinguish between dilational/extensional rheology and shear rheology. These different rheological behaviors are crucial for understanding and predicting how materials respond under different types of applied stress. Dilational or dilatational rheology deals with the mechanical response of systems when are subjected to compression or dilation forces. In this context, the applied stimulus induces a change in the characteristic dimension of the material's constituent elements, such as volumes, surfaces, and/or lengths (see **Figure 1. 1** (a)). This type of rheology is particularly relevant in understanding the behavior of materials like foams, emulsions, and lung surfactant or biological membranes, where the expansion or compression of their structures significantly affects their properties. On the other hand, shear rheology concerns the mechanical response of systems that are subdued to a stimulus that results in a change of shape of the body constituting element, without involving any change in volume, surface and/or length (see **Figure 1. 1** (b)). This behavior is typically observed in fluids and soft solids, where shear stress leads to deformation in shape while maintaining the overall size and dimensions constant. Understanding shear rheology is crucial for applications in fields such as polymer science, lubrication, and the processing of complex

[†] The part of this Chapter corresponding to interfacial dilational rheology is partially published in: Guzmán, E.; Maestro, A.; Carbone, C.; Ortega, F.; Rubio, R.G. Dilational Rheology of Fluid/Fluid Interfaces: Foundations and Tools. *Fluids* **2022**, *7*, 335. https://doi.org/10.3390/fluids7100335

fluids. The distinction between these two types of rheology allows one to analyze and predict the behavior of materials under different mechanical stimuli, leading to a more effective and efficient material design and utilization in various industrial and scientific applications.

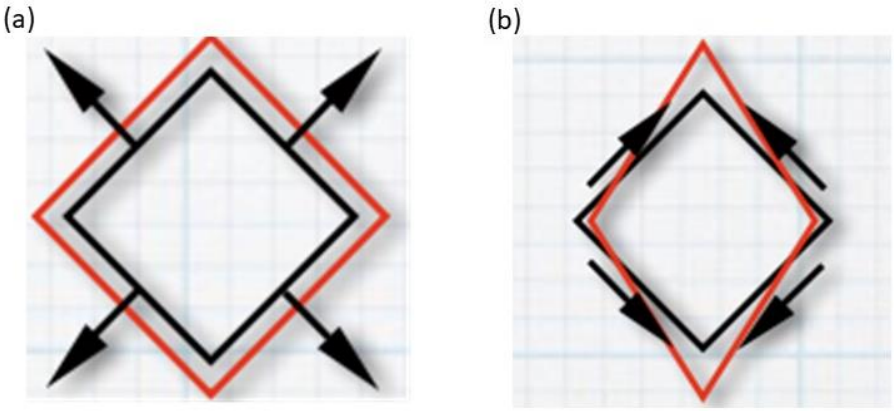

Figure 1. 1. Schematic representation of common dilational (a) and shear (b) deformation in a 2D perspective.

To understand the flow and deformation behavior of materials, it is essential to introduce the constitutive equations that describe the rheological properties. Constitutive equations form the backbone of rheological modeling, providing a mathematical framework that relates the stress within a material to its deformation and flow properties. These equations capture the response of the material, strain, under various conditions of applied stresses, allowing prediction of its behavior in practical applications. In the context of complex fluids and soft solids, constitutive equations account for the intricate interactions between different phases and microstructures that are critical to the design and optimization of materials in industries ranging from pharmaceuticals to polymer processing, and from cosmetics to drug delivery systems. In this context, defining the stress applied in the k-direction as S_{jk}, where j represents the direction perpendicular to the plane to which S_{jk} belongs (**Figure 1. 2**). Similarly, defining the strain in the l-direction as D_{lm}, which belongs to the plane perpendicular to the m-direction. It is possible to define the relationship between the stress tensor S_{jk} and the strain tensor D_{lm} by the constitutive equation of the system, which provides information in how a specific material responds against different mechanical stimulus.

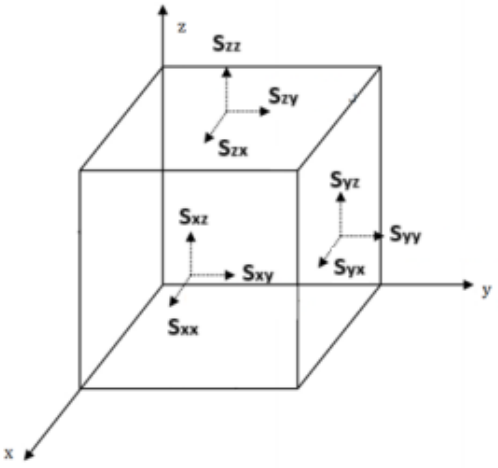

Figure 1. 2. Graphical representation of the reference system and the notation of S_{jk} stress components.

The constitutive equation is not universal; it depends on the specific behavior and properties of the material under study. It encompasses both linear and non-linear responses, capturing the complexity of real-world materials. For instance, in simple fluids, the relationship might be relatively straightforward, often described by Newtonian or non-Newtonian fluid models. In contrast, complex fluids and soft solids exhibit more intricate behaviors due to their microstructure and phase interactions, requiring more sophisticated models. Two limiting cases can be distinguished within the framework of the constitutive equations:

- Linear elastic solids: they exhibit a solid-like behavior, where the stress and strain are directly proportional, obeying Hooke law [3]. This behavior is common in materials that return to their original shape upon the removal of stress, provided the deformation is within the elastic limit. The constitutive equation for linear elastic materials can be expressed as,

$$S_{\mathrm{jk}} = E_{\mathrm{jklm}} D_{\mathrm{lm}}, \tag{1.1}$$

  where E_{jklm} is the fourth Cauchy elastic tensor, or simply the elasticity tensor. If the strain is small enough, there is a linear relationship between the strain and the stress. In case of purely extensional deformation (j=k=l=m=1), $E_{\mathrm{jklm}} = E$ is the dilational elastic modulus, while in case of shear stress/deformation, (e.g., j=l=1 and k=m=2), $E_{\mathrm{jklm}} = G$ is the shear elastic modulus: both quantities *G* and *E* refer to the elasticity of the system, so its capability to restore initial configuration after an applied stimulus, and to store mechanical energy without dissipation.

- Viscous liquids: they undergo a continuous shape change under the applied stress, and obey Newton law [4],

$$S_{\mathrm{jk}} = \eta \dot{D}_{\mathrm{lm}}, \tag{1.2}$$

  where $\dot{D}_{\mathrm{lm}}$ is the strain rate tensor, and η is the viscosity. Purely viscous fluids are usually incompressible, so $\dot{D}_{\mathrm{lm}}$, S_{jk} and η refer to shear flow rather than extensional flow. Viscosity is related to the energy dissipated during flow, and accounts for the hindrance to fluid motion due to viscous friction.

Many complex fluids, as well as many polymer solutions and, in general, soft matter, exhibit a viscoelastic behavior. In this situation, the relationship between stress and strain is more complex than those discussed above, often involving time-dependent behavior. Materials exhibiting viscoelasticity have both viscous and elastic characteristics, meaning their response to stress includes both immediate elastic deformation and delayed viscous flow. However, elasticity or viscosity may prevail according to the involved timescale corresponding to the material relaxation process and the frequency of the applied stimulus. As will be discussed in the following, viscoelasticity is always associated with time-dependence (or frequency-dependence) of the rheological parameters (both elasticity and viscosity). Thus, the stress response not only depends on the value of strain and/or strain rate, but also on the past mechanical history of the applied stimuli. Viscoelasticity also implies a temporal delay between the applied stimulus and the response, associated to viscous dissipation.

1.2. Bulk and interfacial rheology in fluid system

The rheological characterization may concern to either the entire volume of the fluid, or its interface with other fluids. This distinction is crucial because the rheological properties and behaviors can differ significantly between the bulk and the interface. For instance, bulk rheology focuses on the material's response throughout its volume, encompassing the overall mechanical properties and flow behavior under various stresses and strains. On the other hand, interfacial rheology examines the properties and behaviors at the boundary between two phases, such as liquid-gas, liquid-liquid, or liquid-solid interfaces. This is particularly important in systems where surface phenomena dominate, such as emulsions, foams, and surfactant solutions. Thus, it is essential to distinguish between bulk rheology and interfacial rheology to accurately understand and predict the material's response in different applications.

- Bulk or 3D rheology involves the application of a mechanical stimulus to the entire volume of the fluid. Usually, fluids are incompressible, so many times bulk shear modes play a more important role than dilational bulk modes. In bulk shear rheology, the applied stresses and the resulting deformations are measured throughout the fluid volume. The units of the applied stresses, as well as the elastic modulus, are the same as pressure ([Pa]) and the units of viscosity are [Pa∗s]. This three-dimensional approach is crucial for understanding the overall mechanical properties and flow behavior of fluids under various stresses and strains.

- Interfacial or quasi-2D rheology. Interfacial rheology focuses on the behavior of complex fluid-fluid interfaces, such liquid-vapor or liquid-liquid interfaces, where the presence of surface-active chemical species influence the value of surface tension, i.e., the energy per unit area required to increase the contact surface between the two fluid phases. Any deformation applied to this interface, can significantly modify its state. On one side, dilational deformations can modify the surface concentration of chemical species, leading to changes in surface tension. On the other hand, shear deformations can change the arrangement of chemical species and the shape of the interface. The resulting changes can impact the stability and behavior of the interface. In interfacial rheology, it is useful to define also elasticity and viscosity associated with stresses and strains applied at fluid-fluid interfaces. Surface stress and elasticity have the same unit as surface tension ([N/m]), while surface viscosity unit is [N·s/m].

By distinguishing between bulk and interfacial rheology, it is possible to obtain a better understanding and prediction on how materials will behave under different mechanical stimuli. **Table 1. 1** reports the different rheological properties of fluids, summarizing the above discussion.

Table 1. 1. Summary of the different rheological schematic properties of fluids. The shaded part of the table indicates the main focus of this PhD Thesis.

	Bulk	**Interfacial**
Shear	Bulk Shear Elastic Modulus [Pa] Bulk Shear Viscosity [Pa∗s]	Interfacial Shear Elastic Modulus [N/m] Interfacial Shear Viscosity [N∗s/m]
Dilational	Bulk Dilational Elastic Modulus [Pa] Bulk Dilational Viscosity [Pa∗s]	Interfacial Dilational Elastic Modulus [N/m] Interfacial Dilational Viscosity [N∗s/m]

Concerning bulk rheology, the fluids that will be studied in this work are incompressible (although, as explained before, liquid-vapor interface is compressible), which means that only bulk shear rheology deserves to be investigated. To give an exhaustive characterization of the mechanical properties of complex fluids, bulk shear rheology must be considered, so in this chapter a brief overview on bulk shear rheology will be provided. Bulk shear rheology helps on the understanding of the industrial processability of complex fluids, as well as the performance of products. Furthermore, as mentioned in reference [5], the presence of viscoelasticity in the bulk must be taken into account in order to fully characterize high frequency dilational interfacial rheology of some systems (e.g., concentrated polymeric solutions, gels…). This latter aspect will be deepened in *Chapter IX: Interfacial rheology of PVA/Borax viscoelastic solutions*.

1.3. Bulk Shear Rheology

The 3D stress tensor of an isotropic fluid can be expressed as [6],

$$\boldsymbol{S} = \begin{pmatrix} S_{11} & S_{12} & 0 \\ S_{12} & S_{22} & 0 \\ 0 & 0 & S_{33} \end{pmatrix}, \tag{1.3}$$

where S_{jj} are the normal stresses along j direction which can produce elongation or compression, and S_{12} is the shear stress. This latter induces shape deformation into the fluid, without any volume variation. Normal stresses are associated with dilational bulk rheology, while bulk shear rheology concerns shear strain responses to shear stress stimuli.

Understanding the stress tensor components is crucial for analyzing the mechanical behavior of isotropic fluids under various conditions. In many practical applications, such as in fluid dynamics and material science, it is essential to distinguish between the effects of normal and shear stresses. Normal stresses, which relate to elongation or compression, contribute to changes in volume and are primarily linked to the fluid's dilational properties. On the other hand, shear stresses, responsible for shape deformation, are key to understanding the fluid's shear rheology without altering its volume. To further illustrate the concept of shear stress in an isotropic fluid, consider a fluid element with a thickness *h* that undergoes a simple shear flow occurring at a certain velocity *U*. At a given time *t*, this flow induces a displacement *d=Ut*. The shear strain, can be then defined as as the ratio of this displacement to the thickness of the fluid element $D_{12} = d/h$. Correspondingly, the shear strain rate is given by $\dot{D}_{12} = U/h$ (**Figure 1. 3**).

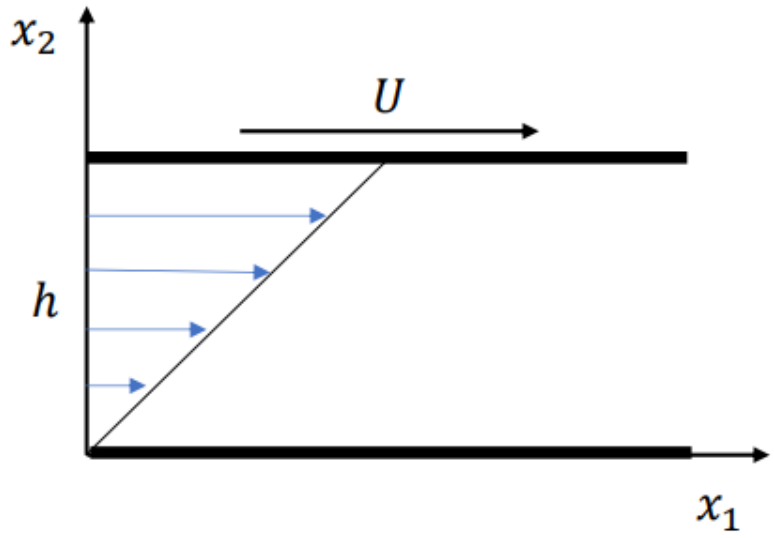

Figure 1. 3. Schematic representation of a simple shear flow in a fluid element.

S_{12} and $\dot{D}_{12}$ are related by means of a constitutive equation, that depends on the system. For a purely viscous fluid, this constitutive equation is given by,

$$S_{12} = \dot{D}_{12}\eta(\dot{D}_{12}), \tag{1.4}$$

where $\eta(\dot{D}_{12})$ is the bulk shear viscosity, that may be either shear-rate-independent as occurs in Newtonian fluids where there is a linear dependence between shear stress and shear strain rate, or shear-rate-dependent as in the case of Non-Newtonian fluids where a non-linear dependence between shear stress and shear strain rate is found. In general, the shear stress can be expressed by means of a power law function, according to the following equation,

$$S_{12}(\dot{D}_{12}) = \tau_y + k\dot{D}_{12}{}^{n+1}, \tag{1.5}$$

where τ_y represents the yielding stress of the fluid, i.e., the threshold stress above which the fluid starts to flow, *k* is the consistency, and *n* the viscosity exponent. If both $\tau_y = 0$ and n=0, the fluid shows a Newtonian behaviour as occurs in many simple fluids, such as water. When *n*>1, the system undergoes a dilatant flow or shear-thickening process, that implies an increase of bulk shear viscosity with shear strain rate as occurs in quicksand or starch concentrated solutions. On the other hand, if *0*<*n*< 1 the system undergoes a pseudoplastic flow or shear thinning process. This involves an increase in the shear strain rate as a result of the decrease in system viscosity. This type of behavior is common in blood, ketchup or polymer solutions. Whenever $\tau_y > 0$, the presence of a yielding stress is known as Bingham flow or plastic flow, depending on whether, respectively, *n*=0 or 0<*n*<1. This type of behavior is typically observed in mayonnaise, whipped cream or toothpastes. **Figure 1. 4** summarized the qualitative dependences for the shear stress on the shear rate for each one of the aforementioned cases.

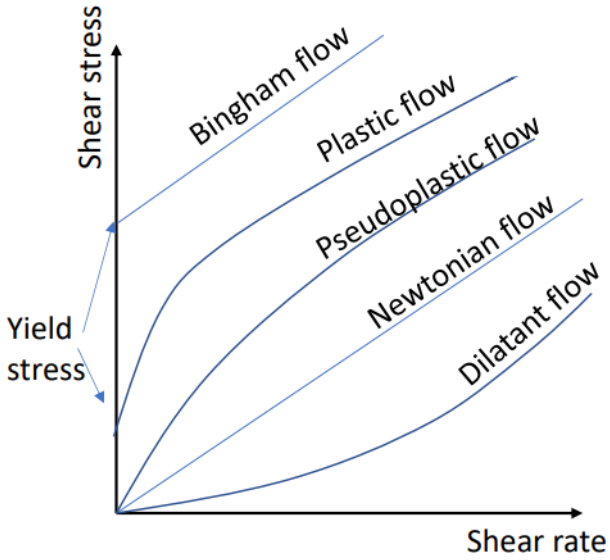

Figure 1. 4. Shear stress/strain-rate curves of different types of flows.

Let us now consider the case of a viscoelastic fluid. The coexistence of elasticity and viscosity in such fluid requires a more comprehensive characterization. To fully describe the behavior of a viscoelastic fluid, it is needed to define an elastic shear relaxation modulus *G(t)* and a time-dependent shear viscosity *η(t)*. These two quantities are interrelated, as expressed by the following equation,

$$\eta(t) = \int_0^t G(t - t')dt'. \tag{1.6}$$

This relationship underscores the complexity of viscoelastic fluids, which exhibit both solid-like and liquid-like behavior depending on the timescale of observation. In order to understand the physical meaning of *G(t)* and *η(t),* it is worth to introduce Meyer constitutive equation, that relates S_{12}, $\dot{D}_{12}$ and D_{12},

$$S_{12}(t) = G(t)D_{12}(t) + \eta(t)\dot{D}_{12}(t). \tag{1.7}$$

According to this model, in a viscoelastic fluid, the stress response $S_{12}(t)$ is the result of the sum between an elastic component $G(t)D_{12}(t)$, which is related to the deformation *D(t)*, and a viscous component $\eta(t)\dot{D}_{12}(t)$, which is related to the strain rate $\dot{D}_{12}(t)$. Notice that, in a viscoelastic fluid, the stress response, as well as the viscoelastic functions *G(t)* and *η(t),* are time dependent, i.e., the behaviour of a viscoelastic fluid depends on the mechanical history of the strain.

A more sophisticated constitutive equation is given by the so-called Boltzmann's model, that considers the past history of the strain, and determines the stress response as a linear superposition of the stresses that result from strains at present and past times,

$$S_{12}(t) = \int_0^t G(t - t')\dot{D}_{12}(t')dt'. \tag{1.8}$$

Let us now consider the case of an oscillatory flow in a viscoelastic fluid, occurring at a certain angular frequency ω, and a certain strain amplitude $D_0 = \delta/h$, where δ represent the displacement amplitude of the oscillatory flow (see **Figure 1. 5**).

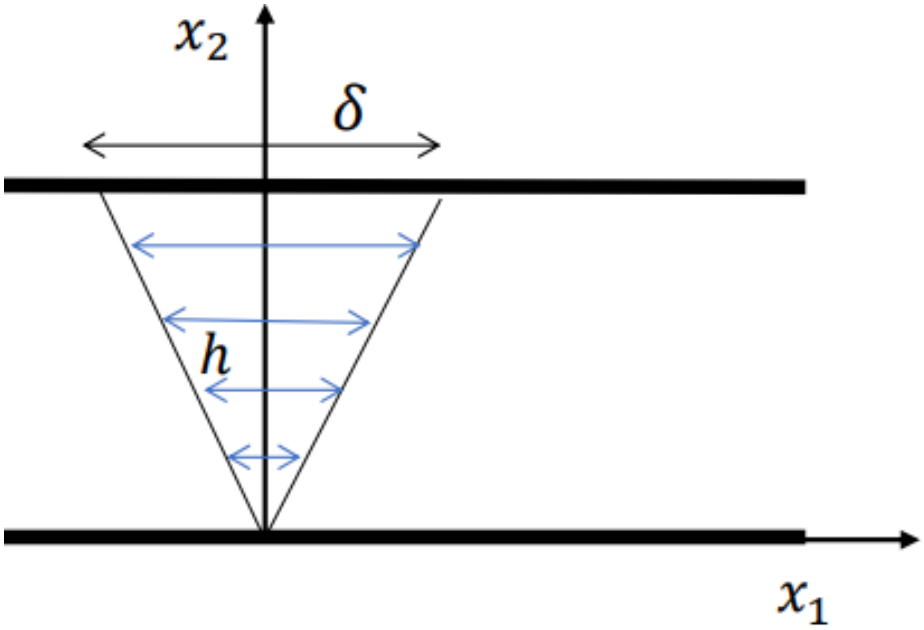

Figure 1. 5. Schematic representation of an oscillatory flow in a viscoelastic fluid element with h being thickness and and δ the displacement amplitude.

In the above oscillatory flow, the strain $D_{12}(t)$ varies in time according to a sine function,

$$D_{12}(t) = D_0\, sin(\omega t). \tag{1.9}$$

Consequently, the strain rate can be represented as,

$$\dot{D}_{12}(t) = \omega D_0\, cos(\omega t) = \dot{D}_0\, cos(\omega t). \tag{1.10}$$

If the strain amplitude is small enough ($\delta << h$), the stress response is linear, i.e., does not depend on strain amplitude. Therefore, it can be expressed, by means of Boltzmann's model, in the following way,

$$\begin{aligned} S_{12}(t) &= \int_{-\infty}^{t} G(t-t')\dot{D}_0\, cos(\omega t)\, dt' = \int_{0}^{\infty} G(s)\dot{D}_0\, cos(\omega(t-s))\, ds \\ &= G'(\omega)D_0\, sin(\omega t) + \eta'(\omega)\dot{D}_0\, cos(\omega t), \end{aligned} \tag{1.11}$$

where $G'(\omega)$ is the storage dynamic shear modulus, which can be defined as,

$$G'(\omega) = \int_{0}^{\infty} \omega G(s)\, sin(\omega s)\, ds, \tag{1.12}$$

and $\eta'(\omega)$ is the loss dynamic shear modulus,

$$\eta'(\omega) = \int_0^\infty G(s)\, cos(\omega s)\, ds. \tag{1.13}$$

Notice that the last part of equation (1.11) exactly corresponds to the Meyer constitutive relation. Based on that, we can define the loss dynamic shear modulus as,

$$G''(\omega) = \omega\eta'(\omega), \tag{1.14}$$

and the storage dynamic shear viscosity as,

$$\eta''(\omega) = \frac{G'(\omega)}{\omega}. \tag{1.15}$$

In complex notation, the complex dynamic shear modulus can be expressed as,

$$G^*(\omega) = G'(\omega) + iG''(\omega). \tag{1.16}$$

The storage modulus $G'(\omega)$ represents the stored energy in the material, which is recoverable upon removing the deformation, while the loss modulus $G''(\omega)$ corresponds to the energy dissipated, commonly as heat during deformation. Similarly to the definition of the complex dynamic shear modulus, it is possible to define the complex dynamic shear viscosity as,

$$\eta^*(\omega) = \frac{G^*(\omega)}{i\omega} = \eta'(\omega) - i\eta''(\omega). \tag{1.17}$$

Notice that the imaginary part of the $\eta^*(\omega)$ is related to the storage component of $G^*(\omega)$, i.e., it associated with the elastic behaviour of the fluid.

It is worthy to show that the stress response can be also expressed in an alternative form, underlining the fact that there is a certain phase shift φ between $S_{12}(t)$ and $D_{12}(t)$, and that phase shift is due to the time lag ($\Delta t = \varphi/\omega$) between the response and the applied stimulus, which is typically observed in any viscoelastic fluid. This is an intermediate behaviour between an elastic solid ($\varphi = 0$, the stress is in phase with the strain) and a viscous fluid ($\varphi = \pi/2$, the stress is delayed $\pi/2$ with the strain). **Figure 1. 6** shows an idealized representation of the temporal profiles for the shear strains and stresses obtained in an elastic solid, viscous fluid and viscoelastic fluid.

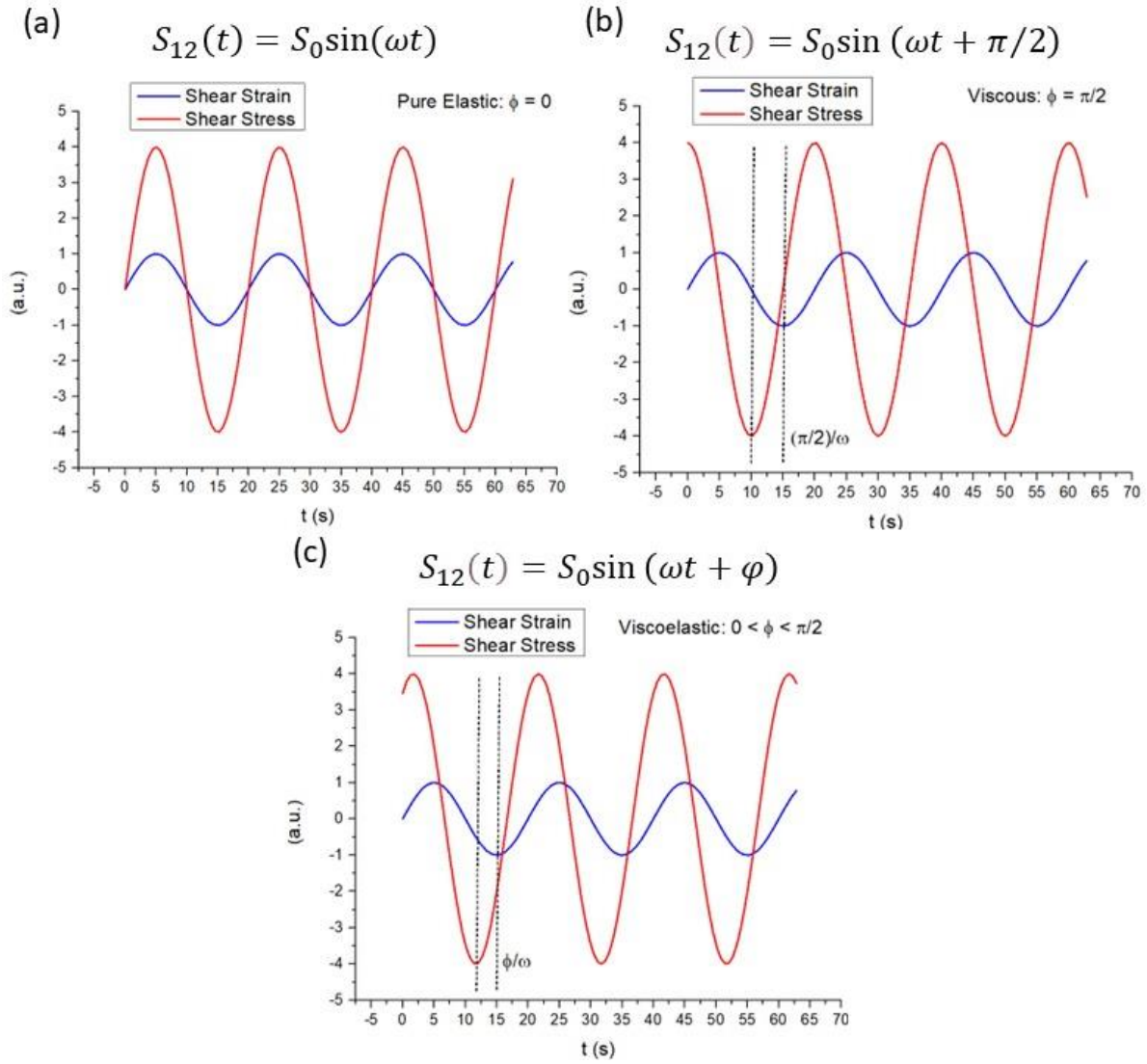

Figure 1. 6. Idealized strain and stress profiles for shear deformations in an elastic solid (a), viscous fluid (b), and viscoelastic fluid (c).

So, in a viscoelastic fluid, the stress response can be also represented by the sum of two components, the in-phase component (elastic) and the delayed component (viscous),

$$S_{12}(t) = S_0\, sin(\omega t + \varphi) = S_0\, cos(\varphi) sin(\omega t) + S_0 sin\,(\varphi) cos(\omega t). \tag{1.18}$$

In analogy with equation (1.11) it is easy to prove that,

$$G'(\omega) = \frac{S_0}{D_0} cos(\varphi) = |G^*(\omega)| cos(\varphi), \tag{1.19}$$

and that,

$$G''(\omega) = \frac{S_0}{D_0} sin(\varphi) = |G^*(\omega)| sin(\varphi). \tag{1.20}$$

Also the phase angle φ depends on ω, and its tangent, the so called loss tangent expresses, somehow, the amount of viscous dissipation that occurs into a viscoelastic fluid subjected to shear deformation:

$$tan(\varphi) = \frac{G''(\omega)}{G'(\omega)} \tag{1.21}$$

There are theoretical models that provide valuable insights into predicting the trends of $G'(\omega)$ and $G''(\omega)$ as a function of the angular frequency ω. Thus, it is possible to define how the elastic shear relaxation modulus $G(t)$ relaxed over time as follows [7],

$$G(t) = \sum_{j=1}^{n} G_j e^{-\frac{t}{\lambda_j}}. \tag{1.22}$$

Equation (1.22) is known as Maxwell relaxation spectrum, where λ_j is the characteristic relaxation time of j-*th* relaxation process ($\nu_j = 1/\lambda_j$ is the relaxation frequency). This exponential decay function is typical for viscoelastic materials, capturing the essence of their time-dependent behavior. Let us consider the simplest case where the system undergoes a single relaxation process (n=1, $\lambda_1=\lambda$ and $G_1=G$). In this situation, the complex dynamic shear modulus, according to equations (1.12) and (1.13), can be defined as,

$$\begin{aligned} G^*(\omega) &= \int_0^\infty \omega G(s)\, sin(\omega s)\, ds + i\omega \int_0^\infty G(s)\, cos(\omega s)\, ds \\ &= \frac{G\omega^2\lambda^2}{\lambda^2\omega^2 + 1} + i\frac{G\omega\lambda}{\lambda^2\omega^2 + 1}. \end{aligned} \tag{1.23}$$

Figure 1. 7 shows an idealized representation of the dependences of the magnitudes involved in equation (1.23) $G''(\omega)$ reaches the maximum at the value of relaxation frequency $\omega=1/\lambda$, and when $\omega \to \infty$, $G'(\omega)$ reaches the upper-bound value of $G(t=0)=G$.

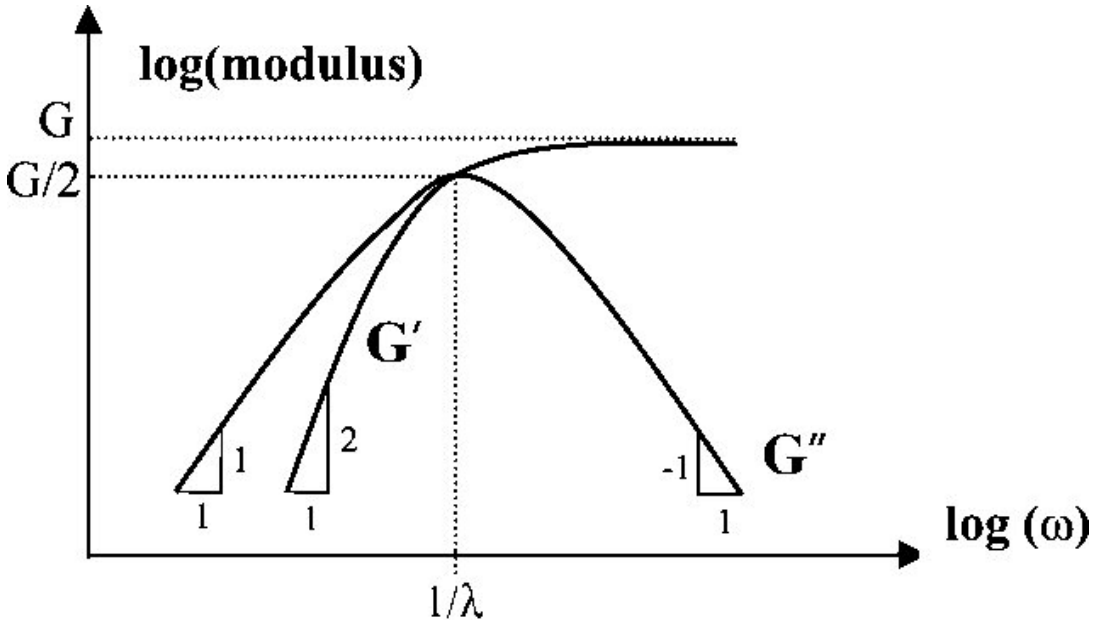

Figure 1. 7. Idealized representation of Plot the frequency dependence of G'(ω) and G''(ω) according to the Maxwell model, in the case of a single relaxation process.

1.4. The importance of Interfacial Rheology

Complex fluid/fluid interfaces are ubiquitous in nature appearing in many industrial processes or academia. For instance, they can be exploited to provide structure to different products, including foam and emulsion-based ones. Moreover, they are present in a broad range of chemical processes, including liquid-liquid extraction, froth flotation, wastewater treatment or tertiary oil recovery. On the other side, fluid/fluid interfaces can be used as platforms for nanostructured material fabrication, or as model to elucidate problems with biological and medical relevance [8-12]. Therefore, it may be expected that most of the fluid/fluid interfaces with technological or scientific relevance involves systems operating under dynamic conditions, and hence the understanding of the dynamic and mechanical properties of interfacial layers at fluid/fluid interfaces is of a paramount importance for living systems, foods, personal care products, and the environment [13].

The rheological performance of fluid/fluid interfaces can be modulated almost at will to design soft interface-dominated materials for specific applications [14,15]. This makes of the understanding of the deformation and flow of fluid/fluid interfaces under the application of mechanical stresses, i.e., the rheological properties of the interface, a matter of key importance for scientific and technologist [16,17]. For instance, the understanding and control of the rheological response of fluid/fluid interfaces plays a very important role in the control of emulsion stability [18,19], foamability and foam stability (resistance against drainage) [20], lung surfactant performance [11,21], aerosol formation [22], tear film stability [23,24], encapsulation processes [25], coffee ring formation [26], tertiary oil recovery [27] or remote sensing [28,29].

The description of the rheological response of 2D systems (or more correctly quasi-2D systems), i.e., layers of surface-active compounds confined at fluid/fluid interfaces, is not always trivial. In fact, interfacial rheology relies on the confinement of the applied deformation within the interface xy plane, which requires to introduce specific modification to the classical rheological formalism used for the study of the mechanical response of bulk systems. This is

of a paramount importance because in most of the cases the small thickness of fluid/fluid interfaces makes difficult to decouple the pure interfacial rheological response from the contribution associated with the response of the adjacent bulk phases to the applied stress. Therefore, it is necessary to develop suitable experimental and theoretical methodologies enabling such decoupling [30,31]. This is significant because the combination of experimental and theoretical tools may contribute to deep on the impact of the stress boundary conditions on the behavior and breakup of thin films [32].

Despite the critical importance of the mechanical properties of fluid/fluid interfaces for a wide range of technological and scientific purposes, there is a broad range of aspects that remains poorly understood and deserve further investigation. Therefore, our focus will be on providing an updated and comprehensive perspective on the current understanding of how fluid/fluid interfaces perform when subjected to dilational stresses, highlighting recent advances and identifying key areas where more research is needed. This is important because dilational rheology plays an essential role in a broad range of scientific and technological aspects, ranging from the formation and stability of foams to the respiratory cycle, and from tertiary oil recovery to demulsification processes [33-35]. However, the study of the performance of interfaces under dilational stresses is particularly challenging because it requires to deconvolute the changes in thermodynamic properties associated with the changes in the interfacial concentration and the intrinsic compressional viscoelasticity, which is not always easy [36].

1.5. Equilibrium properties of interfaces

Given two phases (i.e., portions of space characterized by homogeneous chemical composition and physical properties), the interface can be defined as the boundary surface separating one phase to the other. It is important to highlight that the boundary between the two phases is not commonly sharp, existing a smooth transition between one phase and the other, i.e., a boundary layer where the properties smoothly change between one phase and another (usually, few nm), and therefore, the concept of interface is rather a "mathematical idealization".

An important equilibrium property to describe the thermodynamic behavior of a fluid/fluid interface is the interfacial tension γ, which is defined as the energy W per unit area A that must be spent to increase the contact surface between two phases,

$$\gamma = \frac{dW}{dA}. \tag{1.24}$$

In case of liquid/vapor interfaces (which will be deeply studied in this thesis), it is common to refer to "surface tension" rather than to "interfacial tension". The surface tension is the result of the cohesive forces of the molecules of a liquid placed at liquid/vapor interface, which is due in turn to the unbalance of forces that molecules at the interface experience. In fact, while molecules in the bulk are equally pulled in all directions by the surrounding similar molecules (so, their net force is zero), in molecules at the interface the attraction from other bulk molecules prevails, causing a force unbalance that results in the onset of cohesion forces, hence to the appearance of a "surface tension" (see **Figure 1. 8**).

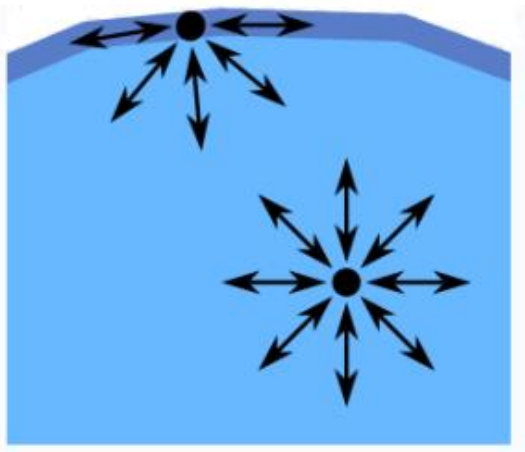

Figure 1. 8. Sketch of intramolecular forces of a liquid, in the bulk and at the interface.

The adsorption of soluble species to the interface from a bulk solution, or the direct deposition of insoluble surface-active species at the interface leads to the formation of the so-called Gibbs and Langmuir monolayers, respectively (**Figure 1. 9**). There are many types of surface-active molecules, but they all have one aspect in common: the amphiphilic character, since they consist of a hydrophobic tail and a hydrophilic head. Examples of surface active molecules are given by surfactants and amphiphilic copolymers.

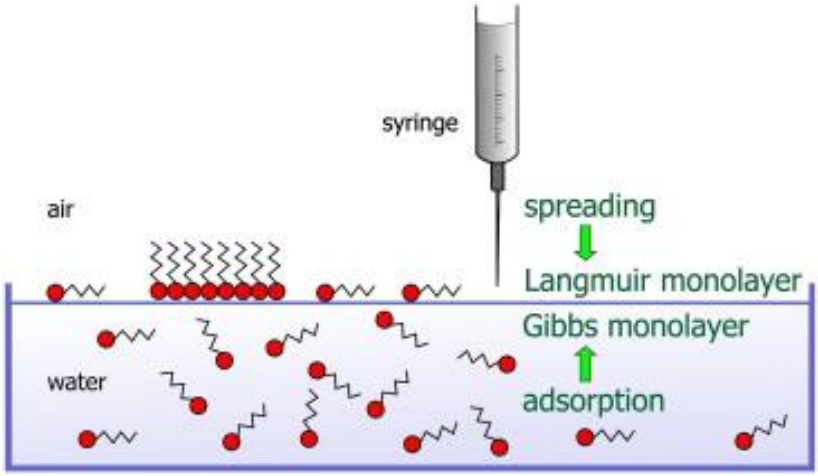

Figure 1. 9. Comparison between Gibbs monolayer (formed by adsorption of surface-active molecules from the bulk to the interface) and Langmuir monolayer (formed by deposition of surface-active molecules directly at the interface). Adapted from ref. [37].

The formation of these interfacial layers is accompanied by a variation of chemical potential *u*, as well by a decrease in the interfacial tension *γ* (with respect to the value associated to the bare interface, γ_0), according to the following equation [38],

$$-d\gamma = \Gamma_s du, \tag{1.25}$$

with Γ_s being the surface excess concentration of surface-active molecules adsorbed at the interface. Since $du = RTd[\ln(a)]$, where *T* is the temperature, *R* the ideal gas constant, *a* the activity coefficient of the surface active molecules (for diluted mixtures, the activity can be assumed to be equal to the bulk concentration of surface active molecules *C*), equation (1.25) can be expressed in the following form (Gibbs equation),

$$\Gamma_s = -\frac{1}{RT}\left(\frac{d\gamma}{d[ln(C)]}\right)_{T,P}. \tag{1.26}$$

It is worth to highly that Γ_s and γ must be considered as equilibrium properties of the interface, and therefore the Gibbs equation is only valid at equilibrium, where neither Γ_s or γ considerably change in time (ideally, at $t \to \infty$). Nevertheless, surfactant adsorption at fluid/fluid interface, is commonly guided by diffusion, and it is a time dependent process. This leads to a situation in which the surface concentration $\Gamma(t)$ varies with time, according to the following equation [39],

$$\frac{d\Gamma(t)}{dt} = D\left(\frac{\partial C(x,t)}{\partial x}\right)_{x=0}, \tag{1.27}$$

where D is the diffusion coefficient of surfactant into the solvent (typically, in water). $C(x,t)$ varies in space and time according to Fick equation,

$$\frac{dC(x,t)}{dt} = D\frac{\partial^2 C(x,t)}{\partial x^2}. \tag{1.28}$$

By setting boundary conditions ($C(0,t) = C_s(t)$ and $C(x,0) = C_0$), and solving equations (1.27)-(1.28), it is possible to obtain $\Gamma(t)$ (Ward-Tordai equation),

$$\Gamma(t) = \sqrt{\frac{D}{\pi}}\left[2C_0\sqrt{t} - \int_0^t \frac{C_s(\tau)}{\sqrt{t-\tau}}d\tau\right]. \tag{1.29}$$

At equilibrium, the surface excess concentration is defined as: $\Gamma_s = \lim_{t\to\infty}\Gamma(t)$. In common experimental practice, this condition is observed whenever γ keeps almost constant in time. In order to establish a relationship between Γ_s and C, there are many models describing adsorption equilibrium. The simplest one is given by Langmuir [38] which assumes an equilibrium between adsorption and desorption process, with no mutual interaction between adsorbed molecules, which can adsorb at the interface until all the sites are occupied. Let $\theta = \Gamma_s/\Gamma_\infty$ be the fraction of occupied sites, where Γ_∞ is the maximum surface excess concentration associated to interface saturation, related to surfactant molecular area: $\tilde{A} = 1/N_A\Gamma_\infty$ (with N_A being the Avogadro number). Adsorption rate is given by $v_A = k_A C(1-\theta)$ (where k_A is the adsorption kinetic constant), while desorption rate is given by $v_D = k_D\theta$ (where k_D is the adsorption kinetic constant). At equilibrium, by setting $v_A = v_D$, the following relation can be obtained:

$$\Gamma_s = \Gamma_\infty\frac{K_L C}{1 + K_L C}, \tag{1.30}$$

where K_L is the Langmuir equilibrium constant. By replacing equation (1.30) into (1.26), and integrating with respect to C, the so-called Langmuir-Gibbs isotherm can be easily obtained,

$$\gamma = \gamma_0 - RT\Gamma_\infty \, ln(1 + K_L C) = \gamma_0 - RT\Gamma_\infty \, ln\left(1 + \frac{\frac{\Gamma_s}{\Gamma_\infty}}{K_L\left(1 - \frac{\Gamma_s}{\Gamma_\infty}\right)}\right). \quad (1.31)$$

Equation (1.31) is valid in dilute and semi-dilute regime, far below Γ_∞ (corresponding to the saturation of the interface). Langmuir-Gibbs isotherm is not the only existing theoretical model to predict the behavior of monolayers. A more sophisticated model, taking into account the interaction energy between adsorbed molecules, is given by Frumkin isotherm [40],

$$\gamma = \gamma_0 - RT\Gamma_\infty \left[\ln\left(1 - \frac{\Gamma_s}{\Gamma_\infty}\right) + \alpha\left(\frac{\Gamma_s}{\Gamma_\infty}\right)^2\right], \quad (1.32)$$

where α is a parameter related to the interaction energy. In Frumkin isotherm, Γ_s can be related to surfactant bulk concentration C by means of the following equation:

$$C = \frac{\Gamma_s/\Gamma_\infty}{k_F(1 - \Gamma_s/\Gamma_\infty)} e^{-2\alpha\Gamma_s/\Gamma_\infty}, \quad (1.33)$$

With k_F being the Frumkin equilibrium constant. An example of experimental data fitting with Frumkin isotherm is shown in **Figure 1. 10**. Equation (1.32) fits with experimental data only in dilute and semi-dilute regime, while it does not foresee the plateau at higher concentration (associated to the formation of micelles, above CMC).

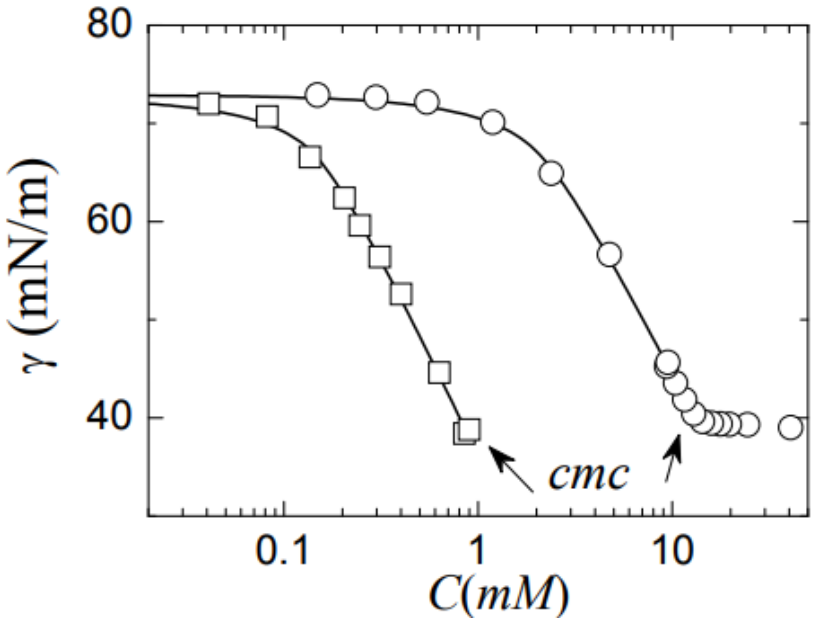

Figure 1. 10. Example of surface tension data fitting with Frumkin isotherm of two different surfactants: hexadecyl trimethylammonium bromide or CTAB (squares) and dodecyl trimethylammonium bromide or DTAB (circles). Solid line represents the best fit to equation (1.32). Adapted from ref. [41].

1.6. Interfacial Rheology: Foundations

The interfacial tension only provides an equilibrium picture of the true situation of the interface, and as it was mentioned above this is not enough in most practical applications of fluid/fluid interfaces. In fact, fluid/fluid interfaces with technological and scientific relevance are commonly subject to external mechanical perturbations that results in a modification of

their size or shape [42]. The understanding of the response of fluid/fluid interfaces to mechanical processes is essential, because even the simplest deformation process can yield very complex responses including multiple dynamic processes or deformation mixing different interfacial modes [43].

The interfacial response against perturbations that modify the size of the interface without affecting to its shape is defined in terms of the dilational elasticity and viscosity, whereas the modification of interfacial shape at constant size can be described in terms of the shear elasticity and viscosity [42,44]. Moreover, under specific stress conditions, fluid/fluid interfaces can undergo out-of-plane deformations. These are characterized by an out of interfacial plane displacement of the whole monolayer or parts of the monolayer (splaying or bending), resulting in the emergence of different phenomena, e.g., buckling of the monolayer, expulsion of material into the bulk or the formation of multilayers [45]. This transverse out-of-plane deformations are restored under the action of interfacial-tension-driven forces, whereas in-plane modes (shear and dilation) are directly restored by interfacial tension gradients associated with the interfacial concentration [31,46]. The interfacial tension gradients can emerge due to different factors, including the interfacial convection of adsorbed species or the heterogeneity of the adsorbed layers. However, the origin of the interfacial tension gradients occurring during interfacial rheology experiments is found in an externally triggered modification of properties, e.g., interfacial concentration, affecting directly to the interfacial tension. This drives the Marangoni flows trying to restore the interfacial equilibrium [43]. **Figure 1. 11** shows a sketch representing the in-plane and out-of-plane deformation modes that can occur in fluid/fluid interfaces under the action of mechanical stresses.

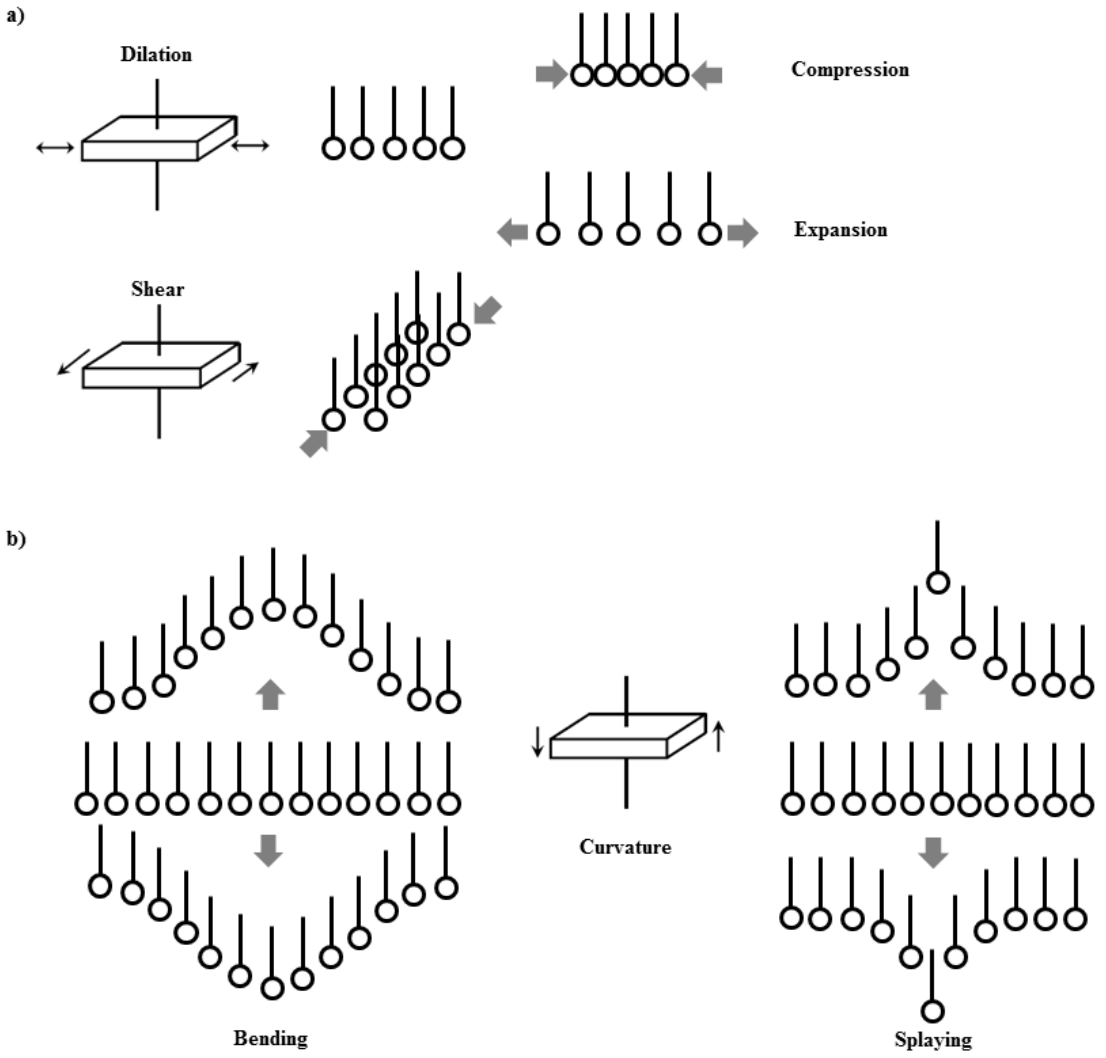

Figure 1. 11. Sketch of different surface relaxation modes: a) in-plane-modes (dilation and shear) and (b) out of plane modes (bending and splaying). Reprinted from Maestro and Guzmán [46].

It should be noted that in most of cases, the out-of-plane deformations can be rigorously modelled, whereas the in-plane modes have been commonly analyzed for long time using very simplified models that may be considered as a generalization of the bulk behavior to the interface, which neglects some subtle aspects of the interfacial rheology, e.g., the existence of a finite dilational modulus which is not considered in bulk models designed for incompressible fluids or the role of the curvature modes [17,47]. Moreover, in most cases, the different rheological modes are coupled, and hence the determination of the real (storage modulus) and imaginary (loss modulus) components of the corresponding viscoelastic moduli is not always trivial. This can be understood considering that the origin on the interfacial properties gradient can arise from different processes, e.g., interfacial tension gradients can be originated by a gradient of the interfacial concentration, or as a result of the convective transport that generate a concentration gradient. This makes difficult, in some cases, to obtain independently the different modes of the rheological response from a single experiment [43]. However, this coupling presents interest in specific cases, e.g., for obtaining dilational moduli from experiments involving capillary waves [48]. Moreover, the coupling between the interfacial

response and the mechanical properties of the adjacent fluids or their structure introduces additional problems for a proper evaluation of the viscoelastic moduli [30].

The rheological analysis of interfaces requires to use a continuum approach, which considers that the bulk flows can be described in terms of the conservation equations for mass, momentum and energy, and specific coupling conditions. This results in an interface that can be defined as a 2D dividing surface located between two adjacent fluid phases ("sharp interface" framework) [17]. Considering the above picture, it is possible to define the Cauchy interfacial stress tensor σ_s as a combination of two contributions: (i) the interfacial energy, which accounts for the energetic cost associated with the presence of a fluid/fluid interface of fixed area, and provides information of any process changing the interfacial concentration and affecting the interfacial tension, and (ii) the Marangoni stresses emerging as a result of spatial interfacial tension gradients [16,17]. Thus, it is possible to define the interfacial stress tensor according to the following expression,

$$\sigma_s = \gamma(\Gamma_s, T)\delta_s + T, \tag{1.34}$$

with δ_s being the surface unit tensor, and γ is the interfacial tension which is a state variable depending on the surface excess concentration and the temperature. The second contribution to the interfacial stress tensor is the anisotropic tensor or interfacial extra stress ($T = [T_{jk}]$), and accounts for the energy required to deform the interface [8,49]. The surface stress tensor can be considered as a 2D second-order symmetric and tangential tensor embedded in 3D space [16].

Considering a purely viscous fluid/fluid interface, it is possible to provide a definition of the anisotropic tensor in terms of the Boussinesq-Scriven model [16],

$$T_v = [(\kappa_s - \eta_s)\nabla_s \cdot v]\delta_s + 2\eta_s D_s, \tag{1.35}$$

where κ_s and η_s are the interfacial dilational and shear viscosities, respectively. ∇_s is the interfacial gradient operator, v is the velocity vector on the interface and D_s is the interfacial rate-of-deformation tension [50].

$$D_s = \frac{[(\nabla_s v) \cdot \delta_s + \delta_s \cdot (\nabla_s v)^T]}{2}. \tag{1.36}$$

In general, the Boussinesq-Scriven model is used for describing the rheological properties of fluid/fluid interfaces due to viscoelastic character of most fluid/fluid interfaces, constituting . a very useful building block for creating a complete rheological model for a viscoelastic fluid/fluid interface [51].

In the case of the purely elastic fluid/fluid interface, it is possible to define the anisotropic tensor by a linear elastic model, according to the following expression (only valid for infinitely small deformations) [17],

$$T_{\mathrm{e}} = [(E_{\mathrm{s}} - G_{\mathrm{s}})\nabla_{\mathrm{s}} \cdot u]\delta_{\mathrm{s}} + 2G_{\mathrm{s}}U_s, \tag{1.37}$$

with E_{s} and G_{s} being the interfacial dilational and shear elasticity, respectively; u the displacement vector on the interface, and U_{s} the interfacial infinitesimal strain tensor,

$$U_{\mathrm{s}} = \frac{[(\nabla_{\mathrm{s}} u) \cdot \delta_{\mathrm{s}} + \delta_{\mathrm{s}} \cdot (\nabla_{\mathrm{s}} u)^T]}{2}. \tag{1.38}$$

It should be noted that bending stresses can also play a very important role under specific conditions, e.g., densely packed particle-laden fluid/fluid interfaces. However, for simplicity they are commonly not included [16].

The description of elastic interfaces against larger stresses requires to introduce a finite strain tensor. This is possible by separating the dilational and shear contributions in an interfacial elastic stress described by the following expression [52]:

$$T_{\mathrm{e}} = \frac{E_s}{u}\ln(u)\,\delta_{\mathrm{s}} + \frac{G_{\mathrm{s}}}{u}\left(\frac{B_{\mathrm{s}}}{u} - \frac{1}{2}tr\left(\frac{B_{\mathrm{s}}}{u}\right)\delta_{\mathrm{s}}\right), \tag{1.39}$$

where the deformations are defined by the left-Cauchy-Green interfacial strain tensor B_{s}, and u is the relative area deformation, i.e., the ratio between the instantaneous interfacial area and the interfacial area in a reference state. The combination of the two limit cases, i.e., the Newtonian and the quasi-linear neo-Hookean, is essential for a realistic description of real fluid/fluid interfaces, where viscoelasticity is of a paramount importance [16]. Let u_{j} be the j-component of the displacement vector, at a certain angular frequency ω:

$$u_{\mathrm{j}} = u_{\mathrm{j(0)}}e^{i(\omega t)}. \tag{1.40}$$

The jk-component of the anisotropic stress tensor in viscoelastic interfaces, in case of linear response, can be expressed as a linear combination between the elastic component $T_{\mathrm{e(jk)}}$ in phase with *uj* and $T_{\mathrm{v(jk)}}$ in quadrature with respect to u_{j} [53,54],

$$T_{\mathrm{ve(jk)}}(t) = T_{\mathrm{e(jk)}} + T_{\mathrm{v(jk)}} = T_{\mathrm{e0(jk)}}e^{i(\omega t)} + T_{\mathrm{v0(jk)}}e^{i(\omega t + \pi/2)} = T_{\mathrm{ve0(jk)}}e^{i(\omega t + \phi)}. \tag{1.41}$$

Figure 1. 12 represents the time evolution of μ_{j}, $T_{\mathrm{ve(jk)}}$, $T_{\mathrm{e(jk)}}$ and $T_{\mathrm{v(jk)}}$. Based on the above, the anisotropic stress tensor for a viscoelastic fluid, can be expressed in the following form,

$$T_{ve} = [(K_s{}^*(\omega) - \eta_s{}^*(\omega))\nabla_s \cdot v]\delta_s + 2\eta_s{}^*(\omega)D_s, \tag{1.42}$$

where $K_s{}^*$ is the complex dilational interfacial viscosity,

$$K_s{}^*(\omega) = \kappa_s(\omega) - i\frac{E_s(\omega)}{\omega}, \tag{1.43}$$

and $\eta_s{}^*$ is the complex shear interfacial viscosity defined as,

$$\eta_s^*(\omega) = \eta_s(\omega) - i\frac{G_s(\omega)}{\omega}. \tag{1.44}$$

Furthermore, we can define the complex dilational interfacial modulus:

$$E_s^*(\omega) = i\omega K_s^*(\omega) = E_s(\omega) + i\omega\kappa_s(\omega) = E_s(\omega) + iE_i(\omega) \tag{1.45}$$

and, eventually, the complex shear interfacial modulus:

$$G_s^*(\omega) = i\omega\eta_s^*(\omega) = G_s(\omega) + i\omega\eta_s(\omega) = G_s(\omega) + iG_i(\omega) \tag{1.46}$$

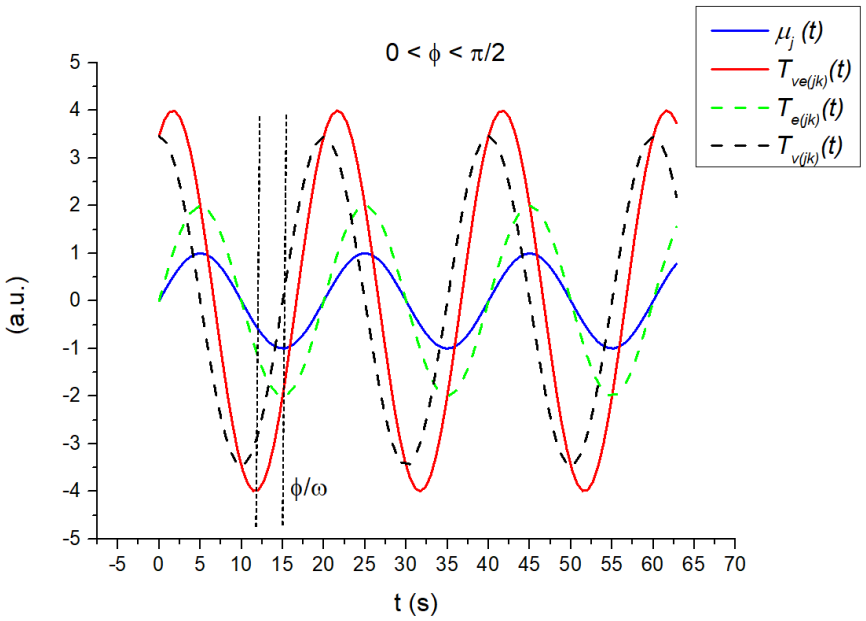

Figure 1. 12. Plot displaying the time evolution of μj, $T_{ve(jk)}$, $T_{e(jk)}$ and $T_{v(jk)}$.

1.7. Interfacial Dilational Rheology

The determination of the response of interfaces against dilation offers different experimental and theoretical challenges that are not present when the properties against shear stresses are evaluated. In fact, the application of isotropic dilational stresses to the interface, without any shear influence, is very difficult [16,55]. Moreover, the change of the interfacial area leads to modification of the interfacial concentration of the surface-active molecules existing at the interface, which yields a change in the state variable, i.e., the interfacial tension. On the other side, when soluble surface active molecules are concerned, the modification of the interfacial concentration may be the result of exchange processes involving the transference of molecules between the interface and the bulk, which introduces in many cases additional relaxation processes to the problem [16]. In fact, the ability of surface active soluble molecules to diffuse (diffusivity) from the adjacent fluid phases to the interface, and from the interface into the adjacent fluid phases as result of the modification of the interfacial area can originate surface tension changes, which are counteracted by the Marangoni flows aimed to re-establish the interfacial equilibrium.

The application of an infinitesimal uniaxial mechanical perturbation to a fluid/fluid interface leads to a small change of the surface area, δ*A*, which induces a time dependence modification of the interfacial pressure by a δ*Π* quantity (with *Π* being the interfacial pressure defined as $\Pi = \gamma - \gamma_{12}$, and γ_{12} the interfacial tension of a fluid/fluid interface loaded with surface active molecules, and γ the surface tension of fluid/fluid interface free of surface active molecules). This change emerges strongly dependent on the timescale probed during the specific experiment, and can be approximated according to the following expression,

$$\delta\Pi(t) = \Pi(t) - \Pi_0 = \frac{\partial \Pi}{\partial t}\delta A = -E_s(t)u(t), \tag{1.47}$$

where $u(t)$ and $E_s(t)$ account for the temporal dependence of the compressional strain and dilational viscoelastic modulus, respectively, and $\Pi(t)$ and Π_0 the temporal evolution of the interfacial pressure and the initial interfacial pressure, respectively. Thus, it possible to define the time evolution of the viscoelastic dilational modulus in terms of the following expression:

$$E_s(t) = -A_0\left(\frac{\partial \Pi}{\partial A}\right)_T, \tag{1.48}$$

and that corresponding to the compressional strain as,

$$u(t) = \frac{\delta A(t)}{A_0}. \tag{1.49}$$

From an experimental perspective, the dilational rheology measurements rely on the application of a time-dependent stress to the interface, and the evaluation of the time-dependence change of the interfacial tension. This type of measurements allows evaluating the ratio between the temporal evolution of the interfacial tension and the time-dependent stress. Assuming an oscillatory deformation of small amplitude and a fixed angular frequency ω (linear regime), this ratio is defined as the complex dilational interfacial modulus [56],

$$E_s{}^*(\omega) = \frac{\mathcal{F}\{\Delta\gamma(t)\}}{\mathcal{F}\{\Delta\, ln(A(t))\}} \tag{1.50}$$

where $\mathcal{F}$ is the Fourier transform operator, $\Delta\gamma(t)$ is the time evolution of the interfacial tension, $A(t)$ is the time evolution surface area and $E_s{}^*(\omega)$ is the same as defined in equation (1.45). The complex modulus can be split in its real (E_s) and imaginary components (E_v), which correspond to the storage and loss moduli, respectively [57,58]. It should be stressed that the constitutive viscoelastic parameters $E_s(\omega)$ and $\omega\kappa_s$ are functions of ω. Therefore, they provide information about the time-dependent response of the system subject to small perturbations of the interfacial area, playing a central role for probing the interfacial dynamics of adsorbed films. The definition of the viscoelastic interfacial dilational modulus accounts for a change of the applied stress as result of the adsorption/desorption state of the molecules and the interfacial structure. Thus, the interfacial area change can promote different relaxation processes, with different characteristic timescales, that are associated with the different

mechanisms involved in reestablishing the equilibrium state of the interface after the dilational deformation [59-61].

For fluid layers under equilibrium conditions, or when the layers are disturbed following a quasi-static path ($\omega \to 0$), the interfacial dilation forces leads to an instantaneous modification of the interfacial concentration ($\delta A/A = -\delta\Gamma/\Gamma$), and it is possible to define a limit value for the dynamic modulus at zero frequency. This is the so-called static modulus which is given by the Gibbs elasticity ε_0 defined as,

$$E_s(\omega \to 0) \to \varepsilon_0 = \Gamma\left(\frac{\partial \Pi}{\partial \Gamma}\right)_{eq}, \tag{1.51}$$

and hence this apparent elasticity can be considered a result of the deformation induced change in the interfacial concentration ($\Gamma = 1/A$), which in turn modifies the interfacial tension. This magnitude can be obtained from the relative slope of the equilibrium isotherm [42]. According to the above discussion, it is possible to define a dilational viscosity at zero frequency in terms of the frequency independent Newtonian limit,

$$\kappa_s(\omega \to 0) = \kappa_0 \tag{1.52}$$

Figure 1. 13 summarizes the typical material response expected for a viscoelastic layer undergoing a single relaxation process as result of the dilational deformation.

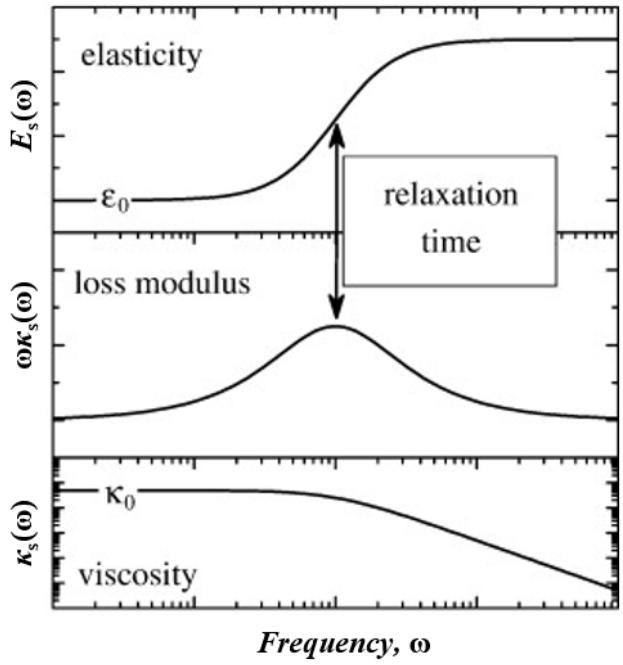

Figure 1. 13. Sketch of the typical material response for a viscoelastic layer undergoing a single relaxation process upon the application of a dilational stress. Adapted from Mendoza et al. [42].

1.8. Rheological tools for evaluating the response of planar fluid/fluid interfaces against dilation

Most of the tools to measure the response of planar fluid/fluid interfaces against dilational deformation provide information of the response against deformations within the linear response regime, which does not provide, in most of the case, a suitable representation of

some of the phenomena occurring in complex fluid/fluid interfaces with technological and scientific interest [13,16,62,63]. However, these tools provide importance information about the relaxation mechanism driving the re-equilibration of the interface upon dilational deformations. In fact, the experimental and theoretical tools of the interfacial dilational rheology provide information about the exchange mechanisms of material between the interface and the adjacent fluid phases as well as about the different reorientation and exchange process occurring between molecules confined within the interface [64-66]. This section will be devoted to the description of the most fundamental methodological aspects of the determination of the dilational response of planar fluid/fluid interfaces. However, it should be stressed that the description of the mechanical response of curved interfaces will not be considered for the aim of this PhD Thesis, the understanding of the rheological response of curved interfaces is gaining importance due to their recognized role in aspects of technological importance, including the stability of emulsions and foams, or the coffee-ring formation upon the evaporation of liquid droplets deposited on solid substrates [26,67,68].

One of the main challenges when dilational rheology experiments are performed is related to the evaluation of the mechanical response of fluid/fluid interfaces in a broad range of frequency. Unfortunately, this is not trivial because it requires to combine techniques which is not always easy due to two main factors: (i) the accessibility to the different required techniques is not always easy, and (ii) some devices are only designed for studying soluble or insoluble interfacial layers [69]. **Figure 1. 14** presents a summary of some of the experimental techniques accessible for evaluating the dilational response of fluid/fluid interfaces as well as the frequency range in which they can be used.

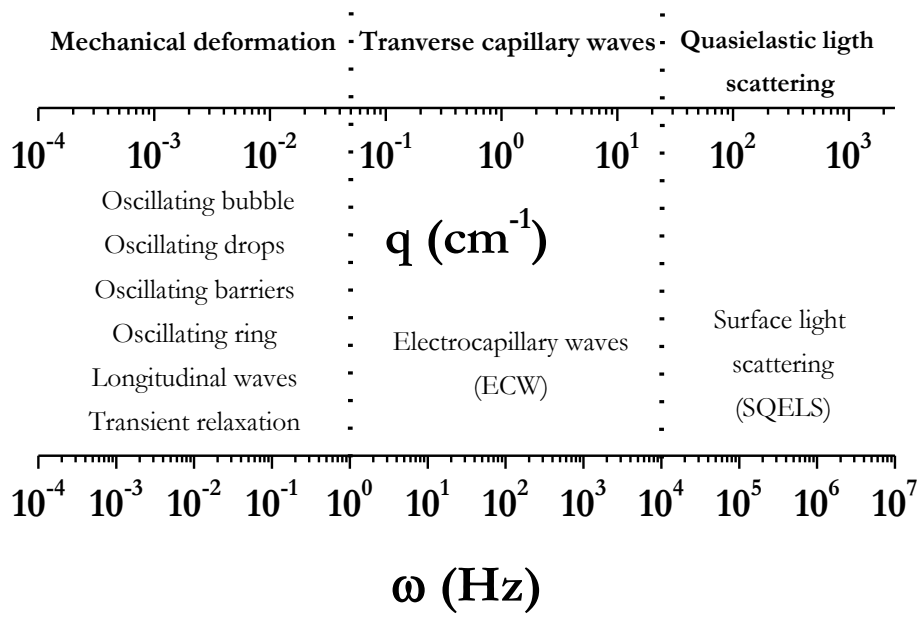

Figure 1. 14. Summary of some of the most extended methodologies for evaluating the dilational response of fluid/fluid interface together to the accessible frequency ranges for such techniques. Reprinted from Guzmán et al. [69].

To date, there is only one study dealing with the whole relaxation spectrum in the frequency range 10^{-3}-10^{3} Hz [70]. This requires combining an oscillatory drop tensiometer, a capillary pressure tensiometer and electrocapillary wave instrument for accessing to the whole frequency range. Moreover, there are several studies where the combination of different

techniques has provided information about the mechanical relaxation spectrum, even the information of the real and imaginary part of the viscoelastic modulus values from the whole frequency range are not available [69,71-73].

Assuming the difficulties associated with performing dilational rheology experiments in a broad frequency range, it is necessary to adapt classical approaches of conventional rheology to the study of fluid/fluid interfaces. An example of these approaches is to adapt the widely used time-temperature superposition principle for extending the range of frequencies accessible for the analysis of data [74]. The applicability of this type of superposition is only possible for thermo-rheologically simple cases, which are characterized for the presence of a single relaxation mechanism over the whole temperature and frequency range explored. Despite the proved effectiveness of the superposition principle for describing the bulk rheology of different systems, its application to the study of fluid/fluid interfaces is recent [66].

1.8.1. Experimental tools

The characterization of the dilational response of interfacial layers requires a careful election of the most suitable technique as well as appropriate experimental conditions. Several experimental techniques can be applied to evaluate the response of fluid/fluid interfaces to dilational stresses, offering different sensitivities and measuring ranges. This section will provide a brief overview of the types of experiments and experimental techniques that are currently available for studying fluid/fluid interfaces subjected to dilational deformations.

1.8.1.1. Experimental techniques

This section includes a brief overview of the most common methodologies used for evaluating the dilational properties of fluid/fluid interfaces.

- Drop/bubble shape tensiometers. The use of drop/bubble shape tensiometers on the evaluation of the dilational viscoelasticity of fluid/fluid interfaces relies on the determination of the time evolution of the interfacial tension during harmonic changes of the area at a fixed frequency. This information can be extracted from the analysis of the changes occurring in the drop/bubble shape profile during the process, which can be done by applying the Young-Laplace equation. This approach provides a framework to calculate the interfacial tension, by assuming that the contributions associated with shear are negligible. Therefore, the analysis of the drop/bubble shape profile can be only exploited for rheological simple interfaces characterized by an isotropic and constant stress along the whole interface.
  It should be noted that in most of the cases the deformation of drops/bubbles cannot be considered as purely radial. Moreover, the drop/bubble requires to be in instantaneous mechanical equilibrium for a correct evaluation of the interfacial tension, which limits the applicability of drop/bubble shape tensiometers for the evaluation of the interfacial dilational modulus to deformation frequencies in the range 10^{-3}-0.2 Hz [75]. In general, the use of drop/bubble shape tensiometers for evaluating the dilational properties assumes the existence of a single isotropic and constant tension for the entire interface. This allows applying the generalized Young-Laplace equation [76]. This technique will be discussed in details in *Chapter II* (2.1.3. Profile Analysis Tensiometer (PAT)).
- Capillary pressure tensiometers. An alternative approach for evaluating the dilational rheological properties of fluid/fluid interfaces relies on the determination of the capillary pressure inside droplets or bubbles together to their dimensions. In this case,

the determination of the interfacial tension does not require a strong gravitational deformation of the drops/bubbles, which was necessary on conventional drop/buble shape tensiometers [77]. This allows reducing the size of the drops/bubbles used (in the range 20-200 μm). Thus, it is possible to reduce the capillary and inertial relaxation times, enabling an extension of the probed frequencies up to 100 Hz [59]. Moreover, this approach reduces the role of the shear contributions on the deformation, making acceptable the isotropic assumption for the resolution of the Young-Laplace equation to determine the interfacial tension [16,17,78].

In recent years, the methods using oscillating drops/bubbles have been furtherly developed to extend the frequency range that can be probed. One of the most popular alternatives for this purpose, it is to design a device consisting in a closed cell, a pressure sensor, and a piezo translator, which allows monitoring the time evolution of the capillary pressure during the experiments. Thus, it is possible to determine the rheological properties of fluid/fluid interfaces in the 0.5-450 Hz range. Moreover, this type of devices allows measuring the rheological properties of interfaces formed for two fluids with very similar densities [79,80].

Langmuir troughs. The Langmuir trough is a common experimental setup used for studies dealing with the dilational properties of fluid/fluid interfaces [81,82]. It consists of two barriers arranged parallel in opposite extremes of the trough that can be used for compress or expand the area available for the interface under controlled conditions. During the compression/expansion of the interface, the interfacial tension is monitored by using a surface balance fitted with a contact probe, generally a Wilhelmy plate. This allows deducing the interfacial stress for specific deformation conditions [11]. This technique will be discussed in details in *Chapter II* (2.1.1. Langmuir trough). It is worth mentioning that the interfacial stress measured in the Langmuir trough as a result of a uniaxial deformation includes, in many cases, both dilational and shear components [83]. Moreover, special care is required for interpreting the rheological properties of solid-like layers obtained using Langmuir troughs because in many cases the deformation field cannot be defined as homogeneous, and hence it depends on the specific geometric constrains of the used trough [52,84]. The inability to apply a purely isotropic stress, which leads to rheological responses containing dilational and shear contributions, is a very important problem when interfaces with a complex microstructure are analyzed. The application of anisotropic stresses to such complex systems results in a rheological response characterized for the change of the area and the shape under compression [17,52]. This can be solved by introducing several modifications to the Langmuir trough for ensuring a purely dilational deformation of fluid/fluid interfaces [52]. The most useful design of Langmuir trough for ensuring a pure dilational deformation of planar fluid/fluid interfaces is the proposed by Pepicelli et al. [52]. This relies on a radial trough which is isotropically deformed by an elastic band held by twelve “fingers”. The interfacial pressure is determined by using a Wilhelmy rod ensuring a radial symmetry. This type of devices allows applying isotropic deformation, avoiding any shear effect on the interfacial deformation [85].

- Wave damping. A traditional approach to evaluate the mechanical response of fluid/fluid interfaces against high frequency dilational deformations relies on the study of the damping of capillary waves. These can be generated upon the application of mechanically, thermally or electrically-driven perturbation of the interface, with their

propagation occurring along the fluid/fluid interface. During their propagation, the waves are dampened by the action of the surface forces that try to restore the flatness of the interface [29,86-90]. The study of the rheological properties by the evaluation of the damping of surface waves allows obtaining information of the dilational properties of fluid/fluid interfaces up to frequencies of about 100 kHz [91]. Information about dilation properties of fluid/fluid interfaces can be also obtained from the longitudinal wave damping. These are propagated mainly by interfacial tension gradients, allowing one to probe the dilational rheology of fluid/fluid interfaces at lower values of deformation frequencies than when capillary waves are used [64,92-94]. Despite the broad range of frequencies (0.1-10^5 Hz) that can be probed by the evaluation of the damping of waves generated at fluid/fluid interfaces, and the contactless character of this type of techniques, the interpretation of the data is not straightforward, limiting their applicability [91,95]. Recently, Slavchov et al. [87] reviewed the most fundamental aspects of capillary waves damping as a tool for evaluating the mechanical response of fluid/fluid interfaces. Moreover, they analyzed recent theoretical developments on the use of capillary waves. Rajan [96] solved the problems associated with the use of the damping of interfacial waves for the determination of the rheological properties of liquid/liquid interfaces, providing results of the interfacial elasticity and viscosity of water/oil interfaces. The use of Faraday waves can be an alternative for studying the rheological properties of fluid/fluid interfaces [97,98]. Henderson [99] used the analysis of Faraday waves to evaluate the mechanical response of interfaces with monolayers of different insoluble molecules, and found that the effectiveness of the wave damping was enhanced as the interfacial packing of the interfacial film is increased. Similar results were found for monolayers of wheat storage protein [100].

1.8.1.2. Experimental methods

The experimental methods used for studying the dilational rheological response of fluid/fluid interfaces rely on the mechanical perturbation of the interfacial area, and the measurement of the response.

Stress relaxation experiments. Relaxation experiments can be performed by applying a sudden perturbation of a controllable parameter defining the equilibrium state of a monolayer at a fluid/fluid interface, e.g., interfacial area or interfacial concentration. This type of perturbation takes the system to an out-equilibrium situation, and hence the system undergoes a relaxation process to reestablish the equilibrium state [101]. Stress relaxation experiments can be performed using Langmuir troughs or drop/bubble shape tensiometers [102]. In a stress relaxation experiment, the time evolution of the interfacial tension $\gamma(t)$ or the interfacial pressure $\Pi(t)$ are recorded, after the sudden change (compression or expansion) of the interfacial area. This change of the interfacial area takes the interfacial pressure far from its equilibrium value, inducing a change of the interfacial pressure $\Delta\Pi$ that defines the interfacial stress. This acts as a restoring force which recovers the equilibrium state of the interface once the strain ceases [103].

Creep experiments. Creep experiments are commonly performed by using Langmuir troughs. In this type of experiments, an equilibrated interface characterized by its equilibrium interfacial pressure Π_0 is suddenly compressed as fast as possible till reach

a desired interfacial pressure value; then the surface pressure is maintained constant by changing the interfacial area. Thus, the excess of interfacial pressure is adjusted considering the area relaxation process, allowing one to define the creep compliance as [104],

$$J(t) = \frac{u(t)}{\sigma} = \frac{\frac{\delta A}{A_0}}{\Pi - \Pi_0}. \tag{1.53}$$

The creep compliance $J(t)$ is a phenomenological function, providing information on how the structure of the film resists the application of a controlled stress [104,105].

Oscillatory area experiments. Oscillatory area experiments rely on the application of a sinusoidal perturbation to the interface at a constant frequency ω. This oscillatory deformation presents a profile described as $u(t) = \delta A/A_0 = (u_0/2)\exp(\mathrm{i}\omega t)$. The deformation of drops or bubbles at low frequency almost guarantee a pure dilational deformation of the interface. However, for planar films studied in Langmuir trough, the in-plane shear components can appear coupled to the dilational ones in both the applied strain and the response stress, which makes difficult to extract true information of the dilational viscoelastic moduli. This may also occur in relaxation and creep experiments. It should be noted that the shear contributions present for films at fluid/fluid interface values that are smaller value than those obtained for the dilational contributions, and hence it can be neglected in oscillatory area experiments [42,106]. A more detailed description of oscillatory area experiments will be given in *Chapter II* (2.1.2. Oscillatory barrier experiments).

Surface waves experiments. Interfacial rheology experiments using surface waves are possible following two different approaches. The first one take advantage of the waves originated as result of the "natural" thermal fluctuations of the surface position, which can be explained in terms of the second law of thermodynamics, whereas the second approach is based on the production of "artificial" surface waves upon the application of external stimuli, e.g., electrical, or mechanical perturbation. Independently of the nature of the used waves, the features of the fluctuations (amplitude, frequency, damping, etc.) can be related to the interfacial rheological properties of the probed systems [107-109]. In fact, any displacement of the fluid/fluid interface in relation to their flat level shape can be interpreted as an interfacial motion guided by an external force and restored as result of the viscoelastic properties of the fluid phases and the interface itself [48,110].

One of the most common techniques based on the study of surface waves is the surface quasi-elastic light scattering (SQELS) technique which relies on the light scattered by transverse surface waves. These provide a measurement of the dynamics associated with the thermal induced roughness of the interface [48,110,111]. Thus, it is possible to evaluate the interfacial dynamics under equilibrium conditions by observing the dynamics of thermal fluctuations around the equilibrium state. These fluctuations present a very small length scale (a few Angstrom), allowing one to probe the interfacial rheology in the linear regime. SQELS experiments can be based on the determination of the heterodyne autocorrelation function or the capillary wave's power spectrum of the scattered light (See *Chapter II*, *2.1.4.3. Power spectra and Resonance condition*) $P(q, \omega)$,

$$P(q,\omega) = \frac{k_B T}{\pi\omega}\left[\frac{\mathrm{i}\omega\eta(m+q) + {E_s}^*(\omega)q^2}{D(q,\omega)}\right], \tag{1.54}$$

where k_B is the Boltzmann constant and η the subphase viscosity. $q = \frac{2\pi n}{d}cos(\theta)$ is the wave-vector (experimentally fixed), associated to the n-th diffraction order of a light beam passing through a diffraction grating with constant spacing *d*. ${E_s}^*(\omega)$ is the complex dilational modulus, and $D(q,\omega)$ the surface wave dispersion relation defined by the following expression [48],

$$D(q,\omega) = [{E_s}^*(\omega)q^2 + \mathrm{i}\omega(m+q)]\left[\gamma q^2 + \mathrm{i}\omega(m+q) - \frac{\rho\omega^2}{q}\right] - [\mathrm{i}\omega\eta(q-m)]^2 \tag{1.55}$$

with $m = \sqrt{q^2 + \frac{\mathrm{i}\omega\rho}{\eta}}$ (capillary penetration length). The technique allows to measure the response in frequency (which is a complex quantity) $\omega = \omega_0 + i\Delta\omega$, where ω_0 represents the central value of the power spectrum $P(q,\omega)$ and $\Delta\omega$ is its width (see See *Chapter II*, *2.1.4.3. Power spectra and Resonance condition*). The dilational elasticity and viscosity can be determined by experimentally measuring $P(q,\omega)$ and the interfacial tension. SQELS allows probing the dilational viscoelastic properties of interfaces in the frequency range 10^3-10^6 Hz [112]. A second example of experiments based on surface waves relies on the excitation of surface waves with higher amplitudes than those obtained in SQELS experiments (~1µm). This is possible under the application of an external physical stimulus, commonly mechanical or electrical, as excitation force. In general, electrical stimuli are preferred than mechanical ones because they present a non-invasive character, allowing an easier experimental design [42].

Electrically excited surface waves are the so called Electro-Capillary waves (ECW), and they can be evaluated by measuring the spatial profile of the generated waves by using spatially resolved laser reflectometry. Thus, it is possible to obtain a spatial profile that follows a damped wave function defined as,

$$A \sim cos\left(\frac{2\pi x}{\lambda} + \phi\right)\exp(-\beta x) \tag{1.56}$$

where λ accounts for the capillary wavelength and β for the spatial damping constant of the capillary wave oscillations. ϕ defines a phase term obtained as a function of the excitation frequency. ECW experiments requires to perform measurements at different frequencies to obtain the group velocity, and to transform the results obtained from the space domain to the time one. Then, combining the frequency, the independently measured interfacial tension and the values of λ and β obtained in the fitting of the spatial profile of the damped wave, it is possible to calculate the interfacial dilational elasticity and viscosity by solving numerically the dispersion equation (1.55) (by imposing $q = \frac{2\pi}{\lambda} - i\beta$) for each measured frequency (in the range 20-10^3 Hz) [42]. This

technique will be discussed in deeper details in *Chapter II* (*2.1.4. Electro-Capillary Waves (ECW)*). It should be noted that, in ECW technique, the frequency is fixed, and the wave vector response (which is a complex quantity) is experimentally determined, while, in SQELS technique, the wave vector is fixed, and the complex frequency must be measured.

The above discussion about wave damping considers a sharp fluid/fluid interface, which is coated by a thin monomolecular film. However, the situation becomes trickier when thick films are adsorbed at the fluid/fluid interface. A detailed discussion of the role of the interface thickness on the ability of fluid/fluid interfaces for dampening waves can be found in the literature [113-115].

1.8.2. Interface Dilational Rheology: Theoretical models

The use of suitable theoretical models for analyzing the frequency dependence of the dilational viscoelastic properties of fluid/fluid interfaces can shed light on the relaxation mechanism involved in the reestablishment of the interfacial equilibrium after a dilational deformation [59,116]. The Lucassen-Van den Tempel model assumes that the adsorption-desorption equilibrium occurs freely, and no adsorption barriers are present, thus the material exchange between the bulk and the interface is governed by diffusion [59,117,118]. This is only possible assuming that the formation of an interfacial layer of the interface requires the equilibrium between the interface and the species existing in the bulk, i.e., the formation of a soluble or Gibbs monolayers. Thus, it is possible to define the complex viscoelastic modulus according to the following relationship,

$$E_s^*(\omega) = \frac{1 + \xi(\omega) + i\xi(\omega)}{1 + 2\xi(\omega) + 2\xi(\omega)^2}\varepsilon_0, \tag{1.57}$$

where $\xi(\omega) = \sqrt{\frac{\omega_D}{\omega}}$, with $\omega_D = D\left(\frac{dc}{d\Gamma}\right)_{eq}^2$ being the characteristic frequency of the exchange process, D the diffusion coefficient of the surfactant and c the bulk concentration. The qualitative behavior is the same as the one sketched in **Figure 1. 13**. From the above definition, it is possible to assume two limits. In the first limit, $\omega \to \infty$ and $\omega_D \to 0$, which results in $E_s \to \varepsilon_0$ and $E_v \to \omega\kappa_s \to 0$, and the monolayer behaves as an insoluble one (Langmuir monolayer), i.e., there are no possibilities for material exchange between the interface and the adjacent fluid phases. The opposite situation occurs when $\omega \to 0$ and $\omega_D \to \infty$ which results in $E_s, \omega\kappa_s \to 0$, leading to a situation where the resistance to the compression is negligible, and the equilibrium between the bulk and the interface can occur instantaneously during the compression process. For those cases in which the frequency assumes intermediate values, the condition $0 < E_s < \varepsilon_0$ and $\omega\kappa_s \neq 0$ is fulfilled.

The above model assumes that the interfacial concentration only changes as result of the exchange of molecules between the fluid/fluid interface and the adjacent bulk phases (Gibb monolayers). However, this is not possible when insoluble layers are considered. In these cases, it can be only expected relaxation processes that are circumscribed to the fluid/fluid interface. This type of relaxation mechanism can also appear in soluble monolayers. There are

several possible interfacial tension relaxation processes that can affect directly at the interface upon a dilational deformation [119]. These correspond to the internal reorganization of the adsorption layer, which can occur according to different mechanisms, e.g., phase transitions, molecular reorientation, and molecular folding/unfolding [24,59,120-122].

The existence of a relaxation mechanism involving only the interface requires introducing a generic thermodynamic variable *X*, which gives a description of the advancement of the relaxation process. This new variable combined with the interfacial tension and the interfacial concentration allows describing the state of the interface. Thus, it is possible to define a state equation for the interface according to the following expression:

$$\gamma = \gamma(\Gamma, X) \tag{1. 58}$$

Assuming a relaxation process following a first order kinetics, it is possible to define the kinetic equation as:

$$\frac{dX}{dt} = -k\left(X - X_{eq}\right) \tag{1. 59}$$

where *k* is the characteristic constant of the process and X_{eq} is the value of the thermodynamic variable under equilibrium conditions [59,70]. The above framework allows describing the dependence of the viscoelastic modulus in terms of the frequency as:

$$E_s{}^*(\omega) = \varepsilon_0 + \sum_{j=1}^{N}\left(\varepsilon_j - \varepsilon_{j-1}\right)\frac{1 + i\lambda_j(\omega)}{1 + \lambda_j(\omega)^2} \tag{1. 60}$$

where $\lambda_j(\omega) = \omega_j/\omega$ and ω_j provide information about the characteristic frequency of the j-th relaxation processes, and ε_j and ε_{j-1} are thermodynamic parameters related to the limit elasticities. For insoluble systems, ε_0 stands for the limit elasticity when the deformation tends to zero.

The frequency dependence of the imaginary part of the dilational viscoelastic modulus is characterized by peaks with their maximum corresponding to the characteristic frequency of the involved relaxation processes. The maxima of the peaks in the imaginary part correspond to the inflection points in the real part curves. **Figure 1. 15** represents the frequency dependence of the real or imaginary parts of the dilational viscoelastic modulus for fluid/fluid interfaces presenting different relaxation processes.

For systems presenting several relaxation processes, it is possible to superimpose them following a linear combination scheme to fabricate an expression for the frequency dependence of the dilational viscoelastic modulus containing an arbitrary number of processes [59,60,122,123].

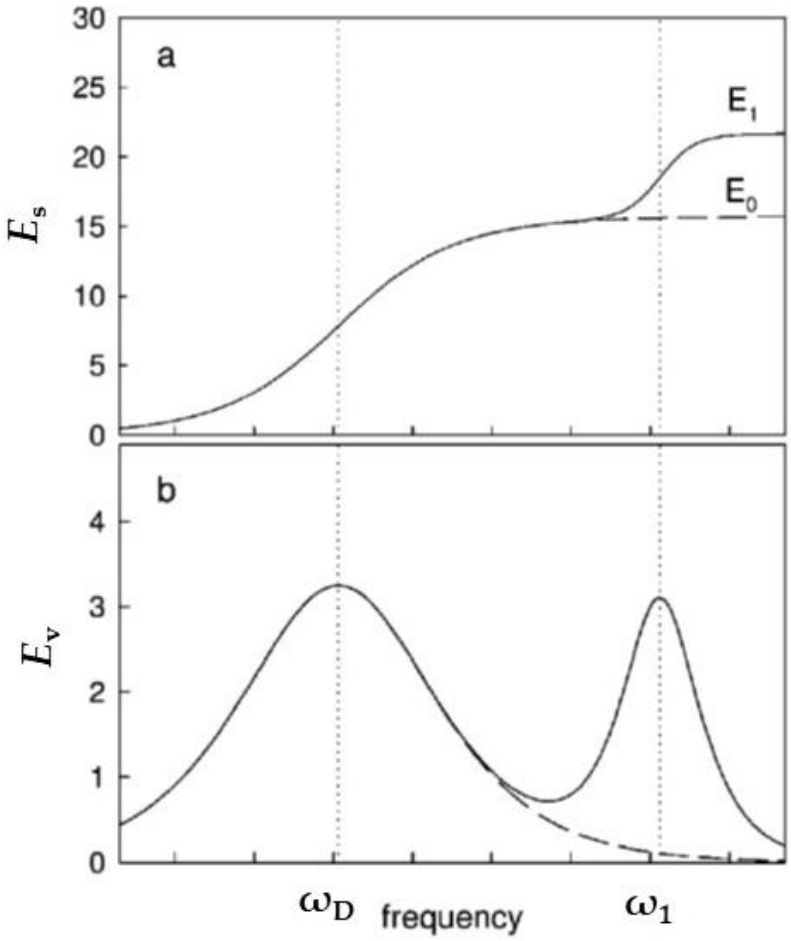

Figure 1. 15. Sketch of the typical dependences of the real (a) and imaginary (b) parts of the viscoelastic modulus for fluid/fluid interfaces presenting different relaxation process. The dashed lines correspond to a system presenting a relaxation process characterized by a relaxation process defined in terms of the Lucassen-van der Tempel model, and the continuous lines represent the typical behavior of a fluid/fluid interfaces where a relaxation process affecting only to the interface is coupled to a Lucassen-van der Tempel-like relaxation. Reprinted from Liggieri et al. [70],with permission from Royal Society of Chemistry, Copyright (2011).

1.9. Non-Linear Surface rheology

The above discussion deals so far with the dilational response of fluid/fluid interfaces to small amplitude deformations. However, the situation changes significantly when the amplitude of the deformation is large enough to push the response of interfacial films far from the linear regime. It should be noted that in some systems, the onset on the region of non-linear response is reached even with deformations of very small amplitude [124-126].

The analysis of the non-linear response in dilational rheology is not straightforward, mainly due to the difficulties to provide a suitable definition of the applied deformation [127]. This may be understood considering the axisymmetric drop shape analysis as an example. This type of experiments relies in many cases in inhomogeneous deformation which depends on the position [128]. This is a very critical issue because the stretching can be very different depending on the interface area, even though this is not considered in most cases for the data analysis. Moreover, the interference of time-dependent and deformation-dependent rheological properties also complicates the analysis of non-linear behavior of fluid/fluid interfaces.

Figure 1. 16 shows a schematic representation of the stress decomposition to obtain the four contributions.

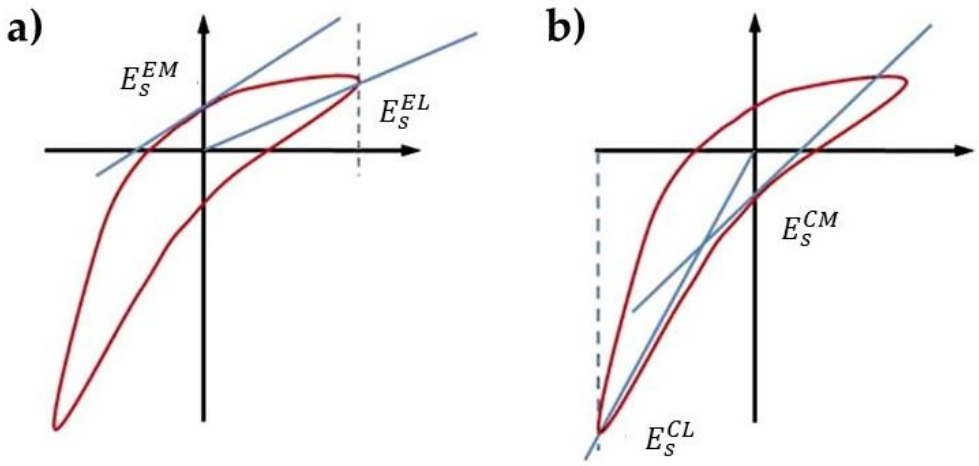

Figure 1. 16. Definition of minimum and large-strain moduli. (a) Minimum and large deformation dilational moduli in extension. (b) Minimum and large deformation dilational moduli in compression. Adapted from Sagis and Fischer [127],with permission from Elsevier, Copyright (2014).

Using the above mentioned four contributions, it is possible to define two parameters defining the non-linearity, the first one defining the compression part of the cycle:

$$S_c = \frac{E_S^{CL} - E_S^{CM}}{E_S^{CL}} \tag{1. 61}$$

and the second one accounting for the extension part of the cycle:

$$S_E = \frac{E_S^{EL} - E_S^{EM}}{E_S^{EL}} \tag{1. 62}$$

The evaluation of the S factors as a function of the applied strain provides quantitative information on the non-linearity of the interface [127].

As alternative to the graphical analysis in terms of a stress decomposition, the non-linear rheological signals of interfaces can be also analyzed by representing the stress by using Fourier series, making use of the Fourier-transform rheology [125]. This relies on defining the stress response in terms of a Fourier expansion:

$$\sigma(t) = \sigma_0\, exp(i\omega t) + \sigma_1\, exp(2i\omega t) + \sigma_2\, exp(3i\omega t) + \cdots \tag{1. 63}$$

where σ_0 defines the amplitude of the stress response defined with respect to the initial interfacial pressure, and σ_1, σ_2, etc. correspond to the amplitudes of the harmonic terms of the non-linear response. The use of Fourier transform rheology for modelling the non-linear dilational response of fluid/fluid interfaces is limited. This can be understood considering that this methodology considers the stress as an expansion around a zero-interface deformation rate, which can provide only information for systems with small deviations from the linearity. A very useful methodology for quantifying non-linearity of the rheological response of fluid/fluid interfaces is by introducing the concept of the Total Harmonic Distortion (THD) defined as [129].

$$THD = \frac{\sqrt{\sum_{k>0} \sigma_k}}{\sigma_0} \quad (1.\ 64)$$

with σ_k corresponds to the amplitudes of the harmonic terms of the non-linear response. The above definition of the *THD* indicates that when this parameter assumes a null value, the systems present a linear rheological response, while larger values of this parameter show the emergence of non-linear response of the fluid/fluid interface.

Another alternative to decompose the stress response in non-linear systems is the Volterra series [130].

1.10. Aims, scope and structure of the PhD Thesis

The study of interfacial rheology has broad applications, particularly in complex fluids where the properties of the adsorbed layer are crucial. Examples include surfactant solutions, foams, and emulsions [131], which are widespread in many industries, such as cosmetics, oil industry, food industry, pharmaceutical and biomedical industry, among others [132]. Furthermore, interfacial rheology is instrumental in advancing our understanding of various biological systems, including pulmonary surfactants, eye drops, blood flow dynamics, protein adsorption, bacterial adhesion, and biofilm formation [133-136].

The main aim of this PhD Thesis is to study the interfacial properties —specifically surface tension and surface dilational rheology— of various complex fluids, divided into 4 main categories: surfactant solutions, monolayers in presence of high ionic strength, dispersions of polymer-capped nanoparticles, and concentrated polymeric solutions. This research seeks to address and resolve several longstanding open questions in the literature related to the dilational surface rheology and the interfacial behavior of these systems. The study will be carried out across two different frequency ranges: low frequency (10^{-3}-10^{-1} Hz) and high frequency (10-1000 Hz). The PhD Thesis will primarily focus on the high-frequency range, utilizing the Electro-Capillary Waves technique. A central objective is to explore and delineate both the theoretical and experimental limits of this technique, thereby advancing our understanding of the interfacial rheology of complex fluids at high frequencies. Therefore, this research aims not only to contribute novel insights into the interfacial dynamics of these systems but also to provide a robust framework for future studies in the field, with potential applications across various industrial and scientific domains. For this purpose, the PhD Thesis will be divided into several sections consisting of several chapters.

In Section 1, Chapter I gives a brief overview of rheology (both bulk and interfacial) and of the interfacial properties of complex fluids. On the other hand, Chapter II provides a deep description of the experimental techniques used to characterize the interfacial rheology and/or surface tension (Langmuir trough with oscillating barriers, Pendant drop tensiometer, Electro-Capillary Waves), the bulk rheology (flow rheometers and Diffusing Wave Spectroscopy) and other ancillary techniques (Dynamic Light Scattering, electrophoretic mobility measurement, contact angle and spreading dynamics characterization).
In Section 2, two different type of surfactant aqueous solutions will be studied. In such systems, surfactant molecules get quickly adsorbed at liquid/vapor interface, forming Gibbs monolayers. In Chapter III, the scope is to study the interfacial rheology of adsorption-dominated systems (Alkyl polyglucoside surfactant aqueous solutions), focusing on the

experimental problems of electro-capillary waves technique, underlining the need of an improvement in data and error bar analysis. Chapter IV is aimed at studying the interfacial properties of trisiloxanes, comparing a superspreader with a non-superspreader surfactant. The idea is to relate interfacial rheology to spreading kinetics, and compare the oscillation parameters (i.e., frequency and damping) of sessile drops with the propagation parameters of capillary waves determined by ECW technique (wavelength, frequency, damping), trying to understand what is the dominating mechanism that rules drop oscillation after impact (either capillarity, gravity, inertia…). The lack of models predicting drop oscillation accompanied by spreading reveals the need of experimental data and discussion about this topic.

Section 3 deals with the study of interfacial properties of monolayers in presence of high ionic strengths. The demand of a deeper understanding of the effect of ionic strength comes from the fact that several studies on dilational surface rheology (by means of oscillating barriers, ECW and SQELS technique), in presence of ionic strength, reported non-physically sound values of dilational moduli (such as negative storage modulus, negative loss modulus…) [137-144]. In Chapter V, the impact of NaCl on interfacial tension and dilational surface rheology of Pluronic F-68 (an amphiphilic triblock copolymer) Gibbs monolayers will be assessed, in order to understand the interactions between surfactant and salt ions, and to point out some of the technical and theoretical limitations for obtaining reliable dilational rheological data within ECW frequency range (10-1000 Hz). Chapter VI has a similar purpose with respect to the one of Chapter V, but it is focused on the interfacial properties of a Langmuir monolayer instead: the surface tension and the dilational surface rheology of Poly-tert-butyl acrylate (a water insoluble polymer) Langmuir monolayers, with dissolved NaCl in aqueous subphase, will be studied.

Section 4 is focused on the study of the interfacial properties of polymer-capped particles water dispersions, in order to provide a deep understanding on the interaction between particles and surface active molecules, and assess its influence on liquid/vapor interface stability and properties. Chapter VII is aimed at investigating the effect of Pluronic F-127 (an amphiphilic triblock copolymer) on silica nanoparticles adsorption at water/vapor interfaces, as well as on the interfacial rheology (at low frequency, 10^{-3}-10^{-1} Hz) of the formed layers. Chapter VIII has the purpose of evaluating the interaction between chitosan (a polyelectrolyte) and silica nanoparticles, and the stability of the resulting dispersions at different pH and concentration conditions. The main goal is to understand how chitosan changes the hydrophobicity of silica, affecting the adsorption of complexes at liquid/vapor interface. Finally, the chapter is aimed at studying the high-frequency dilatational rheological response of the formed layers by using ECW technique, paving the way in understanding the stabilization of foams.

In Section 5, Chapter IX scope is to study the dilational interfacial response of a system exhibiting shear bulk viscoelasticity in the subphase, which is not taken into account by the classical hydrodynamic models used to determine the dilational interfacial modulus by surface wave damping propagation parameters. Poly vinylalcohol/BORAX solutions will be chosen as potential candidates for this study, because they exhibit bulk viscoelasticity effects within ECW

frequency range. The goal is to collect experimental results in order to validate (and point out the limits of) some hydrodynamic models describing surface modes on viscoelastic fluids that are already present in literature [5].

1.11 References

1. Steffe, J.F. *Rheological Methods in Food Process Engineering*; Freeman Press: East Lansing, MI, USA, 1992.
2. Beris, A.; Giacomin, A.J. πάντα ῥεῖ: Everything flows. *Appl. Rheol.* **2014**, *24*, 52918, doi:10.3933/ApplRheol-24-52918.
3. Itin, Y.; Hehl, F.W. The constitutive tensor of linear elasticity: Its decompositions, Cauchy relations, null Lagrangians, and wave propagation. *J. Math. Phys.* **2013**, *54*, 042903, doi:doi.org/10.1063/1.4801859.
4. Landau, L.D.; Lifshitz, E.M. *Fluid Mechanics*; Pergamon Press: Elmsford, New York, USA, 1987; Vol. 6.
5. Wang, C.H.; Huang, Q.R. Hydrodynamic surface waves in concentrated polymer solutions in the presence of surface adsorption. *J. Chem. Phys.* **1997**, *107*, 5898–5906 doi:doi.org/10.1063/1.474315.
6. Phan-Thien, N. *Understanding Viscoelasticity*; Springer Berlin: Heidelberg, Germany, 2013.
7. Verdier, C. Rheological Properties of Living Materials. From Cells to Tissues. *Journal of Theoretical Medicine* **2003** *5*, 67–91.
8. Forth, J.; Kim, P.Y.; Xie, G.; Liu, X.; Helms, B.A.; Russell, T.P. Building Reconfigurable Devices Using Complex Liquid–Fluid Interfaces. *Adv. Mat.* **2019**, *31*, 1806370, doi:10.1002/adma.201806370.
9. Guzmán, E. Current Perspective on the Study of Liquid–Fluid Interfaces: From Fundamentals to Innovative Applications. *Coatings* **2022**, *12*, 841, doi:10.3390/coatings12060841
10. Guzmán, E.; Martínez-Pedrero, F.; Calero, C.; Maestro, A.; Ortega, F.; Rubio, R.G. A broad perspective to particle-laden fluid interfaces systems: from chemically homogeneous particles to active colloids. *Adv. Colloids Interface Sci.* **2022**, *302*, 102620, doi:10.1016/j.cis.2022.102620.
11. Guzmán, E. Fluid Films as Models for Understanding the Impact of Inhaled Particles in Lung Surfactant Layers. *Coatings* **2022**, *12*, 277, doi:10.3390/coatings12020277.
12. Guzmán, E.; Santini, E. Lung surfactant-particles at fluid interfaces for toxicity assessments. *Curr. Opin. Colloid Interface Sci.* **2019**, *39*, 24-39, doi:10.1016/j.cocis.2019.01.003.
13. Klein, C.O.; Theodoratou, A.; Rühs, P.A.; Jonas, U.; Loppinet, B.; Wilhelm, M.; Fischer, P.; Vermant, J.; Vlassopoulos, D. Interfacial Fourier transform shear rheometry of complex fluid interfaces. *Rheol. Acta* **2019**, *58*, 29-45, doi:10.1007/s00397-018-01122-y.
14. Masuda, T.; Takai, M. Design of biointerfaces composed of soft materials using controlled radical polymerizations. *J. Mat. Chem. B* **2022**, *10*, 1473-1485 doi:10.1039/D1TB02508B.
15. Sagis, L.M.C.; Liu, B.; Li, Y.; Essers, J.; Yang, J.; Moghimikheirabadi, A.; Hinderink, E.; Berton-Carabin, C.; Schroen, K. Dynamic heterogeneity in complex interfaces of soft interface-dominated materials. *Sci. Rep.* **2019**, *9*, 2938, doi:10.1038/s41598-019-39761-7.

16. Jaensson, N.; Vermant, J. Tensiometry and rheology of complex interfaces. *Curr. Opin. Colloid Interface Sci.* **2018**, *37*, 136-150, doi:10.1016/j.cocis.2018.09.005.
17. Jaensson, N.O.; Anderson, P.D.; Vermant, J. Computational interfacial rheology. *J. Non-Newton. Fluid Mech.* **2021**, *440*, 110413, doi:10.1016/j.jcp.2021.110413.
18. Wei, Y.; Xie, Y.; Cai, Z.; Guo, Y.; Zhang, H. Interfacial rheology, emulsifying property and emulsion stability of glyceryl monooleate-modified corn fiber gum. *Food Chem.* **2021**, *343*, 128416, doi:10.1016/j.foodchem.2020.128416.
19. Botti, T.C.; Hutin, A.; Quintella, E.; Carvalho, M.S. Effect of interfacial rheology on drop coalescence in water–oil emulsion. *Soft Matter* **2022**, *18*, 1423-1434, doi:10.1039/D1SM01382C.
20. Wang, H.; Wei, X.; Du, Y.; Wang, D. Experimental investigation on the dilatational interfacial rheology of dust-suppressing foam and its effect on foam performance. *Process. Saf. Environ. Prot.* **2019**, *123*, 351-357, doi:10.1016/j.psep.2019.01.027.
21. Thai, L.P.A.; Mousseau, F.; Oikonomou, E.K.; Berret, J.F. On the rheology of pulmonary surfactant: Effects of concentration and consequences for the surfactant replacement therapy. *Colloids Surf. B* **2019**, *178*, 337-345, doi:10.1016/j.colsurfb.2019.03.020.
22. Haslbeck, K.; Schwarz, K.; Hohlfeld, J.M.; Seume, J.R.; Koch, W. Submicron droplet formation in the human lung. *J. Aerosol Sci.* **2010**, *41*, 429-438, doi:10.1016/j.jaerosci.2010.02.010.
23. Svitova, T.F.; Lin, M.C. Tear lipids interfacial rheology: effect of lysozyme and lens care solutions. *Optom. Vis. Sci.* **2010**, *87*, 10-20, doi:10.1097/OPX.0b013e3181c07908.
24. Rubio, R.G.; Guzmán, E.; Ortega, F.; Liggieri, L. Monolayers of Cholesterol and Cholesteryl Stearate at the Water/Vapor Interface: A Physico-Chemical Study of Components of the Meibum Layer. *Colloids and Interfaces* **2021**, *5*, 30, doi:10.3390/colloids5020030.
25. Zhang, H.; Lamnawar, K.; Maazouz, A. Fundamental studies of interfacial rheology at multilayered model polymers for coextrusion process. *AIP Conf. Proc.* **2015**, *1664*, 100008, doi:10.1063/1.4918475.
26. Perrin, L.; Akanno, A.; Guzman, E.; Ortega, F.; Rubio, R.G. Pattern Formation upon Evaporation of Sessile Droplets of Polyelectrolyte/Surfactant Mixtures on Silicon Wafers. *Int. J. Mol. Sci.* **2021**, *22*, 7953, doi:10.3390/ijms22157953.
27. Sun, H.-Q.; Zhang, L.; Li, Z.-Q.; Zhang, L.; Luo, L.; Zhao, S. Interfacial dilational rheology related to enhance oil recovery. *Soft Matter* **2011**, *7*, 7601-7611, doi:10.1039/C1SM05234A.
28. Gade, M.; Byfield, V.; Ermakov, S.; Lavrova, O.; Mitnik, L. Slicks as Indicators for Marine Processes. *Oceanography* **2013**, *26*, 138–149, doi:10.5670/oceanog.2013.39.
29. Ermakov, S.A.; Khazanov, G.E. Resonance damping of gravity–capillary waves on water covered with a visco-elastic film of finite thickness: A reappraisal. *Phys. Fluids* **2022**, *34*, 092107, doi:10.1063/5.0103110.
30. Sánchez-Puga, P.; Tajuelo, J.; Pastor, J.M.; Rubio, M.A. Flow field-based data analysis in interfacial shear rheometry. *Adv. Colloids Interface Sci.* **2021**, *288*, 102332, doi:10.1016/j.cis.2020.102332.
31. Guzmán, E.; Tajuelo, J.; Pastor, J.M.; Rubio, M.Á.; Ortega, F.; Rubio, R.G. Shear rheology of fluid interfaces: Closing the gap between macro- and micro-rheology. *Curr. Opin. Colloid Interface Sci.* **2018**, *37*, 33-48, doi:10.1016/j.cocis.2018.05.004.
32. Wong, W.-H.B.; Hulsen, M.A.; Anderson, P.D. A numerical model for the development of the morphology of disperse blends in complex flow. *Rheol. Acta* **2019**, *58*, 79-95, doi:10.1007/s00397-018-01126-8.

33. Sun, H.-Q.; Zhang, L.; Li, Z.-Q.; Zhang, L.; Luo, L.; Zhao, S. Interfacial dilational rheology related to enhance oil recovery. *Soft Matter* **2011**, *7*, 7601-7611 doi:10.1039/C1SM05234A.
34. Perez, P.L.; Zaragoza, J.N.; Patel, N.K.; Dion, M.A. Impact of Asphaltene Stabilizers on the Elasticity of a Crude Oil–Water Interface and Its Correlation to Demulsification under Desalting Conditions. *Energy Fuels* **2022**, *36*, 275–289, doi:10.1021/acs.energyfuels.1c03360.
35. Guzmán, E.; Santini, E.; Ferrari, M.; Liggieri, L.; Ravera, F. Evaluating the Impact of Hydrophobic Silicon Dioxide in the Interfacial Properties of Lung Surfactant Films. *ACS Env. Sci. Technol.* **2022**, *56*, 7308–7318, doi:10.1021/acs.est.1c06885.
36. Nagel, M.; Tervoort, T.A.; Vermant, J. From drop-shape analysis to stress-fitting elastometry. *Adv. Colloids Interface Sci.* **2017**, *247*, 33-51, doi:10.1016/j.cis.2017.07.008.
37. Vollhardt, D.; Fainerman, V.B. Characterisation of phase transition in adsorbed monolayers at the air/water interface. *Adv Colloid Interface Sci* **2010**, *154*, 1-19, doi:10.1016/j.cis.2010.01.003.
38. Martínez-Vitela, M.A.; Gracia-Fadrique, J. The Langmuir-Gibbs surface equation of state. *Fluid Phase Equilibria* **2020**, *506*, 112372, doi:10.1016/j.fluid.2019.112372.
39. Ward, A.F.H.; Tordai, L. Time-Dependence of Boundary Tensions of Solutions I. The Role of Diffusion in Time-Effects. *The Journal of Chemical Physics* **1946**, *14*, 453-461, doi:10.1063/1.1724167.
40. Zawala, J.; Wiertel-Pochopien, A.; Kowalczuk, P.B. Critical Synergistic Concentration of Binary Surfactant Mixtures. *Minerals* **2020**, *10*, 192, doi:10.3390/min10020192.
41. Maestro Martín, A. Dymanics of interfacial systems. Universidad Complutense de Madrid, 2010.
42. Mendoza, A.J.; Guzmán, E.; Martínez-Pedrero, F.; Ritacco, H.; Rubio, R.G.; Ortega, F.; Starov, V.M.; Miller, R. Particle laden fluid interfaces: Dynamics and interfacial rheology. *Adv. Colloids Interface Sci.* **2014**, *206*, 303-319, doi:10.1016/j.cis.2013.10.010.
43. Manikantan, H.; Squires, T.M. Surfactant dynamics: hidden variables controlling fluid flows. *J. Fluid Mech.* **2020**, *892*, P1, doi:10.1017/jfm.2020.170.
44. Krotov, V.V. Basics of Interfacial rheology. In *Interfacial rheology*, Miller, R., Liggieri, L., Eds. Brill: Leiden, The Netherlands, 2009; pp. 1-37.
45. Garbin, V. Collapse mechanisms and extreme deformation of particle-laden interfaces. *Curr. Opin. Colloid Interface Sci.* **2019**, *39*, 202-211, doi:10.1016/j.cocis.2019.02.007.
46. Maestro, A.; Guzmán, E. Colloids at Fluid Interfaces. *Processes* **2019**, *7*, 942, doi:10.3390/pr7120942.
47. Nitschke, I.; Voigt, A. Observer-invariant time derivatives on moving surfaces. *J. Geom. Phys.* **2022**, *173*, 104428, doi:10.1016/j.geomphys.2021.104428.
48. Langevin, D. Light scattering by liquid surfaces, new developments. *Adv. Colloids Interface Sci.* **2021**, *289*, 102368, doi:10.1016/j.cis.2021.102368.
49. Fuller, G.G.; Vermant, J. Complex Fluid-Fluid Interfaces: Rheology and Structure. *Annu. Rev. Chem. Biomol. Eng.* **2012**, *3*, 519-543, doi:10.1146/annurev-chembioeng-061010-114202.
50. Stone, H.A.; Leal, L.G. The effects of surfactants on drop deformation and breakup. *J. Fluid Mech.* **1990**, *220*, 161-186, doi:10.1017/S0022112090003226.
51. Kinkelder, E.d.; Sagis, L.; Aland, S. A numerical method for the simulation of viscoelastic fluid surfaces. *J. Comput. Phys.* **2021**, *440*, 110413, doi:10.1016/j.jcp.2021.110413.

52. Pepicelli, M.; Verwijlen, T.; Tervoort, T.; Vermant, J. Characterization and modelling of Langmuir interfaces with finite elasticity. *Soft Matter* **2017**, *13*, 5977-5990, doi:10.1039/C7SM01100H.
53. Petkov, J.T.; Gurkov, T.D.; Campbell, B.E.; Borwankar, R.P. Dilatational and Shear Elasticity of Gel-like Protein Layers on Air/Water Interface. *Langmuir* **2000**, *16*, 3569-4054, doi:doi.org/10.1021/la991287k.
54. Tajuelo, J.; Pastor, J.M.; Rubio, M.A. A magnetic rod interfacial shear rheometer driven by a mobile magnetic trap. *J. Rheol.* **2016**, *60*, 1095–1113 doi:doi.org/10.1122/1.4958668.
55. Sagis, L. Dynamic surface tension of complex fluid-fluid interfaces: a useful concept, or not? . *Eur. Phys. J.: Spec. Top.* **2013**, *222*, 39–46, doi:10.1140/epjst/e2013-01824-1.
56. Reichert, M.D.; Alvarez, N.J.; Brooks, C.F.; Grillet, A.M.; Mondy, L.A.; Anna, S.L.; Walker, L.M. The importance of experimental design on measurement of dynamic interfacial tension and interfacial rheology in diffusion-limited surfactant systems. *Colloids Surf. A* **2015**, *467*, 135-142, doi:10.1016/j.colsurfa.2014.11.035.
57. Miller, R.; Ferri, J.; Javadi, A.; Krägel, J.; Mucic, N.; Wüstneck, R. Rheology of interfacial layers. *Colloid Polym. Sci.* **2010**, *288*, 937-950, doi:10.1007/s00396-010-2227-5.
58. Karbaschi, M.; Lotfi, M.; Krägel, J.; Javadi, A.; Bastani, D.; Miller, R. Rheology of interfacial layers *Curr. Opin. Colloid Interface Sci.* **2014**, *19*, 514-519, doi:10.1016/j.cocis.2014.08.003.
59. Ravera, F.; Ferrari, M.; Santini, E.; Liggieri, L. Influence of surface processes on the dilational visco-elasticity of surfactant solutions. *Adv. Colloids Interface Sci.* **2005**, *117*, 75-100, doi:10.1016/j.cis.2005.06.002.
60. Guzmán, E.; Liggieri, L.; Santini, E.; Ferrari, M.; Ravera, F. Influence of silicananoparticles on dilational rheology of DPPC–palmitic acid Langmuir monolayers. *Soft Matter* **2012**, *8*, 3938-3948 doi:10.1039/C2SM07097A.
61. Guzmán, E.; Liggieri, L.; Santini, E.; Ferrari, M.; Ravera, F. Mixed DPPC–cholesterol Langmuir monolayers in presence of hydrophilic silica nanoparticles. *Colloids Surf. B* **2015**, *105*, 284-293, doi:10.1016/j.colsurfb.2013.01.020.
62. Omari, Y.E.; Yousfi, M.; Duchet-Rumeau, J.; Maazouz, A. Recent Advances in the Interfacial Shear and Dilational Rheology of Polymer Systems: From Fundamentals to Applications. *Polymers* **2022**, 10.3390/polym14142844, 2844, doi:10.3390/polym14142844.
63. Ravera, F.; Miller, R.; Zuo, Y.Y.; Noskov, B.A.; Bykov, A.G.; Kovalchuk, V.I.; Loglio, G.; Javadi, A.; Liggieri, L. Methods and models to investigate the physicochemical functionality of pulmonary surfactant. *Curr. Opin. Colloid Interface Sci.* **2021**, *55*, 101467, doi:10.1016/j.cocis.2021.101467.
64. Firouzi, M.; Kovalchuk, V.I.; Loglio, G.; Miller, R. Salt effects on the dilational viscoelasticity of surfactant adsorption layers. *Curr. Opin. Colloid Interface Sci.* **2022**, *57*, 101538, doi:10.1016/j.cocis.2021.101538.
65. Akanno, A.; Guzmán, E.; Ortega, F.; Rubio, R.G. Behavior of the water/vapor interface of chitosan solutions with an anionic surfactant: effect of polymer–surfactant interactions. *Phys. Chem. Chem. Phys.* **2020**, *22*, 23360-23373, doi:10.1039/D0CP02470H.
66. Bae, J.-E.; Jung, J.B.; Kim, K.; Lee, S.-M.; Kang, N.-G. A study on time-concentration superposition of dilatational modulus and foaming behavior of sodium alkyl sulfate. *J. Colloid Interface Sci.* **2019**, *55*, 704-716, doi:10.1016/j.jcis.2019.08.102.

67. Suja, V.C.; Rodríguez-Hakim, M.; J.Tajuelo; G.G.Fuller. Single bubble and drop techniques for characterizing foams and emulsions. *Adv. Colloids Interface Sci.* **2020**, *286*, 102295, doi:10.1016/j.cis.2020.102295.
68. Akanno, A.; Perrin, L.; Guzmán, E.; Llamas, S.; Starov, V.M.; Ortega, F.; Rubio, R.G.; Velarde, M.G. Evaporation of Sessile Droplets of Polyelectrolyte/Surfactant Mixtures on Silicon Wafers. *Colloids and Interfaces* **2021**, *5*, 12, doi:10.3390/colloids5010012.
69. Guzmán, E.; Maestro, A.; Carbone, C.; Ortega, F.; Rubio, R.G. Dilational Rheology of Fluid/Fluid Interfaces: Foundations and Tools. *Fluids* **2022**, *7*, 335, doi:10.3390/fluids7100335.
70. Liggieri, L.; Santini, E.; Guzmán, E.; Maestro, A.; Ravera, F. Wide-frequency dilational rheology investigation of mixed silica nanoparticle–CTAB interfacial layers. *Soft Matter* **2011**, *7*, 7699–7709, doi:10.1039/c1sm05257h.
71. Llamas, S.; Mendoza, A.J.; Guzmán, E.; Ortega, F.; Rubio, R.G. Salt effects on the air/solution interfacial properties of PEO-containing copolymers: Equilibrium, adsorption kinetics and surface rheological behavior. *J. Colloid Interface Sci.* **2013**, *400*, 49-58, doi:10.1016/j.jcis.2013.03.015.
72. Maestro, A.; Kotsmar, C.; Javadi, A.; Miller, R.; Ortega, F.; Rubio, R.G. Adsorption of β-Casein–Surfactant Mixed Layers at the Air–Water Interface Evaluated by Interfacial Rheology. *J. Phys. Chem. B* **2012**, *116*, 4898–4907, doi:10.1021/jp301031y.
73. Maestro, A.; Ortega, F.; Rubio, R.G.; Rubio, M.A.; Krägel, J.; Miller, R. Rheology of poly(methyl methacrylate) Langmuir monolayers: Percolation transition to a soft glasslike system *J. Chem. Phys.* **2011**, *134*, 104704, doi:10.1063/1.3560612.
74. Riande, E.; Diaz-Calleja, R.; Prolongo, M.G.; Masegosa, R.; Salom, C. *Polymer Viscoelasticity: Stress and Strain in Practice*; CRC Press, Taylor and Francis: Boca Raton, FL, USA, 2000.
75. Noskov, B.A. Dilational surface rheology of polymer and polymer/surfactant solutions. *Curr. Opin. Colloid Interface Sci.* **2010**, *15*, 229-236, doi:10.1016/j.cocis.2010.01.006.
76. Danov, K.; Stanimirova, R.; Kralchevsky, P.; Marinova, K.; Alexandrov, N.; Stoyanov, S.; Blijdenstein, T.; Pelan, E. Capillary meniscus dynamometry - method for determining the surface tension of drops and bubbles with isotropic and anisotropic surface stress distributions. *J. Colloid Interface Sci.* **2015**, *440*, 168-178, doi:10.1016/j.jcis.2014.10.067.
77. Ravera, F.; Loglio, G.; Kovalchuk, V.I. Interfacial dilational rheology by oscillating bubble/drop methods. *Curr. Opin. Colloid Interface Sci.* **2010**, *15*, 217-228, doi:10.1016/j.cocis.2010.04.001.
78. Kotula, A.P.; Anna, S.L. Regular perturbation analysis of small amplitude oscillatory dilatation of an interface in a capillary pressure tensiometer. *J. Rheol.* **2014**, *59*, 85–117, doi:10.1122/1.4902546.
79. Javadi, A.; Krägel, J.; Makievski, A.V.; Kovalchuk, V.I.; Kovalchuk, N.M.; Mucic, N.; Loglio, G.; Pandolfini, P.; Karbaschi, M.; Miller, R. Fast dynamic interfacial tension measurements and dilational rheology of interfacial layers by using the capillary pressure technique. *Colloids Surf. A* **2012**, *407*, 159-168, doi:10.1016/j.colsurfa.2012.05.026.
80. Kovalchuk, V.I.; Krägel, J.; Makievski, A.V.; Loglio, G.; Ravera, F.; Liggieri, L.; Miller, R. Frequency characteristics of amplitude and phase of oscillating bubble systems in a closed measuring cell. *J. Colloid Interface Sci.* **2002**, *252*, 433-442, doi:10.1006/jcis.2002.8506.

81. Guzmán, E.; Santini, E.; Ferrari, M.; Liggieri, L.; Ravera, F. Evaluation of the impact of carbonaceous particles in the mechanical performance of lipid Langmuir monolayers. *Colloids Surf. A* **2022**, *634*, 127974, doi:10.1016/j.colsurfa.2021.127974.
82. Guzmán, E.; Santini, E.; Ferrari, M.; Liggieri, L.; Ravera, F. Interaction of Particles with Langmuir Monolayers of 1,2-Dipalmitoyl-Sn-Glycero-3-Phosphocholine: A Matter of Chemistry? *Coatings* **2020**, *10*, 469, doi:10.3390/coatings10050469.
83. Petkov, J.; Gurkov, T.; Campbell, B.; Borwankar, R. Dilatational and shear elasticity of gel-like protein layers on air/water interface. *Langmuir* **2000**, *16*, 3703-3711, doi:10.1021/la991287k.
84. Vora, S.; Bognet, B.; Patanwala, H.; Young, C.; Chang, S.; Daux, V.; Ma, A. Global strain field mapping of a particle-laden interface using digital image correlation. *J. Colloid Interface Sci.* **2018**, *509*, 94-101, doi:10.1016/j.jcis.2017.08.082
85. Alicke, A.; Simon, S.; Sjöblom, J.; Vermant, J. Assessing the interfacial activity of insoluble asphaltene layers: interfacial rheology versus interfacial tension. *Langmuir* **2020**, *36*, 14942-14959, doi:10.1021/acs.langmuir.0c02234.
86. Duncan, J.H.; Waxman, A.M.; Tulin, M.P. The dynamics of waves at the interface between a viscoelastic coating and a fluid flow. *J. Fluid Mech.* **1985**, *158*, 177-197, doi:10.1017/S0022112085002609.
87. Slavchov, R.I.; Peychev, B.; Ismail, A.S. Characterization of capillary waves: A review and a new optical method *Phys. Fluids* **2021**, *33*, 101303 doi:10.1063/5.0066759.
88. Sergievskaya, l.; Ermakov, S.; Lazareva, T.; Guo, J. Damping of surface waves due to crude oil/oil emulsion films on water. *Mar. Pollut. Bull.* **2019**, *146*, 206-214, doi:10.1016/j.marpolbul.2019.06.018.
89. Ermakov, S.A. Damping of gravity-capillary waves on water surface covered with a visco-elastic film of finite thickness *Izv. Atmos. Ocean. Phys.* **2003**, *39*, 624-628.
90. Ermakov, S.A.; Kijashko, S.V. Laboratory study of the damping of parametric ripples due to surfactant films. In *Marine Surface Films. Chemical Characteristics, Influence on Air-Sea Interactions and Remote Sensing*, Gade, M., Hühnerfuss, H., Korenowski, G.M., Eds. Berlin, Germany: Springer, 2006; pp. 113-128.
91. Langevin, D. Rheology of adsorbed surfactant monolayers at fluid surfaces. *Annu. Rev. Fluid Mech.* **2014**, *46*, 47-65, doi:10.1146/annurev-fluid-010313-141403.
92. Liu, X.; Duncan, J.H.; Korenowski, G.M.; Kelly, J.S. A laboratory study of longitudinal waves in surfactant films in a water wave tank. *J. Geophys. Res.: Oceans* **2007**, *122*, C06005, doi:10.1029/2006JC003867.
93. Rajan, G.K. Dissipation of interfacial Marangoni waves and their resonance with capillary-gravity waves. *Int. J. Eng. Sci.* **2020**, *154*, 103340, doi:10.1016/j.ijengsci.2020.103340.
94. Rajan, G.K. Solutions of a comprehensive dispersion relation for waves at the elastic interface of two viscous fluids. *Eur. J. Mech. B: Fluids* **2021**, *89*, 241-258, doi:10.1016/j.euromechflu.2021.05.012.
95. Derkach, S.R.; Krägel, J.; Miller, R. Methods of measuring rheological properties of interfacial layers (Experimental methods of 2D rheology). *Colloid J.* **2009**, *71*, 1-17, doi:10.1134/S1061933X09010013.
96. Rajan, G.K. Damping rate measurements and predictions for gravity waves in an air–oil–water system *Phys. Fluids* **2022**, *34*, 022113, doi:10.1063/5.0078160.
97. Lau, Y.M.; Westerweel, J.; Water, W.v.d. Using Faraday Waves to Measure Interfacial Tension. *Langmuir* **2020**, *36*, 5872–5879, doi:10.1021/acs.langmuir.0c00622.

98. Kharbedia, M.; Caselli, N.; Herráez-Aguilar, D.; López-Menéndez, H.; Enciso, E.; Santiago, J.A.; Monroy, F. Moulding hydrodynamic 2D-crystals upon parametric Faraday waves in shear-functionalized water surfaces. *Nat. Commun.* **2021**, *12*, 1130, doi:10.1038/s41467-021-21403-0.
99. Henderson, D.M. Effects of surfactants on Faraday-wave dynamics. *J. Fluid Mech.* **1998**, *365*, 89-107, doi:10.1017/S0022112098001086.
100. Henderson, D.M.; Larsson, K.; Rao, Y.K. A study of wheat storage protein monolayers by Faraday wave damping. *Langmuir* **1991**, *7*, 2731–2736, doi:10.1021/la00059a054.
101. Monroy, F.; Ortega, F.; Rubio, R.G. Dilatational rheology of insoluble polymer monolayers: Poly(vinylacetate). *Phys. Rev. E* **1998**, *58*, 7629, doi:10.1103/PhysRevE.58.7629.
102. Guzmán, E.; Ritacco, H.; Ortega, F.; Svitova, T.; Radke, C.J.; Rubio, R.G. Adsorption Kinetics and Mechanical Properties of Ultrathin Polyelectrolyte Multilayers: Liquid-Supported versus Solid-Supported Films. *J. Phys. Chem. B* **2009**, *113*, 7128–7137, doi:10.1021/jp811178a.
103. Alexandrov, N.A.; Marinova, K.G.; Gurkov, T.D.; Danov, K.D.; Kralchevsky, P.A.; Stoyanov, S.D.; Blijdenstein, T.B.J.; Arnaudov, L.N.; Pelan, E.G. Interfacial layers from the protein HFBII hydrophobin: Dynamic surface tension, dilatational elasticity and relaxation times. *J. Colloid Interface Sci.* **2012**, *376*, 296-306, doi:10.1016/j.jcis.2012.03.031.
104. Hilles, H.; Monroy, F. Dilational creep compliance in Langmuir polymer films. *Soft Matter* **2011**, *7*, 7790-7796 doi:10.1039/C1SM05255A.
105. Findley, W.N.; Lai, J.S.; Onaran, K. *Creep and relaxation of nonlinear viscoelastic materials*; Dover Publications, Inc.: New York, NY, USA, 1976.
106. Ravera, F.; Liggieri, L.; Loglio, G. Dilational rheology of adsorbed layers by oscillating drops and bubbles. In *Interfacial Rheology*, Miller, R., Liggieri, L., Eds. Brill: Leiden, The Netherlands, 2009; pp. 138-173.
107. Lombardini, P.P.; Piazzese, F.; Cini, R. The Marangoni wave in ripples on an air-water interface covered by a spreading film. *Il Nuovo Cimento C* **1982**, *5*, 256–263, doi:10.1007/BF02509014.
108. Ghia, P.L.; Trivero, P. On the vibration modes of the air-water interface in the presence of surface films. *Il Nuovo Cimento C* **1988**, *11*, 305–315, doi:10.1007/BF02507915.
109. Fiscella, B.; Lombardini, P.P.; Trivero, P.; Cini, R. Ripple damping on water surface covered by a spreading film: Theory and experiment. *Il Nuovo Cimento C* **1985**, *8*, 491–500, doi:10.1007/BF02582676.
110. Monroy, F.; Ortega, F.; Rubio, R.G.; Velarde, M.G. Surface rheology, equilibrium and dynamic features at interfaces, with emphasis on efficient tools for probing polymer dynamics at interfaces. *Adv. Colloids Interface Sci.* **2007**, *134-135*, 175-189, doi:10.1016/j.cis.2007.04.023.
111. Cicuta, P.; Hopkinson, I. Recent developments of surface light scattering as a tool for optical-rheology of polymer monolayers. *Colloids Surf. A* **2004**, *233*, 97-107, doi:10.1016/j.colsurfa.2003.11.025.
112. Sutherland, G.; Halsne, T.; Rabault, J.; Jensen, A. The attenuation of monochromatic surface waves due to the presence of an inextensible cover. *Wave Motion* **2017**, *68*, 88-96, doi:10.1016/j.wavemoti.2016.09.004.
113. Jenkins, A.D.; Jacobs, S.J. Wave damping by a thin layer of viscous fluid. *J. Fluid Mech.* **1997**, *9*, 1256, doi:10.1063/1.869240.

114. Monroy, F. Surface hydrodynamics of viscoelastic fluids and soft solids: Surfing bulk rheology on capillary and Rayleigh waves. *Adv. Colloid Interface Sci.* **2017**, *247*, 4-22, doi:10.1016/j.cis.2017.07.006.
115. Muñoz, M.G.; Monroy, F.; Hernández, P.; Ortega, F.; Rubio, R.G.; Langevin, D. Anomalous Damping of the Capillary Waves at the Air−Water Interface of a Soluble Triblock Copolymer. *Langmuir* **2003**, *19*, 2147–2154, doi:10.1021/la0206007.
116. Baidakov, V.G.; Protsenko, S.P.; Bryukhanov, V.M. Relaxation processes at liquid-gas interfaces in one- and two-component Lennard-Jones systems: Molecular dynamics simulation. *Fluid Ph. Equilibria* **2019**, *481*, 1-14, doi:10.1016/j.fluid.2018.10.012.
117. Lucassen, J.; Van Den Tempel, M. Dynamic measurements of dilational properties of a liquid interface. *Chem. Eng. Sci.* **1972**, *27*, 1283-1291, doi:10.1016/0009-2509(72)80104-0.
118. Van den Tempel, M.; Lucassen-Reynders, E. Relaxation processes at fluid interfaces. *Adv. Colloid Interface Sci.* **1983**, *18*, 281-301, doi:10.1016/0001-8686(83)87004-3.
119. Liggieri, L.; Miller, R. Interfacial rheology—The response of two-dimensional layers on external perturbations. *Curr. Opin. Colloid Interface Sci.* **2010**, *15*, 256–263, doi:10.1016/j.cocis.2010.05.001.
120. Muñoz-López, R.; Guzmán, E.; Velázquez, M.M.; Fernández-Peña, L.; Merchán, M.D.; Maestro, A.; Ortega, F.; Rubio, R.G. Influence of Carbon Nanosheets on the Behavior of 1,2-Dipalmitoyl-sn-glycerol-3-phosphocholine Langmuir Monolayers. *Processes* **2020**, *8*, 94, doi:10.3390/pr8010094.
121. Guzmán, E.; Fernández-Peña, L.; Akanno, A.; Llamas, S.; Ortega, F.; Rubio, R.G. Two Different Scenarios for the Equilibration of Polycation—Anionic Solutions at Water–Vapor Interfaces. *Coatings* **2019**, *9*, 438, doi:10.3390/coatings9070438.
122. Llamas, S.; Guzmán, E.; Akanno, A.; Fernández-Peña, L.; Ortega, F.; Campbell, R.A.; Miller, R.; Rubio, R.G. Study of the Liquid/Vapor Interfacial Properties of Concentrated Polyelectrolyte–Surfactant Mixtures Using Surface Tensiometry and Neutron Reflectometry: Equilibrium, Adsorption Kinetics, and Dilational Rheology. *J. Phys. Chem. C* **2018**, *122*, 4419–4427, doi:10.1021/acs.jpcc.7b12457.
123. Akanno, A.; Guzmán, E.; Fernández-Peña, L.; Llamas, S.; Ortega, F.; Rubio, R.G. Equilibration of a Polycation–Anionic Surfactant Mixture at the Water/Vapor Interface. *Langmuir* **2018**, *34*, 7455–7464, doi:10.1021/acs.langmuir.8b01343.
124. Hilles, H.; Maestro, A.; Monroy, F.; Ortega, F.; Rubio, R.G. Polymer monolayers with a small viscoelastic linear regime: Equilibrium and rheology of poly(octadecyl acrylate) and poly(vinyl stearate) *J. Chem. Phys.* **2007**, *126*, 124904, doi:10.1063/1.2714514
125. Hilles, H.; Monroy, F.; Bonales, L.J.; Ortega, F.; Rubio, R.G. Fourier-transform rheology of polymer Langmuir monolayers: Analysis of the non-linear and plastic behaviors. *Adv. Colloid Interface Sci.* **2006**, *122*, 67-77, doi:10.1016/j.cis.2006.06.013.
126. Guzmán, E.; Santini, E.; Ferrari, M.; Liggieri, L.; Ravera, F. Effect of the Incorporation of Nanosized Titanium Dioxide on the Interfacial Properties of 1,2-Dipalmitoyl-sn-glycerol-3-phosphocholine Langmuir Monolayers. *Langmuir* **2017**, *33*, 10715-10725, doi:10.1021/acs.langmuir.7b02484.
127. Sagis, L.M.C.; Fischer, P. Nonlinear rheology of complex fluid–fluid interfaces. *Curr. Opin. Colloid Interface Sci.* **2014**, *19*, 520–529, doi:10.1016/j.cocis.2014.09.003.
128. Ferri, J.K.; Fernandes, P.A.L.; McRuiza, J.T.; Gambinossi, F. Elastic nanomembrane metrology at fluid–fluid interfaces using axisymmetric drop shape analysis with anisotropic surface tensions: deviations from Young–Laplace equation†. *Soft Matter* **2012**, *8*, 10352-10359 doi:10.1039/C2SM26604K.

129. Loglio, G.; Pandolfini, P.; Miller, R.; Makievski, A.V.; Krägel, J.; Ravera, F.; B.A. Noskov, C.S., A, 2005, 261, 57–63. Perturbation–response relationship in liquid interfacial systems: non-linearity assessment by frequency–domain analysis. *Colloids Surf. A* **2005**, *261*, 57-63, doi:10.1016/j.colsurfa.2004.10.130.
130. Bykov, A.G.; Liggieri, L.; Noskov, B.A.; Pandolfinib, P.; F.Ravera; Loglio, G. Surface dilational rheological properties in the nonlinear domain☆. *Adv. Colloid Interface Sci.* **2015**, *222*, 110-118, doi:10.1016/j.cis.2014.07.006.
131. Wilde, P.J. Interfaces: their role in foam and emulsion behaviour. *Current Opinion in Colloid & Interface Science* **2000**, *5*, 176-181, doi:10.1016/s1359-0294(00)00056-x.
132. Rawate, H.; Goswami, A. Importance of Interfacial Rheology and its Applications - Review of the Interfacial Rheology. *JETIR* **2018**, *5*, 312.
133. Leiske, D.; Leiske, C.; Leiske, D.; Toney, M.; Senchyna, M.; Ketelson, H.; Meadows, D.; Fuller, G.G. Temperature-induced transitions in the structure and interfacial rheology of human meibum. *Biophys J* **2012**, *102*, 369-376, doi:10.1016/j.bpj.2011.12.017.
134. Bertsch, P.; Bergfreund, J.; Windhab, E.J.; Fischer, P. Physiological fluid interfaces: Functional microenvironments, drug delivery targets, and first line of defense. *Acta Biomater* **2021**, *130*, 32-53, doi:10.1016/j.actbio.2021.05.051.
135. Wu, C.; Lim, J.Y.; Fuller, G.G.; Cegelski, L. Quantitative analysis of amyloid-integrated biofilms formed by uropathogenic Escherichia coli at the air-liquid interface. *Biophys J* **2012**, *103*, 464-471, doi:10.1016/j.bpj.2012.06.049.
136. Warburton, B. Interfacial rheology. *Current Opinion in Colloid & Interface Science* **1996**, *1*, 481-486, doi:10.1016/s1359-0294(96)80116-6.
137. Safouane, M.; Langevin, D. Surface viscoelasticity of concentrated salt solutions: specific ion effects. *Chemphyschem* **2009**, *10*, 222-225, doi:10.1002/cphc.200800527.
138. Monroy, F.; Giermanska Kahn, J.; Langevin, D. Dilational viscoelasticity of surfactant monolayers. *Colloids and Surfaces A: Physicochemical and Engineering Aspects* **1998**, *143*, 251-260, doi:10.1016/s0927-7757(98)00373-2.
139. Monroy, F.; Giermanska-Kahn, J.; Langevin, D. Anomalous Damping of Capillary Waves With Surfactant Solutions. *Journal of Non-Equilibrium Thermodynamics* **2001**, *25*, doi:10.1515/jnetdy.2000.019.
140. Stenvot, C.; Langevin, D. Study of viscoelasticity of soluble monolayers using analysis of propagation of excited capillary waves. *Langmuir* **2002**, *4*, 1179-1183, doi:10.1021/la00083a022.
141. Earnshaw, J.C.; McCoo, E. Surface Light-Scattering Studies of Surfactant Solutions. *Langmuir* **2002**, *11*, 1087-1100, doi:10.1021/la00004a011.
142. Sharpe, D.; Eastoe, J. Properties of Surfactant Monolayers Studied by Surface Light Scattering. *Langmuir* **1996**, *12*, 2303-2307, doi:10.1021/la951078+.
143. Monroy, F.; Muñoz, M.G.; Rubio, J.E.F.; Ortega, F.; Rubio, R.G. Capillary Waves in Ionic Surfactant Solutions: Effects of the Electrostatic Adsorption Barrier and Analysis in Terms of a New Dispersion Equation. *The Journal of Physical Chemistry B* **2002**, *106*, 5636-5644, doi:10.1021/jp012044f.
144. Cuenca, V.E.; Ferna Ndez Leyes, M.; Falcone, R.D.O.; Correa, N.M.; Langevin, D.; Ritacco, H.N. Interfacial Dynamics and Its Relations with ?Negative? Surface Viscosities Measured at Water?Air Interfaces Covered with a Cationic Surfactant. *Langmuir* **2019**, *35*, 8333-8343, doi:10.1021/acs.langmuir.9b00534.

Chapter II: Experimental methods

In this chapter, an overview of the experimental set-ups utilized in this PhD Thesis, as well as the theoretical frameworks used to obtain physico-chemical information from the performed measurements, will be introduced. The presentation of the techniques will be divided in 3 categories:

- Interfacial dilational rheology. In this PhD Thesis, information of the interfacial dilational properties of fluid interfaces has been obtained by means of oscillatory barriers in Langmuir troughs and oscillatory drops in Profile Analysis Tensiometers (PAT) at low frequency, and by Electro-Capillary Waves (ECW) at high frequencies.
- Bulk rheology. The description of techniques used for the characterization of the bulk rheology of different systems will put the focus on the Ubbelohde viscometer and Diffusing Wave Spectroscopy (DWS).
- Ancillary techniques. A brief description of some ancillary techniques used for the characterization of different bulk properties of the complex fluids used in this PhD Thesis will be provided. These techniques include Dynamic Light Scattering (DLS) for the characterization of the dimensions of the macromolecules or colloidal particles dispersed in a liquid phase, and the determination of the electrophoretic mobility of them to evaluate the Z-potential of macromolecules or particles. Moreover, some details of the technique used for the characterization of the contact angle of solution droplets deposited on solid surface will be introduced.

2.1. Interfacial dilational rheology measurements

2.1.1. Langmuir trough

A Langmuir tensiometer is an instrument used to evaluate the properties of interfacial films at the fluid/fluid interface. It allows the precise control and measurement of the interfacial tension (γ) as a function of the area occupied by the film. It consists of a Teflon trough with a depth of a few millimeters, coupled to two computer-controlled barriers arranged in parallel at opposite ends of the trough. The barriers can be used to compress or expand the area available for the interface under controlled conditions. The barriers are usually made of a hydrophilic material, such as polyoxymethylene (Delrin), which makes it possible to prevent film leakage at low interfacial tension values. The interfacial tension is commonly measured by using a force balance fitted with a Wilhelmy plate as contact probe. Temperature control of the liquid in the trough is achieved (precision ±0.1ºC) by circulating water from a thermostatic bath through a jacket at the bottom of the trough. In this PhD Thesis, it has been used a commercially available Langmuir trough model 701 (Nima Technologies, Coventry, United Kingdom). **Figure 2. 1** shows a scheme of the equipment and the image of the one used in the present PhD Thesis.

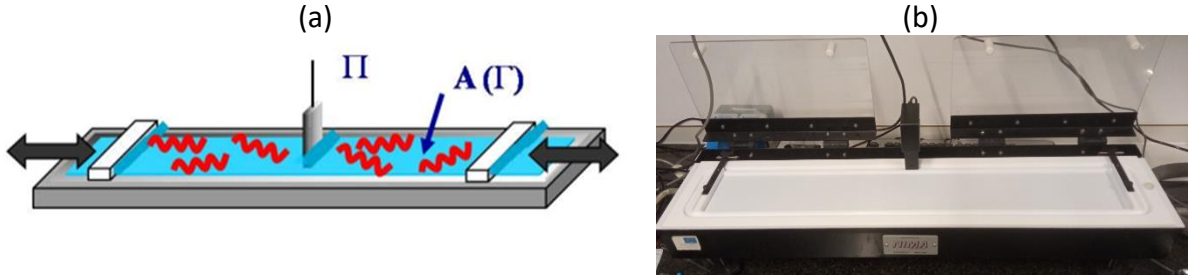

Figure 2. 1. (a) Scheme and (b) picture (Nima 701 model, Nima Technologies, Coventry, United Kingdom) of a Langmuir trough. Adapted from reference [1].

The Langmuir trough can be either used to characterize Langmuir or Gibbs monolayers. Langmuir monolayers are prepared by spreading a small amount of the surfactant, polymer and/or particle solution (usually dissolved in a non-polar solvent, like chloroform) onto a bare air-water interface. On the other hand, Gibbs Monolayers are merely prepared by pouring the solution onto the trough and waiting for equilibrium adsorption.

The interfacial tension is determined by measuring the maximum force required to detach a plate from the interface. The Wilhelmy plate method is particularly advantageous when using a Langmuir trough because it measures the relative force between the monolayer and the bare interface, rather than the maximum detachment force. Additionally, it does not require additional corrections. The plate, which can be made of rough platinum or chromatography paper, is suspended from a hook of a microbalance and moved until it contacts the air-water interface (refer to the diagram in **Figure 2. 2**. In the case of the Langmuir trough used in this PhD Thesis, a surface force balance (NIMA PS4, manufactured by Nima Technology, Coventry, UK) is installed above the Langmuir trough, and it is used to measure interfacial tension variations. The surface balance is fitted with disposable chromatography-quality pure cellulose paper Wilhelmy plates (Whatman CHR1 chromatography paper, Merck, Darmstadt) of 20.6 mm of perimeter. A fresh paper plate is used for each measurement to prevent any potential modifications in the plate surface caused by material adsorption.

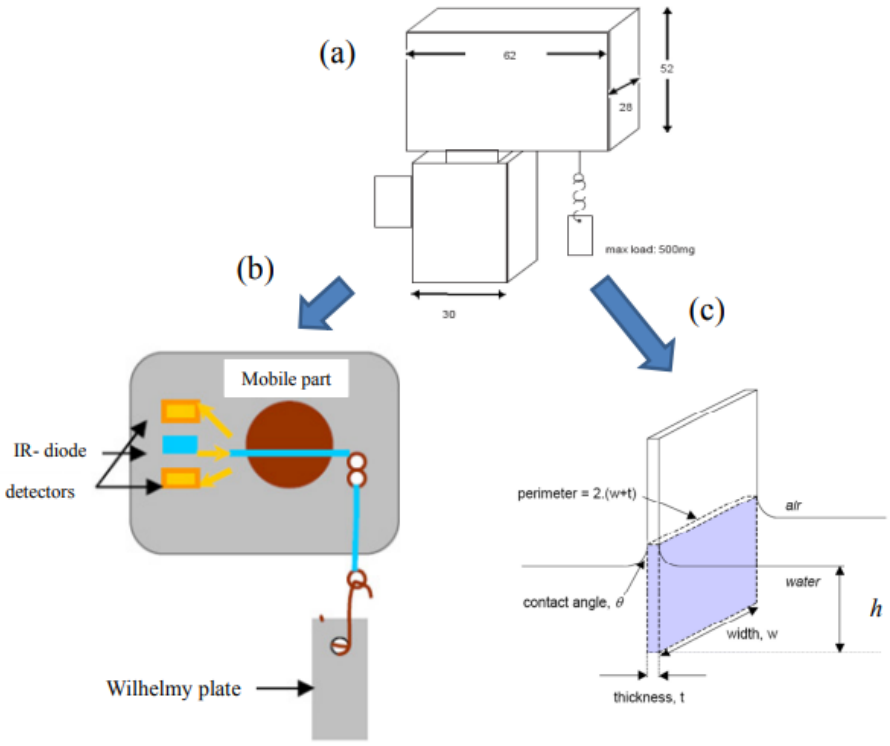

Figure 2. 2. Scheme of the surface force microbalance and the Wilhelmy plate. (a) General aspect of the Wilhelmy plate hung from the hook of the surface force microbalance. (b) Internal scheme of the microbalance. (c) Detail of the Wilhelmy plate. Adapted from reference [1].

When the plate is placed at liquid/vapor interface, the weight (*W*) of the plate increase by the force (F) exerted by the interface, consequently, this increment of weight (ΔW) is related to the surface tension (γ) by the following expression [1,2],

$$\gamma = \frac{\Delta W}{L cos\theta}, \tag{2. 1}$$

where *L* is the plate perimeter, and θ is the contact angle between the liquid and the plate,

$$\theta = arcsin\left[1 - \left(\frac{h}{a}\right)^2\right], \tag{2. 2}$$

where *a* is the capillary length and *h* accounts for the height of the plate as shown in **Figure 2. 2**. The set up works under the hypothesis of zero contact angle. Experimentally, in the microbalance device the detection of the interfacial tension γ is based on the deflection of a mechanical mobile part produced by the increment of weight (ΔW) of the plate fixed by a hook when it is placed at the interface. Each reading of the surface tension made by the microbalance is determined within ±0.1 mN/m.

The force exerted on a Wilhelmy plate immersed in the water, measured with a microbalance, gives the surface pressure, Π, defined as the difference between, γ_0, the interfacial tension of the bare interface, and γ the interfacial tension in presence of the monolayer ($\Pi = \gamma_0 - \gamma$) . The surface pressure is related to the surface concentration by the equation of state $\Pi = \Pi(\Gamma, T)$, where *T* is the temperature (other factors like pH, ionic strength and the composition of the subphase and of the monolayer are kept constant).

The set-up can be used to perform creep experiments, stress relaxation experiments, and oscillatory area experiments (see *Chapter II*, 2.1.2. Oscillatory barrier experiments). In this PhD thesis, only oscillatory area experiments have been performed, hence they will be discussed in further details. In addition to the experiments performed in the Langmuir trough, independent interfacial tension measurements were performed using a force tensiometer K10T Digital Tensiometer (KRÜSS GmbH, Hamburg, Germany), fitted with a platinum Wilhelmy plate contact probe of 40.5 mm in perimeter.

2.1.2. Oscillatory barrier experiments

Oscillatory barrier experiments in a Langmuir trough are used to characterize the dilational interfacial rheology fluid/fluid interfaces in the frequency range of 10^{-3}-10^{-1} Hz. This type of experiments relies in the application of periodic sinusoidal compression-expansion cycles of the interface by the simultaneous motion of the two barriers with a fixed frequency and deformation amplitude [1,3]. Let $u(t) = \frac{A_0 - A(t)}{A_0}$ be the oscillatory area strain (where A_0 is the initial area, and $A(t)$ is the instantaneous value of area, applied at fixed angular frequency ω and amplitude u_0 [1,3],

$$u(t) = \frac{u_0}{2}\exp(i\omega). \tag{2. 3}$$

If the deformation allows maintaining the monolayer response within the linear regime, this will follow a sinusoidal function with the same frequency of the strain,

$$\Pi(t) = \Pi_0 - \sigma(t), \tag{2. 4}$$

with $\sigma(t) = \frac{\sigma_0}{2}\exp(\mathrm{i}\omega + \phi_\sigma)$. ϕ_σ introduces a phase factor that include the contribution associated with the viscous delays in the rheological response of the interface. From oscillatory area experiments, within the linear regime, it is possible to obtain the elastic modulus E_s and the dilational viscosity κ_s as follows,

$$E_s = E cos\phi_\sigma, \tag{2. 5}$$

and

$$\omega\kappa_s = E sin\phi_\sigma, \tag{2. 6}$$

with $E = {}^{\sigma_0}/_{u_0}$.

2.1.3. Profile Analysis Tensiometer (PAT)

The Profile Analysis Tensiometer (PAT) or Drop Shape Tensiometer (DST) is typically employed for dynamic and equilibrium interfacial tension measurements on static drop or bubble surfaces, but also to assess dilational viscoelasticity of the interface at frequencies similar to that probed by oscillatory barrier experiments. When a bubble or a drop of one liquid is placed within another fluid, its shape is influenced by surface tension and the density difference between the two fluids under the effect of gravity. An experiment in a Profile Analysis Tensiometer relies on the fact that the hydrostatic pressure in each coordinate of the drop or bubble *P=(x;z)* is balanced by capillary pressure, according to Young-Laplace equation [4],

$$\left(\frac{1}{R_1}+\frac{1}{R_2}\right)\gamma = \Delta p - \Delta\rho g z, \tag{2. 7}$$

where Δp is the pressure difference between the bulk of the drop and the external fluid surrounding the drop, ρ is the difference of densities between the inner and outer fluid, γ is the interfacial tension, R_1 and R_2 are the two main curvature radii along two independent directions. In small droplets (nearly spherical interfaces), $R_1 = R_2 = R$. It should be noted that in most of the cases the deformation of drops/bubbles cannot be considered as purely radial. Furthermore, many times is very difficult to obtain accurate values of the curvature radius. This can be commonly solved by considering that drops/bubbles undergo an axisymmetric deformation under the application of an external force. However, this condition is not fulfilled when densely coated drops and bubbles are considered [5,6]. In general, the use of drop/bubble shape tensiometers for evaluating the dilational properties assumes the existence of a single isotropic and constant tension for the entire interface. This allows applying the generalized Young-Laplace equation [4],

$$\kappa_\phi \sigma_\phi + \kappa_s \sigma_s = p - \rho g z \tag{2. 8}$$

with κ_ϕ and σ_ϕ defining the principal curvature and stress in circumferential direction, respectively, whereas κ_s and σ_s account for the principal curvature and stress in meridional direction, respectively. The interfacial stresses are magnitudes that depends on the interfacial deformation, and hence its evaluation should be locally performed because the deformation may not be constant within the whole drop/bubble. On the other side, when the deformations are non-isotropic, the principal interfacial stresses become equal [7]. If the drop is axis-symmetric (that condition holds for spherical drops, of course), its profile fits with the Bashforth-Adams equation, which provides an integration of the Laplace equation to represent the mechanical equilibrium at every point on the surface [8],

$$2 + \frac{\beta z}{b} = \left(\frac{b}{R^*} + \frac{b\sin(\phi)}{x}\right), \tag{2. 9}$$

where R^* is the curvature radius of the meridian section at the point $P \equiv (x,z)$, b is the curvature at drop apex and ϕ the angle between the normal to the surface at the same point and the vertical axes and b the curvature radius at the drop apex (**Figure 2. 3**).

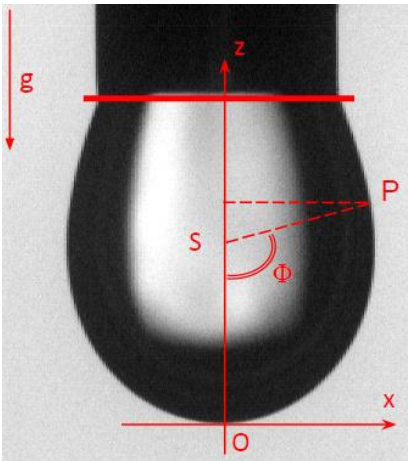

Figure 2. 3. Sketch of the meridian section of a pendant drop.

β is the shape factor, obtained from the best fit of the Bashforth-Adams equation to the drop profile coordinates. (β < 0 for Pendant/Emerging drops),

$$\beta = \frac{\Delta\rho|\boldsymbol{g}|b^2}{\gamma}\left(\frac{\boldsymbol{e_z}\cdot\boldsymbol{g}}{|\boldsymbol{g}|}\right), \tag{2. 10}$$

where $\Delta\rho$ is the density difference between the bulk of the drop (i.e., density of the sample) and the external ambient surrounding the drop (usually, air), $\boldsymbol{g}$ is the earth gravity acceleration vector, oriented in opposite direction with respect to the z-axis unit vector $\boldsymbol{e_z}$. In many cases, accurate data are obtained whenever $|\beta|$>0.1. Moreover, such technique is valid if the surface of the drop is close enough to the mechanical equilibrium. Hence, the technique is typically employed for measuring the dynamic surface tension at constant area (adsorption dynamics), or for measuring the instantaneous surface tension at slow variations of the surface area (surface dilational rheology at low frequency). For area oscillations with amplitude below 10% (at liquid/air interface), the drop can be approximately considered at quasi-mechanical equilibrium for frequencies below 1 Hz, although, accurate rheology measurements are usually guaranteed within 0.005-0.2 Hz frequency range [9].

The interfacial tension is determined by comparing the drop profile obtained theoretically to the experimental one. By varying the interfacial tension, a series of theoretical curves are generated. The optimal interfacial tension value corresponds to the theoretical curve that best fits the experimental data points (highlighted in red). This fitting process ensures accurate measurement of the interfacial tension, as depicted in **Figure 2. 4**.

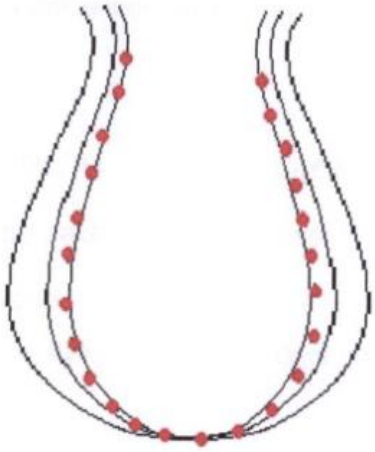

Figure 2. 4. Illustration of a pendant drop and the concept of fitting the Laplace equation with the drop profile. Adapted from reference [1].

A typical PAT consists of a cell where a drop or bubble is formed in the tip of a capillary inside another fluid, continuously monitored by a camera. This setup allows for automatic acquisition of the drop profile, enabling precise control of the drop volume and area. In addition, the apparatus presents a pump connected to one or several syringes that aspires and pumps liquid to modify the drop/bubble volume in such a way that it is possible to modify the interfacial area. A light is used to enhance the contrast of drop profile, and the temperature is kept constant by means of a thermostatic bath. When conducting adsorption experiments with a PAT, the surface area is typically maintained constant while the drop profile is recorded as the surface tension changes. On the other hand, for dilational viscoelasticity measurements, the

interfacial tension is obtained continuously under the application of a harmonic small amplitude perturbation to the drop area, typically a few percent. Practically, this involves forcing the area of a drop, which is in an equilibrium state with a defined interfacial tension, to oscillate around its reference with a fixed frequency.

Let *A(t)* be the drop area, as a function of time, subjected to an oscillatory variation occurring at fixed angular frequency ω and at constant amplitude ΔA, around the average value of A_0, and with a certain phase angle φ_A [10],

$$A(t) = A_0 + \Delta A cos(\omega t + \varphi_A). \quad (2.\ 11)$$

Then, in linear regime (small area deformation amplitude), the surface tension $\gamma(t)$ varies according to a profile defined by a cosine-like harmonic function, oscillating around the average value γ_0 (which is the value of surface tension when $A(t=0)=A_0$, with the same angular frequency ω, at constant amplitude $\Delta\gamma(\omega)$ (in the linear regime $\Delta\gamma(\omega)$ should not depend on the area deformation amplitude, but only on ω) and a certain phase angle $\varphi_\gamma(\omega)$,

$$\gamma(t) = \gamma_0 + \Delta\gamma(\omega)\, cos\left[\omega t + \varphi_\gamma(\omega)\right]. \quad (2.\ 12)$$

The experimental values of *A(t)* and $\gamma(t)$ are fitted with equation (2. 11) and (2. 12) respectively, and the dilational interfacial modulus can be determined as follows,

$$E_s^*(\omega) = \frac{A_0\Delta\gamma(\omega)}{\Delta A} cos[\Delta\varphi(\omega)] + i\frac{A_0\Delta\gamma(\omega)}{\Delta A} sin[\Delta\varphi(\omega)], \quad (2.\ 13)$$

with $\Delta\varphi(\omega) = \varphi_\gamma(\omega) - \varphi_A$ being the phase lag between *A(t)* and $\gamma(t)$.

In this PhD Thesis, three different Profile Analysis Tensiometers, two home-built ones and a commercial one, have been used. The two home-built PAT were designed and fabricated at the University of Granada (Granada, Spain). These devices were based on the Axisymmetric Drop Shape Analysis (ADSA) method, which is described in detail elsewhere [11]. The setup, including the image capturing, the microinjector, the ADSA algorithm, and the fuzzy pressure control, was managed by a Windows-integrated program (DINATEN(R)) [12]. The main difference between the two home-built Profile Analysis Tensiometers is related to the implementation of the hardware and software required for performing oscillating experiments for evaluating the dilational response of the interface. The commercial tensiometer was a PAT 1 from SINTERFACE (Berlin, Germany).

2.1.4. Electro-Capillary Waves (ECW)

2.1.4.1. Capillary waves: the hydrodynamic problem.

Capillary waves can be generated upon the application of mechanically, thermally or electrically-driven perturbations on the surface of a liquid. These waves propagate along the parallel direction to the fluid/fluid interface, and are damped by the action of the surface forces that try to restore the flatness of the interface itself [13-18]. In capillary waves, the dominating contribution of the restoring force, is given by the capillary contribution, associated with the surface tension, rather than by gravity ones [19,20]. The parameters that allow to distinguish between capillary waves and gravity waves is the wavevector (related to

the wavelength, λ) $k = 2\pi/\lambda$, the phase velocity ($v_p = \frac{\omega}{k}$), and the group velocity ($v_G = \frac{d\omega}{dk}$). Thus,

- For small wavelength (ripples), the main restoring force is given by capillarity, and in this case, $v_p = \frac{2}{3} v_G$.
- For large wavelengths, gravity prevails over capillarity, and the group velocity is half the phase velocity, i.e., $v_G = \frac{1}{2} v_p$.

The boundary between those two limits depends also on the surface tension, γ, associated to the interface between fluid 1 and fluid 2, and the density of both fluids, ρ_1 and ρ_2). There is a threshold value of wavelength ($\lambda_{(C)}$) and of phase velocity ($v_{p(C)}$) that allows to distinguish between capillary wave regime and gravity wave ones. This can be defined by the following set of equations,

$$\lambda_{(C)} = 2\pi \sqrt{\frac{\gamma}{g(\rho_1 - \rho_2)}}, \tag{2. 14}$$

And

$$v_{p(C)} = \sqrt{\frac{2\sqrt{\gamma g(\rho_1 - \rho_2)}}{(\rho_1 + \rho_2)}}. \tag{2. 15}$$

In the case of air/water interface, for example, the threshold value of the wavelength is about 1.7 cm, and the threshold group velocity is around 0.23 m/s. So, if $\lambda < \lambda_{(C)}$, the restoring force is essentially given by capillarity. In the experimental work discussed in this PhD Thesis (where only liquid/air interfaces are analyzed), wavelength is always in the range of 0.1-0.6 cm, which means that our experiments are in the capillary regime.

A traditional approach exploited for the evaluation of the mechanical response of fluid/fluid interfaces against high frequency dilational deformations relies on the study of the damping of capillary waves. If the excitation force comes from the application of an external physical stimulus, commonly mechanical or electrical, the amplitude of the waves is higher than thermally excited waves, and it can reach values of few μm [21]. In general, electrical stimuli are preferred than mechanical ones because they present a non-invasive character, allowing an easier experimental design [22]. Although information about dilational properties of fluid/fluid interfaces can be also obtained from the longitudinal wave damping (mainly given by interfacial tension gradients, allowing to probe the dilational rheology at low values of the deformation frequency [23-26]), in this PhD Thesis it has been preferred the evaluation of the dilational response in terms of the damping of capillary waves propagated along the interface. For the experiments of this PhD Thesis, the analysis of transversal capillary waves, generated by applying an electrical stimulus at liquid/air interface (see *2.1.4.4. Experimental set up* description), i.e., Electro-Capillary Waves (ECW), have been used to obtain information on the dilational response by using a home-built device. In practice, viscoelastic properties of the interface depend on the coupling between transverse (capillary) and longitudinal (dilational) modes [27], and the ECW technique allows to experimentally determine the propagation parameters of capillary modes, which can be related to the properties of the fluid/fluid

interface (surface tension and dilational interfacial modulus) and of the bulk properties of each fluid (density and shear viscosity).

The interface is characterized by its own dilational interfacial modulus $E_s^*(\omega) = E_s(\omega) + i\omega\kappa_s(\omega)$, its shear interfacial modulus $G_s^*(\omega) = G_s(\omega) + i\omega\eta_s(\omega)$, and a complex surface tension (which expresses the elastic and viscous behaviour of transversal modes): $\gamma^*(\omega) = \gamma + i\omega\gamma_T$. In case of thin monolayers, where the length of perturbation is much greater than monolayer thickness *d* ($\lambda \gg d$), transversal viscosity γ_T is negligible, so $\gamma^* \approx \gamma$ [28]. This is in agree with the assumption by Buzza, who considered that since the viscoelastic constitutive equations of Scriven model are independent on rotation of the frame of reference (frame invariance), γ_T should be null anyway [29]. On the other hand, the fluid/fluid interface is described parallel to xy-plane, and perpendicular to z-axis as shown in **Figure 2. 5** [29]. In this situation, the surface displacement vector in a point of coordinates $\boldsymbol{X} = (x, y, z)$ of the interface at a certain time *t* is defined as $\boldsymbol{u}(\boldsymbol{X}, t) = [u_x(\boldsymbol{X}, t), u_y(\boldsymbol{X}, t), u_z(\boldsymbol{X}, t)]$**.** On the other hand, each phase *j* is characterized by its own density ρ_j, bulk viscosity η_j, and the velocity profile $\boldsymbol{v_j}(\boldsymbol{X}, t) = [v_{j(x)}(\boldsymbol{X}, t), v_{j(y)}(\boldsymbol{X}, t), v_{j(z)}(\boldsymbol{X}, t)]$.

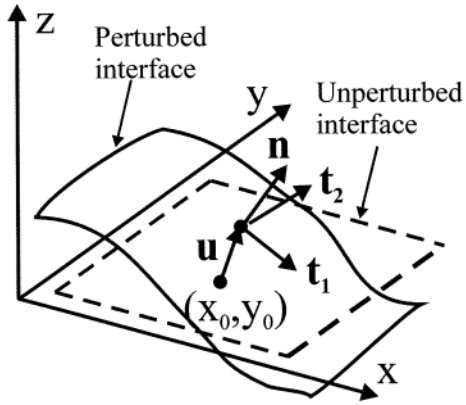

Figure 2. 5. Surface geometry of fluid/fluid interface and reference system.

In the linear viscoelastic regime (small surface deformation, $u_z \ll \lambda$), the constitutive equation that relates the surface stress $\boldsymbol{F} = (F_x, F_y, F_z)$ to the interface displacement $\boldsymbol{u}(x, y, 0, t)$ (*at z = 0*) is [29] defined according to the following matrix,

$$\boldsymbol{F} = \begin{bmatrix} E_s^*(\omega)\left(\frac{\partial^2 u_x}{\partial x^2} + \frac{\partial^2 u_y}{\partial x \partial y}\right) + G_s^*(\omega)\left(\frac{\partial^2 u_z}{\partial x^2} + \frac{\partial^2 u_x}{\partial y^2}\right) \\ E_s^*(\omega)\left(\frac{\partial^2 u_y}{\partial y^2} + \frac{\partial^2 u_x}{\partial x \partial y}\right) + G_s^*(\omega)\left(\frac{\partial^2 u_y}{\partial x^2} + \frac{\partial^2 u_y}{\partial y^2}\right) \\ \gamma\left(\frac{\partial^2 u_z}{\partial x^2} + \frac{\partial^2 u_z}{\partial y^2}\right) \end{bmatrix}. \quad (2.\ 16)$$

The motion along x-axis (longitudinal, dilational modes) is mechanically coupled with motion occurring on z-axis (transversal, capillary modes), while motion on y-axis evolves independently [28,29]. This is the reason to consider only the horizontal (x) and vertical (z) components of each variable ($\boldsymbol{F}, \boldsymbol{u}$ and $\boldsymbol{v_j}$). Thus, only capillary and dilational stresses will be considered, while shear stresses will be neglected. The idea underlying ECW measurements is to determine the spatial and temporal profile of $\boldsymbol{u}$ and $\boldsymbol{v_j}$, in presence of small capillary

perturbations. Thus, it is possible to determine the propagation features of the waves (wavelength, damping, frequency), and to relate them to the dilation properties of the interface ($E_s{}^*(\omega)$), and its interfacial tension.

The hydrodynamic problem of capillary waves was firstly solved by Levich, who proposed a solution based on a linearization Navier-Stokes equation constrained to 2D [27,29,30],

$$\begin{cases} \dfrac{\partial v_{j(x)}}{\partial t}\boldsymbol{v_j}\cdot\nabla v_{j(x)} = -\dfrac{1}{\rho_j}\dfrac{\partial P_j}{\partial x} + \dfrac{\eta_j}{\rho_j}\nabla^2 v_{j(x)} \\ \dfrac{\partial v_{j(z)}}{\partial t}\boldsymbol{v_j}\cdot\nabla v_{j(z)} = -\dfrac{1}{\rho_j}\dfrac{\partial P_j}{\partial z} + \dfrac{\eta_j}{\rho_j}\nabla^2 v_{j(z)} - g \\ \nabla\cdot\boldsymbol{v_j} = \mathbf{0} \end{cases} \quad (2.\ 17)$$

where $P_j(x,z,t)$ is the pressure in phase-j, g is the gravity, "∇" is the gradient operator $\nabla f = (\frac{\partial f}{\partial x}, \frac{\partial f}{\partial z})$ and "∇^2" is the Laplace operator $\nabla^2(f) = \frac{\partial^2 f}{\partial x^2} + \frac{\partial^2 f}{\partial z^2}$. The last equation represents the incompressible character of the fluid phase *j*. This is strictly true for liquids in phase 1, and approximately valid for air in phase 2, and contributes to a fast propagation of the perturbations. Levich proposed a solution of this equation, in presence of capillary perturbations, based on the idea that the velocity field can be expressed as follows,

$$\boldsymbol{v_j} = \boldsymbol{v_j^{(c)}} + \boldsymbol{v_j^{(r)}} = -\nabla\varphi + curl(\boldsymbol{\psi}), \quad (2.\ 18)$$

where φ is the potential function, associated with the conservative component of velocity ($\boldsymbol{v_j^{(c)}}$) in an ideal fluid (zero viscosity). The stream vectorial field $\boldsymbol{\psi}$, on the other hand, measures the amount of rotational motion (vorticity), determining the dissipation due to viscous friction, appearing associated with the rotational component $\boldsymbol{v_j^{(r)}}$) [31]. "curl" is the rotor operator applied to a vectorial field $\boldsymbol{f} = (f_x, f_y, f_z)$: $curl(\boldsymbol{f}) = [\left(\frac{\partial f_z}{\partial y} - \frac{\partial f_y}{\partial z}\right), \left(\frac{\partial f_x}{\partial z} - \frac{\partial f_z}{\partial x}\right), \left(\frac{\partial f_z}{\partial y} - \frac{\partial f_y}{\partial z}\right)]$. Based on the fact that $curl\left(\boldsymbol{v_j^{(c)}}\right) = \mathbf{0}$ and $\nabla\cdot\boldsymbol{v_j^{(r)}} = 0$, Levich obtained an expression of $\boldsymbol{v_j}$and $\boldsymbol{P_j}$, as a function of *t* and (*x,z*), for both phases [27,29,30].

Phase 1:

$$v_{1(x)}(x,z,t) = (-iqA_1e^{qz} - m_1B_1e^{m_1z})\,e^{i(qx+\omega t)} \quad (2.\ 19)$$

$$v_{1(z)}(x,z,t) = (-qA_1e^{qz} + iqB_1e^{m_1z})\,e^{i(qx+\omega t)} \quad (2.\ 20)$$

$$P_1(x,z,t) = P_0 - \rho_1 gz + i\omega\rho_1A_1e^{qz}\,e^{i(qx+\omega t)} \quad (2.\ 21)$$

Phase 2:

$$v_{2(x)}(x,z,t) = (-iqA_2e^{-qz} + m_2B_2e^{-m_2z})\,e^{i(qx+\omega t)} \quad (2.\ 22)$$

$$v_{2(z)}(x,z,t) = (qA_2e^{-qz} + iqB_2e^{-m_2z})\,e^{i(qx+\omega t)} \quad (2.\ 23)$$

$$P_2(x,z,t) = P_0 - \rho_2 gz + i\omega\rho_2A_2e^{-qz}\,e^{i(qx+\omega t)} \quad (2.\ 24)$$

Where P_0 is the atmospheric pressure. q is the complex wavevector, defined as follows,

$$q = k - i\beta = \frac{2\pi}{\lambda} - i\beta. \tag{2. 25}$$

where λ is the wavelength of the capillary perturbation, and β is the damping coefficient, representing the decay of every quantity ($\boldsymbol{v_j}$, P_j or $\boldsymbol{u}$) along x-direction.

m_j is the capillary penetration depth into phase j, and it is defined as follows,

$$m_j = \sqrt{q^2 + \frac{i\omega\rho_2}{\eta_j}}. \tag{2. 26}$$

The real part of this quantity, which must be positive ($Re(m_j) > 0$), represents the characteristic length of penetration of the capillary wave into phase j. Based on Levich's solution of the hydrodynamic problem, the displacement at the interface (at $z = 0$) can be easily determined as follows [27,31],

$$u_x(x,0,t) \approx \int_{-\infty}^{t} v_{1(x)}(x,0,t)dt = \frac{(-iqA_1 - m_1B_1)}{i\omega}\, e^{i(qx+\omega t)}, \tag{2. 27}$$

and

$$u_z(x,0,t) \approx \int_{-\infty}^{t} v_{1(z)}(x,0,t)dt = \frac{(-qA_1 + iqB_1)}{i\omega}\, e^{i(qx+\omega t)}. \tag{2. 28}$$

2.1.4.2. Dispersion equation

In order to solve the hydrodynamic problem, the value of the constants A_1, B_1, A_2 and B_2 must be determined, by setting the following 4 boundary conditions at the interface (at $z = 0$) [27],

$$v_{1(x)}(x,0,t) = v_{2(x)}(x,0,t) \tag{2. 29}$$

$$v_{1(z)}(x,0,t) = v_{2(z)}(x,0,t) \tag{2. 30}$$

$$\eta_1\left(\frac{\partial v_{1(x)}}{\partial z}(x,0,t) + \frac{\partial v_{1(z)}}{\partial x}(x,0,t)\right) - \eta_2\left(\frac{\partial v_{2(x)}}{\partial z}(x,0,t) + \frac{\partial v_{2(z)}}{\partial x}(x,0,t)\right) = F_x(x,0,t) \tag{2. 31}$$

$$2\eta_1\left(\frac{\partial v_{2(z)}}{\partial z}(x,0,t)\right) - 2\eta_2\left(\frac{\partial v_{2(z)}}{\partial z}(x,0,t)\right) - i[P_1(x,0,t) - P_2(x,0,t)] = F_z(x,0,t) \tag{2. 32}$$

Equations (2. 29) and (2. 30) represent the continuity condition of the velocity fields at the interface, while equations (2. 31) and (2. 32), are, respectively, the momentum balance along x-direction and z-direction. The latter two state that the difference between bulk stresses in phase 1 and 2 in k-direction should be equal to the interface stress along the same k-direction. As mentioned above, motion along z-axis and x-axis evolve independently with respect to the one occurring along y-direction, so only capillary and dilational contributions will be taken into account in the surface stress, neglecting the contribution of shear stresses. This is the reason why equation (2. 16) reduces to,

$$\boldsymbol{F}(x,0,t) = [F_x(x,0,t), F_z(x,0,t)] = \begin{bmatrix} {E_s}^*(\omega)\dfrac{\partial^2 u_x}{\partial x^2}(x,0,t) \\ \gamma\dfrac{\partial^2 u_z}{\partial x^2}(x,0,t) \end{bmatrix}. \tag{2. 33}$$

By replacing equations (2. 19)-(2. 24) and equation (2. 33) into equations (2. 29)-(2. 32), a linear system of 4 equations in 4 unknowns can be easily obtained. This system can be expressed in tensorial form according to the following expression,

$$\boldsymbol{M}\cdot\boldsymbol{S} = \boldsymbol{M}\cdot\begin{bmatrix} A_1 \\ A_2 \\ B_1 \\ B_2 \end{bmatrix} = \boldsymbol{0}, \tag{2. 34}$$

where $\boldsymbol{S} = (A_1, A_2, B_1, B_2)$ is the vector of the unknowns (it is a column vector), and $\boldsymbol{M}$ is the matrix of the coefficients defined as follows,

$$\boldsymbol{M} = \begin{bmatrix} \dfrac{i(gq\rho_1+\gamma q^3)}{\omega} - 2\eta_1 q^2 - i\rho_1\omega & 2\eta_2 q^2 - \dfrac{igq\rho_2}{\omega} + i\omega\rho_2 & \dfrac{gq\rho_1+\gamma q^3}{\omega} + 2iq\eta_1 m_1 & 2iqm_2\eta_2 - \dfrac{gq\rho_2}{\omega} \\ -\dfrac{{E_s}^* q^3}{\omega} - 2\eta_2 q^2 & -2i\eta_2 q^2 & -\eta_1(m_1^2+q^2) + \dfrac{i{E_s}^* m_1 q^2}{\omega} & \eta_2(m_2^2+q^2) \\ q & -iq & m_1 & m_2 \\ 1 & 1 & -i & i \end{bmatrix}. \tag{2. 35}$$

By setting $\det(\boldsymbol{M}) = 0$, which means that the system has a unique solution, it is possible to obtain the following equation [27,29],

$$D[\gamma, {E_s}^*(\omega), \omega, q] = T(\gamma,\omega,q)\cdot L[{E_s}^*(\omega),\omega,q] + C(\omega,q) = 0. \tag{2. 36}$$

Equation (2. 36) is known as dispersion equation and expresses the relationship between the wavevector q and the angular frequency ω, which are propagation mutually dependent parameters of the capillary wave. $T(\gamma,\omega,q)$ represents the propagation of transversal modes, which is controlled by capillary stresses,

$$T(\gamma,\omega,q) = \gamma q^2 + i\eta_1\omega(q+m_1) + i\eta_2\omega(q+m_2) - \frac{\rho_1+\rho_2}{q}\omega^2 + \frac{g(\rho_1-\rho_2)}{\omega}. \tag{2. 37}$$

$L[{E_s}^*(\omega),\omega,q]$ represents the propagation of longitudinal modes, which are dominated by interfacial dilational stresses,

$$L[{E_s}^*(\omega),\omega,q] = {E_s}^*(\omega)q^2 + i\eta_1\omega(q+m_1) + i\eta_2\omega(q+m_2). \tag{2. 38}$$

$C(\omega,q)$ is the coupling term, which appears because longitudinal and transversal motion are mechanically coupled,

$$C(\omega,q) = [\eta_1\omega(q-m_1) - \eta_2\omega(q-m_2)]^2. \tag{2. 39}$$

The coupling term only depends on density and shear or dynamic viscosity of the adjacent bulk phases and becomes negligible in the limit case that the densities and viscosities of both bulk

phase are equal. Usually, the gravity term ($\frac{g(\rho_1-\rho_2)}{\omega}$) can be neglected, because the restoring force is mainly given by capillarity, so gravity forces have a small impact on wave propagation. Furthermore, in case of liquid/air interface, $\eta_2 \ll \eta_1$ and $\rho_2 \ll \rho_1$, and therefore equation (2. 36) can be rewritten using a more compact form [31],

$$\left[\gamma q^2 + i\eta_1\omega(q+m_1) - \frac{\rho_1\omega^2}{q}\right][E_s{}^*(\omega)q^2 + i\eta_1\omega(q+m_1)] + [\eta_1\omega(q-m_1)]^2 = 0. \quad (2.\ 40)$$

2.1.4.3. Power spectra and Resonance condition

For real ω equation (2. 36) is a 10-th degree equation (with respect to the complex variable q) which means that, at a fixed value of $E_s{}^*(\omega)$, γ, ρ_j, and η_j, there are 10 complex solutions that comply with such equation. However, only two of them have physical meaning. The first is defined by $q(\omega) = q_D(\omega) = \frac{2\pi}{\lambda_D} - i\beta_D$ which corresponds to longitudinal/dilational modes, whereas the second reads as $q(\omega) = q_c(\omega) = \frac{2\pi}{\lambda_c} - i\beta_c$, and corresponds to transversal/capillary modes. Both solutions must comply with the following conditions: $Re(q) > 0$ and $Im(q) < 0$. The capillary solution $q = q_c$ correspond to those values of λ_c that are within the capillary wave range (0.1-1 cm). As shown in **Figure 2. 6**, by setting $q(\omega) = q_D$, and trying to solve equation (2. 36) with respect to $E_s{}^*(\omega, q_D)$, the value of $E_s{}^*$ does not depend on γ. In fact, as expected, longitudinal modes are not governed by capillarity. On the other hand, by imposing that $q(\omega) = q_c$, the value of $E_s{}^*(\omega, q_c)$ strongly depends on γ (because transversal modes are ruled by surface tension).

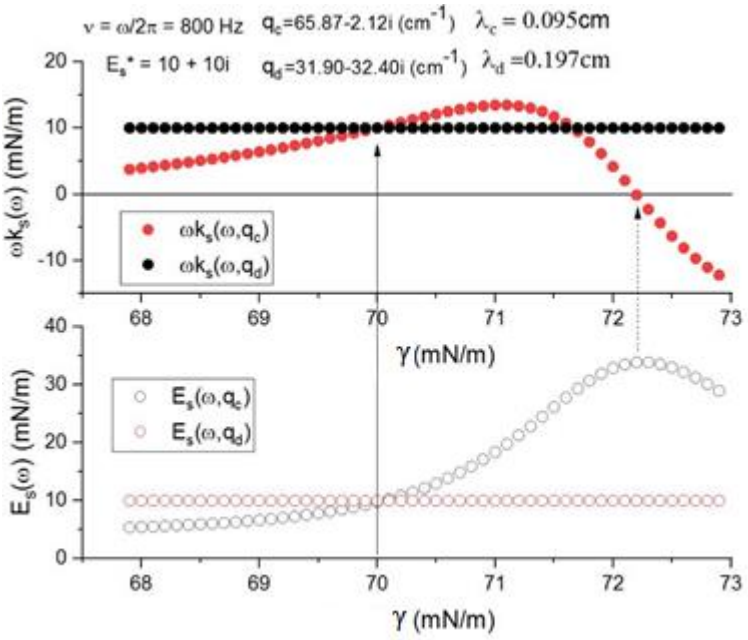

Figure 2. 6. $E_s{}^*(\omega, q_c) = E_s(\omega, q_c) + i\omega k_s(\omega, q_c)$ and $E_s{}^*(\omega, q_D) = E_s(\omega, q_D) + i\omega k_s(\omega, q_D)$ expressed as a function of γ. The values of q_c and q_d were obtained by solving equation (2. 36), by setting: $\gamma = 70\, mN/m$, $E_s{}^* = 10 + 10i\ \left[\frac{mN}{m}\right]$, $\upsilon = \frac{\omega}{2\pi} = 800\, Hz$. The values of density and viscosity of phase 1 (water) and phase 2 (air) were taken at a temperature of 25 °C [32].

As shown **Figure 2. 7**, a variation of either E_s or E_i (at fixed ω, γ, η_1 and ρ_1), does not have a huge impact on the values of neither the real part (**Figure 2. 7** (a)) nor the imaginary part

(**Figure 2. 7** (b)) of the capillary wave vector q_c, while both the real (**Figure 2. 7** (a)) and imaginary (**Figure 2. 7** (b)) parts of the dilational wave vector q_d are way more sensitive to both E_s or E_i variations. Anyway, at higher values of E_s (> 100 mN/m), q_D and q_c remain almost unchanged, and are practically not affected by E_i (i.e., all of the curves are overlapped, and almost constant with E_s).

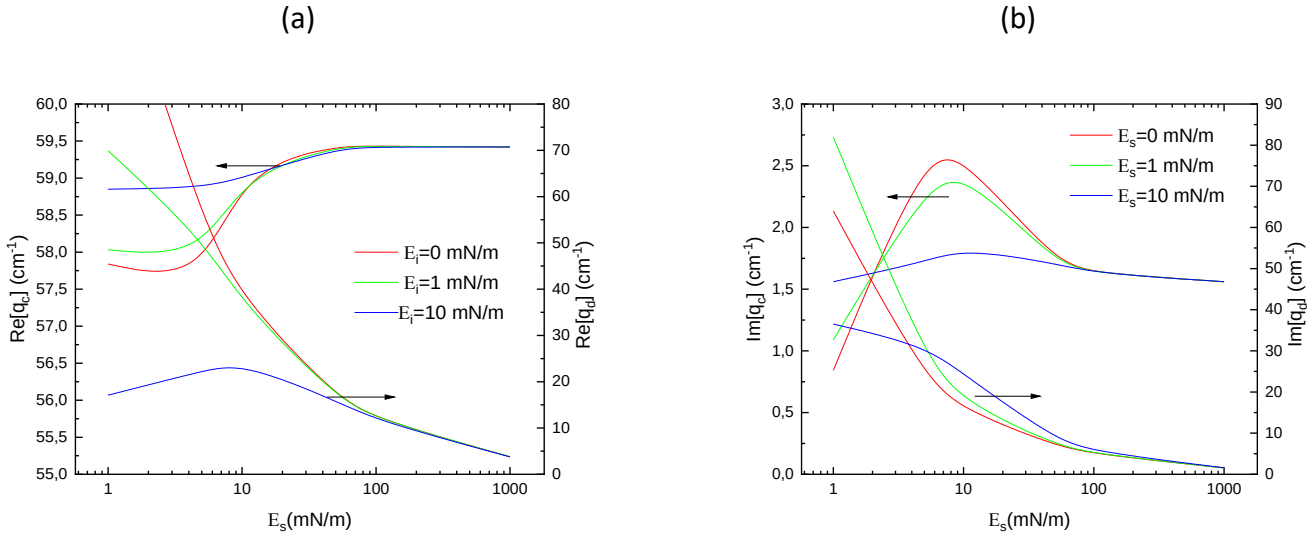

Figure 2. 7. (a) Real part of capillary wave vector ($Re(q_c)$) and dilational wave vector ($Re(q_d)$) as a function of storage dilational interfacial modulus E_S, at different values of loss dilational interfacial modulus (E_i); (b) Imaginary part of capillary wave vector ($Im(q_c)$) and dilational wave vector ($Im(q_d)$) as a function of storage dilational interfacial modulus E_S, at different values of loss dilational interfacial modulus (E_i). All of the wave vector data were determined at a frequency of 500 Hz, a temperature of 25 °C, and a surface tension $\gamma = 50\ mN/m$.

ECW technique, as shown in the following section (See *2.1.4.4. Experimental set up description*) allows to determine the capillary wavevector ($q_c = \frac{2\pi}{\lambda_c} - i\beta_c$) at a fixed frequency ω. This is possible by measuring also γ, ρ_1, and η_1. On the other hand, ${E_s}^*(\omega)$ can be easily determined by solving the dispersion equation. This method is valid when transversal and longitudinal motion are mechanically coupled, which occurs if the frequency of capillary modes (ω_c) is equal to that of dilational modes (ω_D), i.e., when the resonance condition is fulfilled [33]. Equivalently, resonance condition can be defined in terms of wavevectors as well: $q_c(\omega) = q_d(\omega)$; in fact, it must be considered that equation (2. 36) can be solved for real frequency giving two complex wavevector solutions (as above) or for real wavevector giving then two complex frequency solutions (capillary, ω_c, and dilational, ω_D).

In order to determine ω_c and ω_D, it is useful to define the concept of power spectrum. The power spectrum represents the spectral probability density of the square displacement of either transversal or dilational modes, as a function of the frequency. The power spectrum of dilational modes, according to the dissipation theorem, can be expressed as follows [33],

$$P_D(q,\omega) = <|u_x|^2> = -\frac{2k_BT}{\omega} Im\left(\frac{L[{E_s}^*(\omega),\omega,q]}{D(q,\omega)}\right). \qquad (2.\ 41)$$

On the other hand, the power spectrum of capillary modes is defined as

$$P_c(\omega,q) =< |u_z|^2 >= -\frac{2k_BT}{\omega} Im\left(\frac{T(\gamma,q,\omega)}{D(q,\omega)}\right), \tag{2. 42}$$

where k_B is the Boltzmann constant, and T is the absolute temperature. The qualitative sketch of both $P_c(\omega,q)$ and $P_D(q,\omega)$ is shown in **Figure 2. 8**.

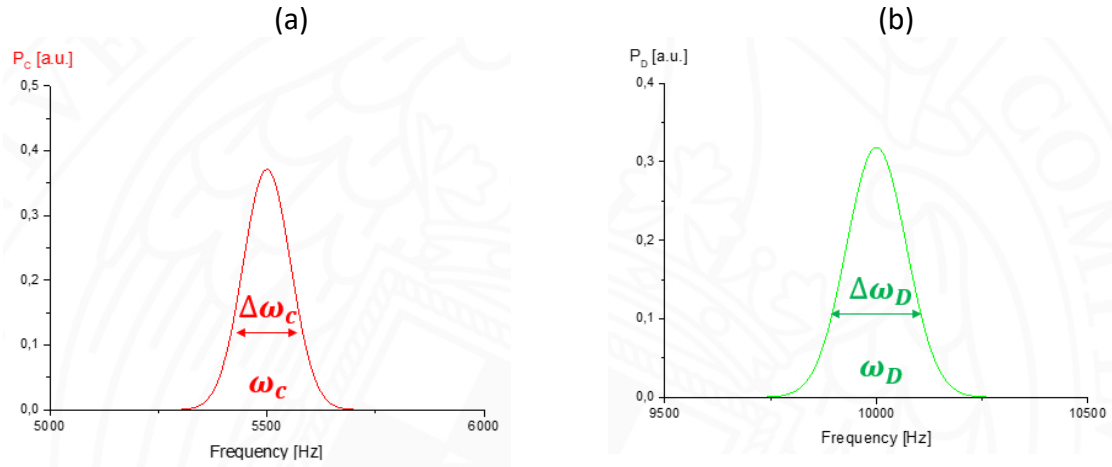

Figure 2. 8. Qualitative sketch of $P_c(\omega,q)$ and $P_D(q,\omega)$: ω_c and $\Delta\omega_c$ represent, respectively, the average value and the bandwidth of $P_c(\omega,q)$, while ω_D and $\Delta\omega_D$ represent, respectively, the average value and the bandwidth of $P_D(\omega,q)$.

As shown in **Figure 2. 8**, where ω_c accounts for the frequency associated to the peak of $P_c(\omega,q)$, and $\Delta\omega_c$ the band width of the spectrum, the complex frequency of capillary modes can be defined as follows [33],

$$\omega_c^* = \omega_c + i\Delta\omega_c. \tag{2. 43}$$

Similarly, the complex frequency of dilational modes, can be expressed as,

$$\omega_D^* = \omega_D + i\Delta\omega_D. \tag{2. 44}$$

The imaginary part of ω_c^* and ω_D^* has a physical meaning, which is associated with the temporal-damping of capillary and dilational modes, respectively. Actually, between space damping and time damping, there is a straightforward relationship. In fact, for capillary waves, frequency ($\Delta\omega_c$) and space (β_c) damping are related to each other through the group velocity ($v_{G(c)} = \frac{d\omega_c}{dk_c}$),

$$\beta_c = -\frac{d\omega_c}{dk_c}\Delta\omega_c. \tag{2. 45}$$

The resonance condition is given when $P_c(\omega,q)$ and $P_D(q,\omega)$, within their band width, overlap, which means that longitudinal and transversal motion are coupled and occur at the same frequency. Nevertheless, the estimation of ω_c^* and ω_D^* through calculation of the corresponding power spectra, may be time consuming, requiring a lot of calculations and/or experiments. Hence, there is a more straightforward way to determine these complex frequencies, based on the so called "Zero-order approximation" to the dispersion equation. The first assumption of this approach is that the capillary number (ratio between capillary forces and viscous forces) is larger than the unity,

$$N_c = \frac{\rho_1 \gamma}{4\eta_1^2 Re(q)} \gg 1. \tag{2. 46}$$

Secondly, to determine an expression for ω_c^* and ω_D^*, two cases should considered:

- For capillary modes, ${E_s}^*(\omega) = 0$, and hence considering equation (2. 46), and setting $q = k_c$ and $\omega = \omega_c^*$ in equation (2. 40), the expression of ω_c^* can be easily obtained as,

$$\omega_c^* = \sqrt{\frac{\gamma}{\rho_1}} {k_c}^{\frac{3}{2}} + i\frac{2\eta_1 {k_c}^2}{\rho_1}. \tag{2. 47}$$

Equation (2. 47) represents the dispersion equation of capillary waves corresponding to a viscous fluid where the surface adsorption is negligible, i.e., capillary waves propagating on the free surface of a liquid. The real part of this equation is called Kelvin equation,

$$Re(\omega_c^*) = \omega_c = \sqrt{\frac{\gamma}{\rho_1}} {k_c}^{\frac{3}{2}}, \tag{2. 48}$$

while the imaginary part, which accounts for the spatial damping due to the viscous friction with the liquid surface, is known as Stokes equation,

$$Im(\omega_c^*) = \Delta\omega_c = \frac{2\eta_1 {k_c}^2}{\rho_1}. \tag{2. 49}$$

Kelvin equation can be expressed in terms of wavelength λ_c and frequency $\nu_c = \omega_c/2\pi$:

$$\lambda_c = \left(\frac{2\pi\gamma}{\rho}\right)^{\frac{1}{3}} {\nu_c}^{-2/3}, \tag{2. 50}$$

Similarly, Stokes equation can be expressed in terms of spatial capillary damping β_c and frequency ν_c. In fact, eq. (2. 49), taking into account eq. (2. 45), can be expressed as follows:

$$\beta_c = \frac{8\eta\pi\nu_c}{3\gamma}. \tag{2. 51}$$

- For dilational modes, $\gamma = 0$, considering equation (2. 46), and setting $q = k_D$, ${E_s}^*(\omega) = E_s$, i.e., the elastic part prevails on surface viscosity, and $\omega = \omega_D^*$ in equation (2. 40), the expression for ω_D^* reads as follows,

$$\omega_D^* = \frac{1}{2}\left(\sqrt{3} + i\right)\left(\frac{(E_s k_D)^4}{\eta_1 \rho_1}\right)^{\frac{1}{3}}. \tag{2. 52}$$

Figure 2. 9 shows the qualitative trend of both $Re(\omega_c^*)$ and $Im\ (\omega_c^*)$. It should be noted that, if $N_c \ll 1$, the waves are overdamped, and the first order approximation used to derive equation (2. 47) is no longer valid.

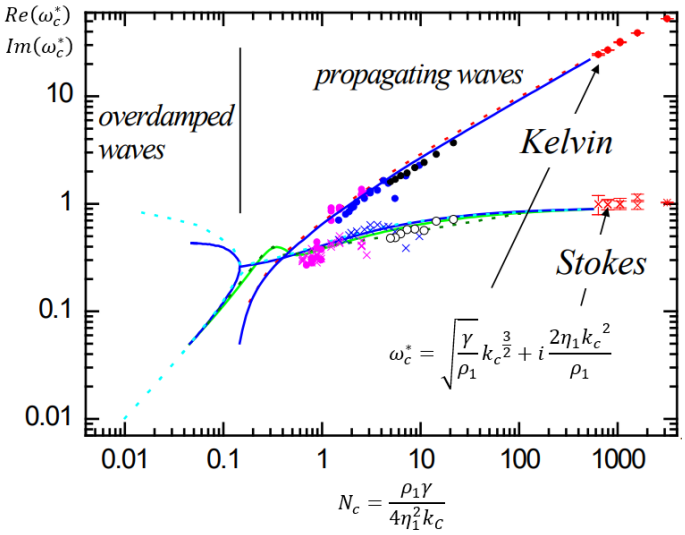

Figure 2. 9. Representation of Stokes and Kelvin limit of capillary modes.

The resonance condition occurs when $Re(\omega_c^*) \approx Re(\omega_D^*)$ (within the frequency bandwidth). Thus, the resonance wavevector can be obtained (by setting $k_D = k_c = q_R$) as follows [33],

$$q_R = \left(\frac{3}{4}\right)^3 \frac{{E_s}^4 \rho_1}{\gamma^3 {\eta_1}^2} \tag{2. 53}$$

It should be noted that the damping of waves is maximum when the resonance phenomenon occurs. Under this condition, the propagative parameters of the capillary waves are sensible to dilational elasticity, and therefore meaningful values of the dilational parameters can be obtained. **Figure 2. 10** provides a graphical representation of the dependence of q_R on ε, at different values of γ. In the figure, two different regions can be distinguished. At lower-left corner, the typical experimental conditions of Electro-Capillary Waves (ECW) are depicted. In this case, q_R ranges between 1 and 100 cm^{-1} (typical values associated with capillary waves). ECW technique allows obtaining experimental value of k_c, which must be compared to q_R. When $k_c \approx q_R$, the resonance condition is fulfilled and hence there is perfect coupling between transversal and longitudinal modes. In this case, the results of ${E_s}^*(\omega)$ obtained by means of equation (2. 40) are physically consistent. In general, this occurs when $\frac{E_S}{\gamma}$ ratio is close enough to the resonance value:

$$\left(\frac{E_s}{\gamma}\right)_R = \left(\frac{q\eta^2}{\gamma\rho}\right)^{1/4} \approx 0.1 - 0.15 \tag{2. 54}$$

For values of this ratio exceeding this threshold (estimation based on aqueous solutions with bulk viscosity comparable to the one of water), ${E_s}^*(\omega)$ is more sensitive to any experimental error associated with the measurement of γ, and thus ${E_s}^*(\omega)$ results are affected by a larger error. Similar considerations apply to the upper-right corner, which represents the typical experimental conditions of SLDS technique (or SQELS, see *Chapter I*, 1.8.1. Experimental tools). Here, the resonance condition is found at higher values of ε, for the experimentally accessible wavevectors, and the $\frac{E_S}{\gamma}$ ratio can expand to values of around 0.2.

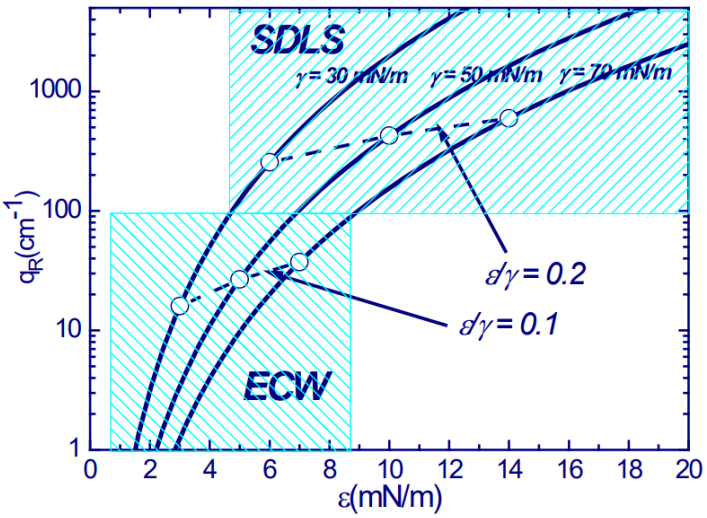

Figure 2. 10. Resonance wavevector q_R as a function of the elastic dilational modulus (here indicated with ε), at different values of surface tension γ.

Figure 2. 11 shows how, when $\frac{E_S}{\gamma}$ ratio is around the resonance value (≈ 0.1), both $Re(q_c)$ and $Im(q_c)$ values are widely affected by any change in E_s and E_i. On the other hand, far enough from resonance ($\frac{E_S}{\gamma} \gg 0.1$), q_c remains almost unchanged, even with huge variations of E_s and E_i.

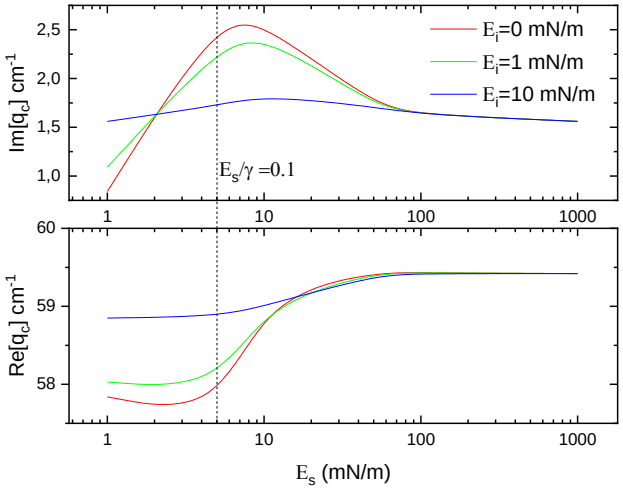

Figure 2. 11. (a) Imaginary part ($Im(q_c)$) and (b) real part ($Re(q_c)$) of capillary wave vector, as a function of storage dilational interfacial modulus E_S, at different values of loss dilational interfacial modulus (E_i). All of the wave vector data were determined at a frequency of 500 Hz, a temperature of 25 °C, and a surface tension $\gamma = 50\ mN/m$.

2.1.4.4. Experimental set up description

Electro-Capillary Waves (ECW) method is based on the generation of capillary waves by applying, at a certain frequency and amplitude, an oscillating voltage at the liquid/air interface. This leads to a situation, in which, as a result of the difference in dielectric permittivity between air and sample, the onset of ponderomotive force produces ripples on the surface of the liquid. The study of these ripples allows to measure the propagation parameters of the capillary waves (wavelength and damping coefficient) and to characterize surface dilational rheology in the range of (10-1000 Hz), depending on the sample [34-36]. The technique used in this PhD

Thesis is very similar to the one described in previous works [37,38], with some improvements, such as extension of the frequency range, possibility to investigate viscoelasticity in non-linear regime, laser optical path increase and size reduction of the equipment (making it more compact).

Figure 2. 12 and **Figure 2. 13** show, respectively, a picture and a scheme of ECW experimental set-up, with all of its constituting components. The liquid sample is poured into a Teflon-covered Langmuir trough: length L = 100 cm, width B = 7 cm and total area A = 700 cm^2. It has been designed to have such large length in order to let the damped capillary waves have sufficient space to propagate without being constrained by the size of the trough, avoiding simultaneously that the through boundaries can introduce any perturbation to the experiments. It can be used either to prepare Gibbs monolayers (by adsorption) or Langmuir monolayers (by spreading). The Langmuir trough is placed inside a transparent polyethylene box to control the atmosphere of the system and limit any contamination from the surrounding environment. The temperature inside the box was controlled by using a thermostatic bath) that push water through the jacket placed at the bottom of the trough. On the other hand, the interfacial tension of the fluid/fluid interface was measured using the surface force tensiometers described in the section corresponding to the utilization of the Langmuir trough.

Figure 2. 12. Picture of ECW experimental set-up.

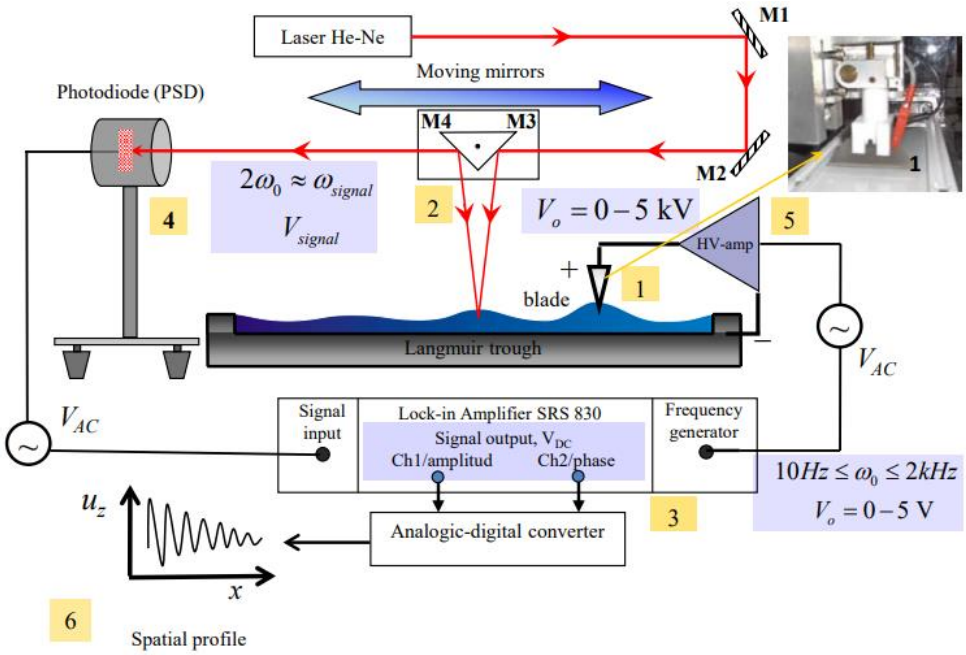

Figure 2. 13. Sketch of ECW experimental set up. The laser beam which scans the entire liquid/air interface is represented by a red solid line). All the main components of the device are: (1) The electrodes: a blade and a needle (details in Figure 2. 14); (2) Moving mirrors prism (Figure 2. 17); (3) Lock-In Amplifier SRS 830 and Frequency generator (Figure 2. 14); (4) Position sensitive photodiode (PSD); (5) Voltage Amplifier (Figure 2. 14); (6) Computer, connected to an Analogic-digital converter, with an implemented software (701. OEC, Nima, UK, Figure 2. 21) that displays the spatial profile of the capillary wave. The PSD, the laser, the Lock-In Amplifier SRS 830 and the voltage amplifier are connected to a tension stabilizer, in order to prevent any damage due to tension overshoots [1].

In an ECW experiment, the generation of the transversal waves along the air/water interface was possible by applying a high electrical field, taking advantage of the electrocapillarity phenomenon. This was done by applying a sinusoidal high voltage between a steel blade and the air/water interface. For this purpose, the function generator of a Lock-in amplifier (830 Stanford Research System) was used. This allows to generate a sinusoidal harmonic voltage at a fixed frequency ω_0 (ranging between 10-2000 Hz) and amplitude V_0 (ranging between 0-5 V) [1],

$$V(t) = V_0 sin(\omega_0 t). \qquad (2.\ 55)$$

The applied voltage is amplified by a factor of 100 using a high voltage amplifier (TREK model 601C) as that shown in **Figure 2. 14**) and applied between two electrodes (see **Figure 2. 14**), one of them (the needle) is submerged into the liquid sample, while the other (the blade) is placed straight and parallel to liquid/vapor interface (at about 0.1 mm of distance).

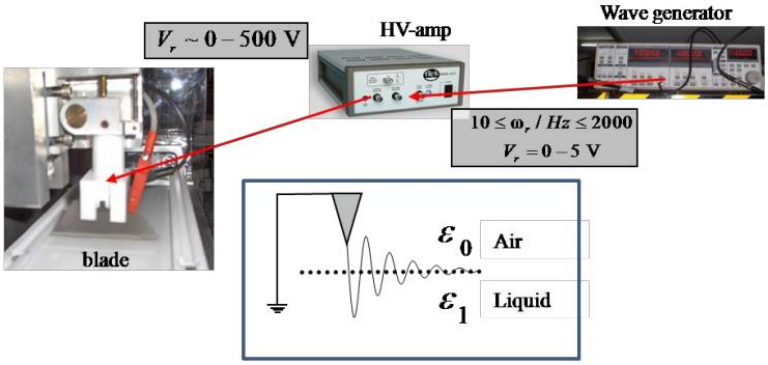

Figure 2. 14. Details of the electrodes (blade and needle), voltage amplifier, and wave generator [1].

Due to the difference in relative dielectric permittivity ($\Delta\varepsilon_r = \varepsilon_{r(1)} - \varepsilon_{r(0)}$) between the liquid sample (similar to water, $\varepsilon_{r(1)} \approx 80$) and air ($\varepsilon_{r(0)} \approx 1$), the ponderomotive force produces a vertical displacement $u_z(x,z,t)$ on the liquid surface, mainly restored by capillary force (that prevails over the gravity force for the typical wavelengths generated in the technique). It is possible to prove that $u_z(x,z,t)$ follows the same spatial and temporal profile of a capillary wave, as the one given by equation (2. 28), with an amplitude proportional to $\Delta\varepsilon_r {V_0}^2$ and with a frequency $\omega = 2\omega_0$. In fact, being ***E*** the electric field and ***D*** the electric displacement (the subscripts *0* and *1* refer, respectively, to before and after the vertical rise of liquid), the energy per unit of length of electrode, i.e., the blade required to produce a vertical displacement of height *h* is defined as [39],

$$\Delta w = \frac{1}{8\pi}\iint (\boldsymbol{D_1 E_0} - \boldsymbol{E_1 D_0})dxdz \tag{2. 56}$$

The double integral is computed in the cross section of the fluid (A'). The boundaries conditions imply that ***D*** is continuous across the surface, so ***D₁ = D₀***, and therefore $\boldsymbol{E_1} = \boldsymbol{D_0}\varepsilon_{r(0)}/\varepsilon_{r(1)}$. Furthermore, since $\varepsilon_{r(1)} \gg \varepsilon_{r(0)}$, $\boldsymbol{E}$ is almost perpendicular to the surface, and as a consequence equation (2. 56) can be rewritten as,

$$\Delta w = \frac{\varepsilon_{r(0)}(\varepsilon_{r(1)} - \varepsilon_{r(0)})}{8\pi\varepsilon_{r(1)}}\iint |\boldsymbol{E_0}(x,z)|^2 dxdz. \tag{2. 57}$$

$\boldsymbol{E_0}$ is only appreciable through the vertical displacement *h* and only in a small region Δx, and therefore, the above equation can be reduced to,

$$\Delta w = \frac{\varepsilon_{r(0)}\left(\varepsilon_{r(1)} - \varepsilon_{r(0)}\right)}{8\pi\varepsilon_{r(1)}} V(t)^2 h \int_0^{\Delta x} |\boldsymbol{g_0}(x,0)|^2 dx, \tag{2. 58}$$

where $\boldsymbol{g_0}(x,0) = \boldsymbol{E_0}(x,z)/V(t)$ is a geometrical factor associated to the electric field. The electro ponderomotive force acting on the surface is defined by,

$$F = \frac{\partial \Delta w}{\partial h} = \frac{\varepsilon_{r(0)} \Delta \varepsilon_r {V_0}^2 [1 + cos(2\omega_0 t)]}{16\pi \varepsilon_{r(1)}} \int_0^{\Delta x} |\boldsymbol{g_0}(x,0)|^2 dx \sim \Delta \varepsilon_r {V_0}^2 [1 + cos(2\omega_0 t)]. \quad (2.\ 59)$$

The electro ponderomotive force, counterbalanced by the capillary force, constitutes a damped harmonic oscillator, and it generates on the surface a standing wave with an amplitude $u_z(x,t)$proportional to $\Delta \varepsilon_r {V_0}^2$ and with a frequency $\omega = 2\omega_0$ (**Figure 2. 15**).

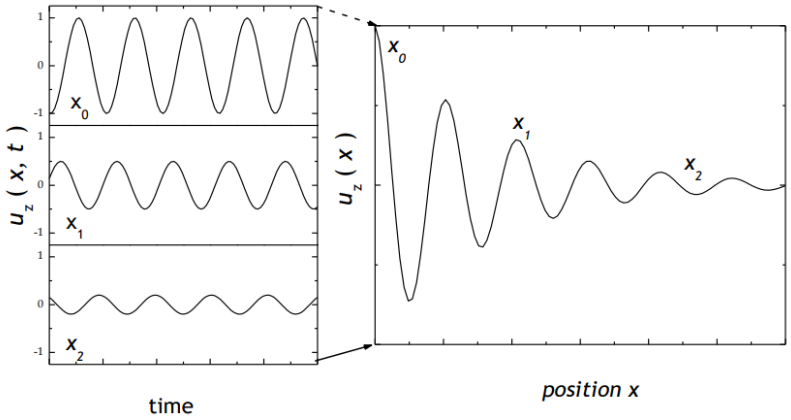

Figure 2. 15. Temporal and spatial profile of the standing wave generated in the ECW equipment.

Experimentally, it has been observed that, at low voltage amplitude, the amplitude associated to the second harmonic of the spectrum of the capillary wave ($\omega = 4\omega_0$) is much smaller than the amplitude associated to the fundamental frequency ($\omega = 2\omega_0$), and, anyway, at higher voltage amplitude (> 4 V, set in the frequency generator), its amplitude is just 10% of the amplitude of the fundamental frequency (**Figure 2. 16**) [1,39].

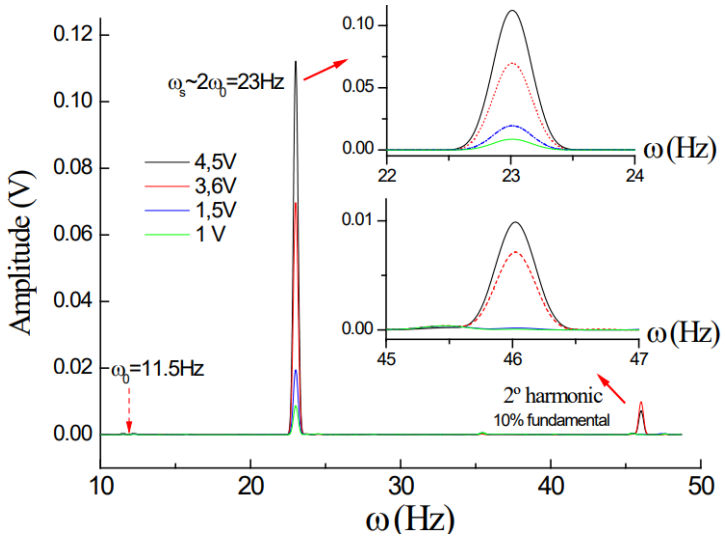

Figure 2. 16. Fourier transform spectrum of the amplitude of an electrocapillary wave, as a function of the frequency (in Hz), corresponding to an experiment with an excitation frequency of 11.5 Hz: the frequency of the capillary wave (fundamental frequency) is just the double of the excitation frequency (23Hz), and largely prevails on the amplitude of the 2-nd harmonic, which appears only when the applied field is high enough (3.5−4V).

It is also worth to show that if the applied potential, contains both an AC and a DC component ($V(t) = V_{AC} sin(\omega_0 t) + V_{DC}$), equation (2. 59) becomes,

$$F \sim {V_{DC}}^2 + \frac{{V_{AC}}^2}{2} + 2V_{DC}V_{AC}cos(\omega_0 t)\frac{{V_{AC}}^2}{2}cos(2\omega_0 t), \quad (2.\ 60)$$

which underlines that waves at both the excitation frequency and the fundamental frequency are present, and that for certain values of V_{DC} and V_{AC} these waves will be comparable in amplitude. Anyway, as shown in **Figure 2. 16**, also the amplitude of the spectrum associated to the excitation frequency ω_0 is negligible, showing that the approximation made in equation (2. 59) is valid in the first order. Anyway, the effect of the amplitude of the excitation frequency can be eliminated using a bandpass filter.

The spatial profile of the excited capillary wave is scanned by laser reflectometry. The laser beam comes from a 15mW He-Ne laser with a wavelength of 633 nm (Coherent Corp., USA). The smallest detectable wavelength of the capillary wave λ is limited by the size of the laser spot. Therefore, to maximize the sensibility of the detection of the surface waves, the laser spot was chosen with a diameter smaller than λ/2 (Note that the common wavelengths in the a capillary range for the experiments performed in this PhD Thesis range between 0.1 and 0.6 mm) [1].

The optical alignment of the set-up is crucial. For this purpose, the laser beam must be accurately focused, by means of a set of mirrors and lenses (technical details are depicted in **Figure 2. 17**), on the fluid surface. Thus, it is possible to get properly the spatial profile of the excited capillary wave. The optical set up allows focusing the low intensity laser beam at the interface, where it is reflected. This is possible by using the mirrors M1 and M2 together with the lens L1 that drive the light from the laser to the moving prism, where M3 and M4 mirrors are located. L1 converges the beam to a single spot at the fluid interface. Thus, it is ensured the beam diameter at the surface is not bigger than 1mm. L2, a lens characterized by infinite focal distance, makes it possible the convergence of the reflected beam reflected from the surface in the front plane of the photodiode.

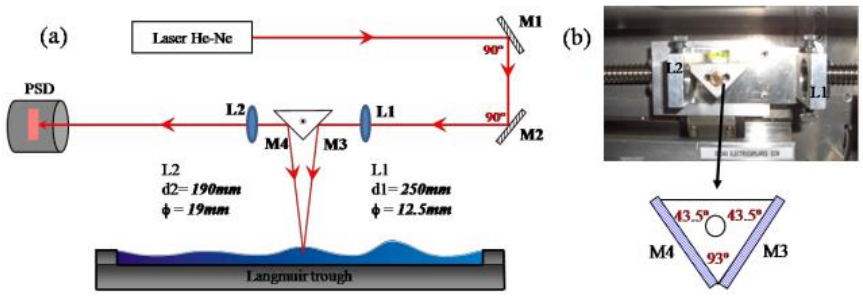

Figure 2. 17. (a) Graphical sketch of the optical set up, showing the trajectory of the laser beam. The beam is led by a set of mirror and lenses, towards liquid surface, which in turn acts as a mirror and reflects the beam and leads it to another set of mirrors and lenses that brings the laser spot to the Position Sensitive photo-Diode (PSD). (b) A detail of the mechanism where the mirrors M3, M4 and the lenses L1, L2 are placed. This component is able to move (by means of a crankshaft connected to the DC-source) in the propagation direction of the capillary wave, screening the entire whole fluid surface. The lateral dimensions of the squared mirrors M1−M4 are 25.0 ± 0.25mm with a thickness of 1.0± 0.25mm model 01 MFG 007/028 from Melles Griot. L1 corresponds to the model 01 LAO 78 and L2 to the 01 LAO 588 from Melles Griot [1].

It should be noted that the optical path between L2 and the detector cannot be too large, otherwise laser spot size exceeds the size of the detection area of the photosensitive detector. Conversely, a large optical path of laser beam, improves the sensitivity of detection, because,

at fixed angular displacement of the beam, which is given by the vertical displacement u_z of the fluid in any point of the surface, it is possible to assume that the larger the optical path the larger the amplitude of the signal (**Figure 2. 18**).

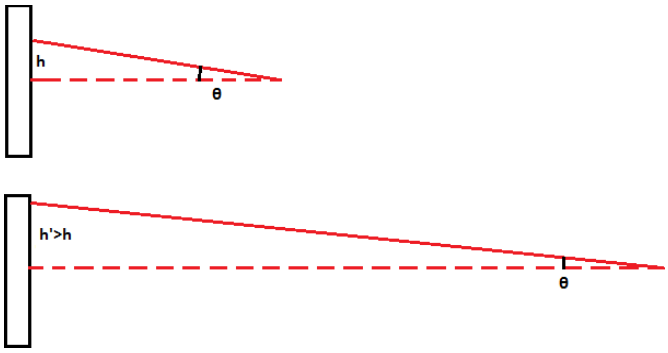

Figure 2. 18. Comparison of the height of the laser spot (h and h') with respect to the detector center, in case of small optical path and large optical path.

Therefore, to optimize the quality of the signal detection, a distance of about 2.33 m was fixed between L2 and the position-sensitive photodiode (PSD) used to detect the signal (**Figure 2. 19**). To maintain this distance and, at the same time, to make the set-up more compact, other two planar mirrors (M5 and M6) have been used, as shown in **Figure 2. 19**. The last optical component before the PSD is a cylindrical converging lens placed at a distance of 28 cm of the PSD (**Figure 2. 20**). The use of a cylindrical converging lens allows obtaining a sharper laser spot.

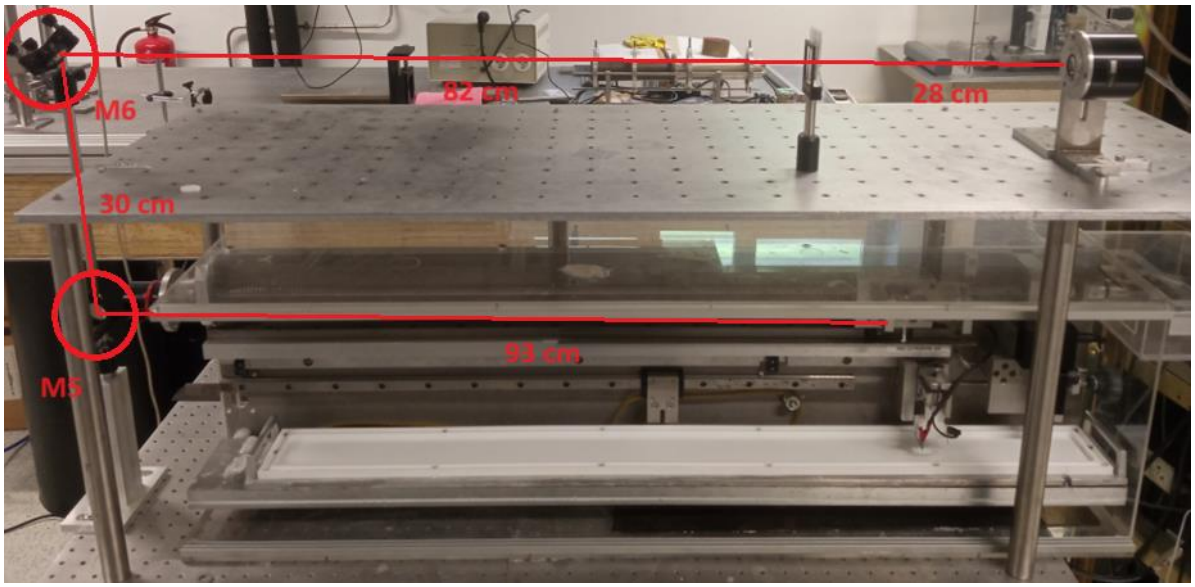

Figure 2. 19. Picture of the whole equipment, showing mirrors M5 and M6, and the optical path of the laser (from L2 to PSD).

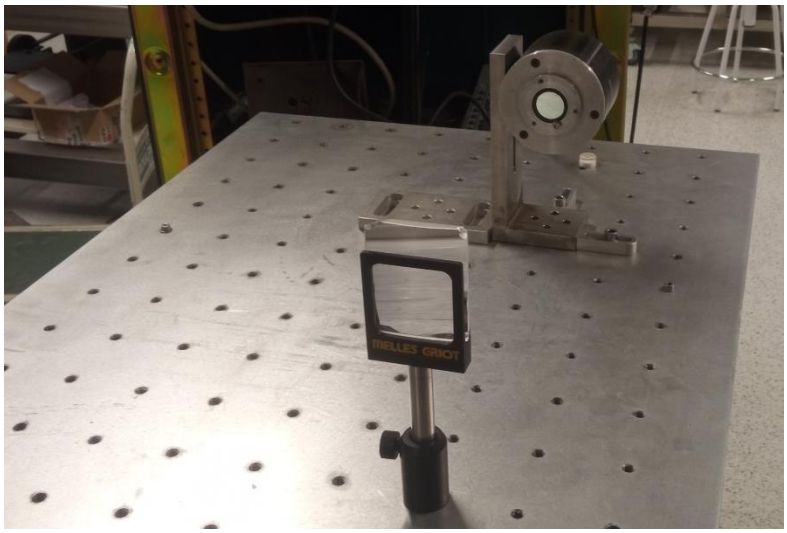

Figure 2. 20. Picture of the PSD and the cylindrical lens.

To scan the fluid surface, the crankshaft where the prism is placed should moves, producing a displacement of M3 and M4 in the direction parallel to the fluid. Thus, the reflection of the laser beam in any point of the liquid surface can be guided to the PSD. A DC power source (RS-PRO 300 SD) supplies the electrical power to move the shaft. Its voltage is fixed to 1 V, which allows to move the prism at a relatively low speed (around $2 \cdot 10^{-2}$ mm/s). This makes is possible to minimize any random noise in the system and collect many points of the capillary wave profile. The position of the prism is measured by means of a ring potentiometer, that transduces the angular rotation of the shaft into a signal collected by an AD interface, and eventually converted to a value of position (x). This system allows the displacement of the prism within a distance of 4 cm.

The last essential part of the hardware of the ECW instrument is the system for the detection of the signal, where the transversal wave profile is given by the detection of the deflection of the laser beam. For detecting this, a position sensitive photodiode (PSD, Hamamatsu) converts the vertical displacement of the laser spot into an equivalent AC electrical signal, with the absolute position of the laser spot being provided by the center of the light intensity distribution on the photodiode. It makes possible to scan the fluid surface with an accuracy of ±0.1 mm. The PSD essentially consists in a photocurrent divider, with two output currents (X_1, X_2). The difference between the two output currents (I_1, I_2) normalized by their sum provide information on the absolute position (x_L) of the laser spot with the center of the sensor: $(I_1-I_2)/(I_1+I_2) \approx 2x_L$. Thus, a sub-micrometer detection is possible even though the size of the laser beam may be larger than 1 mm. The relation between the difference and sum of the currents is necessary to offset the light intensity variation of the laser beam itself o due to other factors [1].

Any accidental vibration of the device may induce oscillations on the fluid surface of the fluid, which may produce experimental noise and disturb the signal. This is minimize by mounting the entire ECW set-up on an active damping anti-vibration platform and situated in a draft-proof enclosure. The PSD is very sensitive to surface vibrations, because it is able to detect very small displacements. However, the noise frequency is mostly below 10 Hz, which is far

away from the usual experimental frequencies, and can be easily filtered out by the lock−in. Under the usual experimental conditions, the amplitude of the noise oscillation on the liquid surface is several orders of magnitude larger than the one of the signals. Nevertheless, measurements with the device can be done perfectly with band-pass filtering and a dynamic reserve of more than 80 dB. The low signal/noise ratio inherent to this detection system is solved using the lock-in amplifier (**Figure 2. 14**). This device is capable to detect weak AC signals from the PSD detector at a frequency and a specific phase, distinguishing over the noise components. The signal ($V_s(t) = {V_s}^{(0)} \cos(\omega_s t + \varphi_s)$) is amplified and combined with the first harmonic of a reference signal ($V_R(t) = {V_R}^{(0)} cos(2\omega_0 t + \varphi_R)$) generated, getting a product ($V_D(t) = V_s(t)V_R(t)$) of two AC signals as follows [1],

$$V_D(t) = \frac{{V_s}^{(0)}{V_R}^{(0)}}{2}[cos[(\omega_s - 2\omega_0)t + \varphi_s - \varphi_R)] - cos[(\omega_s + 2\omega_0)t + \varphi_s + \varphi_R]], \quad (2.\ 61)$$

where one of the two AC-resulting signals has the frequency difference ($\omega_s - 2\omega_0$) of the multiplied signals, and the other one the frequency sum ($\omega_s + 2\omega_0$). The signal obtained is passed through a low-pass filter and then the AC components are removed. If both frequencies are identical ($\omega_s \approx 2\omega_0$), the time average leads to a DC signal, expressed as the time average of $V_D(t)$ as follows,

$$< V_D(t) >= \lim_{\tau \to +\infty} \frac{1}{\tau} \int_0^{\tau} V_D(t)\, dt = \frac{{V_s}^{(0)}{V_R}^{(0)}}{2} \cos(\varphi_D), \quad (2.\ 62)$$

where $\varphi_D = \varphi_s - \varphi_R$ is the phase of the locked DC resulting signal. The phase dependence of $< V_D(t) >$ is eliminated by the lock-in, giving directly 2 DC signals as output corresponding to the "Amplitude" V_A and the "Phase" V_P,

$$\begin{cases} V_A = {V_s}^{(0)}\, cos(\varphi_D) \\ V_P = {V_s}^{(0)}\, sin(\varphi_D) \end{cases}. \quad (2.\ 63)$$

Thus, the noise is eliminated, and both V_A and V_P are collected in any point of the surface of the liquid as the surface wave profile is scanned.

The above discussion was so far focused on the optomechanical and electronic configuration of the ECW instrument. However, in each experiment it is necessary to collect the information corresponding to the capillary wave generated on the surface. For this purpose, a IU4 communication interface (Nima technologies, UK) was used to performs the analog to digital conversion of the acquired electrical signals V_A and V_P. This makes it possible a real time monitorization of the spatial profile of the electrocapillary waves. To control the detection by laser reflectrometry, a graphic interface (GUI) from a specific software package 701.OEC (Nima, UK) implemented in Labview (National instrument, USA) is used. It monitors the averaged signal obtained from the lock−in, as a function of the horizontal displacement (collected by the rotational potentiometer that detects the movement of the screw) and time. This allows

obtaining simply the spatial profile of the capillary wave. At the same time, it is possible to measure the surface tension γ of the fluid surface as a function of time. **Figure 2. 21** shows an example of the graphical interface. The implemented software generates a ".txt" file, with the values of signal amplitude and phase, as a function of time and laser spot position.

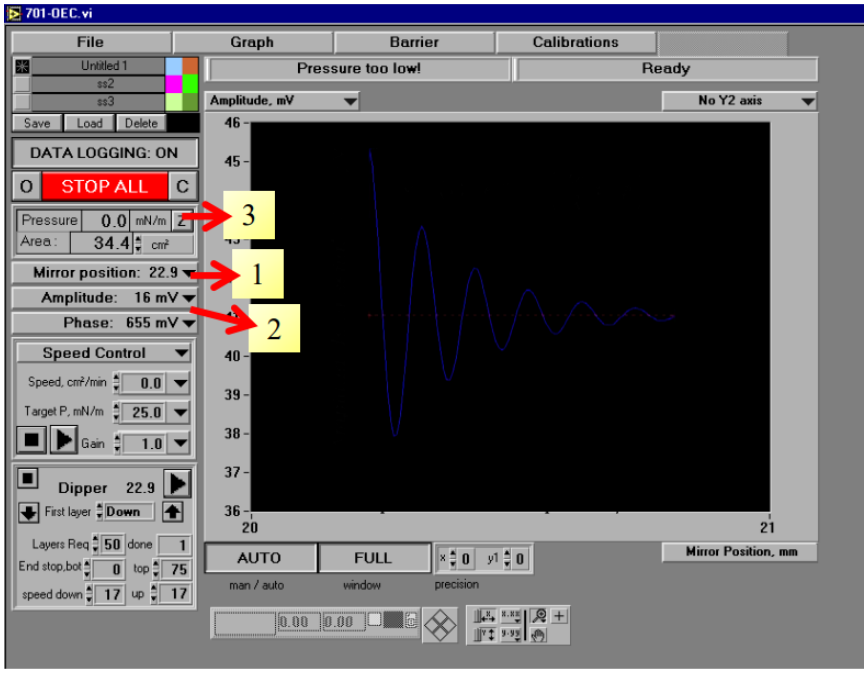

Figure 2. 21. Display of the implemented software (701. OEC, Nima, UK), based on a graphic interface performed in Labview (National Instruments, USA). The picture shows the display corresponding to a generic experiment where a capillary wave is generated and detected onto a fluid surface: the software makes possible to evaluate the spatial evolution of the capillary wave in real time. The program allows to scan the whole surface by the mirror position control (1), and also to get the signals from the detection channels: amplitude and phase (2). In addition, the software provides an accurate measure of the surface pressure (Π) as a function of time (3).

Laser spot, moving along the trough, scans the whole profile of the capillary waves, and is reflected, in any point of its path, arriving the signal to the PSD, which is connected to the lock-in amplifier. The latter is connected to an analog to digital converter, that collects all of the values of the amplitude signal $V_A(x)$ and the phase signal $V_P(x)$, at any point of the wave, obtaining its spatial profile (see **Figure 2. 22**, for example).

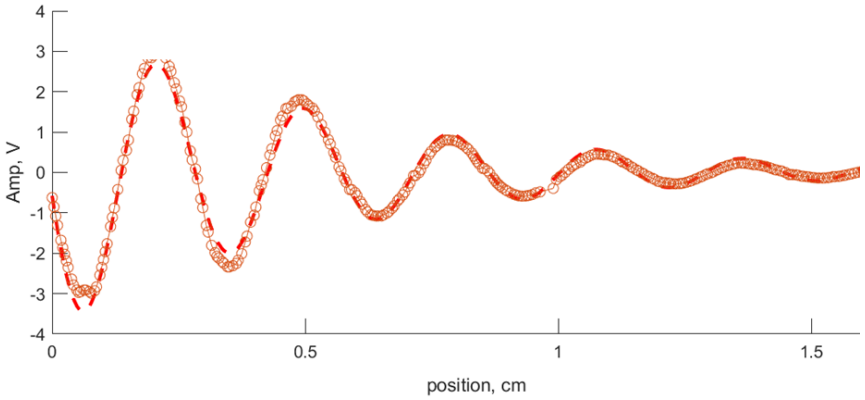

Figure 2. 22. Experimental spatial profile of a damped capillary wave, obtained from the amplitude channel $V_A(x)$ as a function of the laser spot position (x): the red circles correspond to the experimental data of $V_A(x)$, the dashed line is the best fit curve corresponding to eq. (2. 64).

Since the voltage of the signal is proportional to the local vertical displacement ($V_A(x) \propto u_z(x)$), the wave profile obtained experimentally can be fitted to the following equation (exponentially damped cosine function) [33],

$$u_z(x) = {u_z}^{(0)}\, e^{-\beta x} cos\left(\frac{2\pi}{\lambda}x + \varphi_c\right). \quad (2.\ 64)$$

This provides values for λ and β, which are independent on the voltage amplitude. This can be understood considering that the voltage is small enough to obtain a small surface deformation (linear regime) [1,39]. Those values, together with the values of surface tension γ, bulk shear viscosity η, and liquid density ρ, aallow to solve equation (2. 40) (dispersion equation) with respect to the complex dilational interfacial modulus ${E_s}^*(\omega)$, as a function of the angular frequency ω ,

$${E_s}^*(\omega) = E_s(\omega) + i\omega k_s(\omega) = \frac{\dfrac{-\left(\eta\omega(q-m)\right)^2}{\gamma q^2 + i\eta\omega(q+m) - \dfrac{\rho}{q}\omega^2} - i\eta\omega(q+m)}{q^2}. \quad (2.\ 65)$$

The numerical solution of the equation, as well as the fitting algorithm, are implemented in a MATLAB code, which reads the data of the ".txt" file and automatically carries out the data analysis.

2.2. Bulk Rheology Measurement

As mentioned in Chapter I, although this thesis is mainly focused on dilational interfacial rheology, bulk shear rheology characterization is required in order to fully understand the behavior of some complex fluids (see *Chapter V, VII, VII, IX*). Hence, a brief overview of bulk shear rheology techniques will be given, with particular focus on capillary viscometers (Ubbelohde viscometer) and Diffusing Wave Spectroscopy (DWS).

2.2.1. Capillary Viscometers

Capillary viscometers are the simplest instruments to measure shear viscosity of a fluid flowing through a pipe or tube with a large length-to-diameter ratio (capillary tube). Hagen and Poiseuille were first to measure viscosity in laminar flow using concentric tubes of fluid that slide one over the other. The viscous drag of the fluid causes a pressure drop along the capillary, which depends on the resistance of the sample to flow, flow rate, length, and inner diameter of the tube. In glass capillaries (e.g., Ostwald and Ubbelohde viscometers) the fluid hydrostatic head is the driving force that causes the fluid to flow [40],[41].

In this section, special focus will be paid to the Ubbelohde viscometer, which has been widely employed to perform viscosity measurements in this PhD Thesis. This method is used to determine the intrinsic viscosity of fluids, in the Newtonian limit (at zero shear rate and frequency), and it consists in measuring the flowing time of a liquid into a capillary tube. The viscometer must be placed in vertical position and immersed in a thermostatic bath, to control temperature.

Figure 2. 23 shows the aspects of an Ubbelohde viscometer.

(a) (b)

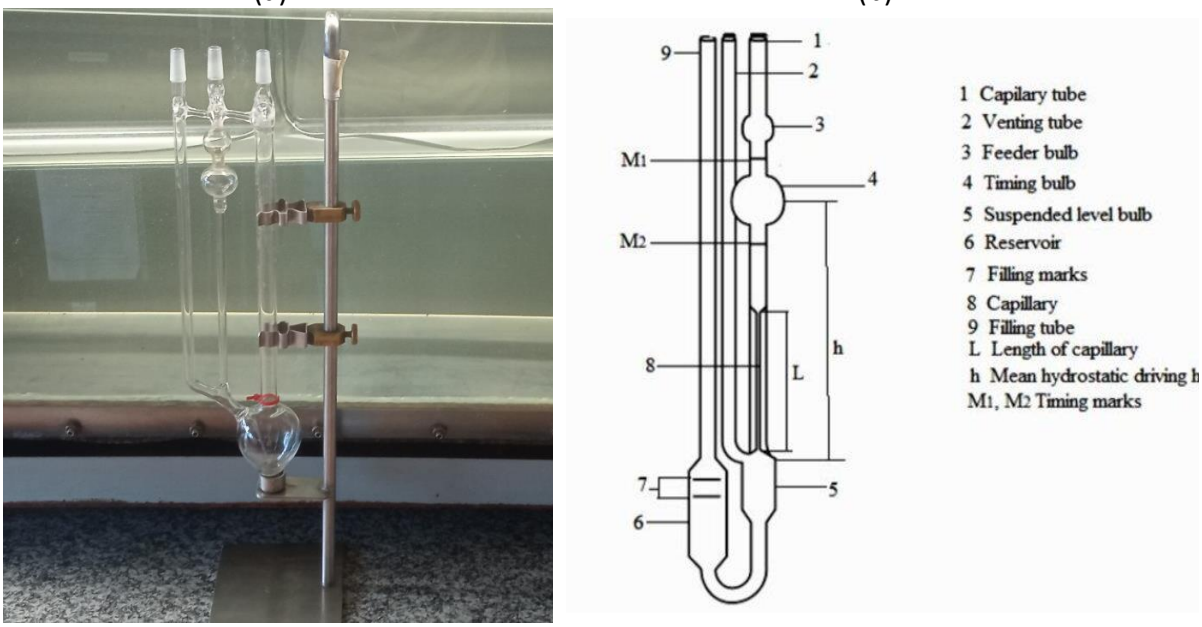

Figure 2. 23. Ubbelohde capillary viscometer: (a) Picture and (b) scheme [42].

The Hagen-Poiseuille law describes the capillary flow for Newtonian fluids, relating the volumetric flow rate Q with the Newtonian viscosity η and the hydrostatic pressure $P = \rho g \Delta h$ [42] according to the following expression,

$$\eta = \frac{\pi R^4 P}{8QL} = \frac{\pi R^4 \rho g \Delta h}{8QL}, \tag{2. 66}$$

where *R* is the diameter of the capillary tube and L is its length, and Δh is the height difference between the markers M1 and M2 (**Figure 2. 23** (b)). Since the volume of the bulb where the fluid flows is fixed (**Figure 2. 23**), Q is inversely proportional to the elution time, i.e., the time that the fluid need to flow between two fixed positions (**Figure 2. 23** (b)). It is worth noting that the elution time *t* is inversely proportional to the viscosity, and directly proportional to the density of the liquid. Therefore, the viscosity of the sample η can be easily determined as follows,

$$\eta = \frac{\eta_0 \rho t}{\rho_0 t_0}, \tag{2. 67}$$

where η_0, ρ_0 and t_0 are the viscosity, the density, and the elution time of the fluids that has been used for calibration (usually, water, at fixed temperature), respectively. Since Hagen-Poiseuille equation does not take into account the pressure drop due to the motion of the fluid, a corrected Poiseuille equation that takes into account this kinetic correction must be employed:

$$\eta = A + Bt^2, \tag{2. 68}$$

where *A* and *B* are two intrinsic constants of the viscometer, and they can be experimentally determined by measuring the viscosity of several pure liquids.

2.2.2. Microrheology

Microrheology is the study of the phenomena involved in the storage and dissipation of mechanical energy in viscoelastic materials at the micrometer or submicrometer scale. They allow to perform rheological measurements with small quantity of sample [43]. Microrheological techniques can be divides into different categories: active and passive techniques. **Figure 2. 24** shows a brief summary of microrheology techniques, indicating the available frequency range and shear moduli.

Active microrheological techniques involve a manual manipulation, which induces a shear stress into the samples. The most extended active techniques are magnetic tweezers (ferromagnetic particles dispersed in the fluid, moved by a magnet), optical Tweezers (a laser is used to trap a colloidal probe which is moved within the fluid) and Atomic Force Microscopy (a force is applied on a very small samples using the cantilever) [43].

Passive microrheological techniques use the Brownian dynamics of embedded colloids to measure the rheology of the materials. The most common passive techniques are Fluorescence Correlation Spectroscopy (FCS), Scattering Particle Tracking (SPT), Fluorescence Particle Tracking (FPT) and Diffusive Wave Spectroscopy (DWS). This latter has been used in this PhD Thesis to characterize the bulk rheological response of complex systems characterized by their viscoelasticity.

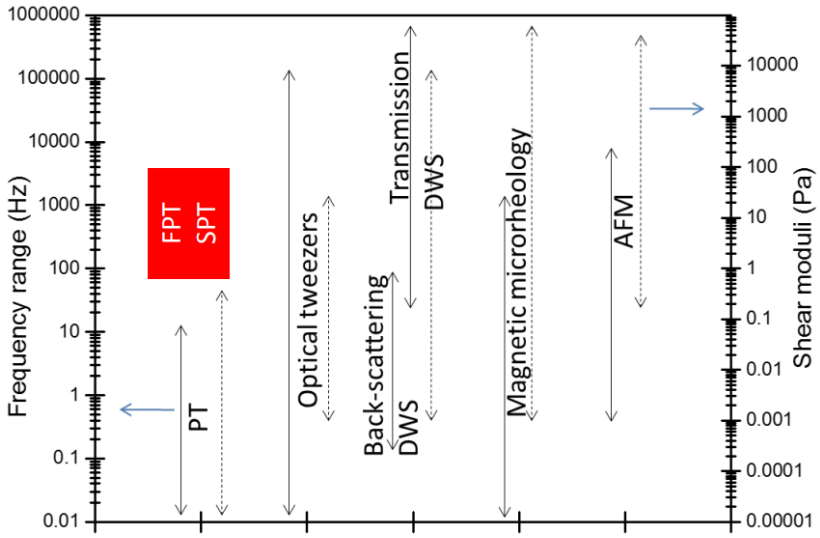

Figure 2. 24. Frequency (solid-line arrows) and elastic/viscous shear moduli (dashed-line arrows) range available to the different microrheology techniques [43,44].

2.2.3. Diffusing Wave Spectroscopy (DWS)

Diffusing Wave Spectroscopy (DWS) is a spectroscopic technique that allows correlating, through a microrheology approach, the parameters associated with the multiple scattering of particles in a fluid to its bulk shear rheology, i.e., DWS relate the dynamic properties of colloidal probes dispersed within the studied systems to its rheological response [45,46]. DWS can be considered as an extension of Dynamic Light Scattering (see *2.3.1. Dynamic Light Scattering (*DLS)), but, instead of single scattering, it collects the light intensity of diffused light, as a result of the multiple-scattering phenomenon (**Figure 2. 25**).

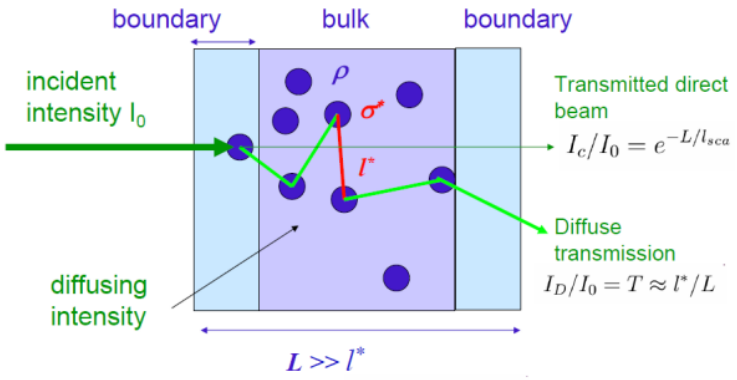

Figure 2. 25. Light diffusion (multiple scattering phenomenon), and definition of mean free path.

Unlike DLS, DWS is based on the so called "diffusion approximation". This relies on the consideration that the angle between incident and detected radiation is not relevant, and wavevector dependence is lost. In fact, light diffusion, especially for small tracker particles, is the result of multiple scattering in various directions. A key parameter that characterizes light diffusion is the so-called transport mean free path (l^*) which relates the concentration of tracker particles φ and the total scattering cross-section σ. If the tracker particles are small enough, scattering is isotropic in all directions, and does not depend on the incident angle θ of light radiation, and therefore the transport mean path is defined according to the following expression,

$$l^* = \frac{1}{\varphi\sigma < 1 - cos\theta >} \approx \frac{1}{\varphi\sigma}. \qquad (2.\ 69)$$

If the total path that light runs (L) is smaller than l^*, transmission prevails on scattering. On the other hand, if $L \gg l^*$, light propagation is diffusive that is the regime used in DWS experiments. Another parameter to take into account is the Mean Square Displacement (MSD or $< \Delta x^2(t) >$) of tracker particles, which are subjected to random motion into the fluid medium [47],

$$< \Delta x^2(t) > = < |x(t_0 + t) - x(t_0)|^2 >. \qquad (2.\ 70)$$

Lag time and MSD are related by a power law ($< \Delta x^2(t) > \sim t^{\alpha}$), and the exponent depends on the diffusion regime (**Figure 2. 26**). In case of subdiffusion, $\alpha < 1$, while if $\alpha > 1$ the system is in superdiffusion regime [48]. Gaussian diffusion regime is observed if $\alpha = 1$. This situation corresponds to a Brownian motion of the particles characterized by a velocity given by the diffusion coefficient.

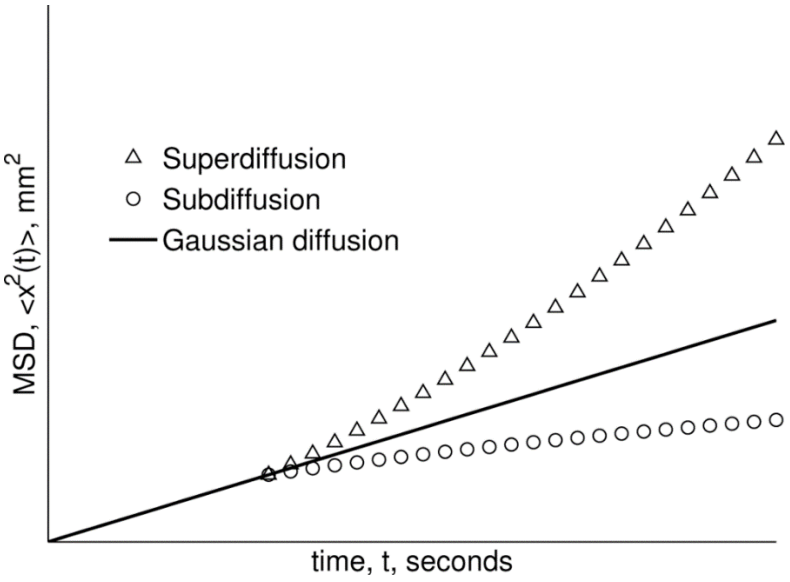

Figure 2. 26. Mean Square Displacement ($MSD \sim t^{\alpha}$) as a function of time, in 3 different regimes: (I) Subdiffusion: $\alpha < 1$; (II) Gaussian Diffusion: $\alpha = 1$; (III) Superdiffusion: $\alpha > 1$ [48].

In a purely viscous fluid (e.g., water), with η being the viscosity of the medium, a the average hydrodynamic radius of tracker particles, T the temperature, and k_B the Boltzmann constant, the diffusion coefficient D can be expressed by Stokes-Einstein equation (See *2.3.1. Dynamic Light Scattering (DLS)* subsection, for further details), and the MSD can be expressed as follows [43],

$$< \Delta x^2(t) > \sim Dt = \frac{k_B T}{6\pi\eta a} t. \tag{2. 71}$$

In case of particles trapped in a spring-like potential (purely elastic case, with a shear elastic modulus G_0), the mean square displacement is constant in time, and it is given by,

$$< \Delta x^2(t) >= \frac{k_B T}{\pi a G_0} \tag{2. 72}$$

In a viscoelastic system, the behavior is intermediate between those described by equations (2. 71) and (2. 72), and the MSD is given by the Generalized Stokes-Einstein (GSE) equation [49]:

$$< \Delta \tilde{x}^2(s) >= \frac{k_B T}{\pi a s \tilde{G}(s)}, \tag{2. 73}$$

where $\tilde{G}(s)$ and $< \Delta \tilde{x}^2(s) >$ are the Laplace Transform of the time-dependent shear modulus $G(t)$ and of the MSD, respectively. Similarly, it can be defined a relationship between the MSD and the time-dependent creep compliance $C(t)$ [50],

$$< \Delta x^2(t) >= \frac{K_B T}{\pi a} C(t). \tag{2. 74}$$

Equation (2. 73) can be also expressed in the angular frequency (ω) Fourier domain, by setting $s = i\omega$ and computing the Fourier transform ($\mathcal{F}$) of MSD and $G(t)$ [49],

$$\mathcal{F}[<\Delta x^2(t)>] =<\Delta x^2(\omega)>= \frac{K_B T}{\pi a i \omega G^*(\omega)}. \tag{2. 75}$$

Mason and Weitz also proposed a numerical method to calculate $G^*(\omega)$, under the assumption that MSD can be expressed by means of a generalized power law $<\Delta x^2(t)> \sim t^{\alpha(\omega)}$, where $\alpha(\omega)$ is determined experimentally, by setting $t = 1/\omega$, as the slope of the natural logarithm of MSD,

$$\alpha(\omega) = \frac{d(\ln[<\Delta x^2(t)>])}{d[ln(t)]}. \tag{2. 76}$$

Based on equation (2. 76), $G^*(\omega)$ can be computed as follows,

$$G^*(\omega) = G'(\omega) + iG''(\omega) = |G^*(\omega)| \cdot \left[\cos\left(\frac{\pi\alpha(\omega)}{2}\right) + i\cos\left(\frac{\pi\alpha(\omega)}{2}\right)\right], \tag{2. 77}$$

where $|G^*(\omega)|$ is given by,

$$|G^*(\omega)| \approx \frac{K_B T}{\pi a <\Delta x^2(\omega)> \Gamma[1+\alpha(\omega)]}, \tag{2. 78}$$

with $\Gamma[1+\alpha(\omega)]$ being the Euler Gamma function, defined as follows,

$$\Gamma[1+\alpha(\omega)] = \int_0^{+\infty} z^{\alpha(\omega)} e^{-z} dz \approx 0.457[1+\alpha(\omega)]^2 - 1.36[1+\alpha(\omega)] + 1.9. \tag{2. 79}$$

There are plenty of ways to calculate $G^*(\omega)$, some of them are summarized in **Figure 2. 27**. Starting from the experimental MSD, $G^*(\omega)$ can be determined by solving equations (2. 73), (2. 75) or (2. 77), or by other methods such as the Kronig-Kramers Fluctuation-Dissipation theorem).

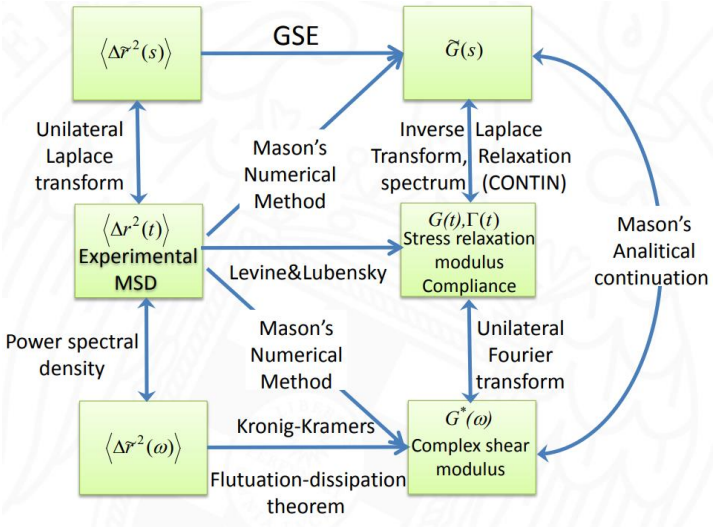

Figure 2. 27. Flow chart of many different methods to compute $G^*(\omega)$, starting from experimental raw data (MSD).

The Mean Squared Displacement can be experimentally determined by measuring the intensity autocorrelation function $g^{(2)}(t)$, associated to the random time fluctuations of the speckle pattern given by diffused and transmitted light intensity [45],

$$g^{(2)}(t) = \frac{< I_d(t')I_d(t+t') >}{< I_d(t') >^2} = 1 + \int_0^{+\infty} P(r) e^{-\frac{rq^2 < \Delta x^2(t) >}{l^*}} dr, \quad (2.\ 80)$$

where $q = 2\pi n/\lambda$ is the wavevector of the incident light beam that gets dispersed into the sample. $P(r)$ is the Gaussian distribution expressing the probability of a photon, travelling at a speed c (light speed in the medium), to run a distance $r = ct$. This probability distribution can be written as follows,

$$P(r) = \left(\frac{3}{4\pi r l^*}\right)^{\frac{3}{2}} e^{-\frac{3r^2}{4rl^*}}. \quad (2.\ 81)$$

Under the plane wave limit and uncorrelated diffusion approximations, being β the coherence factor, $g^{(2)}(t)$ can be expressed as,

$$g^{(2)}(t) = 1 + \beta \left[\frac{\left(\frac{L}{l^*} + \frac{3}{4}\right)\sqrt{q^2 < \Delta x^2(t) >}}{\sinh\left(\left(\frac{L}{l^*} + \frac{3}{4}\right)\sqrt{q^2 < \Delta x^2(t) >}\right)} \right]^2. \quad (2.\ 82)$$

The MSD, as a function of time, can be numerically determined by measuring the intensity autocorrelation function $g^{(2)}(t)$. The size of the cell is chosen in such a way that its size is much larger than the mean free path ($L/l^* > 10$). The sample is mixed, at fixed concentration, with some solid particles of known size. **Figure 2. 28** shows a simple sketch of the set-up (a) required for DWS and a picture (b) of the DWS instrument used in the experiments contained in this PhD Thesis (DWS-ResearchLab from LS instruments, Switzerland) apparatus. In order to make sure that tracker particles concentration is approximately the same in all the samples, the count rate of photon impinging the detector should not vary more than 5-10% between each experiment (it usually ranges between 50-60 kHz).

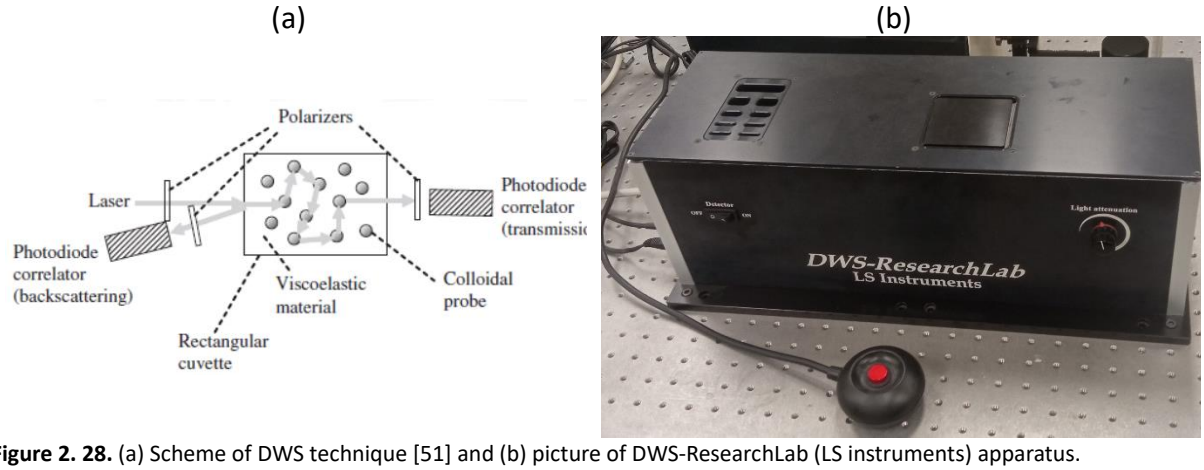

Figure 2. 28. (a) Scheme of DWS technique [51] and (b) picture of DWS-ResearchLab (LS instruments) apparatus.

In order to achieve faster averaging on the determination of $g^{(2)}(t)$, at the larger higher lag times, a reference cell, made of fritted glass, is placed before the sample allowing multi-speckle detection. This allows to characterizing shear rheology in a broad frequency, ranging from 0.1 Hz to 1MHz [43]. This depends on the sample and on the used tracker particles.

The mean free path l^* can be determined by means of a calibration process: in a purely viscous fluid (for instance, water), the set-up can be used to measure $g^{(2)}(t)$, and the MSD is determined under the assumption of pure diffusive motion ($< \Delta x^2(t) > \sim Dt$): the diffusion coefficient can be easily calculated by knowing particles size, according to equation (2. 88) (see *2.3.1. Dynamic Light Scattering (DLS)* subsection). In such a way, by means of equation (2. 80), l^* can be computed, and its value can be used in other experiments, performed with viscoelastic samples. An implemented software (LS Instruments RheoLab **Figure 2. 29**) can be used to perform the calibration, as well as to determine MSD as a function of lag time and all the rheological parameters as a function of: $G^*(\omega)$, $\eta^*(\omega)$.

(a) (b)

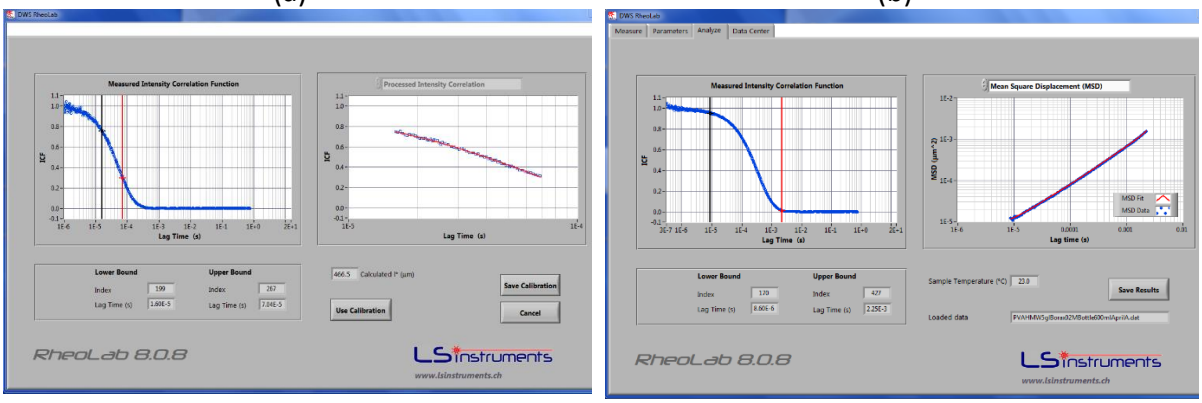

Figure 2. 29. RheoLab (LS Instruments) software: (a) Calibration (determination of l^*) and (b) calculation of MSD, $G^*(\omega)$, $\eta^*(\omega)$.

2.3. Ancillary techniques for bulk and surface characterization

There are many other properties of complex fluids, apart from bulk/interfacial rheology and surface tension, which are of interest for the studies contained in this PhD Thesis. In this section, a brief introduction to such techniques will be provided.

2.3.1. Dynamic Light Scattering (DLS)

Dynamic Light Scattering (DLS) is a technique that allows to characterize many important properties of colloidal dispersions and polymeric solutions (average particles size, polymer chain length, polydispersity index…). It is based on the interaction between electromagnetic radiation and matter. In fact, in a typical DLS experiments, the incidence of radiation of a defined wavelength λ_i, and wavevector $\boldsymbol{k_i}$, on a dispersion of colloidal particles induces an oscillating dipole, which produces, in turn, a secondary radiation (a phenomenon known as Rayleigh dispersion), according to the sketch in **Figure 2. 30** [52].

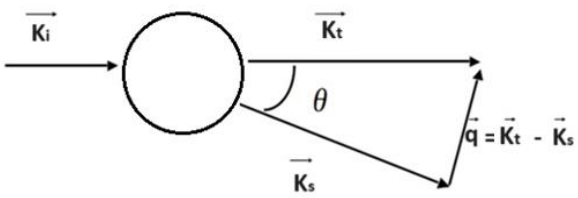

Figure 2. 30. Rayleigh dispersion: the incident radiation ki, is deviated by an angle θ by the particle: this scattering produces a dispersed radiation ks: the difference between ki and ks is represented by the momentum transfer vector q.

In a DLS experiment, the radiation-matter interaction does not provoke any significant change on the wavelength of the radiation, i.e., the wavevectors of the incident radiation and the

dispersed ones are almost the same. Thus, it is possible to consider that $|\boldsymbol{k_i}| = |\boldsymbol{k_s}|$, and as a result, the magnitude of the momentum transfer vector can be defined as,

$$|\boldsymbol{q}| = |\boldsymbol{k_i} - \boldsymbol{k_s}| = \frac{4\pi n_0}{\lambda_i} \sin\left(\frac{\theta}{2}\right). \quad (2.\ 83)$$

where n_0 is the refraction index of the medium and θ is the dispersion angle. Colloidal particles, subjected to Brownian motion, randomly move into the dispersion. Thus, intensity of dispersed light ($I_d(t) = E_d(t)E_d^*(t) = |E_d(t)|^2$, where $E_d(t)$ is the complex electric field associated with the dispersed radiation, and $E_d^*(t)$ is its complex conjugate) randomly varies in time. DLS allows measuring $I_d(t)$ by means of a photosensitive detector that collects the random fluctuations in time of the dispersed light. Smaller particles tend to produce faster fluctuations of $I_d(t)$ (**Figure 2. 31**), because their Brownian motion is faster due to their higher diffusion coefficient *D*, whereas the opposite is true when particles present a big size [53].

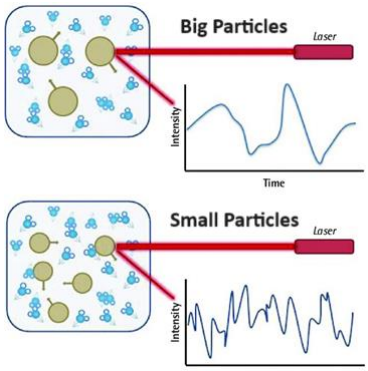

Figure 2. 31. Random fluctuations of $I_d(t)$, in colloidal dispersions with big particles and small particles.

DLS also allows to determine the normalized intensity autocorrelation function $g^{(2)}(\tau)$ associated with the time fluctuations of $I_d(t)$, occurring with a certain lag time τ,

$$g^{(2)}(\tau) = \frac{< I_d(t)I_d(\tau + t) >}{< I_d(t) >^2} = 1 + B\left|g^{(1)}(\tau)\right|^2, \quad (2.\ 84)$$

where *B* is the coherence factor, and $g^{(1)}(\tau)$ electric field autocorrelation function,

$$g^{(1)}(\tau) = \frac{< E_d(t)E_d^*(\tau + t) >}{< E_d(t) >^2}. \quad (2.\ 85)$$

Based on the decay of $g^{(2)}(\tau)$, one can obtain information about the speed of Brownian motion, which is given by the diffusion coefficient *D*. In fact, the autocorrelation function can be expressed by means of a polynomial expansion (Cumulants method) [54],

$$\ln\left(g^{(2)}(\tau) - 1\right) = \sum_{j=1}^{N} \frac{A_j(-\tau)^j}{j!} \quad (2.\ 86)$$

Usually, this expansion, is arrested to j=3. A_1 is associated to the decay time τ_D of the autocorrelation function, and it can be related to the diffusion coefficient by the following equation,

$$A_1 = \frac{1}{\tau_D} = Dq^2. \tag{2. 87}$$

The diffusion coefficient *D* is also related to the hydrodynamic radius of the particles *a*, by means of the Stokes-Einstein equation (valid for very diluted dispersions, with spherical particles, moving in a Newtonian fluid) [55],

$$a = \frac{k_B T}{6\pi D\eta}, \tag{2. 88}$$

where η is the viscosity of the dispersant, K_B is the Boltzmann constant, T is the temperature.

A_2 can be related to the polydispersity index:

$$PDI = \frac{A_2}{A_1^2}. \tag{2. 89}$$

The width of the hydrodynamic radius probability distribution is given by:

$$\sigma = \frac{\sqrt{A_2}}{A_1} a \tag{2. 90}$$

In the case of high polydispersity , *PDI>0.2* the Cumulants method is not safe and a more sophisticated analysis method (CONTIN Algorithm) [56] is usually employed, which expresses $g^{(2)}(\tau)$ as an integral distribution of delay times and determines this distribution combining inverse Laplace Transform and a statistical method (Fisher Test) [57].

A typical size intensity distribution is shown in **Figure 2. 32**, where the peak associated to the hydrodynamic radius corresponds to the characteristic decay time of $g^{(2)}(\tau)$. It is worth to noting that the higher the decay time the higher the hydrodynamic radius, and the broader the intensity distribution the higher the value of σ.

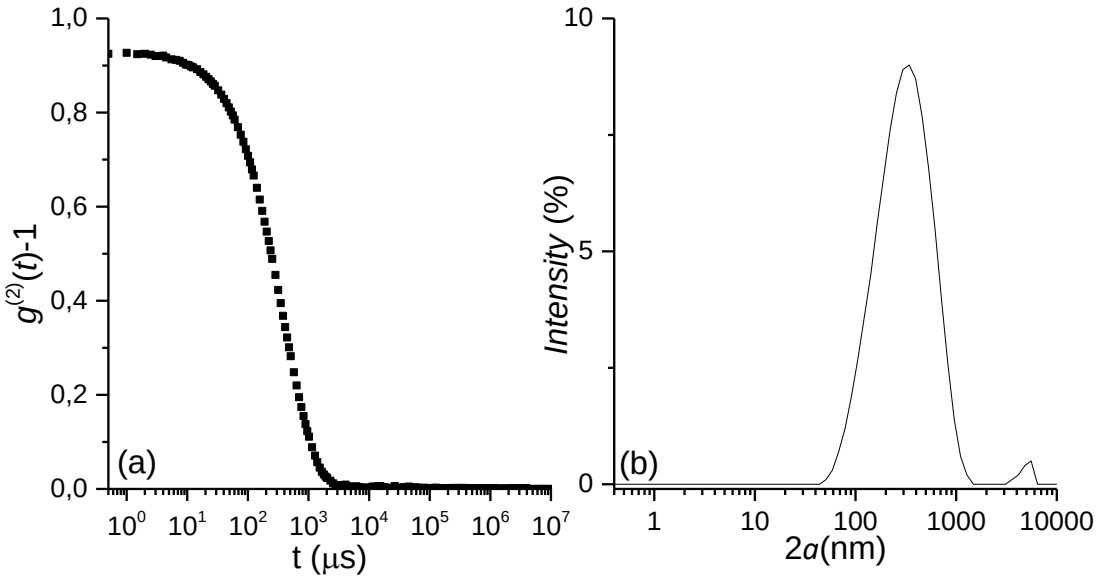

Figure 2. 32. (a) $g^{(2)} - 1$ vs lag time (here indicated with "t"); (b) Intensity size distribution as a function of the apparent hydrodynamic diameter (here, indicated with "2a").

Dynamic Light Scattering (DLS) experiments were performed using a Zetasizer Nano ZS instrument (Malvern Instruments Ltd, Malvern, UK) as shown in **Figure 2. 33**. This devices operates in quasi-backscattering configuration (scattering angle θ = 173°), and it is fitted with a He-Ne laser emitting light with a wavelength λ=632 nm. Temperature is controlled by means of a computer-controlled Peltier system. The technique can only be used to analyze quasi-transparent dispersions in such a way that multiple scattering phenomena must be avoided. Data are analyzed by means of an implemented software, that allows to set the input parameters (temperature, refractive index, density, viscosity, etc…) and automatically determines the $g^{(2)}(\tau)$ function and the intensity size distribution.

Figure 2. 33. Zetasizer Nano ZS (Malvern Instruments Ltd, Malvern, UK).

2.3.2. Zeta-Potential

The interaction potential between particles plays a fundamental role in the stabilization of colloids. The DLVO theory explains the aggregation and kinetic stability of aqueous particles by the combination of van der Waals attraction and electrostatic repulsion due to the so-called double layer (see **Figure 2. 34**) [58]. The electric double layer is a layer of ions surrounding a solid particle dispersed in an aqueous solution, including the ions attached on the particle surface and a film of the counterions. The distribution of ions around the particle is determined by the trade-off between electrostatic forces, entropic dispersion, and Brownian motion [59]. For a spherical particle, with homogeneous surface charge distribution, the electric double layer contains three contributions: (i) particle charge, given by charged ions attached on the particle's surface, (ii) Stern layer consisting in counterions (charged opposite to the ones attached on particle's surface), attracted by the electrostatic force, and (iii) diffuse layer which accounts for a film of the dispersion medium adjacent to the particle, containing free ions with a higher concentration of the counterions. In the diffuse layer, ion distribution is affected by the electrostatic force of the charged particle and the Brownian motion.

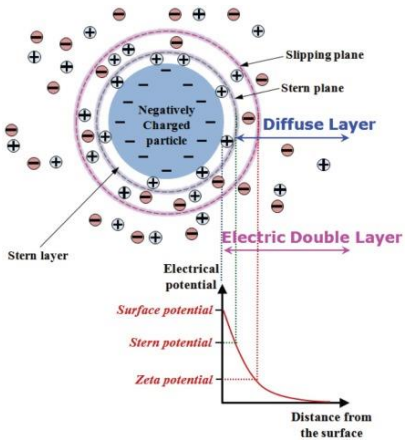

Figure 2. 34. Scheme of ions and potential distribution around a spherical charged particle.

The electrical potential reaches its maximum value on particle's surface, and it decreases with the distance. When the particle moves, the distribution of ions tends to break in proximity of the slipping plane as a result of the shear stress induced by particle's motion. The electric potential at the slipping plane is the so-called Zeta-potential (ζ), and its value can be determined by measuring the electrophoretic mobility of particles in the dispersion.

Given a spherical charged particle in a dispersion medium, characterized by a density ρ, a viscosity η, and a dielectric permittivity k_D, which is subjected to an electric field E, let a be its hydrodynamic radius and q its charge, it is possible to define the limit velocity v_L that the particle can reach as a result of the balance between the electrical force $F_e = qE$ and the viscous friction ($f_v = 6\pi a\eta v_L$) according to the following expression [60],

$$v_L = \frac{qE}{6\pi a\eta}. \tag{2. 91}$$

The electrophoretic mobility u_E, defined as the velocity per unit of electric field that a particle can reach in a dispersion medium, can be related to the Zeta-potential, by means of Henry equation,

$$u_E = \frac{v_L}{E} = \frac{2\pi k_D \zeta f\left(\frac{a}{L_D}\right)}{3\eta}. \tag{2. 92}$$

where L_D is the Debye length, which represent the characteristic thickness of the double layer,

$$L_D = \sqrt{\frac{k_D K_B T}{I}}, \tag{2. 93}$$

$I = \sum_{j=1}^{N} C_j q_j^2$ is the ionic strength of the medium made of N types of ions, each one characterized by a molar concentration C_j and a charge q_j, and $\left(\frac{a}{L_D}\right)$ is the Henry function which can assume values of 1 (Hückel limit: $\frac{a}{L_D} \ll 1$) and 1.5 (Smoluchowski limit: $\frac{a}{L_D} \gg 1$). The value of the Zeta-potential quantifies the stability of dispersions: low ζ (< 15 mV) correspond to dispersions that undergo a fast flocculation, while a good stability is observed when ζ > 30-40 mV [61].

The electrophoretic mobility can be measured by means of laser Doppler velocimetry technique, implemented in the same Zetasizer Nano ZS instrument (Malvern Instrument, Ltd., Malvern, UK). For this purpose, the sample is put into a cell, and a voltage (usually ranging from 1 V to 5 V, making sure that it is not too high, in order to prevent dielectric breakdown in highly conductive dispersions) is applied between the electrodes of this cell. The voltage results in an electric field that moves the particles. The combination between laser Dopler velocimetry and Phase Analysis Light Scattering (PALS) allows to determine the velocity, and, subsequently, the electrophoretic mobility of the dispersion. An implemented software allows an automatic determination of the value of Zeta-Potential.

2.3.3. Contact angle and spreading

The contact angle θ of a liquid on a solid surface is defined as the angle between the plane tangent on the liquid–vapor interface and the solid–liquid interface. Its cosine represents the wettability of a liquid on a specific solid surface. Being γ_{LV} the liquid/vapor surface tension, γ_{LS} the liquid/solid surface tension, and γ_{SV} the vapor/solid surface tension, the cosine of the contact angle on an ideal solid surface (smooth, flat and homogeneous), at chemical/mechanical/thermodynamical equilibrium is given by Young equation (see **Figure 2. 35**) [62],

$$\gamma_{SV} = \gamma_{LV}\cos(\theta) + \gamma_{SL}. \tag{2. 94}$$

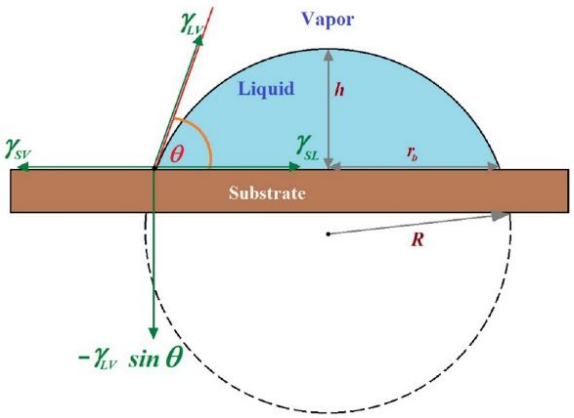

Figure 2. 35. Contact angle and drop geometry [63].

The contact angle is related to the work of adhesion W_a, by means of Young-Dupré equation, i.e., the energy required to separate a liquid drop that is partially wetting a solid substrate [64],

$$W_a = \gamma_{SV} + \gamma_{LV} - \gamma_{SL} = \gamma_{LV}\,(\cos\theta + 1). \tag{2. 95}$$

$W_a < 0$ corresponds to zero-wetting condition. Another useful parameter to characterize wetting is the spreading coefficient, which is defined as follows,

$$S = \gamma_{SV} - \gamma_{LV} - \gamma_{SL} = \gamma_{LV}\,(\cos\theta - 1). \tag{2. 96}$$

If $S > 0$, wetting is complete. Otherwise, wetting is partial (which happens for most liquids). The contact angle predicted by Young equation is given by thermodynamic equilibrium conditions, and it is measured in static conditions. But, in a dynamic contact angle experiment, carried out on a rough, non-homogeneous surface, contact angle hysteresis can appear. The advancing and receding contact angles are measured from dynamic experiments, where

droplets are in motion with respect to the solid substrate. The advancing contact angle, which is the maximum value, is a measure of the liquid/solid cohesion, while the receding contact angle, which is the minimum, accounts for liquid/solid adhesion. Contact angle hysteresis is given by the difference between advancing and receding contact angle, and it is proportional to the capillary number $N_C = \frac{\eta V_C}{\gamma_{LV}}$ (where V_C is the characteristic velocity and η is the bulk shear viscosity of the liquid) [65].

The contact angle can be either measured in sessile (drop placed on a substrate) or pendant drop configuration. A camera records the image of the drop, and by means of image analysis algorithms the profile of the drop can be detected and analyzed, and, by manually setting the contact line, contact angle can determined. In case of sessile drop measurements, in order to assess the uniformity of the substrates, multiple measurements have to be performed in many points of the substrate, comparing the values of contact angle to the left and to the right of the drop. Advanced and Receding Contact Angle (ARCA) can be measured by blowing, by means of the same nozzle, the liquid on the substrate, and progressively collecting the data of contact angle to the left and to the right sizes of the drop. Alternatively, the substrate can be tilted, which allows to measure the contact angle variation, and determining both the minimum (receding) and the maximum (advancing) contact angle.

When a liquid is deposited on a solid surface, the other two parameters are relevant: spreading kinetics and spreading area. These parameters are especially relevant when the wetting of the surface for the fluid is strong, as occurs for tri-siloxanes surfactant solutions [66] (see *Chapter IV*). The temporal evolution of the area of a deposited drop can be measured by means of an equipment that captures images of the spreading drop on the solid substrate, by using high speed cameras, from a top view and a side view. A sketch of the set-up used in this PhD Thesis, developed by TU Darmstadt (Germany), and described elsewhere [67,68] is shown in **Figure 2. 36**. The equipment allows to perform measurements in controlled conditions (at constant temperature and constant humidity, to control evaporation rate, which may affect spreading phenomenon of small droplets). By means of image analysis algorithms, the images of side view and upper view camera can be analyzed, in order to determine, as a function of time, the spreading area, the contact angle, drop radius, height, and volume.

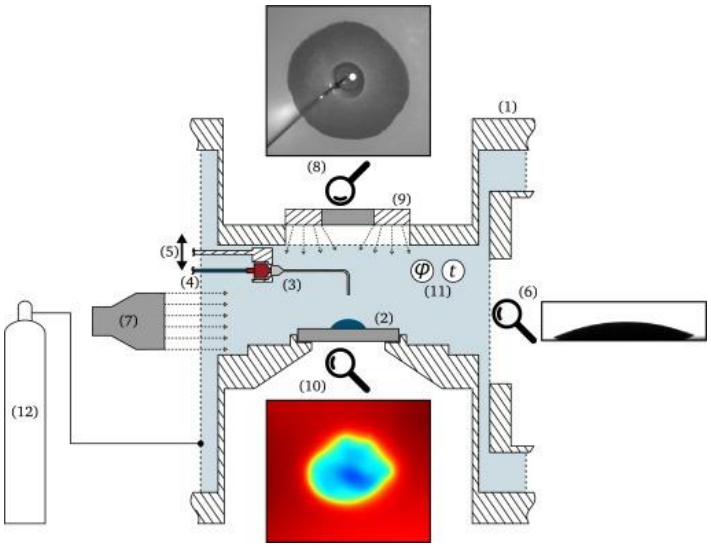

Figure 2. 36. Schematic representation of spreading kinetics experimental setup: (1) test cell, (2) substrate, (3) canula, (4) tube to syringe pump, (5) connection to linear stage, (6) high-speed camera in side view, (7) telecentric light source, (8) camera in top view, (9) ring light, (10) infrared camera in bottom view, (11) temperature and humidity sensor, (12) dry air supply from gas cylinder [67].

2.4. References

1. Maestro Martín, A. Dymanics of interfacial systems. Universidad Complutense de Madrid, 2010.
2. Zhu, J.-Y.; Duan, Y.-Y.; Wang, X.-D.; Min, Q. Forced Wetting Dynamics of Sodium Dodecyl Sulfate Glycerol Solution on Solid Substrates. *International Journal of Thermophysics* **2012**, *34*, 2286-2296, doi:10.1007/s10765-012-1295-9.
3. Mendoza, A.J.; Guzman, E.; Martinez-Pedrero, F.; Ritacco, H.; Rubio, R.G.; Ortega, F.; Starov, V.M.; Miller, R. Particle laden fluid interfaces: dynamics and interfacial rheology. *Adv Colloid Interface Sci* **2014**, *206*, 303-319, doi:10.1016/j.cis.2013.10.010.
4. Danov, K.; Stanimirova, R.; Kralchevsky, P.; Marinova, K.; Alexandrov, N.; Stoyanov, S.; Blijdenstein, T.; Pelan, E. Capillary meniscus dynamometry - method for determining the surface tension of drops and bubbles with isotropic and anisotropic surface stress distributions. *J. Colloid Interface Sci.* **2015**, *440*, 168-178, doi:10.1016/j.jcis.2014.10.067.
5. Javadi, A.; Krägel, J.; Makievski, A.V.; Kovalchuk, V.I.; Kovalchuk, N.M.; Mucic, N.; Loglio, G.; Pandolfini, P.; Karbaschi, M.; Miller, R. Fast dynamic interfacial tension measurements and dilational rheology of interfacial layers by using the capillary pressure technique. *Colloids Surf. A* **2012**, *407*, 159-168, doi:10.1016/j.colsurfa.2012.05.026.
6. Saad, S.; Neumann, A. Axisymmetric drop shape analysis (ADSA): an outline. *Adv. Colloids Interface Sci.* **2016**, *238*, 62-87, doi:10.1016/j.cis.2016.11.001.
7. Jaensson, N.; Vermant, J. Tensiometry and rheology of complex interfaces. *Curr. Opin. Colloid Interface Sci.* **2018**, *37*, 136-150, doi:10.1016/j.cocis.2018.09.005.
8. Anastasiadis, S.H.; Hatzikiriakos, S.G. The work of adhesion of polymer/wall interfaces and its association with the onset of wall slip. *Journal of Rheology* **1998**, *42*, 795-812, doi:10.1122/1.550909.
9. Noskov, B.A. Dilational surface rheology of polymer and polymer/surfactant solutions. *Curr. Opin. Colloid Interface Sci.* **2010**, *15*, 229-236, doi:10.1016/j.cocis.2010.01.006.

10. Ravera, F.; Loglio, G.; Kovalchuk, V.I. Interfacial dilational rheology by oscillating bubble/drop methods. *Current Opinion in Colloid & Interface Science* **2010**, *15*, 217-228, doi:10.1016/j.cocis.2010.04.001.
11. Cabrerizo-Vílchez, M.A.; Wege, H.A.; Holgado-Terriza, J.A.; Neumann, A.W. Axisymmetric drop shape analysis as penetration Langmuir balance. *Review of Scientific Instruments* **1999**, *70*, 2438-2444, doi:10.1063/1.1149773.
12. Torcello-Gómez, A.; Maldonado-Valderrama, J.; Gálvez-Ruiz, M.J.; Martín-Rodríguez, A.; Cabrerizo-Vílchez, M.A.; De Vicente, J. Surface rheology of sorbitan tristearate and β-lactoglobulin: Shear and dilatational behavior. *Journal of Non-Newtonian Fluid Mechanics* **2011**, *166*, 713-722, doi:10.1016/j.jnnfm.2011.03.008.
13. Duncan, J.H.; Waxman, A.M.; Tulin, M.P. The dynamics of waves at the interface between a viscoelastic coating and a fluid flow. *J. Fluid Mech.* **1985**, *158*, 177-197, doi:10.1017/S0022112085002609.
14. Slavchov, R.I.; Peychev, B.; Ismail, A.S. Characterization of capillary waves: A review and a new optical method *Phys. Fluids* **2021**, *33*, 101303 doi:10.1063/5.0066759.
15. Sergievskaya, l.; Ermakov, S.; Lazareva, T.; Guo, J. Damping of surface waves due to crude oil/oil emulsion films on water. *Mar. Pollut. Bull.* **2019**, *146*, 206-214, doi:10.1016/j.marpolbul.2019.06.018.
16. Ermakov, S.A.; Khazanov, G.E. Resonance damping of gravity–capillary waves on water covered with a visco-elastic film of finite thickness: A reappraisal. *Phys. Fluids* **2022**, *34*, 092107, doi:10.1063/5.0103110.
17. Ermakov, S.A. Damping of gravity-capillary waves on water surface covered with a visco-elastic film of finite thickness *Izv. Atmos. Ocean. Phys.* **2003**, *39*, 624-628.
18. Ermakov, S.A.; Kijashko, S.V. Laboratory study of the damping of parametric ripples due to surfactant films. In *Marine Surface Films. Chemical Characteristics, Influence on Air-Sea Interactions and Remote Sensing*, Gade, M., Hühnerfuss, H., Korenowski, G.M., Eds. Berlin, Germany: Springer, 2006; pp. 113-128.
19. Lamb, H. *Hydrodynamics*; Cambridge University Press: Cambridge, UK, 1994; Vol. 6.
20. Rowlinson, J.S.; Widom, B. *Molecular theory of capillarity* Courier Corporation: North Chelmsford, Massachusetts, US, 2002.
21. Guzmán, E.; Maestro, A.; Carbone, C.; Ortega, F.; Rubio, R.G. Dilational Rheology of Fluid/Fluid Interfaces: Foundations and Tools. *Fluids* **2022**, *7*, 335, doi:10.3390/fluids7100335.
22. Mendoza, A.J.; Guzmán, E.; Martínez-Pedrero, F.; Ritacco, H.; Rubio, R.G.; Ortega, F.; Starov, V.M.; Miller, R. Particle laden fluid interfaces: Dynamics and interfacial rheology. *Adv. Colloids Interface Sci.* **2014**, *206*, 303-319, doi:10.1016/j.cis.2013.10.010.
23. Firouzi, M.; Kovalchuk, V.I.; Loglio, G.; Miller, R. Salt effects on the dilational viscoelasticity of surfactant adsorption layers. *Curr. Opin. Colloid Interface Sci.* **2022**, *57*, 101538, doi:10.1016/j.cocis.2021.101538.
24. Liu, X.; Duncan, J.H.; Korenowski, G.M.; Kelly, J.S. A laboratory study of longitudinal waves in surfactant films in a water wave tank. *J. Geophys. Res.: Oceans* **2007**, *122*, C06005, doi:10.1029/2006JC003867.
25. Rajan, G.K. Dissipation of interfacial Marangoni waves and their resonance with capillary-gravity waves. *Int. J. Eng. Sci.* **2020**, *154*, 103340, doi:10.1016/j.ijengsci.2020.103340.
26. Rajan, G.K. Solutions of a comprehensive dispersion relation for waves at the elastic interface of two viscous fluids. *Eur. J. Mech. B: Fluids* **2021**, *89*, 241-258, doi:10.1016/j.euromechflu.2021.05.012.

27. Lucassen-Reynders, E.H.; Lucassen, J. Properties of capillary waves. *Advances in Colloid and Interface Science* **1970**, *2*, 347-395, doi:10.1016/0001-8686(70)80001-x.
28. Kramer, L. Theory of Light Scattering from Fluctuations of Membranes and Monolayers. *The Journal of Chemical Physics* **1971**, *55*, 2097-2105, doi:10.1063/1.1676380.
29. Buzza, D.M.A. General Theory for Capillary Waves and Surface Light Scattering. *Langmuir* **2002**, *18*, 8418-8435, doi:10.1021/la011713d.
30. Levich, V.G. *Physicochemical Hydrodynamics* Prentice-Hall: Englewood Cliffs, New Jersey, US, 1962.
31. Lucassen, J. Longitudinal capillary waves. Part 1.—Theory. *Trans. Faraday Soc.* **1968**, *64*, 2221-2229, doi:10.1039/tf9686402221.
32. Lide, D.R. *Handbook of Chemistry and Physics: A Ready-Reference Book of Chemical and Physical Data*; CRC Press: Boca Raton, FL, USA, 1998.
33. Langevin, D. *Light Scattering by Liquid Surfaces and Complementary Techniques.* ; CRC Press: New York, US, 1992; Vol. 41.
34. Muñoz, M.G.; Monroy, F.; Hernández, P.; Ortega, F.; Rubio, R.G.; Langevin, D. Anomalous Damping of the Capillary Waves at the Air−Water Interface of a Soluble Triblock Copolymer. *Langmuir* **2003**, *19*, 2147-2154, doi:10.1021/la0206007.
35. Carbone, C.; Guzmán, E.; Maldonado-Valderrama, J.; Rubio, R.G.; Ortega, F. Ionic Strength Effect in the Equilibrium and Rheological Behavior of an Amphiphilic Triblock Copolymer at the Air/Solution Interface. *Colloids and Interfaces* **2024**, *8*, 16, doi:10.3390/colloids8020016.
36. Maestro, A.; Ortega, F.; Rubio, R.G.; Rubio, M.A.; Kragel, J.; Miller, R. Rheology of poly(methyl methacrylate) Langmuir monolayers: percolation transition to a soft glasslike system. *J Chem Phys* **2011**, *134*, 104704, doi:10.1063/1.3560612.
37. Ito, K.; Sauer, B.B.; Skarlupka, R.J.; Sano, M.; Yu, H. Dynamic interfacial properties of poly(ethylene oxide) and polystyrene at toluene/water interface. *Langmuir* **2002**, *6*, 1379-1388, doi:10.1021/la00098a011.
38. Jayalakshmi, Y.; Ozanne, L.; Langevin, D. Viscoelasticity of Surfactant Monolayers. *Journal of Colloid and Interface Science* **1995**, *170*, 358-366, doi:10.1006/jcis.1995.1113.
39. Sohl, C.H.; Miyano, K.; Ketterson, J.B. Novel technique for dynamic surface tension and viscosity measurements at liquid-gas interfaces. *Rev Sci Instrum* **1978**, *49*, 1464, doi:10.1063/1.1135288.
40. Ghanbari, A.; Mousavi, Z.; Heuzey, M.C.; Patience, G.S.; Carreau, P.J. Experimental methods in chemical engineering: Rheometry. *The Canadian Journal of Chemical Engineering* **2020**, *98*, 1456-1470, doi:10.1002/cjce.23749.
41. Macosko, C.W. *RHEOLOGY Principles, Measurements and Applications*; Wiley-VCH, Inc: New York, NY, US, 1994.
42. Fakunle, M.A.; Agbaje, W.B.; Aninku, E.A. Evaluation of tomato (Solanum lycopersicum) quality at three different ripening stages using viscometry. *Croatian journal of food science and technology* **2022**, *14*, 164-171, doi:10.17508/cjfst.2022.14.2.01.
43. Bonales, L.J.; Maestro, A.; Rubio, R.G.; Ortega, F. *Microrheology of Complex Fluids*; Prof. Harry Schulz (Ed.): 2011.
44. Waigh, T.A. Microrheology of complex fluids. *Reports on Progress in Physics* **2005**, *68*, 685-742, doi:10.1088/0034-4885/68/3/r04.
45. Weitz, D.A.; Zhu, J.X.; Durian, D.J.; Gang, H.; Pine, D.J. Diffusing-wave spectroscopy: The technique and some applications. *Physica Scripta* **1993**, *T49B*, 610-621, doi:10.1088/0031-8949/1993/t49b/040.

46. Mason, T.G. Estimating the viscoelastic moduli of complex fluids using the generalized Stokes-Einstein equation. *Rheologica Acta* **2000**, *39*, 371-378, doi:10.1007/s003970000094.
47. Watts, F.; Tan, L.E.; Wilson, C.G.; Girkin, J.M.; Tassieri, M.; Wright, A.J. Investigating the micro-rheology of the vitreous humor using an optically trapped local probe. *Journal of Optics* **2014**, *16*, 015301, doi:10.1088/2040-8978/16/1/015301.
48. Ingo, C.; Magin, R.L.; Parrish, T.B. New Insights into the Fractional Order Diffusion Equation Using Entropy and Kurtosis. *Entropy (Basel)* **2014**, *16*, 5838-5852, doi:10.3390/e16115838.
49. Mason, T.G.; Weitz, D.A. Optical measurements of frequency-dependent linear viscoelastic moduli of complex fluids. *Phys Rev Lett* **1995**, *74*, 1250-1253, doi:10.1103/PhysRevLett.74.1250.
50. Levine, A.J.; Lubensky, T.C. One- and two-particle microrheology. *Phys Rev Lett* **2000**, *85*, 1774-1777, doi:10.1103/PhysRevLett.85.1774.
51. Weitz, D.; Pine, D. Dynamic light scattering: The method and some applications. In *Diffusing-wave spectroscopy*, Brown, W., Ed. Oxford University Press: Oxford, UK, 1993.
52. Weiss, J.N. *Dynamic Light Scattering (DLS) Spectroscopy. In: Dynamic Light Scattering Spectroscopy of the Human Eye*; Springer Cham: Cham, Switzerland, 2022.
53. Kim, H.A.; Seo, J.K.; Kim, T.; Lee, B.T. Nanometrology and its perspectives in environmental research. *Environ Health Toxicol* **2014**, *29*, e2014016, doi:10.5620/eht.e2014016.
54. Frisken, B.J. Revisiting the method of cumulants for the analysis of dynamic light-scattering data. *Appl Opt* **2001**, *40*, 4087-4091, doi:10.1364/ao.40.004087.
55. Øgendal, L. *Light Scattering Demystified: Theory and Practice* University of Copenhagen: Copenhagen, Denmark, 2019.
56. Provencher, S.W.; Štêpánek, P. Global Analysis of Dynamic Light Scattering Autocorrelation Functions. *Particle & Particle Systems Characterization* **2006**, *13*, 291-294, doi:10.1002/ppsc.19960130507.
57. Stetefeld, J.; McKenna, S.A.; Patel, T.R. Dynamic light scattering: a practical guide and applications in biomedical sciences. *Biophys Rev* **2016**, *8*, 409-427, doi:10.1007/s12551-016-0218-6.
58. Ohshima, H. The Derjaguin–Landau–Verwey–Overbeek (DLVO) Theory of Colloid Stability. **2012**, 10.1002/9781118135440.ch3, 27-34, doi:10.1002/9781118135440.ch3.
59. Seo, M.-K.; Park, S.-J. *Interface Science and Composites*; Elsevier ldt.: Amsterdam, Netherlands, 2011; Vol. 18.
60. Delgado, A.V.; González-Caballero, F.; Hunter, R.J.; Koopal, L.K.; Lyklema, J. Measurement and Interpretation of Electrokinetic Phenomena (IUPAC Technical Report). *Pure and Applied Chemistry* **2005**, *77*, 1753-1805, doi:10.1351/pac200577101753.
61. Kumar, A.; Dixit, C.K. Methods for characterization of nanoparticles. **2017**, 10.1016/b978-0-08-100557-6.00003-1, 43-58, doi:10.1016/b978-0-08-100557-6.00003-1.
62. Young, T. III. An essay on the cohesion of fluids. *Philosophical Transactions of the Royal Society of London* **1997**, *95*, 65-87, doi:10.1098/rstl.1805.0005.
63. Erbil, H.Y. Dependency of Contact Angles on Three-Phase Contact Line: A Review. *Colloids and Interfaces* **2021**, *5*, 8, doi:10.3390/colloids5010008.

64. Schrader, M.E. Young-Dupre Revisited. *Langmuir* **2002**, *11*, 3585-3589, doi:10.1021/la00009a049.
65. Shi, Z.; Zhang, Y.; Liu, M.; Hanaor, D.A.H.; Gan, Y. Dynamic contact angle hysteresis in liquid bridges. *Colloids and Surfaces A: Physicochemical and Engineering Aspects* **2018**, *555*, 365-371, doi:10.1016/j.colsurfa.2018.07.004.
66. Silva Marques, S.C.; Gambaryan-Roisman, T.; Venzmer, J. Surface tension behavior of superspreading and non-superspreading trisiloxane surfactants. *Colloid and Polymer Science* **2023**, *301*, 739-744, doi:10.1007/s00396-023-05106-0.
67. Heinz, M.; Chowdhury, I.U.; Stephan, P.; Gambaryan-Roisman, T. Water drops on nanofiber-coated substrates: Influence of wall temperature and coating thickness on hydrodynamics and wall heat flux distribution. *International Journal of Heat and Mass Transfer* **2024**, *222*, 125117, doi:10.1016/j.ijheatmasstransfer.2023.125117.
68. Heinz, M.; Stephan, P.; Gambaryan-Roisman, T. Influence of nanofiber coating thickness and drop volume on spreading, imbibition, and evaporation. *Colloids and Surfaces A: Physicochemical and Engineering Aspects* **2021**, *631*, 127450, doi:10.1016/j.colsurfa.2021.127450.

Section 2 Interfacial rheology of non-ionic surfactants

This section deals with two water-surfactant solutions, in which surfactant molecules undergo a fast adsorption to the liquid/vapor interface, forming Gibbs monolayers. In this case, the rheological response of the interface can appear coupled with adsorption-desorption phenomena. It is divided into two chapters:

- *Chapter III: Interfacial Rheology of Alkyl Poly-Glycoside (APG) surfactant*

This chapter deals with alkyl polyglucoside (APG, a non-ionic glucosidic surfactant) aqueous solutions, focusing on the equilibrium surface tension of APG Gibbs monolayers and the dilational interfacial rheology measured by ECW technique.

- *Chapter IV: Interfacial Rheology of non-superspreading and superspreading trisiloxanes surfactants*

The second chapter of this section is aimed at studying the interfacial properties of trisiloxane solutions, comparing a superspreader surfactant (S240) with a non-superspreader one (S233). The aim of this study is to try to relate interfacial rheological response as was determined by ECW technique to the spreading kinetics. Moreover, this study will allow comparing the oscillation parameters (i.e., frequency and damping) of sessile drops on PET substrates with the propagation parameters of capillary waves determined by ECW technique (wavelength, frequency, damping), trying to understand what is the prevailing mechanism that drives drop oscillation after impact on a solid substrate.

Chapter III: Interfacial Rheology of Alkyl Poly-Glycoside (APG) surfactant[‡]

3.1. Introduction

Alkyl Poly Glycosides (APG) are a family of non-ionic surfactants characterized by a good biodegradability and a low toxicity, making them some of the most environmentally friendly surfactants available. They are commonly obtained through glycosylation of a reducing sugar with and excess of molten fatty alcohol. This process, schematized in **Figure 3. 1**,involves the formation of water, as a byproduct, which is progressively removed to drive the reaction to completion. The resulting APGs are widely used in various applications, including personal care products, household cleaners, and industrial formulations, due to their gentle nature and effective cleaning properties [1].

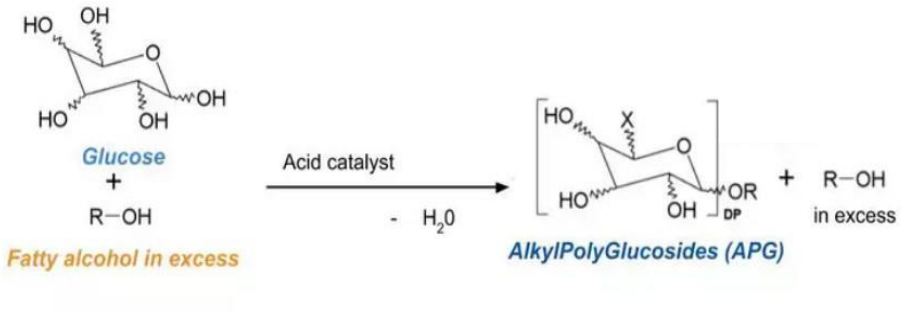

Figure 3. 1. Glycosylation reaction of a fatty alcohol, forming an Alkyl Poly Glycoside (APG).

The physico-chemical properties of the different APG are strongly correlated to the length of the alkyl chain of the fatty alcohol. When the fatty alcohol used in the synthesis of Alkyl Polyglucosides (APGs) contains a short carbon chain, typically shorter 14 carbon atoms, the resulting APG solutions do not have the capability to form stable liquid crystals, in contrast with APGs with longer hydrocarbon chains-. As a result, hence they are highly soluble in water [2]. In the experimental work described in this chapter, the APG employed consist in a mixture of two short chain hydrocarbons (C8 and C10), which each of the component contributing approximately 50% to the mixture (**Figure 3. 2**). The relative short length of these hydrocarbon chains, combined with the polar nature of the glucose groups, significantly enhances the solubility of this molecule in water. This combination also allows the APG to form micellar aggregates in aqueous solutions, which is a key characteristic of its surfactant behavior.. Compared to other synthetic surfactants, APG is characterized by a certain structural heterogeneity. This heterogeneity arises from the variation in both the length of the hydrocarbon chains and the number of glucose units in the polar head group. Such variability can influence the surfactant's physicochemical properties, including its solubility, micelle formation, and interaction with other substances in a formulation. The unique combination of short hydrocarbon chains and glucose groups not only makes this APG highly soluble in water but also imparts it with the ability to effectively reduce surface tension, making it an excellent choice for various applications where mild yet effective surfactants are required. In fact, APG

[‡] Experiments, as well as data analysis, were done in collaboration with Jorge Zaera Martinez, undergraduate student at Universidad Complutense de Madrid: experimental data, as well as their discussion, were partially taken from his bachelor degree thesis, entitled “ESTUDIO DE ONDAS CAPILARES EN INTERFASES FLUIDAS”.

solutions are employed in cosmetic and dermo-pharmaceutical industry, as well as in the production of detergents and lubricants [2-5].

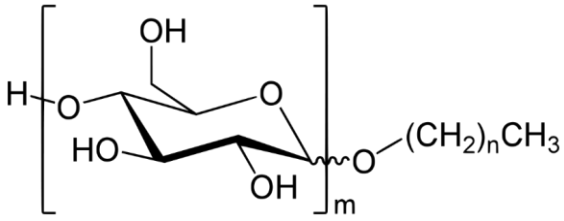

Figure 3. 2. APG structure where (n: C7:C9 50%) with the chain in total between 8 and 10 carbons; m=1-3.

APG surface tension and foaming properties have already been widely studied in literature. However, although there are some works focusing on the interfacial properties of APG surfactants alone [5,6], most of the studies involving APG surfactants combine this type of surfactants with other surfactants. This leads to an enhancement of the performances of the products involving APG. Ahmad et. al proved that the combination of APG surfactants with other surfactants, such as sodium dodecyl sulfate (SDS) or sodium laureth sulfate (SLES) leads to a synergistic reduction of the surface tension in relation to pure surfactants. This results in an improvement of the detergency properties, enhancing the foam stability [7].Kang et al. [8] proved that the surface tension of the mixture between APG and Methyl ether sulfonate (MES) also lower the surface tension with respect to the corresponding to the pure surfactants . Furthermore, the presence of MES reduces the value of the Critical Micellar Concentration (CMC) and bulk shear viscosity of APG. Li et al. [9] studied the surface tension and the foam stability of mixtures of APG surfactants, with C8 and C10 chains, with urea, and found that even though urea does not affect surface tension, it decreases the CMC.

Lemahieu et al. [10] studied the adsorption kinetics of APG surfactant containing different hydrocarbon tails, and found that independently of the type of surfactant, the adsorption process occur at a timescale higher than 10^2 s, when the surfactant concentration overcome a value of 0.02 mM. Thus, it is possible to consider that APG diffusion is relatively fast, and hence any relaxation process associated with changes in the surface concentration should appear at frequencies higher than *1/100 s = 0.01 Hz*. In another study, Jiang et al. studied APG surface tension and surface excess concentration, focusing on molecular area and CMC of APG aqueous solutions [6].

The aim of this chapter is to study the surface tension of APG solutions, focusing on CMC and surface excess concentration, and integrate these data to some experiments aimed at determining the interfacial dilational response of APG Gibbs monolayers by using Electro-Capillary Waves (ECW) frequency range (60-850 Hz).

3.2. Materials and methods

3.2.1. Chemicals and solution preparation

Alkylpolyglucoside (APG), marketed as Oramix GC-110 (a 50:50 molar combination of caprylyl glucoside and capryl glucoside), was supplied by Safic-Alcan (Barcelona, Spain). Ultrapure deionized water of Milli-Q grade, with a resistivity higher than 18 MΩ·cm and a total organic content (TOC) of less than 6 ppm, was used for all experiments and material cleaning purposes. To achieve this level of purity an AquaMAX™-Ultra 370 Series multi-cartridge purification

system (Young Lin Instrument Co., Ltd., Gyeonggi-do, Republic of Korea) was used. All solutions were prepared by weight using an analytical balance accurate to ±0.01 mg.

3.2.2. Experimental methods

A surface force tensiometer model K10T Digital Tensiometer (KRÜSS GmbH, Hamburg, Germany) fitted with a platinum Wilhelmy plate contact probe of 40.5 mm of perimeter was used to measure the interfacial tension. Between each measurement, the platinum plate was cleansed using ethanol and Milli-Q water and then burnt with an ethanol torch to remove any remaining residue of organic matter. For the measurements, the samples were poured into glass cells, previously cleaned with ethanol and Milli-Q water. For all the measurements, the temperature was controlled by using a thermostatic bath set at 25ºC. Each experimental data point reported was an average of at least three independent measurements. The experiments were conducted for a long enough time to ensure that a steady state interfacial coverage was reached.

Dilational interfacial rheology measurements at high frequency (in the range of 60-850 Hz) were performed by using a homemade Electro-Capillary Wave (ECW) device, described elsewhere [11-16] (See *Chapter II*, *2.1.4. Electro-Capillary Waves (ECW)*, for detailed description). Experiments were done at 25 °C (the temperature of the Langmuir Trough was maintained constant by means of a thermostatic bath). The adsorption kinetic was monitored by means of a surface force tensiometer NIMA PS4 manufactured by Nima Technology (Coventry, UK) fitted with disposable Wilhelmy paper plates (Whatman CHR1 chromatography paper, Merck, Darmstadt) of 20.6 mm of perimeter was used for interfacial tension measurements. A fresh paper plate was used for each measurement to prevent any potential modifications on the plate surface as a result of the material adsorption during previous experiments. ECW measurements were done making sure that surfactant adsorption process reached its equilibrium (i.e., constant surface tension in time).

3.3. Results and discussion

3.3.1. Surface tension

The surface tension γ of a surfactant aqueous solution in diluted regime (under the assumption that all sites at liquid/vapor interface have the same probability of being occupied by surfactant molecules) can be expressed by a combination of the Langmuir equation and Gibbs isotherm, according to the following equation (see *Chapter I*, *1.5. Equilibrium properties of interfaces*):

$$\gamma(C,T) = \gamma_0(T) - RT\Gamma_\infty \, ln[1 + K(T)C], \tag{3. 1}$$

with C being surfactant bulk concentration, R the ideal gas constant, T the absolute temperature, $\gamma_0(T)$ the surface tension of the bare interface (essentially, the one of pure water), $K(T)$ the adsorption-desorption equilibrium Langmuir constant. Γ_∞ is the maximum value of surface excess concentration (Γ), i.e., the maximum number of molecules per unit area that can be adsorbed at the interface. Γ can be calculated, as a function of C, by means of the Langmuir equation,

$$\Gamma(T,C) = \Gamma_{\infty} \cdot \frac{K(T)C}{1 + K(T)C}. \quad (3.\ 2)$$

As the interface gets saturated by surfactant molecules, which occurs at large values of C, when $\Gamma(T,C) \to \Gamma_{\infty}$, the equation (3. 1) is no longer valid. In this region, surface tension achieved a constant value, independently of the bulk concentration ($\gamma = \gamma_{\infty}$). Based on the value of Γ_{∞}, the area per surfactant molecule, i.e., the area occupied by a surfactant molecule at the interface under maximum packing conditions can be estimated by means of the following expression,

$$\tilde{A} = \frac{1}{N_A \Gamma_{\infty}}. \quad (3.\ 3)$$

The surface tension γ and the surface excess concentration Γ of APG Gibbs monolayers, as a function of surfactant concentration (C), are plotted in **Figure 3. 3** (a) and (b) respectively:

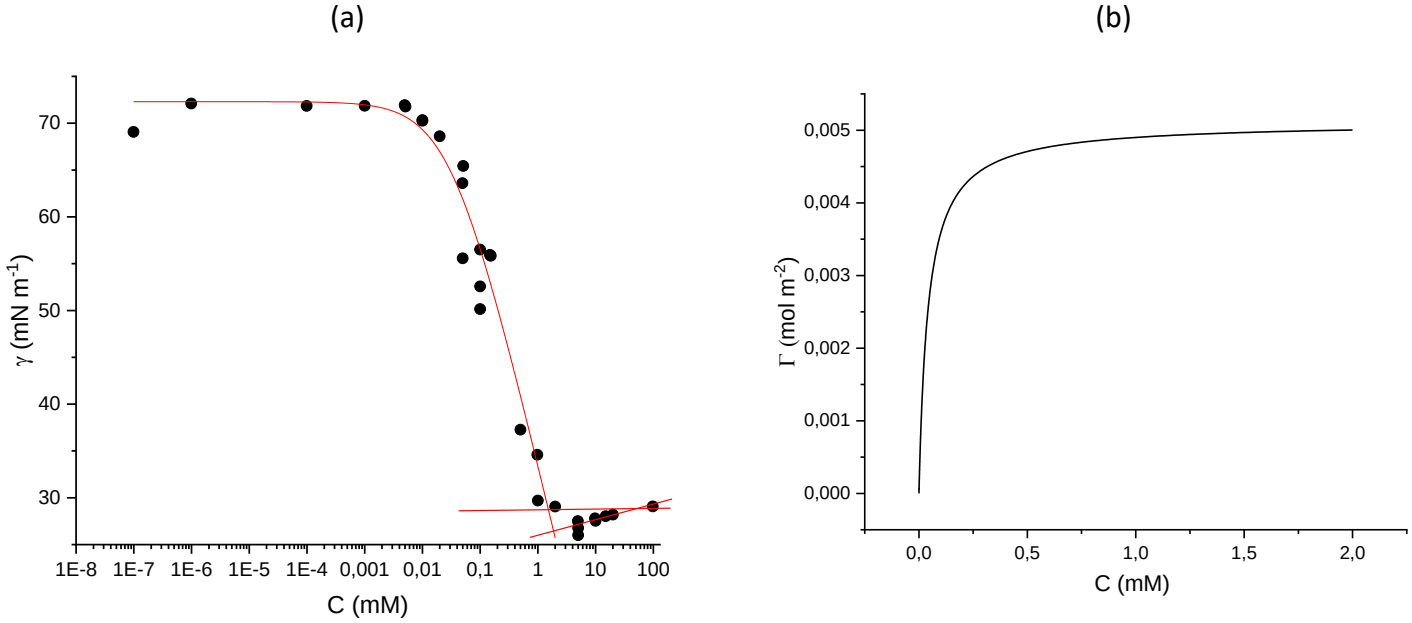

Figure 3. 3. (a) Surface tension γ of APG Gibbs monolayers, versus surfactant bulk concentration C. The red curve to the left (between $C = 10^{-7}\, mM$ and $C = 1\, mM$) represents the Langmuir isotherm curve (equation (3. 1)) that best fits the experimental data (black circles), while the red horizontal line to the right represents the equilibrium surface tension. (b) Surface excess concentration Γ of APG Gibbs monolayers, as a function of surfactant bulk concentration C (computed by means of equation (3. 2)).

γ, after an initial plateau at the lowest values of surfactant concentration ($C = 10^{-7} - 10^{-2}\, mM$) where the surfactant tension assumes values similar to that of the pristine air/water interface, starts to decrease with the increase of the surfactant concentration until reaching a second plateau around $C \approx 1\, mM$, which corresponds with the CMC of the surfactant. The dependence of the surfactant concentration until the CMC value is accounted by the equation (3. 1) as shown **Figure 3. 3** (a). It should be noted that when the CMC value is overcome, the surface tension should remain constant with any further increase in C. However, according to **Figure 3. 3** (a), this is not the case in the results obtained, and a minimum in $\gamma - C$ curve is observed around $C \approx 5\, mM$, which may be explained by considering that the APG that has been employed in this experimental work is not pure, but rather a mixture of different molecules characterized by hydrocarbon chains of different

lengths. As a consequence, when the concentration of surfactant increases, the most hydrophobic molecules of APG (with a longer hydrocarbon chain) tend to preferentially adsorb at the interface, and when the critical micellar concentration is reached, these molecules with higher hydrophobic character begin to form micelles, desorbing from the interface, which will be occupied by the less hydrophobic APG molecules (the ones with shorter hydrocarbon chain), which are less surface active than the ones with longer chain. As a first approximation, the value of the CMC can be estimated by determining the intersection point between the Langmuir isotherm curve (red curve in **Figure 3. 3** (a)) and the horizontal red line in **Figure 3. 3** (a) (corresponding to the value of $\gamma = \gamma_\infty$). The obtained value of CMC is about $\gamma = 1.7\ mM$, which is in agreement with that reported in reference [6].

On the other hand, the $\Gamma(C)$ dependence obtained from the combination of equations (3.1) and (3.2) shows the opposite trend to the surface tension curve, which the surface excess increasing with surfactant concentration until reaching a plateau value, corresponding to the saturation value of Γ_∞. By fitting the data with eq. (3. 1), a value of $\Gamma_\infty \approx 0.005\ mol/m^2$ is obtained, which corresponds to a molecular area of $\tilde{A} \approx 3.22 \cdot 10^{-22}\ m^2$, which is also in agreement with the value reported in reference [6].

3.3.2. Capillary wavelength and damping

For a capillary wave excited in a point of the interface (represented by the xy plane) defined by the coordinate x=0, it is possible to define its spatial profile in terms of a damped cosine according to the following expression (see *Chapter II*, *2.1.4. Electro-Capillary Waves (ECW)*),

$$u_z = u_z^0 e^{-\beta x} \cos\left(\frac{2\pi}{\lambda}x + \varphi\right), \qquad (3.\ 4)$$

where u_z^0 is the wave amplitude, and β, λ and ϕ the damping coefficient, the characteristic capillary wavelength and the phase lag, respectively.

The propagation parameters of surface capillary waves (λ and β), as a function of the frequency (ν), are plotted in **Figure 3. 4**.

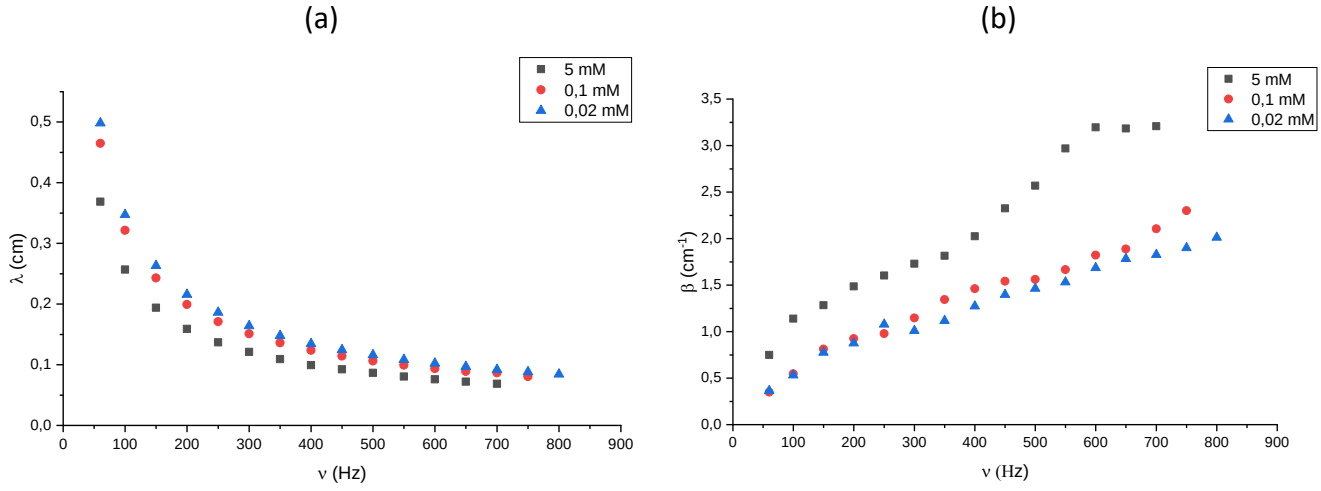

Figure 3. 4. (a) Capillary wavelength (λ) and (b) damping (β) of APG monolayers, as a function of the frequency ($\boldsymbol{\nu}$), at different APG concentration (0.02 mM, 0.1 mM, 5 mM).

According to **Figure 3. 4** (a), the wavelength, at fixed frequency, is directly related to the surface tension of the samples. Therefore, it can be expected that the higher γ the higher λ. The results show that independently of the concentration of the APG solutions, the capillary wavelength decrease with the frequency. In addition, the values of λ at fixed frequency decreases as the surface tension decreases. This difference is very strong when comparing 5 mM APG solution with those with the lowest concentration studied (0.02-0.1 mM). This can be understood considering the big differences existing between the surface tension of the solution with the lowest surfactant concentrations studied and those corresponding to the most concentrated solution studied. On the other hand, the frequency dependence of the capillary wavelength aligns with Kelvin's law [17], previously discussed in *Chapter II* (*2.1.4. Electro-Capillary Waves (ECW)*):

$$\lambda = \left(\frac{2\pi\gamma}{\rho}\right)^{\frac{1}{3}} \nu^{-2/3}, \tag{3. 5}$$

with ρ being the density of the solution. Actually, equation (3. 5) is valid in pure liquids with no surface adsorption, which is not the case of APG aqueous solutions, but, anyway, Kelvin's law still works to qualitatively predict the capillary wavelength of APG solutions. Kelvin's law can be generalized as a power law ($\lambda = A\nu^{-n}$): by fitting $\lambda - \nu$ experimental data in **Figure 3. 4** (a) with the latter equation, an exponent of $n \approx 0.69$, which is close to the value of 2/3 predicted by Kelvin's law. The slight deviation between the predicted value and the experimental value is understandable in view of the limitations of the Kelvin equation.

The damping coefficient follows the opposite trend with γ: a decrease in surface tension, which is in turn associated with an increment in surface excess concentration, results in higher damping coefficient, according to what can be expected from a Stokes-like law [17] (see *Chapter II*, *2.1.4. Electro-Capillary Waves (ECW)*):

$$\beta = \frac{8\eta\pi\nu}{3\gamma} \tag{3. 6}$$

being η the bulk shear viscosity of the solution (being APG concentration very low, it can be approximated with the value of water viscosity at 25 °C: it goes without saying that bulk shear viscosity has no huge impact on the damping coefficient).

Similarly to Kelvin's equation, Stokes-like equation can be generalized in the following power law form: $\beta = A\nu^n$. By fitting $\beta - \nu$ experimental data in **Figure 3. 4** (b) with the previous equation, the value of n ranges between 0.66-0.68. Hence, the system, as expected does not comply with the Stokes-like law, which can be interpreted as a sign of the presence of viscoelasticity at the interface. In 5 mM APG solutions, the values of β at high frequency (> 500 Hz) deviate from the monotonical trend predicted by the power law: these anomalous values are given by random experimental error affecting the measurements at high frequency, due to the fact that the resolution of the set-up is not enough to sharply determine the profile of the wave and obtain data with sufficient precision.

3.3.3. High-frequency dilational rheology

In order to determine the dilational response of the monolayer from ECW experiments, the dispersion equation (a relation between the characteristics parameter associated with the propagation of the transversal waves: the frequency ν, the wavelength λ, and the damping coefficient β) must be solved with respect to the complex dilational modulus $E_s^*(\nu)$ (see *Chapter II*, *2.1.4. Electro-Capillary Waves (ECW)*). Being $\omega = 2\pi\nu$ the angular frequency, $E_s^*(\nu)$ can be determined as follows:

$$E_s^*(\nu) = E_s(\nu) + iE_i(\nu) = \frac{\dfrac{-\left(\eta\omega(q-m)\right)^2}{\gamma q^2 + i\eta\omega(q+m) - \dfrac{\rho}{q}\omega^2} - i\eta\omega(q+m)}{q^2} \tag{3. 7}$$

where *q* is the capillary complex wavevector, defined as,

$$q = \frac{2\pi}{\lambda} - i\beta \tag{3. 8}$$

and *m* is the capillary penetration depth (Re(m) > 0),

$$m = \sqrt{q^2 + i\omega\frac{\rho}{\eta}} \tag{3. 9}$$

In **Figure 3. 5** both the storage dilational modulus E_s and the loss dilational modulus E_i are plotted versus the frequency ν.

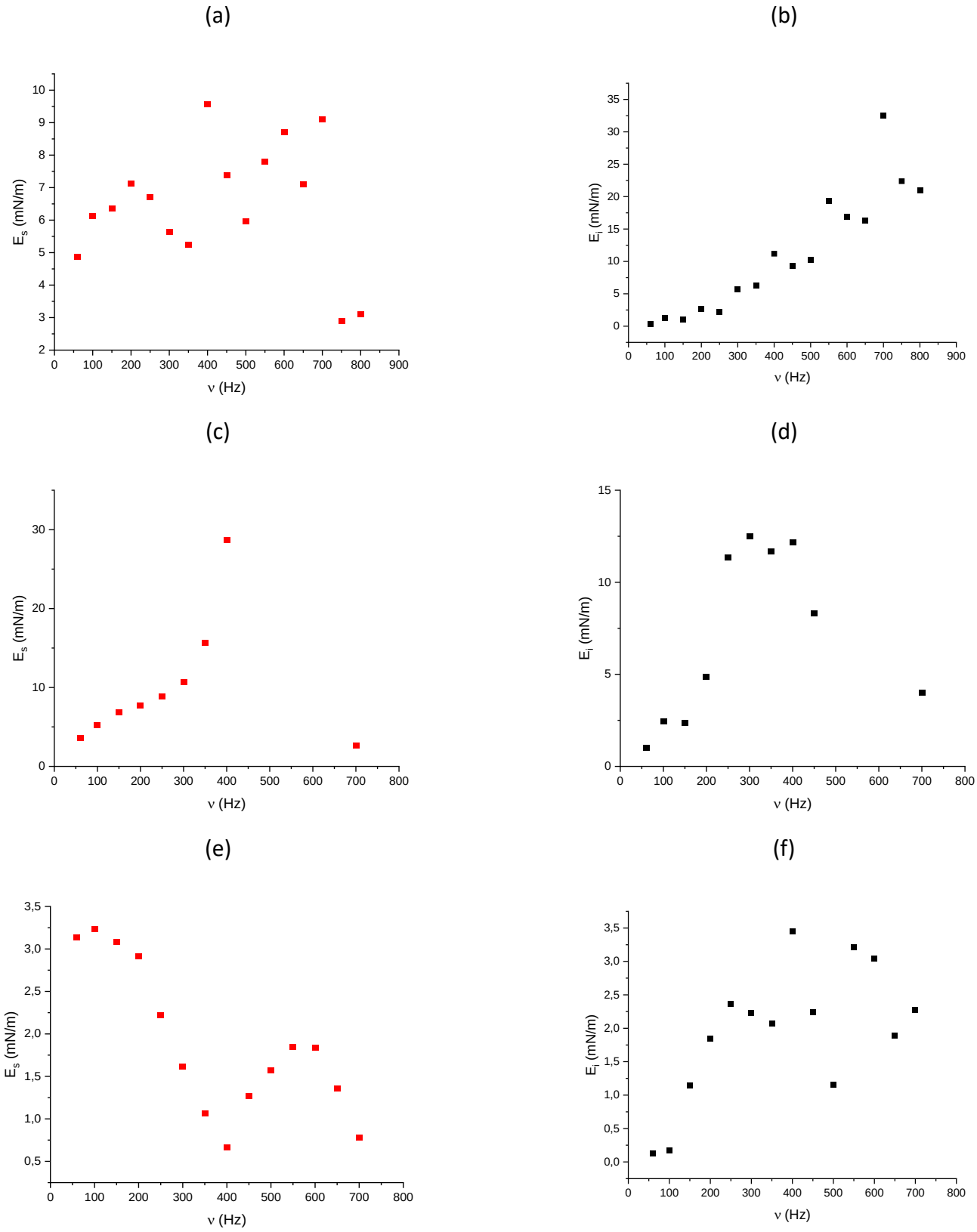

Figure 3. 5. Complex dilational interfacial modulus $E_s^*(\nu) = E_s(\nu) + iE_i(\nu)$ of APG solutions, as a function of the frequency ν: E_s (a) and E_i (b) of 0.02 mM APG solution; E_s (c) and E_i (d) of 0.1 mM APG solution; E_s (e) and E_i (f) of 5 mM APG solution.

In **Figure 3. 5** (a) (storage modulus of 0.02 mM APG solutions), two different trends can be observed: at lower frequencies, E_s is constant with frequency, but when exceeding the frequency of 400 Hz, E_s tend to oscillate. When the monolayer is deformed at low frequency, the prevailing phenomenon is the adsorption-desorption process of the surfactant at the interface (predicted by Lucassen-Van der Tempel model). However, as the frequency increases, this phenomenon becomes less important because the surfactant molecules have less time to adsorb and desorb from the interface. Therefore, at higher frequencies other phenomena dominate the elastic recovery (like the intrinsic elasticity of APG monolayer), producing this change in trend in interfacial elasticity. The change in the trend of E_s may be also a consequence of the experimental error associated to the calculation of E_s itself. Concerning E_i, it linearly varies with ω. Being $k_s(\omega) = E_i(\omega)/\omega$ the interfacial dilational viscosity, if E_i has a linear trend versus ω, then $k_s(\omega)$ is constant and does not depend on frequency.

As well as 0.02 mM APG solution, also 0.1 mM APG sample is far below the CMC. The storage modulus, at the same frequency, of 0.1 mM APG monolayers is slightly higher than the one of 0.02 mM solutions: this may be associated with the increase in the surface concentration of surfactant, which leads to higher adsorption and desorption rates, since there is a greater number of molecules to occupy the gaps in the interface. This corresponds to an increase in the elasticity of the interface, which is able to accumulate a greater amount of elastic energy when the interface is deformed. The observed maximum has a value of about 50 mN/m and may be associated with the change in monolayer regime, previously observed in 0.02 mM APG sample. However, the peak may be associated with the error in determining E_s: in fact, E_s is determined at a certain value of γ, which is in turn subjected to experimental error. In 0.1 mM APG solutions, the influence of the indeterminacy of γ on the value of E_s is even more pronounced than the case of 0.02 mM ones. This aspect will be discussed in further details in the next few chapters of the thesis, by discussing the issue of the resonance condition (see *Chapter II*, *2.1.4. Electro-Capillary Waves (ECW)*). The imaginary part of the dilational modulus, as observed in **Figure 3. 5** (d), shows a peak around $\nu \approx 400\ Hz$, which is the point where E_s increase is more pronounced.

The interfacial elasticity of 5 mM APG solutions, compared with the two previous ones, is way lower. This could be explained by the fact that the 5 mM samples are far beyond the CMC: in this case, the concentration of free surfactant stays constant (hence, the surface tension) independently on the applied area deformation. As a result, E_s is almost nil, and almost constant with frequency (it oscillates between 0-3 mN/m). The same goes for E_i: the combination of the interface occupied by surfactant molecules together with the formation of micelles produces an interface that can be deformed with low energy cost.

3.4. Conclusions

This chapter was aimed at studying the surface tension and the dilational interfacial rheology (in 60 – 850 Hz frequency range) in of APG surfactant solutions.

Surface tension measurements revealed that in both dilute and semi-dilute regime, the isotherm obeys the Gibbs-Langmuir equation. The local minimum observed in in $\gamma - C$ curve suggests that the surfactant is not pure, but different molecules with diverse hydrocarbon

chain length are present in the solution. Nevertheless, the critical micellar concentration was estimated to be around $\sim 1.7\ mM$.

The values of capillary length follow coherently the trend of surface tension, and Kelvin law is qualitatively satisfied. The damping of capillary waves is not ruled by bulk viscosity, but rather by the presence of surfactant molecules that occupy liquid/vapor interface.

The dilational surface modulus in 3 concentration regimes was studied: at $C = 0.02\ mM$ (corresponding to the upper isotherm plateau), adsorption-desorption mechanism dominates in relaxation dynamic. At $C = 0.1\ mM$ (nearby the inflection point of the isotherm), at low frequency diffusional regime dominates, while at higher frequency the intrinsic elasticity of the monolayer prevails. At $C = 5\ mM$ (above CMC), both storage and loss moduli are almost null.

The presence of anomalous peaks in $E_s - \nu$ curves suggests that a deeper analysis of the uncertainty of E_s is required: in some cases, the uncertainty in determining the value of the surface tension may have a huge impact on E_s error bars: this aspect will be further discussed in the next few chapters.

As explained in *3.1. Introduction* subsection, APG is usually used in combination with another surfactant/polymer. A future perspective of this work may be studying the interfacial properties of APG-Chitosan solutions (especially the dilational interfacial rheology at high frequency).

3.5. References

1. DemİRel, V.; Donat, R. Synthesis of Some Alkyl Polyglycosides. *International Journal of Secondary Metabolite* **2022**, *9*, 52-65, doi:10.21448/ijsm.1033290.
2. Hill, K.; Von Rybinski, W.; Stoll, G. *Alkyl Polyglycosides*; Wiley-VCH: Weinheim, Germany, 2008.
3. Von Rybinski, W.; Stoll, G. Alkyl Polyglycosides—Properties and Applications of a new Class of Surfactants. *Angewandte Chemie International* **1998**, *37*, 1328-1345, doi:https://doi.org/10.1002/(SICI)1521-3773(19980605)37:10%3C1328::AID-ANIE1328%3E3.0.CO;2-9.
4. Iglauer, S.; Wu, Y.; Shuler, P.; Tang, Y.; Goddard, W.A. Analysis of the Influence of Alkyl Polyglycoside Surfactant and Cosolvent Structure on Interfacial Tension in Aqueous Formulations versus n-Octane. *Tenside Surfactants Detergents* **2010**, *47*, 87-97, doi:10.3139/113.110056.
5. Sulek, M.W.; Ogorzalek, M.; Wasilewski, T.; Klimaszewska, E. Alkyl Polyglucosides as Components of Water Based Lubricants. *J Surfactants Deterg* **2013**, *16*, 369-375, doi:10.1007/s11743-012-1428-y.
6. Jiang, L.C.; Basri, M.; Omar, D.; Abdul Rahman, M.B.; Salleh, A.B.; Raja Abdul Rahman, R.N.Z. Self-assembly behaviour of alkylpolyglucosides (APG) in mixed surfactant-stabilized emulsions system. *Journal of Molecular Liquids* **2011**, *158*, 175-181, doi:10.1016/j.molliq.2010.11.015.
7. Ahmad, A.; Yeong, S.K.; Ismail, R.; Ooi, T.L.; Ahmad, S. Synergistic effect between sodium lauryl sulphate and sodium lauryl ether sulphate with alkyl polyglycoside. *Journal of Oil Palm Research* **2007**, *19*, 332-337.

8. Kang, P.; Xu, H.; Song, C. Properties of Binary Surfactant System of Alkyl Polyglycosides and α-Sulphonated Fatty Acid Methyl Ester. *Tenside Surfactants Detergents* **2013**, *50*, 192-198, doi:10.3139/113.110248.
9. Li, F.; Yu, X.; Zong, R. Experimental study on the foam performance and fire extinguishing performance of aqueous foam stabilized by alkyl polyglucoside and urea. *IOP Conference Series: Earth and Environmental Science* **2022**, *983*, 012085, doi:10.1088/1755-1315/983/1/012085.
10. Lemahieu, G.; Aguilhon, J.; Strub, H.; Molinier, V.; Ontiveros, J.F.; Aubry, J.M. Hexahydrofarnesyl as an original bio-sourced alkyl chain for the preparation of glycosides surfactants with enhanced physicochemical properties. *RSC Adv* **2020**, *10*, 16377-16389, doi:10.1039/d0ra02326d.
11. Liggieri, L.; Santini, E.; Guzmán, E.; Maestro, A.; Ravera, F. Wide-frequency dilational rheology investigation of mixed silica nanoparticle–CTAB interfacial layers. *Soft Matter* **2011**, *7*, 7699, doi:10.1039/c1sm05257h.
12. Maestro, A.; Ortega, F.; Rubio, R.G.; Rubio, M.A.; Kragel, J.; Miller, R. Rheology of poly(methyl methacrylate) Langmuir monolayers: percolation transition to a soft glasslike system. *J Chem Phys* **2011**, *134*, 104704, doi:10.1063/1.3560612.
13. Monroy, F.; Ortega, F.; Rubio, R.G.; Velarde, M.G. Surface rheology, equilibrium and dynamic features at interfaces, with emphasis on efficient tools for probing polymer dynamics at interfaces. *Adv Colloid Interface Sci* **2007**, *134-135*, 175-189, doi:10.1016/j.cis.2007.04.023.
14. Monroy, F.; Ortega, F.; Rubio, R.G. Dilatational rheology of insoluble polymer monolayers: Poly(vinylacetate). *Physical Review E* **1998**, *58*, 7629-7641, doi:10.1103/PhysRevE.58.7629.
15. Guzmán, E.; Maestro, A.; Carbone, C.; Ortega, F.; Rubio, R.G. Dilational Rheology of Fluid/Fluid Interfaces: Foundations and Tools. *Fluids* **2022**, *7*, 335, doi:10.3390/fluids7100335.
16. Mendoza, A.J.; Guzman, E.; Martinez-Pedrero, F.; Ritacco, H.; Rubio, R.G.; Ortega, F.; Starov, V.M.; Miller, R. Particle laden fluid interfaces: dynamics and interfacial rheology. *Adv Colloid Interface Sci* **2014**, *206*, 303-319, doi:10.1016/j.cis.2013.10.010.
17. Langevin, D. *Light Scattering by Liquid Surfaces and Complementary Techniques.* ; CRC Press: New York, US, 1992; Vol. 41.

Chapter IV: Interfacial Rheology of non-superspreading and superspreading trisiloxanes surfactants[§]

4.1. Introduction

Superspreading is a phenomenon observed in certain chemical compounds that exhibit rapid spreading when they come into contact with hydrophobic solid surfaces characterized by a low surface energy. Moreover, in these compounds, commonly called supespreaders, the molecules have the ability to significantly reduce the surface tension of the solution/air interface, even at relatively low concentrations [1]. The most common case of superspreading occurs in some trisiloxane surfactants. Aqueous droplets containing these surfactants can spread quickly over hydrophobic surfaces [2,3].

Figure 4. 1 depicts a comparison of the wetted areas on a polypropylene (PP) film by droplets of 50 µL of water, a non-superspreader trisiloxane surfactant at a concentration of 0.1%v/v, and a superspreader trisiloxane surfactant at the same concentration, all observed within 1 minute. The figure clearly illustrates the remarkable spreading capability of the superspreader trisiloxane, evident from the significantly larger diameter of the wetted region (70 mm). In contrast, the droplets of non-superspreader surfactant and water exhibit noticeably smaller wetted areas under the same conditions. In fact, the diameter of the wetted area in the case of the non-superspreader surfactant is more than 4-fold lower than in the case of the superspreader one (15 mm vs. 70 mm). This highlights the distinctive effectiveness of superspreader trisiloxane surfactants in facilitating rapid and extensive coverage of hydrophobic surfaces [4].

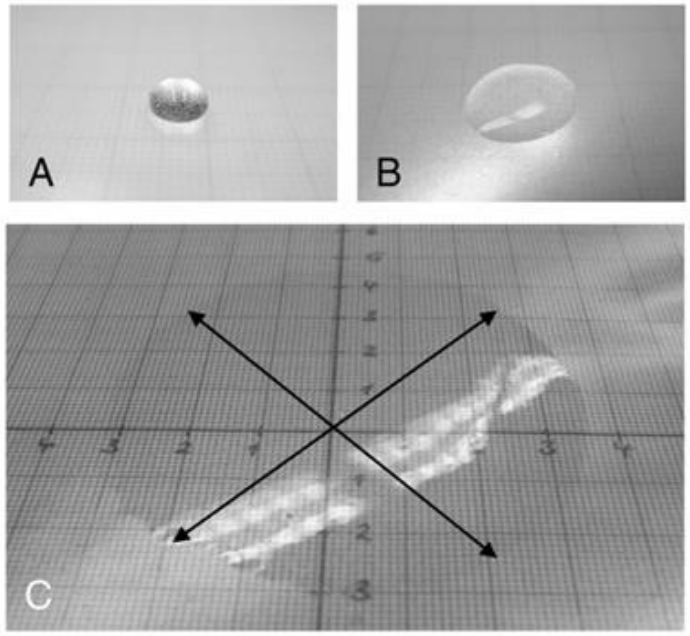

Figure 4. 1. Photos taken 1 min after placing a 50 µL droplet onto a PP film: (A) water; (B) non-superspreading trisiloxane surfactant; (C) superspreading trisiloxane surfactant. Adapted from Venzmer [3].

[§] Part of the experimental work in this chapter (spreading and drop impact experiments) were carried out at TU Darmstadt (Germany), in collaboration with Séforah Carolina Marques Silva (TU Darmstadt, Germany), Tatiana Gambaryan-Roisman (TU Darmstadt, Germany) and Joachim Venzmer (Evonik Operations GmbH).

Trisiloxane surfactants, particularly superspreaders, are widely utilized across diverse industries. For instance, in the agrochemical industry, they play a very important role in the optimization of crop protection strategies. This is possible because they contribute to increase the contact surface of agrochemical solutions on hydrophobic surfaces, such as plant leaves, which enable a more effective adsorption and distribution of active ingredients. Trisiloxane surfactants are also used in the formulation of paints and coatings, where they contribute to improve coverage and prevent phenomena such as uneven drying or surface defects. Additionally, in pharmaceutical formulations, trisiloxane are used to enhance the solubility and bioavailability of drugs [5].

The typical chemical formula of trisiloxane surfactants can be expressed as "M-(D-E_nP_m-OH)-M", where "M" represents trimethylsiloxy group "$(CH_3)_3SiO_{1/2}$-", the term "D" stands for "–$O_{1/2}Si(CH_3)(E_nP_m)O_{1/2}$–", "$E_n$" represents the poly-ethylene oxide group "–$(CH_2–CH_2–O)_n$–" , and P_m stands for poly-propylene oxide "–$(CH_2–CH(CH_3)–O)_m$–' [3]. In this chapter, two different trisiloxane surfactants were studied. The former a superspreader one "M(D'E_6P_3OH)M", which is commercially available as BREAK-THRU® S240, and a non-superspreader counterpart "M(D'$E_{10}P_2$OH)M", commercially available as BREAK-THRU® S233 [2]. Different studies dealing with the spreading of S233 and S240 surfactants have been published by several authors. Bertola [5] studied the wetting behavior and the spreading ratio of S233 and S240 on three different flat substrates (parafilm, acrylic glass and polycarbonate). They found that the superspreader surfactant exhibited an intermittent spreading rate accompanied by peculiar features of the contact line. These were not observed for the non-superspreader surfactant. Moreover, they demonstrated that superspreading was enhanced as the surface energy of the substrate diminished. Tafireyi et al. [6]. studied contact angle and droplet radius dynamics of S240 over porous and non-porous polyvinylidene fluoride substrates, as well as the penetration into the porous substrates. Their results showed that superspreading occurs independently of the porosity of the substrates.

Ananthapadmanabhan et al. [7] claimed that a water soluble trisiloxane surfactant can only behaves as a superspreader when it fulfill four conditions: (i) it reduces liquid/air surface tension to low values; (ii) it presents a high affinity with the substrate; (iii) its adsorption kinetic, both at liquid/air and liquid/solid interface, occurs quickly, and (iv) the trisiloxane group geometry leads to a favorable molecular orientation at the spreading edge. Also air relative humidity has an impact on the occurrence of superspreading, since no superspreading can be observed in a dry atmosphere. This suggests that the interplay between evaporation and condensation near the contact line may play a role in superspreading phenomenon, affecting the adsorption of surfactant molecules at the contact line [6].

Superspreading is thermodynamically favored if total wetting occurs, which means that the spreading coefficient is positive [3],

$$S = \gamma_{SV} - \gamma_{LV} - \gamma_{SL} > 0, \tag{4. 1}$$

where γ_{LV} is the liquid-vapor surface tension, γ_{SL} the liquid-solid surface tension, and γ_{SV} the solid-vapor surface tension. Solutions of superspreading and non-superspreading trisiloxanes both have $\gamma_{LV} \approx 22\ mN/m$, while typically $\gamma_{SV} \approx 30\ mN/m$ when hydrophobic substrates, such as polyolefins, e.g., PE or PP, are considered. Thus, to have superspreading, γ_{SL} must be

very low [4]. The spreading coefficient can only remain positive as long as the surfactant's adsorption rate at the three-phase contact line exceeds the dilution due to the area expansion [3].

Previous works [3,4] state that a plausible explanation of superspreading phenomenon resides in the different phase behavior between a superspreader and a non-superspreader. In particular, the superspreading is considered as a consequence of the ability of the superspreader surfactant to form bilayer structure directly attached to the liquid-vapor interface (**Figure 4. 2**). This type of structures can undergo unzipping process, and therefore they provide a continuous supply of surfactant molecules. This allows to ensure that the solid-liquid surface tension γ_{SL} always remains low enough to guarantee a positive spreading coefficient all along the spreading process, guaranteeing the occurrence of superspreading. On the other hand, non-superspreader surfactants tend to form micellar structures, and surfactant supply at the contact line is not as effective and fast as the one provided by the bilayer structure formed by the superspreader. There are several studies proving that there is a correlation between the capability of trisiloxane surfactants to form a flat bilayer aggregates and the adsorption of surfactant at liquid-solid interface [8]. This is related to their capability to minimize γ_{SL} [4]. On the other hand, non-superspreader surfactants tend to form micelles, which get adsorbed at liquid-solid interface as hemispherical aggregates [9]. The adsorption of this type of aggregates is not as effective as the formation of bilayer aggregates in minimizing γ_{SL}. By observing the stability of foam films and determining the disjoining pressure of superspreader and non-superspreader trisiloxane surfactants was found that the gravitational drainage of foam films constituted by non-superspreader surfactants (more hydrophilic) is relatively fast (and it shows a diffractive ordered pattern), whereas that of films made of superspreader surfactants shows significant disjoining pressures, more stability with time, and surface activity in the interferometric pattern. This was attributed to the presence of long hanging bilayers attached to the air/water interface [4,10]. These bilayer protrusions were assumed to be in the same size range as the objects observed within the air/water interface of superspreaders by Brewster Angle Microscopy [11,12].

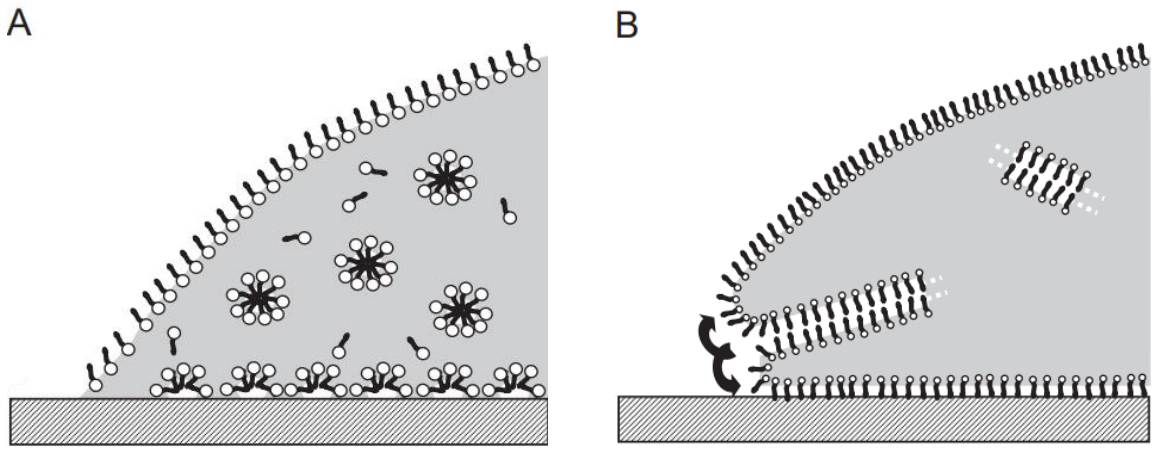

Figure 4. 2. Phase behavior of (A) a non-superspreading surfactant forming micelles and (B) a superspreading surfactant forming an unzippering bilayer. Adapted from Venzmer [4].

Superspreading (and normal spreading) also depends on relative humidity (hence, on evaporation rate). In common laboratory humidity conditions (around 50% relative humidity), final spreading area of liquid drops with 0.1%v/v superspreader surfactants is bigger than the spreading area observed for a solution with a concentration of 0.25%v/v of a non-superspreader surfactant. On the other hand, at 100% relative humidity, the final area is proportional to the amount of surfactant in the droplet. In absence of significant evaporation, i.e., at 100% relative humidity, the final state of superspreading is a thin "water-pancake" with one surfactant monolayer at the air/water, and one at the substrate/water interface [4,13]. Spreading kinetics, in the first few seconds of the spreading process, is almost independent on relative humidity and on surfactant concentration (see **Figure 4. 3**).

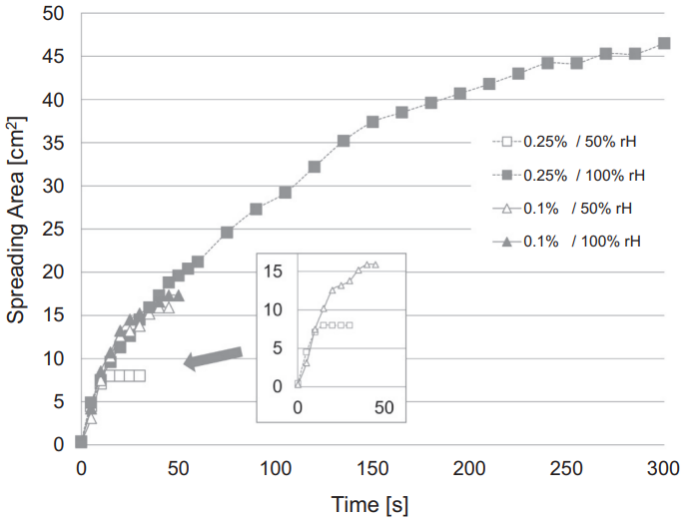

Figure 4. 3. Spreading kinetics of "M(D'E7.5OMe)M" (10 µL on polypropylene film) at different concentrations (0.1 and 0.25%v/v) and relative humidities (50 and 100% rH) [4,14].

The first step of this chapter is the study of the interfacial properties of BREAK-THRU® S240 (superspreader) and BREAK-THRU® S233 (non-superspreader) aqueous solutions at the water-air interface. This includes the evaluation of the equilibrium surface tension and the dilational interfacial rheology of the formed films. It is expected that this information can help on the understanding of the first stages of the spreading process. Dilational interfacial rheology is not expected to have an influence on superspreading, because, at the concentrations at which usually superspreading is observed (> 0.1%), surface tension isotherm already reached a plateau [2], hence Gibbs elasticity is supposed to be zero (this hypothesis will be double checked in the Section 4.3. Results and discussion). Nevertheless, it may have an influence in the kinetics of spreading. In this experimental work, dilational surface rheology was characterized in the frequency range 60–500 Hz by using Electro-Capillary Waves measurements (ECW) technique (see *Chapter II, 2.1.4. Electro-Capillary Waves (ECW)*). In addition, drop impact oscillation dynamics of BREAK-THRU® S240 and S233 sessile drops (at different surfactant concentration in water) on PET substrates will be also analyzed. This phenomenon was studied in previously studied in the literature for other systems [15,16]. In this chapter, the spreading process (i.e., the increase in radius *R(t)* of the sessile drop) and the oscillation of the apex of the drop (point "*P*", **Figure 4. 4**) will be analyzed.

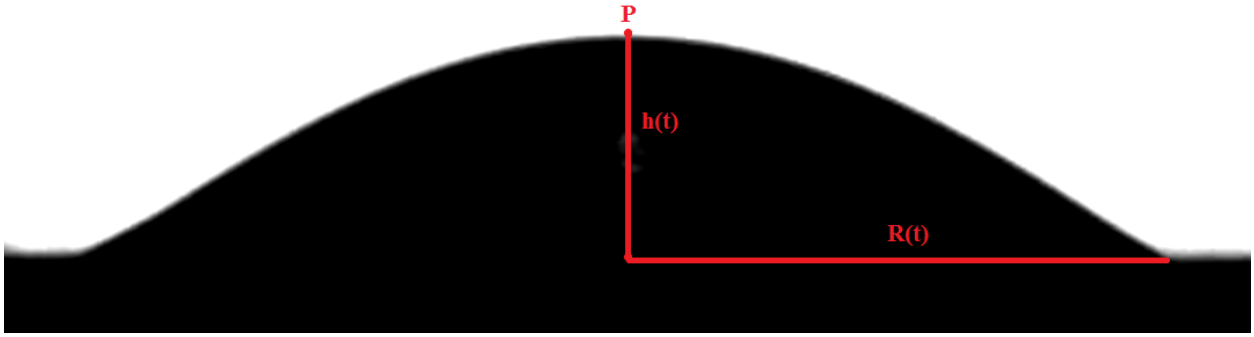

Figure 4. 4. Geometry of a sessile oscillating drop.

The height of an oscillating sessile drop as a function of time $h(t)$ can be expressed according to the following formula [15],

$$h(t) = h_0 + \Delta h e^{-\beta_h t} cos(\omega_h t + \varphi_h), \quad (4.\ 2)$$

where ω_h is the angular frequency of the oscillation around the central value h_0, φ_h is the phase, Δh is the oscillation amplitude. The damping coefficient β_h can be related to ω_h by means of the following relationship,

$$\beta_h = \sqrt{\frac{k}{m} - \omega_h^2}, \quad (4.\ 3)$$

where k is the characteristic spring constant of the system, and m is the mass of the drop. When the effect of gravity is negligible, the capillary frequency of an oscillating sessile drop can be expressed according to the following equation [16],

$$\nu_c = \frac{\omega_c}{2\pi} = \sqrt{\frac{\gamma}{\rho R_0^3}}, \quad (4.\ 4)$$

where γ is the equilibrium surface tension, R_0 is the equilibrium radius, and ρ is the density of the drop fluid. If gravity/inertia effect are negligible, $\omega_h = \omega_c$. The effect of surfactant concentration and type (comparing a superspreader and a non-superspreader surfactants) on the properties of oscillating sessile drops will be investigated, as well as the effect of the advancing three-phases contact line. This study aims at finding a relationship between the oscillation parameters of sessile drops (i.e., β_h and ν_h) and the damping coefficient and the frequency of capillary waves (measured by means of ECW technique). The idea is to understand whether capillary forces prevail on gravitational/inertia ones or vice versa.

4.2. Materials and methods

4.2.1. Chemicals

Two nonionic trisiloxane surfactants were employed. The first one was the superspreader BREAK-THRU® S240, ("M(D'E_6P_3OH)M", M_W: 730 g/mol), and second was the non-superspreader BREAK-THRU® S233 ("M(D'$E_{10}P_2$OH)M", M_W: 850 g/mol), both gifted by Evonik Operations GmbH. All solutions used to perform drop impact and spreading experiments were freshly prepared by dilution of a stock solution of each surfactant in Milli-Q grade water,

shaken by hand and placed in an ultrasonic bath for 10 min. The required quantities of the surfactant were weighted by means of an analytical balance (precision ±0.1 mg).

A transparent polyethylene terephthalate (PET) foil, provided by Evonik Operations GmbH, was used to perform spreading experiments. The foil was cut in smaller pieces, and washed with isopropanol and Milli-Q grade water before its use as surface for spreading experiments. In order to assess substrate homogeneity, the contact angle of water was measured in different points, and estimated to be about 80°.

4.2.2. Experimental methods

The interfacial tension of the air/solution interface was measured by means of a surface force tensiometer (model K10T Digital Tensiometer, KRÜSS GmbH, Hamburg, Germany), fitted with a platinum Wilhelmy plate contact probe of 40.5 mm of perimeter. Each experimental data point was obtained as an average of at least 3 measurements, which were carried out until adsorption equilibrium was reached (i.e., a constant surface tension in time, during at least 10 minutes). Temperature was kept constant at 23.0 °C (with an accuracy of ±0.1 °C), by means of a thermostatic bath.

Dilational interfacial rheology measurements at high frequency (in the range of 60-500 Hz) were performed by using a homemade Electro-Capillary Wave (ECW) device, described elsewhere [17-22] (see *Chapter II*, *2.1.4. Electro-Capillary Waves (ECW)*, for detailed description). Experiments were done at 23 °C (the temperature of the Langmuir Trough was maintained constant by means of a thermostatic bath).

In order to record drop profile evolution in time, a homemade set-up, developed by TU Darmstadt (Darmstadt, Germany) was used [23,24]. The device includes a high-speed camera (Mikrotron MotionBLITZ Cube 4, SVS-Vistek Gmbh, Gilching, Germany) with telecentric optics. This allows recording side view images of the drop, with a frame rate of 1000 Hz (1 captured frame per millisecond). The PET substrate was placed in a chamber, and solution was dispensed by means of a micropipette, with the tip of the pipette placed close to the substrate (at about 1-2 mm). Experiments were done at room temperature, and at ambient relative humidity (about 50%). In order to improve the contrast (therefore, the sharpness of drop profile) a side light was placed in front of the camera. Drop image profiles were analyzed by means of a Matlab code developed by TU Darmstadt (Darmstadt, Germany), that allows obtaining drop radius, contact angle, height of the apex and drop volume.

4.3. Results and discussion

4.3.1. Interfacial tension

The first step of this chapter is focused on the evaluation of the ability to adsorb at the air-water solution of the two surfactants studied: S233 (non-superspreader surfactant) and S240 (superspreader surfactant). For this purpose, equilibrium surface tension measurements have been performed for solutions with different concentrations. According to reference [2], adsorption kinetics of S233 and S240 is very fast at the higher concentrations. In fact, at $C > 5.93 \cdot 10^{-3}\ mM$, adsorption time is always less than 30 min, and even adsorption can occur within few seconds at the highest concentrations. In this work, measurements were performed waiting at least half an hour for samples with $C > 5.93 \cdot 10^{-3}\ mM$. Thus, it was ensured that the adsorption and thermal equilibriums were achieved. On the other hand, for solutions with

concentrations in the range $1.19 \cdot 10^{-3}\ mM - 5.93 \cdot 10^{-3}\ mM$, surface tension measurements were performed after 1 hour. The measurement time was enlarged until 2.5-3 hours for solutions with concentrations in the range $5.93 \cdot 10^{-4}\ mM - 1.19 \cdot 10^{-3}\ mM$, and until 4 hours for solutions with $C < 5.93 \cdot 10^{-4}\ mM$. In all the cases, the achievement of the equilibrium was verified by the absence of surface tension variations higher than 0.1 mN/m during at least 10 minutes. Surface tension measurements were carried out in conjunction with capillary wavelength measurements (see *4.3.2. Capillary Wavelength and* Damping subsection), in order to double check if the equilibrium adsorption was reached (in this case, capillary wavelength should be constant with time).

Figure 4. 5 shows the surface tension isotherms of both S233 and S240 are plotted, as a function of the surfactant bulk concentration. In both cases, the surface tension decreases from a value close to the corresponding to the pristine air-water interface (~72 mN/m) to values slightly above to 20 mN/m as the surfactant concentration increases. The comparison of the isotherms corresponding to both surfactants shows that as expected, the higher hydrophobicity of S240 in relation to S233 leads to prior decrease in the surface tension, reaching the minimum value of the surface tension, corresponding to the critical aggregation concentration (CAC) in the case of S240 for lower concentration that those corresponding to the critical micellar concentration (CMC) of S230. It should be noted that the different definition of the threshold concentration for the formation of supramolecular aggregates in the surfactants considered is due to the differences on the aggregation pattern that they experiment according to the literature [2,4]. It is worth to mention that in the case of the S233 isotherm, the results obtained present a good agreement with those reported in reference [2]. However, this is not the case of the surface tension variation obtained for S240. The results obtained in this chapter for this surfactant, especially those corresponding to the lowest concentrations, appear shifted towards lower values of the concentration in relation to those reported in reference [2]. This apparent discrepancy can be understood considering the different techniques used in both studies. Here, the surface tension isotherm was evaluated by using the Wilhelmy plate method, whereas in the study reported in reference [2], the data were obtained by using a Pendant Drop Tensiometer. These techniques present different surface/volume ratio, which can lead to a depletion phenomenon [25,26]. In fact, in the case of pendant drop tensiometer, the surface/volume ratio is relatively high and the adsorption of the surfactant at the interface can lead to an effective change in the bulk concentration. This leads to a situation in which the adsorbing solution behaves similarly to a solution with lower concentration. This scenario does not apply when techniques such as Wilhelmy plate tensiometer or bubble shape tensiometer are used. In these techniques, the surface/volume ratio is relatively small, and therefore the role of the depletion is almost negligible.

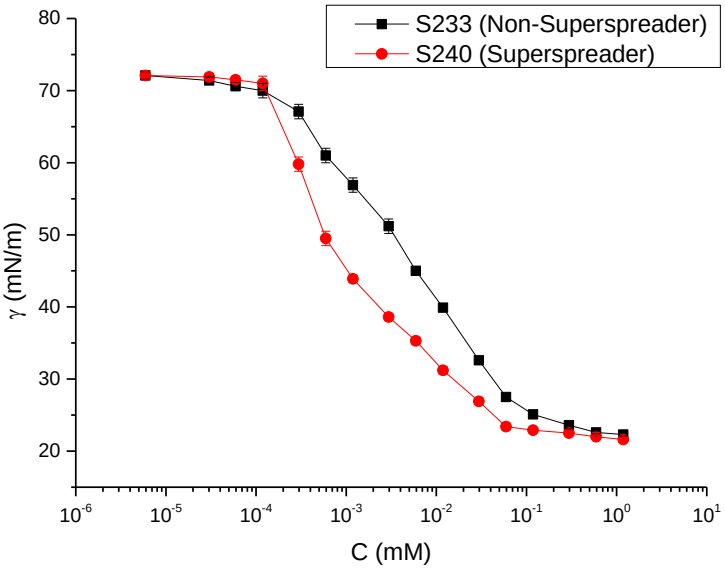

Figure 4. 5. Interfacial tension γ as a function of bulk concentration C, at 23 °C, for Gibbs monolayers of S233 (non-superspreader) and S240 (superspreader) at the liquid/vapor interface.

4.3.2. Capillary Wavelength and Damping

Figure 4. 6 show the plots corresponding to the capillary wavelengths (λ) and damping coefficients (β) as a function of the frequency ν, of both S233 and S240 (at different surfactant concentrations, collected by means of the ECW technique. These data were obtained by obtaining, point by point, the spatial profile of the capillary waves that were fitted according to the following equation that defines the spatial profile of the capillary wave (see *Chapter II*, *2.1.4. Electro-Capillary Waves (ECW)*):

$$u_z(x) = u_z^0 e^{-\beta x} cos\left(\frac{2\pi}{\lambda}x + \varphi\right), \tag{4. 5}$$

where u_z^0 is the wave amplitude at $x = 0$, and φ is the phase lag. β and λ are the damping coefficient and the characteristic wavelength of the capillary wave, respectively.

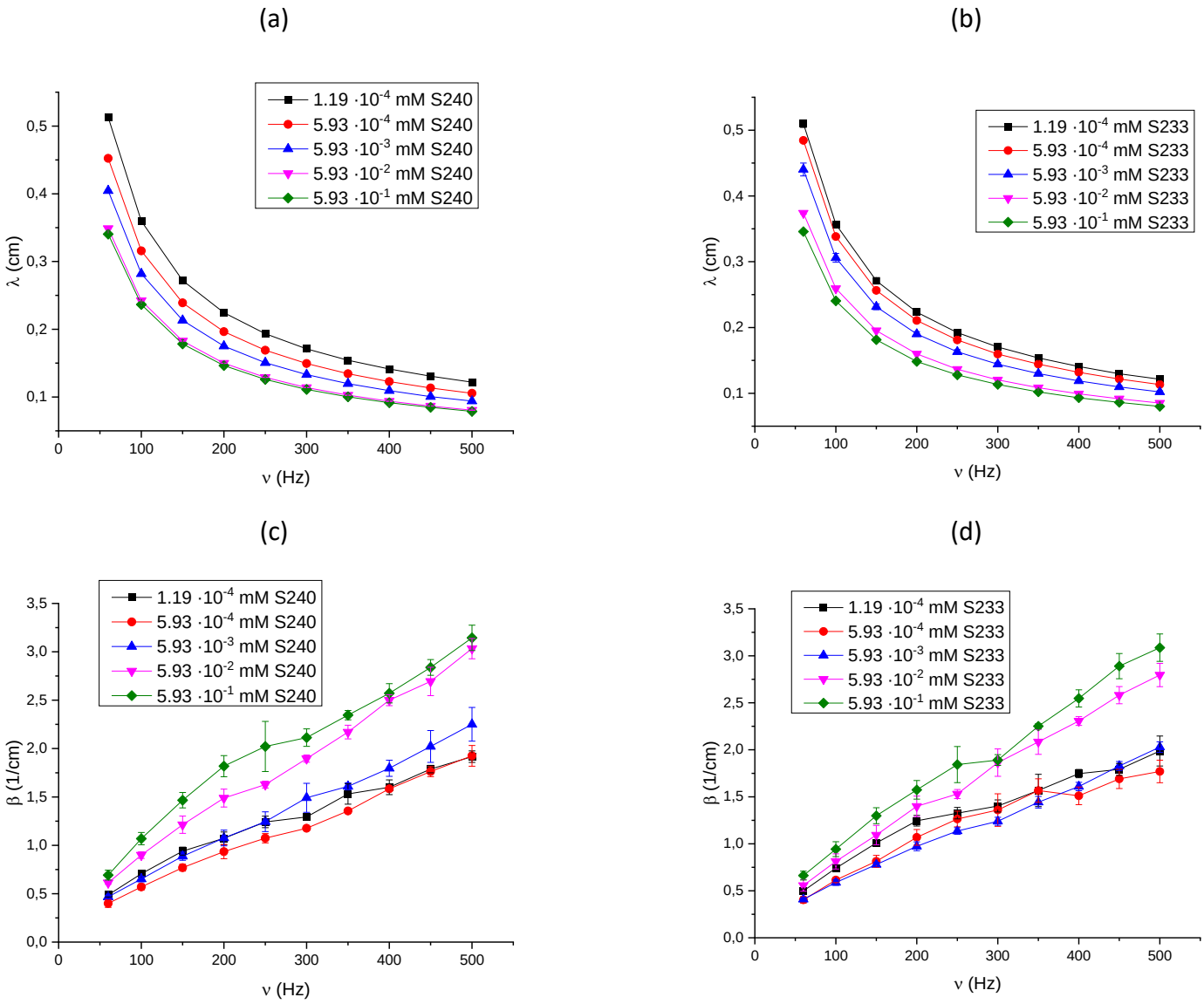

Figure 4. 6. Capillary wavelength (λ) and damping coefficient (β) of S240 (respectively, (a) and (c)) and S233 (respectively, (b) and (d)) as a function of the frequency ν, at different molar concentrations.

The capillary wavelength results reported in **Figure 4. 6** (a-b) align with the surface tension data plotted in **Figure 4. 5**. In fact, as expected, λ (at fixed ν) tends to decrease with surfactant concentration, and the values obtained with S240 seem to be slightly lower than those measured with S233, at the same value of C. This can be understood by considering that for a fixed surfactant concentration, the surface tension for S240 is lower than that corresponding to S233, and therefore the capillary wavelength also assumes lower values. Defining $\omega = 2\pi\nu$ and $k = \frac{2\pi}{\lambda}$, the values of λ versus ν plotted in **Figure 4. 6** (a-b) can be defined in terms of the following scaling-law,

$$\lambda = S\nu^{-n} . \qquad (4.\ 6)$$

If $S = \left(\frac{2\pi\gamma}{\rho}\right)^{\frac{1}{3}}$ (where ρ is the density of the solution, which can be assumed similar to that of the water) and $n = \frac{2}{3}$, equation (4. 6) returns the Kelvin law (see *Chapter II*, *2.1.4. Electro-*

Capillary Waves (ECW)) [27]. The obtained results (see **Figure 4. 6** (a-b)) agrees well with the prediction of the Kelvin law, even though this considers pure liquids, with n assuming a value around 0.68. The values of S depends on concentration, and therefore, on the surface tension. The values of γ obtained by the values of S ($\gamma = \frac{S^3\rho}{2\pi}$) coming from the fitting of the data in **Figure 4. 6** (a-b) with eq. (4. 6) are plotted in **Figure 4. 7**, and they are not strictly the same as the ones reported in **Figure 4. 5**, but they follow the same qualitative trend with respect to the surfactant molar concentration (**Figure 4. 5**). The deviation between the experimental and calculated values can be ascribed to the fact that Kelvin law is obtained for pure liquid interfaces at high values of the capillary number, and the slight change of the real density of the solution in relation to that corresponding to the water with the surfactant concentration.

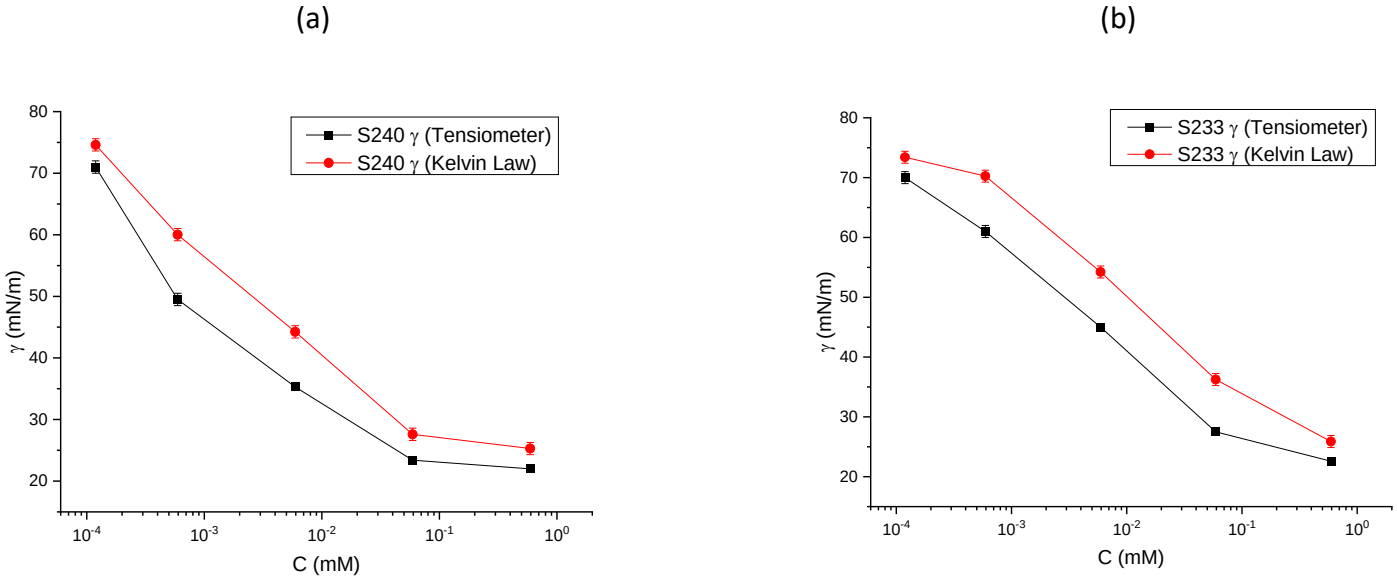

Figure 4. 7. S240 (a) and S233 (b) surface tension experimental data obtained by the tensiometer (replotted from Figure 4. 5) and determined by means of Kelvin law ($\gamma = \frac{S^3\rho}{2\pi}$).

Concerning to the damping coefficient (**Figure 4. 6** (c-d)), no big differences were observed between the values corresponding to S233 and S240. In this case, the bulk viscosity of the solutions of both surfactants are relatively similar. Moreover, in the concentration range analyzed, bulk viscosity is close to the one of pure water. Conversely, in both surfactants, β increases with surfactant concentration, due to the increase in the surface excess concentration. It should be noted that at $C < 5.93 \cdot 10^{-3}\ mM$, the change of the damping coefficient can be considered almost negligible, but as the concentration increases, damping coefficient slightly increases (at fixed ν). As expected, β increases with ν, but, the trend, does not comply with a Stokes-like law that defines $\beta = \frac{4}{3}\frac{\eta}{\gamma}\omega$ (see *Chapter II, 2.1.4. Electro-Capillary Waves (ECW)*) [27]. Nevertheless, the frequency dependence of the damping coefficient can be described by using a modified Stokes-like equation,

$$\beta = P\omega^n\,. \qquad (4.\ 7)$$

The modified Stokes equation gives n values in the range 0.68-0.78, depending on the surfactant considered and the solution concentration. In fact, the increase in the surfactant concentration leads to an increase in n. It should be noted that the discrepancies between the

experimental results and the predictions provided by the Stokes law may be ascribed to the viscoelastic character of the surfactant layers.

4.3.3. ECW Dilational Interfacial Modulus

Based on the data of β and λ as a function of ν plotted in **Figure 4. 6**, and the data of γ reported in **Figure 4. 5**, the dilational interfacial modulus ${E_s}^*(\nu)$ can computed by means of the dispersion equation (previously derived in *Chapter II*, *2.1.4. Electro-Capillary Waves (ECW)*),

$$ {E_s}^*(\nu) = E_s(\nu) + i\omega k_s(\nu) = \frac{\dfrac{-\left(\eta\omega(q-m)\right)^2}{\gamma q^2 + i\eta\omega(q+m) - \dfrac{\rho}{q}\omega^2} - i\eta\omega(q+m)}{q^2}, \tag{4. 8} $$

where ρ and η are, respectively, the density and the viscosity of each surfactant solution, which can be assumed those corresponding to the water at 23°C [28]. q is the complex wavevector, defined as,

$$ q = \frac{2\pi}{\lambda} - i\beta, \tag{4. 9} $$

and *m* is the capillary penetration depth (Re(m) > 0):

$$ m = \sqrt{q^2 + i\omega\frac{\rho}{\eta}}. \tag{4. 10} $$

The results of $E_s(\nu)$ (dilational interfacial elastic modulus) and $k_s(\nu)$ (dilational interfacial viscosity), for both S233 and S240 surfactant, are shown in **Figure 4. 9**. Electrocapillary wave experiments provides information on the elastic and viscous component of the dilational modulus in the frequency range 60-500 Hz. It should be noted that the electrocapillary wave experiments can be performed, even beyond the threshold frequency of 500 Hz. However, no reliable dilational rheology data can be obtained above such threshold due to the strong damping of the capillary waves. This leads to a very fast decay of the spatial profile, which is masked by the noise. This is particularly evident when concentrated surfactant solutions are considered.

The analysis of the dilational rheology data obtained from the analysis of the electrocapillary wave experiments show that whereas the elastic component of the elastic modulus shows measurable values in all the cases, the dilational viscosity can be considered almost negligible, and even under some conditions negative values are obtained. This, a priori, physical unsound results can be considered as a result of the limited precision of the techniques to determine such small values under specific conditions, which can be associated with the fact that under the tested conditions, the systems are far away from the resonance condition, i.e., capillary modes and dilational modes are not coupled (see *Chapter II*, *2.1.4. Electro-Capillary Waves (ECW)*). The resonance condition, according to references [27,29] is fulfilled when $\left(\frac{E_s(\nu)}{\gamma}\right)_R = \left(\frac{q(\nu)\eta^2}{\gamma\rho}\right)^{1/4} \approx 0.10 - 0.15$. **Figure 4. 8** shows for both surfactants, the frequency dependence of the ratio $\frac{E_s}{\gamma}$, showing that only the results corresponding to the lowest probed

concentrations, i.e., $C = 1.19 \cdot 10^{-4}\ mM$ and $C = 5.93\ mM \cdot 10^{-4}$ at the lowest frequencies are close to the resonance condition. In samples with higher concentrations, i.e., lower surface tension), $\frac{E_s(\nu)}{\gamma}$ is above the resonance limit, reaching in the worst situations values in the range 0.4-0.6. This introduces an important uncertainty in the determination of the viscoelastic parameters. As a matter of fact, higher values of the $\frac{E_s(\nu)}{\gamma}$ ratio means that $E_s(\nu)$. is more sensitive to the uncertainty of γ, and therefore a small variation of γ leads to a huge variation of $E_s(\nu)$. As a consequence, also the uncertainty in $k_s(\nu)$ is huge, which may lead to negative values of $k_s(\nu)$, especially if the interface is not particularly viscous (as observed in both S233 and S240).

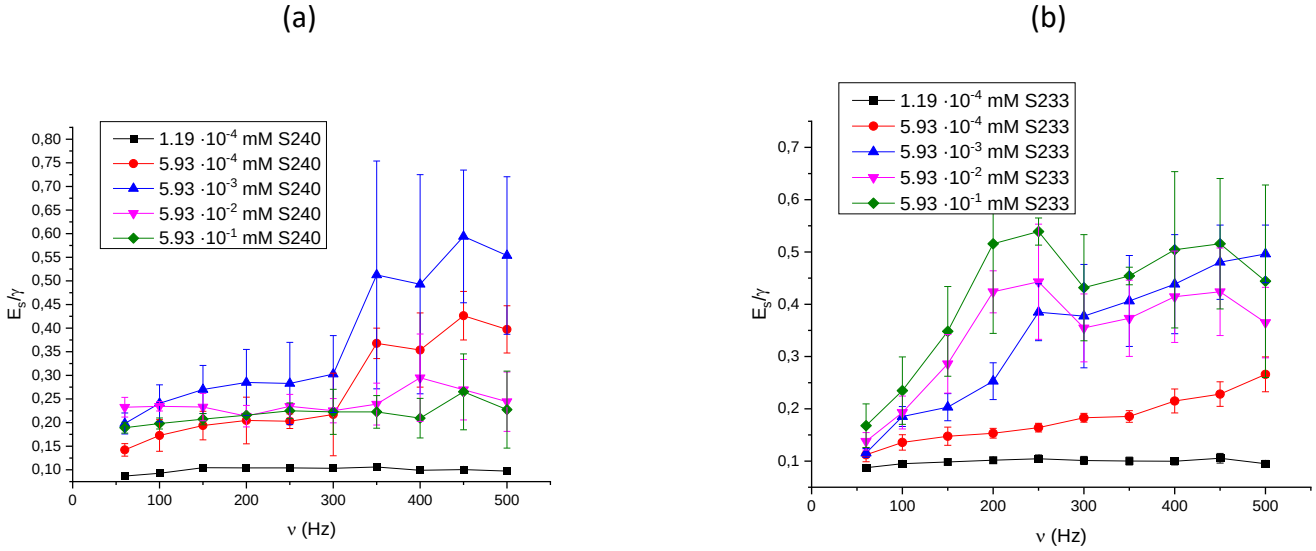

Figure 4. 8. $\frac{E_s}{\gamma}$ ratio, as a function of ν, for S240 (a) and S233 (b) surfactants, at different C.

Considering the challenge related to the determination of the viscoelastic parameters, and in particular the dilational viscosity, the following discussion will be focused on the analysis of the elastic modulus. The results show that in both surfactant the elasticity modulus increase with the concentration, and then decrease again. In fact, within the concentration studies, for both S233 and S240, a maximum of $E_s(\nu)$ is observed at $C = 5.93 \cdot 10^{-3}\ mM$. This is reasonable considering the shape of the surface isotherms of both surfactants. Moreover, the different concentration dependence of the surface tension in both surfactant is also reflected in differences on the dilational modulus. In fact, considering that the concentration dependence of the surface tension is weaker for S233, the difference between the values of $E_s(\nu)$ at different concentrations is less pronounced than the one observed than for S240. On the other hand, for S240, $E_s(\nu)$ at $C = 5.93 \cdot 10^{-3}\ mM$ and at $C = 5.93 \cdot 10^{-4}\ mM$ clearly stand out especially at the highest frequencies probes, while $E_s(\nu)$ values for the rest of concentrations remain very similar one to each other and, simultaneously, they are relatively low. This can be understood considering the region of the surface isotherm to which they belong. In fact, the lowest concentration tested ($C = 1.19 \cdot 10^{-4}\ mM$) correspond to the pseudo-plateau appearing at high surface tension values in the isotherm, and the two highest concentrations are in the plateau of low surfactant tension appearing when C>CAC. Similar discussion can be applied to the results obtained for S233.

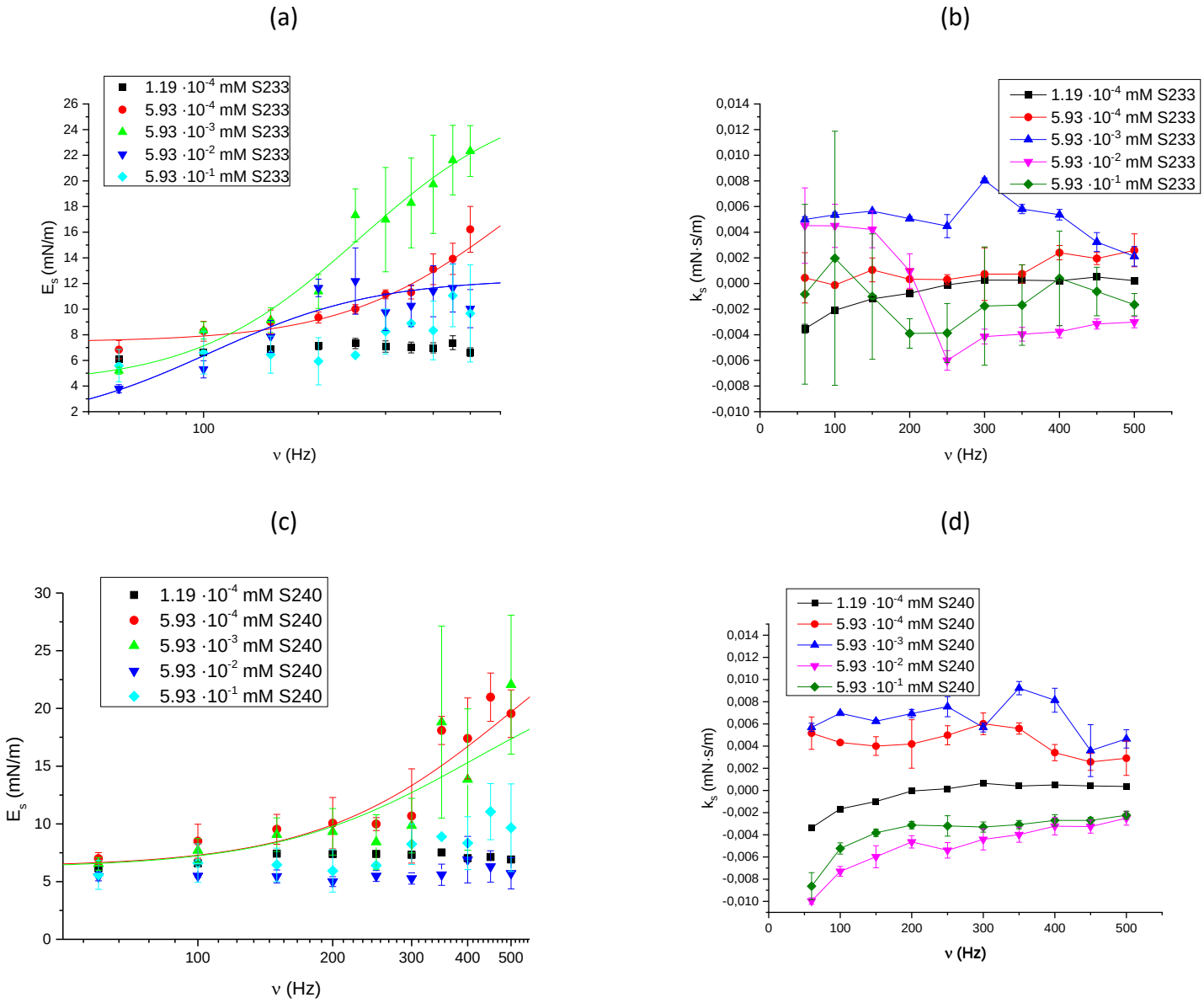

Figure 4. 9. Dilational interfacial elasticity $E_s(\nu)$ and viscosity $k_s(\nu)$ of S233 (respectively, (a) and (b)) and S240 (respectively, (c) and (d)). The symbols correspond to the experimental data and the lines represent the best fit curves to equation 4.11. The color code is the same for experimental data and fitted curves.

Analyzing the frequency dependence of the elastic modulus, it is observed that the for the highest and lowest concentrations probed, there is no dependence of the elastic modulus on the frequency and the elastic modulus remains almost constant with the frequency, which is reasonable considering the above discussion in which the elastic modulus was related to the surface tension isotherm. On the other hand, for intermediate concentrations a relaxation process is observed for both S233 and S240. The observed relaxation process, considering the frequency range probed, may be related to a reorganization occurring within the interface that can be described according to the following equation

$$E = E_s(\nu) + i2\pi\nu k_s(\nu) = E_0 + (E_1 - E_0)\frac{1 + i\chi}{1 + \chi^2}, \qquad (4.\ 11)$$

where E_0 and E_1 are the Gibbs and the high frequency limit elasticities, and $\chi = {\nu_1}/{\nu}$ with ν_1 representing the frequency of the relaxation process. **Table 4. 1** summarizes the limit elasticities values

and the relaxation frequencies obtained from the analysis of the experimental data with the above model. Notice that the absence of a true relaxation for the lowest and the highest concentrations probed makes impossible the use of the above model for the description of the experimental data.

Table 4. 1. Summary of the best fit parameters for the dilational elastic modulus of S240 and S233 using equation 4.11.

10^2·C/mM	S240			S233		
	E_0 (mN/m)	E_1 (mN/m)	ν_1 (Hz)	E_0 (mN/m)	E_1 (mN/m)	ν_1 (Hz)
0.0119	-	-	-	-	-	-
0.0593	7.4±0.4	26±11	626±261	6.3±0.7	26±3	508±35
0.593	4.1±0.4	27±3	256±40	6.2±0.6	25±5	409±64
5.93	1±2	12±1	104±38	-	-	-
59.3	-	-	-	-	-	-

The dependences of the Gibss and high frequency limit elasticities with concentration agree with the above discussion for the concentration dependences of the measured elasticity. In the case of the characteristic frequency of the relaxation process, a decrease of its value is found as the concentration increases. This can be rationalized by considering that the increase of the surface excess hinders the reorganization of the surfactant molecules at the interface, and therefore the characteristic time of the relaxation process increases with concentrations. It should be noted that the dilational responses of S233 and S240 do not show any significant difference.

4.3.4. Drop Equilibration upon deposition on a solid surface

The deposition of a droplet on the surface of a flat substrate follows an equilibration process in which its shape varies until reaching the equilibrium conformation. This process is coupled with the initial stages of the spreading process. The study of the equilibration of a drop deposited on a solid surface can be done in terms of the time evolution of the height of the apex of the deposited drop. It should be note that under the conditions studied, the drop deform as a result of the impact, but its breaking is avoided as a result of the attachment to the solid surface during the whole process, i.e., the drop is directly deposited on the surface of the substrate [30,31].

Figure 4. 10 shows the time evolution of the height $h(t)$ of the apex of the sessile drop.

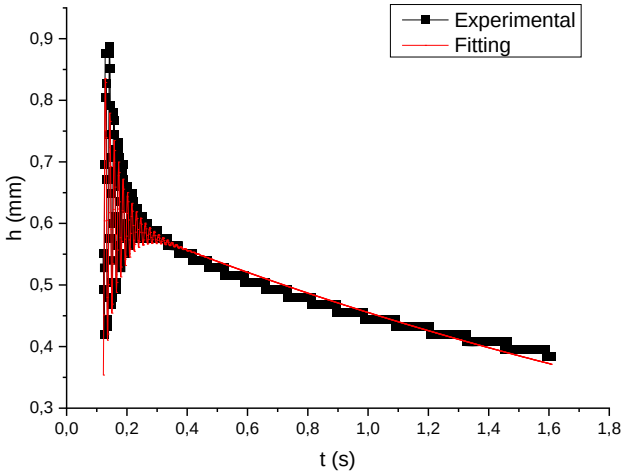

Figure 4. 10. $h(t)$ of a spreading sessile drop: experimental data (black squares) and fitting with eq. (4. 12) (red solid line).

After an initial damped oscillation occurring at constant angular frequency ω_h, and with a certain damping coefficient β_h, as shown in equation (4. 2)), smoothly decays in time at constant decay rate α. α is somehow related to spreading. In fact, the faster the drop spreads on the substrate the higher α. Considering the presence of spreading during the equilibration of the droplet, the equation (4. 2) must include the correction due to the decay of the baseline,

$$h(t) = h_0 e^{-\alpha t} + \Delta h e^{-\beta_h t} cos(\omega_h t + \varphi_h) \qquad (4.\ 12)$$

where h_0 is the initial value of drop apex height, and Δh is the amplitude of the oscillation around the baseline $h_0 e^{-\alpha t}$. The experimental data of the height of the drop can be fitted with equation (4. 12), in order to obtain all of the parameters ($\nu_h = \frac{\omega_h}{2\pi}$, β_h, α). The values of ν_h, β_h, α obtained from the fitting of the experimental decay profiles are plotted versus surfactant concentration (S233 and S240) in **Figure 4. 11**. As will be shown in the next paragraphs, there are several analogies between the capillary wave data of **Figure 4. 6** and the spreading data discussed in *this* subsection.

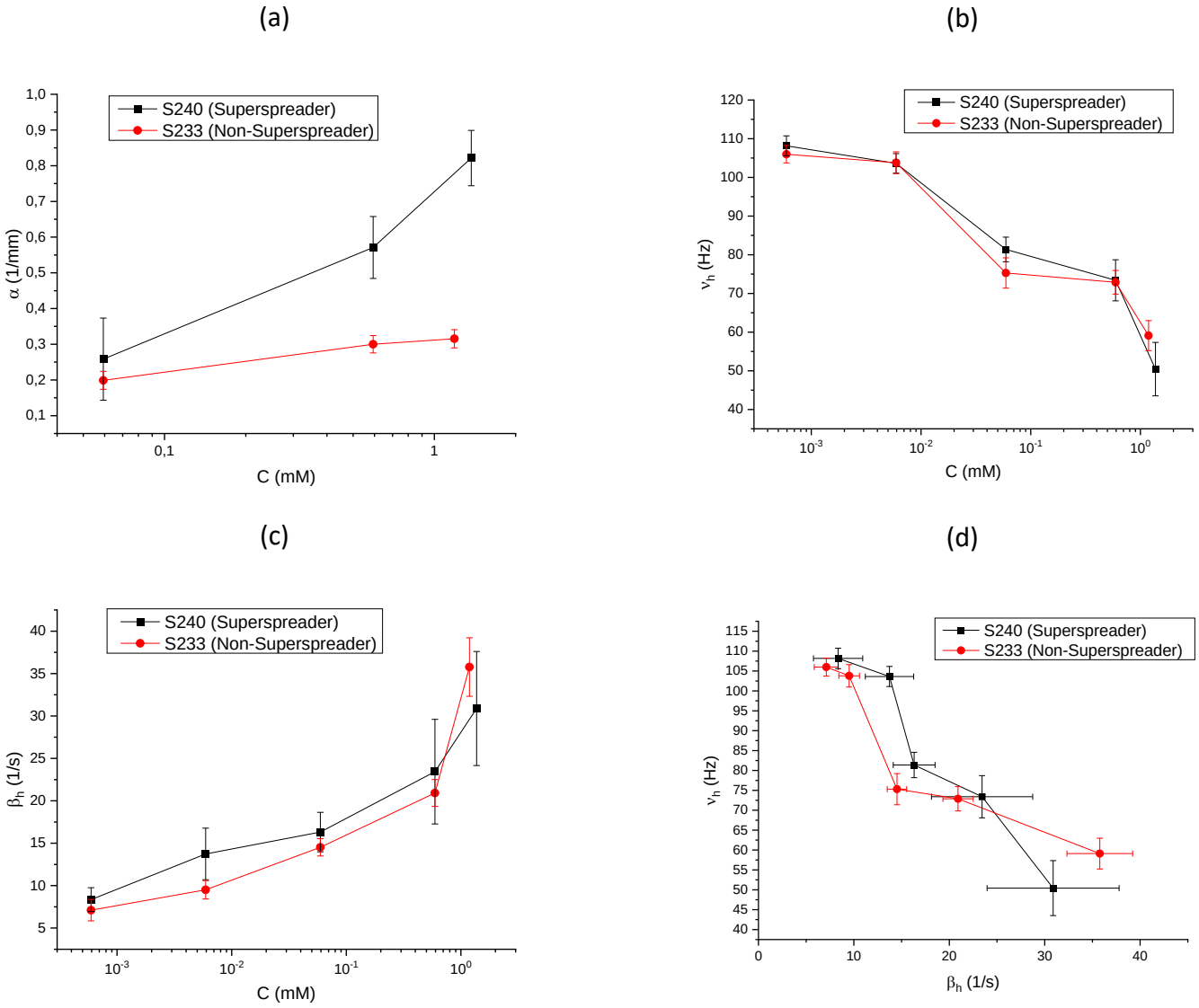

Figure 4. 11. Decay rate α (a), frequency ν_h (b), temporal damping coefficient β_h (c), as a function of surfactant concentration (S233 and S240). (d) ν_h versus β_h of both S233 and S240 surfactant.

The decay rate α is faster as the surfactant concentration increases. This is especially important for the case of S240 surfactant, which present a 4-fold faster reduction of the height of the droplet apex than S233 at the highest surfactant concentration ($C = 1.37\ mM$ or 0.1 %v/v of S240). This can be ascribed to the possible occurrence of superspreading in S240. On the other hand, in S233 surfactant, the increase in the concentration does not lead to any significant change in α. It should be noted that the dependence of α on the surfactant concentration qualitatively resembles to the one observed in **Figure 4. 17** (b) where the spreading rate *V* versus surfactant concentration is displayed. This can be understood by considering that the spreading process is concurrent with the height reduction.

The frequency of drop apex oscillation (ν_h), at different surfactant concentration (S233 and S240) is plotted in **Figure 4. 11** (b), showing that an increase in *C* is associated to a decrease in

ν_h. However, when both surfactants are compared, no huge difference between S233 and S240 were found. On the other hand, the data align with equation (4. 4) which defines the capillary frequency ν_c. Thus, the lower the surface tension and the higher the c the smaller the oscillation frequency. Anyway, as shown in **Figure 4. 12**, $\nu_h$as a function of γ, assumes values that are different to those predicted by eq. (4. 4) for a capillary wave.

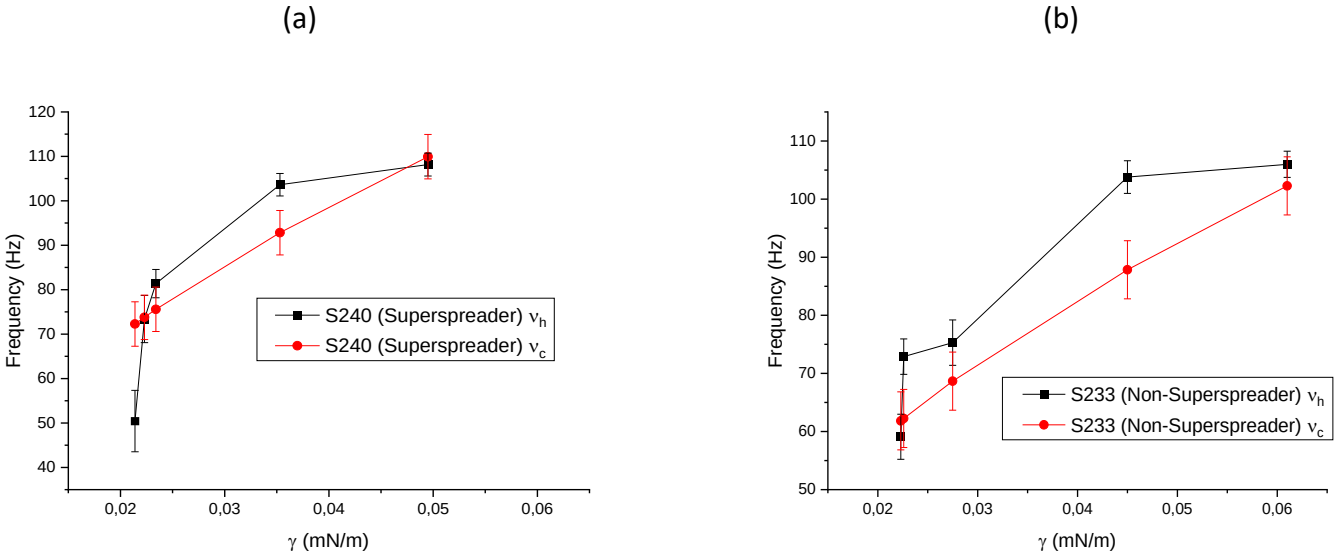

Figure 4. 12. ν_h and ν_c , versus γ, of S240 (a) and S233 (b) surfactant. The values of γ were taken from Figure 4. 5, at the same values of C plotted in Figure 4. 11.

The divergence between ν_h and ν_c may be due to the fact that equation (4. 4) does not consider any spreading phenomenon. In fact, this equation includes the parameter R_0 which accounts for the radius of an equilibrium droplet when spreading process has already finished and radius does not change in time. On the other hand, since the oscillation of the drop mostly occurs at the beginning of the spreading process, ν_c was determined by considering an average value of the initial radius R_0 (see *4.3.5. Spreading experiments and contact angle* subsection). Furthermore, does not consider neither surface tension variation due to drop spreading, nor the effect of surfactant adsorption at both liquid/air and liquid/solid interface. Another issue that needs to be discussed is the fact that the capillary frequency ν_c was determined under the assumption that drop oscillation is mainly ruled by capillary force, which is a reasonable hypothesis, since there is experimental correlation between the values of γ and ν_h. Anyway, this is not enough to prove that the impact of gravity and inertia on the restoring force is negligible, and therefore from the experiments it is not possible to assume that the drop equilibration occurs only mediated by capillary forces.

The capillary wavelength limit (below which gravity effect is negligible) is given by the following equation (see *Chapter II*, *2.1.4. Electro-Capillary Waves (ECW)*) [32],

$$\lambda_{(C)} = 2\pi\sqrt{\frac{\gamma}{g(\rho_1 - \rho_2)}}, \qquad (4.\ 13)$$

where ρ_1 and ρ_2 are, respectively, the densities of surfactant solution and air, and g is earth gravitational acceleration. Depending on the value of γ, $\lambda_{(C)}$ usually ranges between 0.9 cm and 1.6 cm. A larger drop radius means that the wavelength of motion in the droplet is longer

[33]. In an initial approach, it is possible to estimate the drop oscillation wavelength may be given by the initial length of drop profile (when $R(t) = R_0$ and $h(t) = h_0$), which can be calculated by the following elementary geometrical formula:

$$\lambda_G = r\alpha = \frac{R_0\alpha}{\sin\left(\frac{\alpha}{2}\right)}, \tag{4. 14}$$

where $r = \frac{R_0}{\sin\left(\frac{\alpha}{2}\right)}$ is the curvature radius of the drop, and $\alpha = 4\,\mathrm{atan}\left(\frac{h_0}{R_0}\right)$ is the angle that subtends the arch of length λ_G (**Figure 4. 13**). Considering that $R_0 = 1.2 - 2\,mm$ and $h_0 = 0.6 - 1\,mm$, λ_G was estimated to be around 3.5 - 4 mm, which is far below the capillary limit wavelength estimated using equation (4. 13).

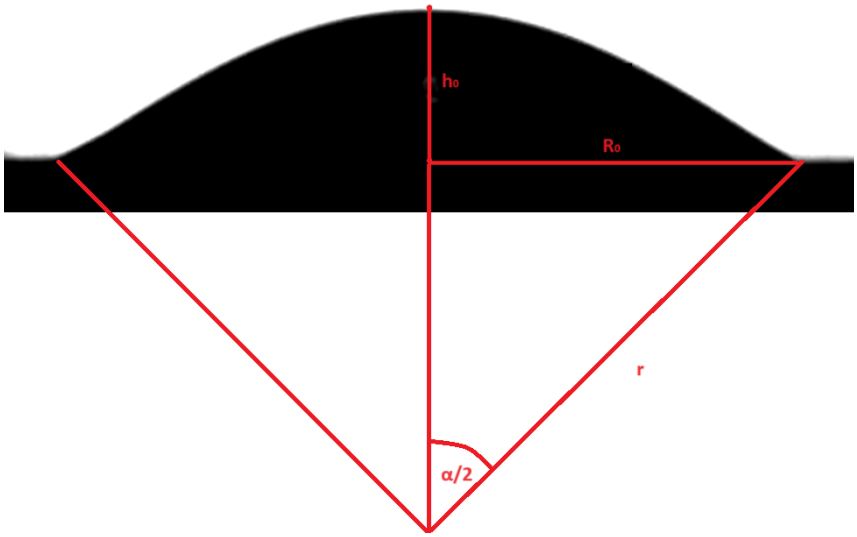

Figure 4. 13. Geometry of the circular cross section of the drop: the angle α subtends the circular arch, and r represents the curvature radius of the drop.

An equivalent capillary wavelength can be also estimated by Kelvin equation (4. 6) where the parameters S and n can be obtained by fitting the data in **Figure 4. 6** (a) and (c) with equation (4. 6) and replacing the data of v_h in **Figure 4. 11** (b):

$$\lambda_k = \left(\frac{2\pi S}{\omega_h}\right)^{1/n} \tag{4. 15}$$

The data of λ_k, for both S233 and S240, as a function of surfactant concentration, are plotted in **Figure 4. 14**.

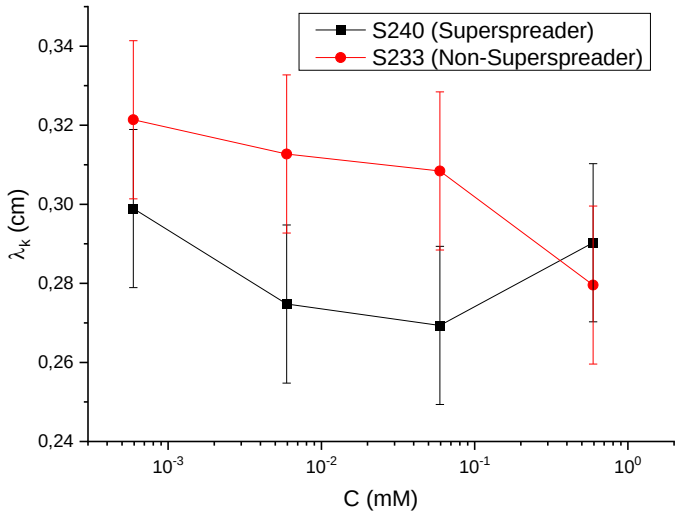

Figure 4. 14. λ_k of both S233 and S240 as a function of C.

Apparently, $\lambda_k$does not seem to be affected by surfactant concentration and type, it seems to be constant (within the error bar). The wavelength is just affected by droplet geometry (radius and height), which, at the beginning of the spreading process, i.e., when the oscillation mostly occurs, does not depend on surfactant concentration. Also, the values of λ_k are below the capillary wavelength limit ($\lambda_{(C)}$), which seems to confirm the hypothesis that capillarity prevails on gravity in drop oscillation. Nevertheless, the value of wavelength predicted by geometric considerations (λ_G) are lower than λ_k. This absence of mismatch may be due to the fact that there is another component, probably the inertia due to drop impact, that may play a key role in drop oscillation. In order to assess the importance of inertia, an additional study should be done, in order to determine drop impact velocity.

The damping coefficient β_h, as shown in **Figure 4. 11** (c), increases with surfactant concentration, independently of the surfactant considered. Moreover, the two surfactants (S233 and S240), present similar values of β_h, within the experimental error bars. This behavior is similar to that observed in **Figure 4. 6** (c) and (d) for the damping coefficient measured by ECW technique. However, it is worth to recall that β_h is a temporal damping, whereas β defines a spatial-damping, and therefore, to performs a homogenous comparison, β_h must be converted to an equivalent spatial-damping coefficient β_{eq}, which can be defined as,

$$\beta_{eq}(\nu_h) = \frac{\beta_h(\nu_h)}{V_g(\nu_h)}, \tag{4. 16}$$

where $V_g(\nu_h)$ is the group velocity determined at frequency ν_h, which can be obtained by fitting the wavelength data plotted in **Figure 4. 6** (a) and (b) with equation (4. 6), and computing the derivative with respect to the wavevector k,

$$V_g(\nu_h) = \frac{d\omega}{dk} = An[k(\nu_h)]^{n-1}, \tag{4. 17}$$

Where $k(\nu_h)$ can be obtained by solving equation (4. 6) with respect to k, and setting $\omega = 2\pi\nu_h$. **Figure 4. 15** shows a comparison between the damping coefficient β determined by ECW and β_{eq} determined by equation (4. 16) as a function of the surfactant concentration. Both coefficients are computed at the value of ν_h associated with a specific value of surfactant concentration (see **Figure 4. 11** (b)). It is worth noting that there are no data of ECW damping coefficient at the set of frequencies ν_h plotted in **Figure 4. 11** (b), but the values of $\beta(\nu_h)$ can be easily obtained by fitting the data in **Figure 4. 6** (b) and (d) with equation (4. 7), and calculating the corresponding values of β at $\nu = \nu_h$.

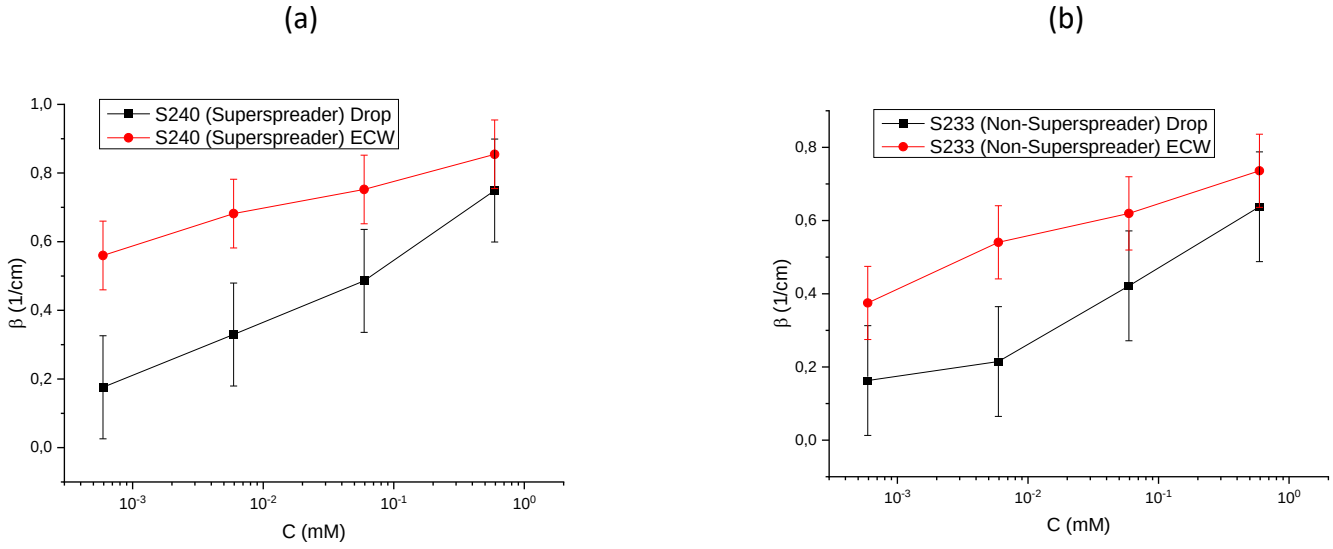

Figure 4. 15. Damping coefficient $\beta(\nu_h)$, determined by ECW, and $\beta_{eq}(\nu_h)$ determined by means of equation (4. 16), versus surfactant concentration C, of both S240 (a) and S233 (b).

As expected, the damping coefficient $\beta(\nu_h)$ obtained by the data of ECW increases with surfactant concentration which aligns to that what was shown in **Figure 4. 6** (b) and (d)). Analogously, $\beta_{eq}(\nu_h)$ also increases with *c*. As expected, no huge difference were observed between the values obtained for the two surfactants. In general, the damping coefficient obtained from ECW data are 2-fold higher than those obtained from the drop experiments, and the differences are reduced as the surfactant concentration. It should be recall that the comparison between the values of damping at different concentrations cannot be done at the same value of frequency, because the frequency itself depends on concentration, and the damping coefficients, either β or β_{eq}, tends to increase by increasing the surfactant concentration, but it is also true that the frequency of oscillation of the drop (ν_h) decreases by increasing concentration, which must be considered. Thus, whereas ECW damping (β) increases with frequency, the damping of the drop oscillation (β_{eq}) has an opposite trend (it decreases with frequency). In fact, according to **Figure 4. 11** (d) the temporal damping β_h is inversely related to ν_h which aligns with the predictions of equation (4. 3). Nevertheless, the plots in **Figure 4. 11** (d) do not fit with equation (4. 3), due to the fact that the values of β_h and ν_h were not determined at the same value of concentration, and the value of the spring constant k may depend on C (possibly, it may be affected by surface elasticity and viscosity, taking into account that equation (4. 3), in principle, it does not consider the viscolaelastic effects of the interface, so the model may be unsatisfactory to describe this particular system). Actually, the values of β_{eq} and β were determined at different conditions. First of all, in

different geometries (β in a planar geometry, and β_{eq} in drop geometry), and second, β was determined at fixed frequency (and the wavelength λ depends on surfactant concentration) while β_{eq} was determined at fixed λ, and their frequency ν_h depends on c. However, the fact that the values of β_{eq} and β are comparable and are in the same order of magnitude, is another hint that suggests that capillarity plays a key role in the damping of oscillating drops.

4.3.5. Spreading experiments and contact angle

The spreading of surfactant droplets is a dynamic process which can be followed through the temporal evolution of drop radius, area or contact angle. In the case considered in this PhD Thesis, the spreading of surfactant drops has been followed by the time evolution of the droplet radius which was observed as a very robust parameter to follow the spreading process. **Figure 4. 16** shows the evolution of drop area with time ($A(t) = \pi[R(t)]^2$) normalized with respect to $A_0 = \pi R_0^2$ (initial area).

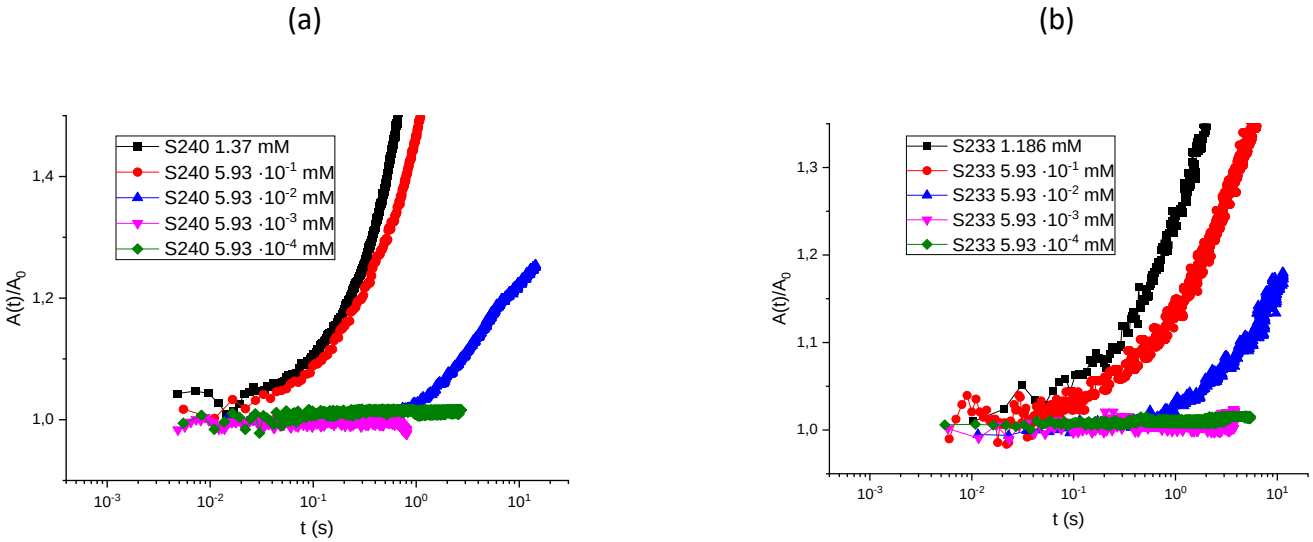

Figure 4. 16. Normalized area $A(t)/A_0$ as a function of time (t), at different surfactant concentrations for S240 (a) and S233 (b).

The results shows than independently of the surfactant concentrations or the surfactant type, spreading proceeds similarly. In fact, in all the studied conditions, it can be assumed that it occurs as a two-step process. During the initial stages of the spreading, it occurs very slowly with the drop area remaining almost unchanged with time during an induction time. This induction time is reduced with the increase of surfactant concentration. This reduction on the induction time is of about 2 orders of magnitude for S233 within the concentration range studied, but it is almost of 3 orders of magnitude for the S240. This may be an indication of the transition from no superspreading-to-superspreading behavior.

A more detailed analysis shows that at $c \leq 5.93 \cdot 10^{-2}\, mM$, the two surfactants behave similarly. Nevertheless, at higher concentration, the area of S240 (superspreader) drops increases faster than S233 ones. In fact, after 1 s the area corresponding to the drops of S240 surfactant of the highest studied concentration is more than 1.4 times the initial value, whereas the area of S233 have not reached $1.2A_0$ yet. It should be note that the value of A_0 (as well as R_0), within the error bar, is not almost affected by surfactant concentration and type, ranging between 1.5 and 2 mm in all the studied cases.

In order to quantify spread rate, data in **Figure 4. 16** were fitted with the following equation [34,35]:

$$\frac{A(t)}{A_0} = 1 + Bt^d. \tag{4. 18}$$

Thus, the spread rate, can be given by,

$$W(t) = \frac{1}{A_0}\frac{d[A(t)]}{dt} = Vt^d \tag{4. 19}$$

The values of $V = Bd$ and d are plotted versus surfactant concentration in **Figure 4. 17**. The superspreader surfactant S240 is characterized by higher spreading rate factor (V) and exponent (d). At S240 concentration of 1.37 mM (0.1% v/v), there is (almost) a linear relationship between $A(t)$ and t: in fact, $d \approx 0.94$, comparable to the value of $d \approx 0.89$ reported in [36] with S240 (1.71 mM) spreading on PVDF substrates. At $C = 5.93 \cdot 10^{-2}\, mM$, the behavior of S233 and S240 is very similar, and corresponds to the one associated to normal spreading. No data of V and d were available at $C < 0.0593\, mM$, because at such low concentrations no spreading was observed within the experimental window, and $\frac{A(t)}{A_0}$ remains close to 1 within the whole experiment (spreading is hindered under such conditions). This negligible spreading at low surfactant concentrations can be understood considering the fact that mass transfer and adsorption kinetics at the interface appears as limiting process in the spreading of surfactant solutions [37].

(a) (b)

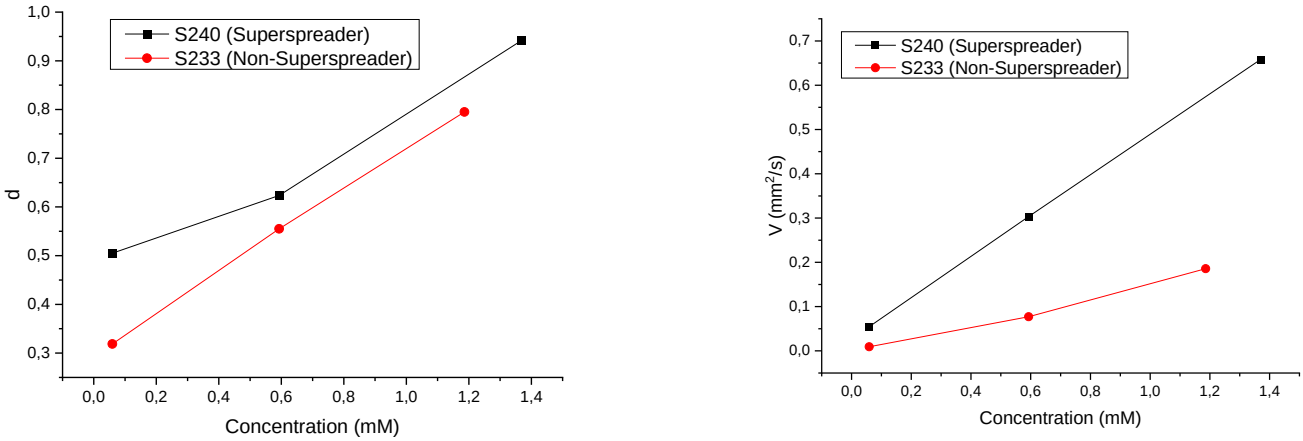

Figure 4. 17. Spreading exponent d (a) and spreading rate factor V (b), as a function of surfactant concentration, for S233 and S240.

The contact angle of S240 and S233 solutions on PET substrates (at the end of the spreading process) is shown in **Figure 4. 18**.

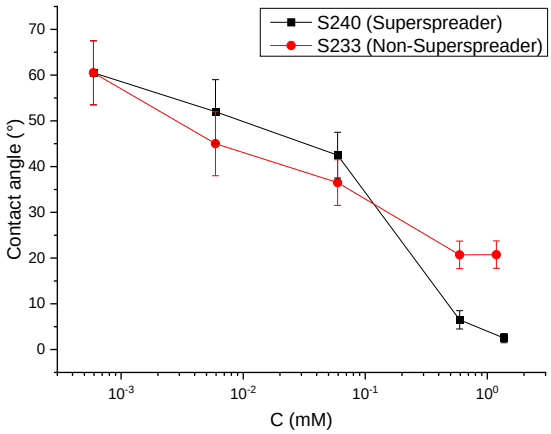

Figure 4. 18. Contact angle on PET, of S233 and S240 solutions, at different concentrations.

The values of $C = 1.37\, mM$ (S240) and C= $1.186\, mM$ (S233) correspond to 0.1% v/v of surfactant in water, which is the concentration at which superspreading is supposed to occur [3,4]. As expected, in both surfactants the contact angle decreases with c. in fact, according to Young equation (see *Chapter II*, 2.3.3. Contact angle and spreading), the wettability (i.e., the cosine of the contact angle θ) decreases with γ_{LV}:

$$\cos(\theta) = \frac{\gamma_{SV} - \gamma_{SL}}{\gamma_{LV}}. \qquad (4.\ 20)$$

However, the superspreader (S240), above the CAC, exhibits a lower contact angle, with respect to S233. On the other hand, below CAC/CMC, the contact angle of S233 and S240, at the same concentration, are very similar.

4.4. Conclusions

The aim of this chapter was to study and compare the interfacial properties (surface tension and dilational interfacial rheology) of a superspreading (S240) and non-superspreading (S233) surfactant, and relate them to spreading kinetics and impact drop oscillation on solid substrates. The experimental results have shown that the surface activity of S240 is higher than that of the S233 surfactant, which is reasonable considering that a high hydrophobicity is essential for superspreading. Nevertheless, the minimum equilibrium surface tension in both surfactants are comparable, and relatively low (around 21 mN/m). The values of capillary wavelength measured by means of ECW technique are coherent with the trend of the surface tension isotherms. The damping coefficient of S233 and S240 are very similar, and both tend to increase by increasing the surfactant concentration.

The dilational surface elastic modulus of S233 and S240, in 60-500 Hz frequency range, follow similar trends with surfactant concentration *C*, with a maximum on E_s appearing at about $C = 5.93 \cdot 10^{-3}\, mM$, independently of the considered surfactant. For the intermediate concentration, a relaxation process was observed within the explored frequency range. This process may be related to the reorganization of the surfactant layer. On the other hand, E_s is almost constant with frequency for the lowest and the highest surfactant concentrations which is compatible with the surface tension isotherm. The dilational interfacial viscosity k_s is very

low in all the cases, and can be considered as almost negligible. The fact that, at most of the surfactant concentrations studied, the resonance frequency is not fulfilled, leads to huge error bars, in both E_s and k_s.

Concerning spreading kinetics, S240, at $C > 5.93 \cdot 10^{-2}\ mM$, spread faster than S233, while, below this threshold, no difference in spreading kinetics was observed. Apparently, there is no direct relationship between spreading kinetics and dilational interfacial rheology: dilational interfacial elasticity shows a peak around $C = 5.93 \cdot 10^{-3}\ mM$, while spreading rate monotonically increases with concentration, hence the two properties do not seem to be straightforwardly related, although it is interesting to notice that superspreading is observed in S240 only when storage dilational modulus vanishes. Similarly to spreading kinetics, the contact angle of S240 on PET, at $C > 5.93 \cdot 10^{-2}\ mM$, is lower than the one of S233 (at fixed *c*), while no difference was detected at lower concentrations.

Drop impact oscillation of S233 and S240 solutions, at different surfactant concentrations, was studied as well, determining the decay rate α, the oscillation frequency ν_h, temporal damping coefficient β_h of drop apex. The decay rate of drop height seems to follow the same trend of spreading rate, as expected. The oscillation frequency ν_h increases with surface tension, despite not following the trend predicted by the equations reported in literature, which may be unsatisfactory to describe the oscillation of spreading drops with surfactant adsorption. The capillary wavelength associated to ν_h, determined by Kelvin equation, seem to be independent on surfactant concentration, and uniquely determined by drop geometry. The temporal damping coefficient β_h increases with surfactant concentration. An equivalent spatial damping coefficient as determined in order to compare the damping of oscillating drop with the one determined by ECW technique: results follow the same qualitative trend, and the values are comparable, despite not being strictly the same. Based on the fact that drop oscillation parameters are comparable to the ones determined by ECW technique, capillarity seems to play a key role in drop oscillation, and it seems to prevail on gravity, although other factors may affect oscillation as well (e.g., inertia).

4.5. References

1. Nikolov, A.; Wasan, D. Superspreading mechanisms: An overview. *The European Physical Journal Special Topics* **2011**, *197*, 325-341, doi:10.1140/epjst/e2011-01476-1.
2. Silva Marques, S.C.; Gambaryan-Roisman, T.; Venzmer, J. Surface tension behavior of superspreading and non-superspreading trisiloxane surfactants. *Colloid and Polymer Science* **2023**, *301*, 739-744, doi:10.1007/s00396-023-05106-0.
3. Venzmer, J. Superspreading — 20 years of physicochemical research. *Current Opinion in Colloid & Interface Science* **2011**, *16*, 335-343, doi:10.1016/j.cocis.2010.11.006.
4. Venzmer, J. Superspreading - Has the mystery been unraveled? *Adv Colloid Interface Sci* **2021**, *288*, 102343, doi:10.1016/j.cis.2020.102343.
5. Bertola, V. The Onset and Early Stages of Dynamic Wetting of Superspreading and Non-Superspreading Trisiloxane Surfactant Solutions on Hydrophobic Surfaces. *Colloids and Interfaces* **2024**, *8*, 5, doi:10.3390/colloids8010005.
6. Tafireyi, W.; Littlewood, M.; Bandulasena, H.C.H.; Trybala, A.; Starov, V.M. Superspreading Surfactant on Hydrophobic Porous Substrates. *Colloids and Interfaces* **2023**, *7*, 38, doi:10.3390/colloids7020038.

7. Ananthapadmanabhan, K.P.; Goddard, E.D.; Chandar, P. A study of the solution, interfacial and wetting properties of silicone surfactants. *Colloids and Surfaces* **1990**, *44*, 281-297, doi:10.1016/0166-6622(90)80202-f.
8. Dong, J.; Mao, G.; Hill, R.M. Nanoscale aggregate structures of trisiloxane surfactants at the solid-liquid interface. *Langmuir* **2004**, *20*, 2695-2700, doi:10.1021/la036059b.
9. Manne, S.; Gaub, H.E. Molecular Organization of Surfactants at Solid-Liquid Interfaces. *Science* **1995**, *270*, 1480-1482, doi:10.1126/science.270.5241.1480.
10. Sett, S.; Sahu, R.P.; Sinha-Ray, S.; Yarin, A.L. Superspreaders versus "cousin" non-superspreaders: disjoining pressure in gravitational film drainage. *Langmuir* **2014**, *30*, 2619-2631, doi:10.1021/la404754d.
11. Ritacco, H.A.; Ortega, F.; Rubio, R.G.; Ivanova, N.; Starov, V.M. Equilibrium and dynamic surface properties of trisiloxane aqueous solutions. *Colloids and Surfaces A: Physicochemical and Engineering Aspects* **2010**, *365*, 199-203, doi:10.1016/j.colsurfa.2010.01.053.
12. Ritacco, H.A.; Fainerman, V.B.; Ortega, F.; Rubio, R.G.; Ivanova, N.; Starov, V.M. Equilibrium and dynamic surface properties of trisiloxane aqueous solutions. Part 2. Theory and comparison with experiment. *Colloids and Surfaces A: Physicochemical and Engineering Aspects* **2010**, *365*, 204-209, doi:10.1016/j.colsurfa.2010.01.052.
13. Zhu, X. Surfactant fluid microstructure and surfactant aided spreading. University of Minnesota, 1992.
14. Venzmer, J.; Wilkowski, S.P. Trisiloxane Surfactants — Mechanisms of Spreading and Wetting. **1998**, 10.1520/stp14161s, 140-151, doi:10.1520/stp14161s.
15. Lin, S.; Zhao, B.; Zou, S.; Guo, J.; Wei, Z.; Chen, L. Impact of viscous droplets on different wettable surfaces: Impact phenomena, the maximum spreading factor, spreading time and post-impact oscillation. *J Colloid Interface Sci* **2018**, *516*, 86-97, doi:10.1016/j.jcis.2017.12.086.
16. Sakakeeny, J.; Ling, Y. Natural oscillations of a sessile drop on flat surfaces with mobile contact lines. *Physical Review Fluids* **2020**, *5*, doi:10.1103/PhysRevFluids.5.123604.
17. Liggieri, L.; Santini, E.; Guzmán, E.; Maestro, A.; Ravera, F. Wide-frequency dilational rheology investigation of mixed silica nanoparticle–CTAB interfacial layers. *Soft Matter* **2011**, *7*, 7699, doi:10.1039/c1sm05257h.
18. Maestro, A.; Ortega, F.; Rubio, R.G.; Rubio, M.A.; Kragel, J.; Miller, R. Rheology of poly(methyl methacrylate) Langmuir monolayers: percolation transition to a soft glasslike system. *J Chem Phys* **2011**, *134*, 104704, doi:10.1063/1.3560612.
19. Monroy, F.; Ortega, F.; Rubio, R.G.; Velarde, M.G. Surface rheology, equilibrium and dynamic features at interfaces, with emphasis on efficient tools for probing polymer dynamics at interfaces. *Adv Colloid Interface Sci* **2007**, *134-135*, 175-189, doi:10.1016/j.cis.2007.04.023.
20. Monroy, F.; Ortega, F.; Rubio, R.G. Dilatational rheology of insoluble polymer monolayers: Poly(vinylacetate). *Physical Review E* **1998**, *58*, 7629-7641, doi:10.1103/PhysRevE.58.7629.
21. Guzmán, E.; Maestro, A.; Carbone, C.; Ortega, F.; Rubio, R.G. Dilational Rheology of Fluid/Fluid Interfaces: Foundations and Tools. *Fluids* **2022**, *7*, 335, doi:10.3390/fluids7100335.
22. Mendoza, A.J.; Guzman, E.; Martinez-Pedrero, F.; Ritacco, H.; Rubio, R.G.; Ortega, F.; Starov, V.M.; Miller, R. Particle laden fluid interfaces: dynamics and interfacial rheology. *Adv Colloid Interface Sci* **2014**, *206*, 303-319, doi:10.1016/j.cis.2013.10.010.

23. Heinz, M.; Stephan, P.; Gambaryan-Roisman, T. Influence of nanofiber coating thickness and drop volume on spreading, imbibition, and evaporation. *Colloids and Surfaces A: Physicochemical and Engineering Aspects* **2021**, *631*, 127450, doi:10.1016/j.colsurfa.2021.127450.
24. Heinz, M.; Chowdhury, I.U.; Stephan, P.; Gambaryan-Roisman, T. Water drops on nanofiber-coated substrates: Influence of wall temperature and coating thickness on hydrodynamics and wall heat flux distribution. *International Journal of Heat and Mass Transfer* **2024**, *222*, 125117, doi:10.1016/j.ijheatmasstransfer.2023.125117.
25. Fainerman, V.B.; Lylyk, S.V.; Aksenenko, E.V.; Makievski, A.V.; Petkov, J.T.; Yorke, J.; Miller, R. Adsorption layer characteristics of Triton surfactants. *Colloids and Surfaces A: Physicochemical and Engineering Aspects* **2009**, *334*, 1-7, doi:10.1016/j.colsurfa.2008.09.015.
26. Llamas, S.; Fernandez-Pena, L.; Akanno, A.; Guzman, E.; Ortega, V.; Ortega, F.; Csaky, A.G.; Campbell, R.A.; Rubio, R.G. Towards understanding the behavior of polyelectrolyte-surfactant mixtures at the water/vapor interface closer to technologically-relevant conditions. *Phys Chem Chem Phys* **2018**, *20*, 1395-1407, doi:10.1039/c7cp05528e.
27. [Langevin, D. *Light Scattering by Liquid Surfaces and Complementary Techniques.* ; CRC Press: New York, US, 1992; Vol. 41.
28. Lide, D.R. *Handbook of Chemistry and Physics: A Ready-Reference Book of Chemical and Physical Data*; CRC Press: Boca Raton, FL, USA, 1998.
29. Maestro Martín, A. Dymanics of interfacial systems. Universidad Complutense de Madrid, 2010.
30. Kovalchuk, N.M.; Simmons, M.J.H. Surfactant-mediated wetting and spreading: Recent advances and applications. *Current Opinion in Colloid & Interface Science* **2021**, *51*, 101375, doi:10.1016/j.cocis.2020.07.004.
31. Yarin, A.L. DROP IMPACT DYNAMICS: Splashing, Spreading, Receding, Bouncing…. *Annual Review of Fluid Mechanics* **2006**, *38*, 159-192, doi:10.1146/annurev.fluid.38.050304.092144.
32. Lamb, H. *Hydrodynamics*; Cambridge University Press: Cambridge, UK, 1994; Vol. 6.
33. Banks, D.; Ajawara, C.; Sanchez, R.; Surti, H.; Aguilar, G. Effects of Liquid and Surface Characteristics on Oscillation Behavior of Droplets Upon Impact. *Atomization and Sprays* **2014**, *24*, 895-913, doi:10.1615/AtomizSpr.2014007590.
34. Kovalchuk, N.M.; Sagisaka, M.; Komiyama, H.; Simmons, M.J.H. Spreading of aqueous surfactant solutions on oil substrates: Superspreaders vs non-superspreaders. *J Colloid Interface Sci* **2024**, *661*, 1046-1059, doi:10.1016/j.jcis.2024.02.031.
35. Tanner, L.H. The spreading of silicone oil drops on horizontal surfaces. *Journal of Physics D: Applied Physics* **1979**, *12*, 1473-1484, doi:10.1088/0022-3727/12/9/009.
36. Kovalchuk, N.M.; Dunn, J.; Davies, J.; Simmons, M.J.H. Superspreading on Hydrophobic Substrates: Effect of Glycerol Additive. *Colloids and Interfaces* **2019**, *3*, 51, doi:10.3390/colloids3020051.
37. Svitova, T.F.; Hill, R.M.; Radke, C.J. Spreading of Aqueous Trisiloxane Surfactant Solutions over Liquid Hydrophobic Substrates. *Langmuir* **2000**, *17*, 335-348, doi:10.1021/la000019f.

Section 3 Interfacial rheology of high ionic strength systems

This section deals with the study of interfacial properties of monolayers onto subphases with high ionic strength. The necessity to obtain a deep understanding of the effect of ionic strength comes from the fact that several studies on dilational surface rheology (by means of oscillating barriers, ECW and SQELS technique), in presence of solutions with high ionic strength, reported non-physical values of dilational moduli (such as negative storage modulus, negative loss modulus…).

- *Chapter V: Ionic strength effect in the equilibrium and rheological behavior of an amphiphilic triblock copolymer at the air/solution interface*

In Chapter V, the impact of NaCl on interfacial tension and dilational surface rheology of Pluronic F-68 (an amphiphilic triblock copolymer) Gibbs monolayers at both low frequency (with oscillating barriers and pendant drop, 10^{-3}-10^{-1} Hz) and high frequency (by means of ECW, 80-400 Hz) was explored, trying assess the impact of ionic strength on their interfacial properties.

- *Chapter VI: Interfacial rheology of PtBA/NaCl solutions Langmuir monolayers*

Chapter VI has a similar purpose to the previous chapter, but in this case, the study is focused on the interfacial properties of a Langmuir monolayer of poly(tert-butylacrylate) (PtBA, a water insoluble polymer) with NaCl content in the aqueous subphase

Chapter V: Ionic strength effect in the equilibrium and rheological behavior of an amphiphilic triblock copolymer at the air/solution interface**

5.1. Introduction

Poly(ethylene oxide)$_n$–b-poly(propylene oxide)$_m$–b-poly(ethylene oxide)$_n$ -or PEO–PPO–PEO- triblock copolymers, commonly referred to as Pluronics, Poloxamers, or Synperionics, are a family of polymeric materials that has gained a lot of attention in both scientific and manufacturing fields. The general molecular structure of Pluronic polymers consists of two lateral blocks of poly(ethylene oxide) and a central one of poly(propylene oxide) (see **Figure 5.1**). The specific molecular weight of each block defines important physico-chemical properties of these polymers, e.g., hydrophilic-lipophilic balance (HLB), critical micellar concentration or their ability to adsorb at fluid interfaces. Moreover, the unique amphiphilic nature of Pluronics allows them to self-assemble into micelles and gels, making them invaluable in formulations requiring precise control over solubility and viscosity. Pluronics also exhibit excellent biocompatibility and thermoresponsive behavior, enabling their use in temperature-sensitive biomedical applications such as targeted cancer therapy and tissue engineering. Furthermore, their ability to stabilize emulsions and enhance the bioavailability of poorly soluble molecules underscores their versatility in food, pharmaceutical and cosmetic industries [1–7]. Most of the above applications derives from their surfactant properties, which enable them to modify surface interactions and stabilize different types of systems, including emulsion droplets, colloidal particles, capsules, or liposomes [8–14]. In addition, their remarkable versatility enhances material properties, including mechanical strength, and biodegradability in various matrices. One of the most fascinating features of Pluronic copolymers is their capacity to reduce protein adsorption on solid surfaces. This has significant implications, notably in biomedical applications where avoiding undesired specific protein adsorption (biofouling) is critical for implantable devices, biosensors, and drug delivery systems [15,16].

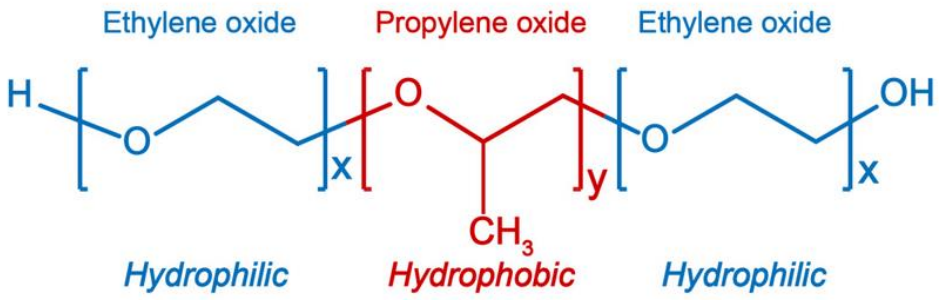

Figure 5.1. General molecular structure of Poly(ethylene oxide)n–b-poly(propylene oxide)m–b-poly(ethylene oxide)n triblock copolymers. x and y indicate the number of monomers of each type of block, and it may have a broad range of values.

To date, several studies have provided comprehensive insights into the intricate phase behavior of Pluronic solutions [17–20]. These studies have outlined the rich phase diagram

** This chapter is in part included in the publication: Carbone, C.; Guzmán, E.; Maldonado-Valderrama, J.; Rubio, R.G.; Ortega, F. Ionic Strength Effect in the Equilibrium and Rheological Behavior of an Amphiphilic Triblock Copolymer at the Air/Solution Interface. *Colloids Interfaces* **2024**, *8*, 16. https://doi.org/10.3390/colloids8020016

exhibited by these systems. In fact, Pluronic solutions can lead to a wide range of phases including isotropic liquid solutions, spherical, and rod-like micellar aggregates, as well as lamellar and gel phases [21–23]. It is worth noting that the addition of salt, which increases the ionic strength of the solution, does not impact the fundamental structure of the phase diagram. In fact, it remains qualitatively unaltered, providing a consistent framework under different conditions. However, the introduction of salts modifies the specific area occupied by each phase within the system [19,23–25]. For instance, the addition of salts can reduce the solubility of Pluronic molecules in water and disrupt the micellar structure [26]. These modifications, intricately linked to the Hofmeister series but also to the specific ratio between the number of monomers in the poly(ethylene oxide) and poly(propylene oxide) blocks, establish a relationship between the behavior of ions as promoters or disruptors of water structure, depending on their ability to remain hydrated [25,27,28]. Such intricate correlations between ionic properties and phase changes within Pluronic solutions continue to foster further investigations to unravel the underlying mechanisms governing these complex systems [26,27,29]. This has revealed that some ions can interact with the polymer chains in a very specific way leading to a behavior that cannot be explained based on the Hofmeister series [30,31]. In fact, several studies have suggested that ions act only locally on the water structure [32–34].

Many of the applications of Pluronics involve complex mixtures containing salts, e.g., those in biological systems, in some cases at non-negligible concentrations, and rely on the ability of this type of copolymer to adsorb at fluid/fluid interfaces. Understanding the effect of salts on the interfacial behavior of Pluronic solutions is therefore essential to exploit the full potential of this family of polymers [3,35,36]. However, to date, the effect of salt on the formation of Pluronic layers at the air/solution interface, and the properties of such layers, remain almost unexplored, and only a few works can be found in the literature [37–39]. These works suggest that the effect of salts in Pluronic-laden interfaces responds to a complex interplay between the modification of the water structure at the copolymer/water interface, and the adsorption of ions on the hydrophobic part of the copolymer. This has a dramatic effect on the interfacial properties with respect to salt-free solutions [39–43].

In a previous work [39], it was shown that the effect of Li^+ ions on the air/solution interface when Pluronic layers are present does not follow the Hofmeister series due to the specific interaction of the lithium cations with the ether groups of PEO. In fact, the polydentate character of PEO allows the coordination of Li^+ ions trough the oxygen [44,45]. This does not occur with other cations such as Na^+ and K^+, which have a direct interaction with the ether group of PEO blocks but no evidences of a true coordination are reported [46]. Therefore, the work by Llamas et al. [39] cannot be used to shed light on the effect of the ionic strength alone. It is expected that the ionic strength will modify the solubility of Pluronic in the subphase, thus changing the formation of loops and tails in relation to what happens in pure water [47]. This phenomenon was also observed in insoluble polystyrene-PEO-polystyrene monolayers [43].

This chapter aims to investigate the influence of an inert salt (NaCl) on the equilibrium interfacial tension and the dilatational modulus of Pluronic F68 copolymer, a Pluronic copolymer with two lateral blocks of poly(ethylene oxide) formed by 76 monomers (3.35 kDa) and a central block of poly(propylene oxide) composed of 29 monomers (1.7 kDa). For aim of

this study, interfacial tension measurements and rheological measurements in two different frequency ranges obtained by combining the oscillatory barrier/droplet method and electrocapillary wave measurements with an appropriate theoretical background were applied. This allows one to elucidate the role of salt in the interfacial behavior of Pluronic F-68 laden interfaces as well as to point out some of the technical and theoretical limitations for obtaining reliable dilational rheological data at high frequencies (in the range 50 Hz-1 kHz) using electrocapillary wave measurements.

5.2. Materials and methods

5.2.1. Chemicals

Pluronic F68, with an average molecular weight of 8.4 kDa, and NaCl with purity >99.9 % were supplied by Sigma-Aldrich (Saint Louis, MO, USA). Ultrapure deionized water of Milli-Q grade, with a resistivity higher than 18 MΩ·cm and a total organic content (TOC) of less than 6 ppm, was used for all experiments and material cleaning purposes. To achieve this level of purity, AquaMAX™-Ultra 370 Series multi-cartridge purification system (Young Lin Instrument Co., Ltd., Gyeonggi-do, Republic of Korea) was used. All solutions were prepared by weight using an analytical balance accurate to ±0.01 mg. Throughout the experiments, temperature was maintained at 23.0ºC with an accuracy of ±0.1 °C.

5.2.3. Experimental methods

The interfacial tension of the air/solution interface was measured by using two different surface force tensiometers and a drop shape tensiometer. The measurements obtained with each tensiometer showed good agreement within the combined error bar (approximately ± 1 mN/m). For all the measurements, the temperature was controlled by using a thermostatic bath set at 23ºC. Each experimental data point reported was an average of at least three independent measurements. The experiments were conducted for a long enough time to ensure that a steady state interfacial coverage was reached.

A surface force tensiometer model K10T Digital Tensiometer (KRÜSS GmbH, Hamburg, Germany) fitted with a platinum Wilhelmy plate contact probe of 40.5 mm of perimeter was used to measure the interfacial tension. Between each measurement, the platinum plate was cleansed using ethanol and Milli-Q water and then flared with an ethanol torch to eliminate any remaining residue of organic matter. For the measurements, the samples were poured into a glass cell, previously cleaned with ethanol and Milli-Q water. Additionally, surface force tensiometer NIMA PS4 manufactured by Nima Technology (Coventry, UK) fitted with disposable Wilhelmy paper plates (Whatman CHR1 chromatography paper, Merck, Darmstadt) of 20.6 mm of perimeter was used for interfacial tension measurements. A fresh paper plate was used for each measurement to prevent any potential modifications on the plate surface as a result of the material adsorption during previous experiments. The same glass cells used for the measurements obtained using the surface force tensiometer KRÜSS K10T Digital Tensiometer (KRÜSS GmbH, Hamburg, Germany) were used in this case.

The interfacial tension of the air/solution interface was also measured by using a pendant drop tensiometer designed and fabricated by the University of Granada. This device is based on the Axisymmetric Drop Shape Analysis (ADSA) method, which is described in detail elsewhere [48]. The setup, including the image capturing, the microinjector, the ADSA algorithm, and the fuzzy

pressure control, is managed by a Windows-integrated program (DINATEN(R)) [49]. For the experiments, a solution microdroplet (15 µL) is formed at the tip of a PTFE capillary (0.2 cm) introduced in a thermostatized glass cuvette (Hellma GmbH & Co. KG, Müllheim, Germany). This leads to experiments characterized by a Worthington number, Wo, above 0.4, which guarantees a good precision of the experimental results [50].

Three different experimental techniques have been used to study the dilational rheological response of the Gibbs monolayers of the Pluronic F-68 in two different frequency (ν) ranges. In the low-frequency range (10^{-3}-10^{-1} Hz), two different techniques were used: (i) oscillating barrier measurements in a Langmuir balance (model 702 from Nima Technology, Coventry, UK) with a total area of 700 cm^2 (70 cm length x 10 cm width), and (ii) oscillating drop measurements, using a deformation amplitude of 8%, in the same pendant drop tensiometer used for equilibrium interfacial tension measurements. For obtaining data on the dilational response at higher frequencies (in the range of 10-10^3 Hz) a homemade electrocapillary wave device was used [51,52]. In order to minimize the effect of shear on the results obtained using the oscillatory barrier method, the experiments were carried out using a relatively small deformation amplitude (5%). In addition, the paper Wilhelmy plate was placed parallel to the barrier movement in the center of the trough and the barrier oscillations were performed far enough from the contact probe to avoid any possible role of unintended flows in the dilation response.

The three techniques and the methods for calculating E_s from the raw data have already been described in detail previously [53–56]. It should be noted that the imaginary component of the dynamic interfacial modulus (E_i) related to the viscous loss (loss modulus) remained below 5% of the real component or storage modulus (E_s) in all measurements. As a result, the detailed discussion of the imaginary part provides limited insight into the clarity of the results included in this chapter and is therefore not discussed here. It is worth noting that the low values obtained for the loss modulus in this study agree with previous results for adsorption layers formed by different copolymers of the Pluronic family at fluid interfaces [42,57].

A capillary-based method (Ubbelohde viscometer) was used to measure the bulk viscosity of the samples. The liquid was introduced into a glass viscometer thermostatized at 23ºC, pumped up through a capillary and a measuring bulb and the time taken for the liquid to fall through the bulb was recorded. The viscometer was calibrated against filtered Milli-Q water and each sample was filtered before entering the viscometer. The determination of viscosity is based on the assumption that the flow time is directly proportional to the viscosity and inversely proportional to the density of the solution (see *Chapter II*, 2.2.1. Capillary Viscometers).

5.3. Results and discussion

5.3.1. Bulk viscosity, density and interfacial tension of salty aqueous solutions

The determination of the viscosity and density of aqueous solutions of surface-active molecules is essential for an accurate evaluation of the high-frequency dilational rheological data obtained from electrocapillary wave experiments. In the context, **Table 5.1** reports the salt concentration dependence of the bulk viscosity, η, obtained using a capillary viscometer

(Ubbelohde) together with the bibliographic densities ρ [69] and interfacial tensions [70] for NaCl aqueous solutions.

It should be noted that the addition of Pluronic F-68 to salty water does not provoke any significant modification in the bulk viscosity in relation to that of NaCl aqueous solution. For instance, the bulk viscosity of a solution of Pluronic F-68 with concentration 10^{-1} mM and a NaCl concentration of 3 M was about 1.3 mPa·s, which is equivalent to that obtained for the NaCl solution of the same concentration. In the case of the density, it is not expected a strong change on the density in relation to the NaCl solution for the diluted solutions studied in this chapter (Pluronic F-68 bulk density assumes a value of about 1.06 g/cm^3). This is the reason why, to solve equation (5.4), the data of η and ρ can be taken from **Table 5.1** and combined with the experimentally obtained interfacial tension values (see the following sub-section).

Table 5.1. Viscosity η and density ρ of NaCl aqueous solutions at 23ºC.

NaCl [M]	η (mPa·s)	ρ (g/cm^3) (*)	γ (mN/m)(**)
0	0.90±0.03	0.998	72.72
0.1	0.91±0.03	1.002	-
1	1.05±0.03	1.038	73.77
2	1.15±0.03	1.075	74.94
3	1.30±0.03	1.111	76.61

(*) Density data taken from reference [69]. (**) Surface tension data taken from reference [70].

5.3.2. Interfacial tension

Figure 5.2 shows the interfacial tension (γ) isotherm for the Gibbs monolayers obtained by the adsorption of aqueous solutions of Pluronic F-68 (ionic strength 0 mM) at 23 °C to the air/solution interface. The results show that after the initial sharp decrease in interfacial tension with Pluronic F-68 concentration (*c*), from values close to those corresponding to the pristine air/water interface (around 72 mN/m), the interfacial tension isotherm enters a less steep reduction region, commonly defined as a pseudo-plateau, for concentrations in the range 10^{-4}-10^{-2} mM, this can be seen more clearly in the surface pressure representation (see inset in **Figure 5.2**). The existence of such pseudo-plateau has been observed in previous studies of the adsorption of Pluronic F-68 at the air/solution interface, and it is commonly ascribed to the transition from a dilute interfacial layer to a brush organization of the Pluronic F-68 at the interface [39,53,58]. Once the pseudo-plateau region is overcome, the interfacial tension starts to decrease again with the Pluronic F-68 concentration. It is worth noting that in the present study, the investigated concentration range remains below the critical micelle concentration (CMC) of Pluronic F-68 (around 10 mM) [59,60] in agreement with the continues decrease of interfacial tension recorded. It should be noted that for the investigated region, the interfacial tension values obtained are in agreement with the interfacial tension isotherms reported in the literature for the same copolymer under similar conditions [39,61].

Figure 5.3 shows a sketch of the different configurations of Pluronic F-68 at the air/solution interface as a function of interfacial density. At high interfacial tensions, corresponding to high surface pressures and low surface excesses, the chains are placed at the interface forming a

layer of 2D stretched chains. Then, for intermediate interfacial tensions, corresponding to the pseudo-plateau of the isotherm, the copolymer molecules start to reorganize at the interface and undergo stretching into the aqueous phase. Finally, at the lowest values of surface tension, most of the copolymer molecules adopt a brush organization to form a 3D structure [57].

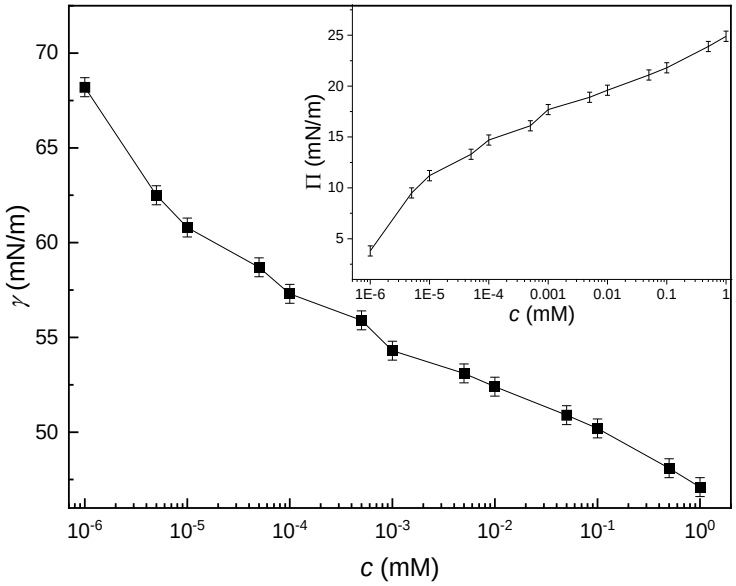

Figure 5.2. Interfacial tension as a function of the Pluronic F-68 concentration (c), at 23 °C, for Gibbs monolayers of Pluronic F-68 at the air/solution interface. Inset correspond to interfacial pressure ($\Pi = \gamma_0 - \gamma$), where γ_0 is the pure water surface tension at the same temperature vs. Pluronic F-68 concentration. The line is a guide by the eyes.

Considering that the main aim of this work is to elucidate how the change in the ionic strength (*I*) of the solution by the addition of NaCl affects the equilibrium properties and dilational rheological response of Gibbs monolayers of Pluronic F-68, interfacial tension measurements were performed for solutions with different copolymer concentration by varying *I*, which is equivalent to vary the NaCl concentration. **Figure 5.4** shows the dependence of the interfacial tension on the ionic strength of the solution for the adsorption of Pluronic F-68 with different copolymer concentrations at the air/aqueous solution interface. The results show that an increase in ionic strength produces a very marked decrease in surface tension, compared to the Gibbs monolayers in absence of salt. This is exactly the opposite behavior to that expected for the change in interfacial tension at the air/water interface due to salt addition (see ref. [70] and **Table 5.2**). However, this is not an unexpected result, as previous studies with different copolymers belonging to the Pluronic family have shown that the addition of electrolytes to Pluronic solutions induces a salting-out phenomenon, which enhances the surface activity of the copolymer, and thus leads to a strong decrease in the interfacial tension [19,39]. This can be understood by considering that the electrolytes disrupt favorable hydrogen bond interactions between PEO block and water, leading to a dehydration of the hydrophilic blocks, which in turn results in an increase in the hydrophobicity of the copolymer and enhances their adsorption efficiency to the air/solution interface.

A detailed analysis of the dependence of the interfacial tension on the ionic strength points out that the salting-out produced by NaCl addition is almost negligible for low salt concentration, independently of the copolymer concentration. However, when *I* reached values ≥ 1M, the presence of the electrolyte leads to a significant enhancement of the surface

activity of Pluronic F-68, corresponding to an increase in copolymer surface excess, and the higher the copolymer concentration, the greater the effect. It is worth noting that the observed effect of ionic strength is only evidenced for NaCl concentrations above those typically studied in most of the work in the literature. This pronounced enhancement at higher ionic strengths suggests that the electrolyte-induced changes in the interfacial properties of Pluronic F-68 are likely related to alterations in the molecular conformations of the copolymer and interactions at the interface. This underscores the importance of considering electrolyte concentration in applications and studies involving copolymer-surfactant systems, as it can significantly influence their interfacial behavior and performance in various applications.

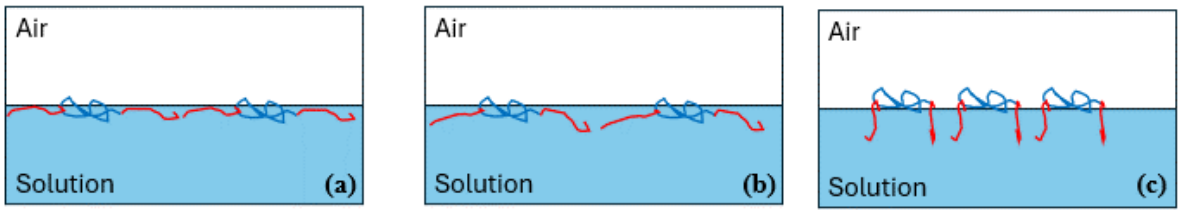

Figure 5.3. Sketch of the different conformation of Pluronic F-68 at the air/solution interface. (a) High interfacial tension values. (c) Intermediate interfacial tension values (pseudo-plateau region). (c) Low interfacial tension values. The central poly(propylene oxide) blocks are indicated in blue and the lateral poly(ethylene oxide) blocks are represented in red.

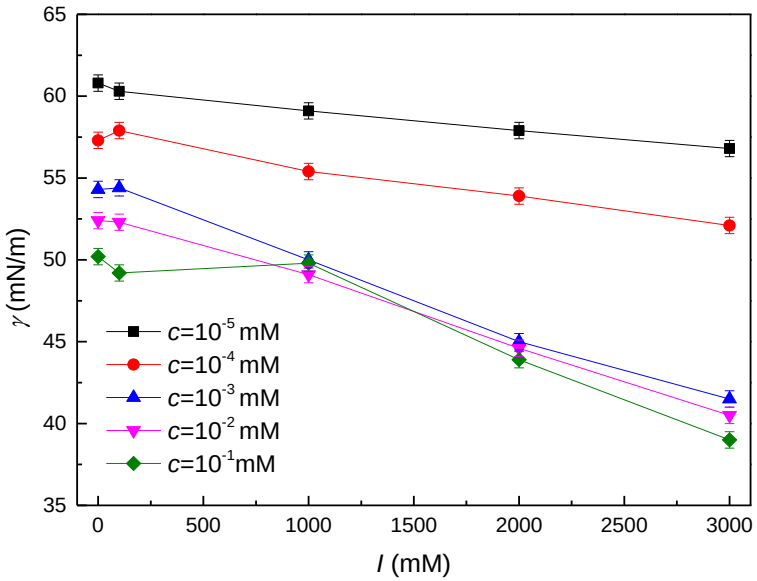

Figure 5.4. Ionic strength (I) dependence of the interfacial tension (γ) at 23 °C for the adsorption of Pluronic F-68 solutions of different concentrations at the air/solution interface. The symbols correspond to the experimental data, and the lines are guides by the eyes.

5.3.3. Low-frequency dilational rheology

The first step in the evaluation of the interfacial response against dilational deformations was carried out at low frequencies (in the range of 10^{-3}-10^{-1} Hz). Thus, it is possible to evaluate the slow relaxation processes that can occurs at the interface upon a dilational deformation. For this purpose, oscillatory barrier and oscillatory droplet experiments were performed. The results obtained by both techniques show good agreement within the combined error bars (see **Figure 5.5** (a)). The observed consistency between the two experimental techniques underscores the reliability of the data, and allows deepening into the viscoelastic behavior of the interfacial layer. **Figure 5.5** (b) and (c) shows the frequency dependences of the dilational storage modulus obtained for Gibbs monolayers of Pluronic F-68 at different ionic strengths.

The analysis of the frequency-dependence of the dilational storage modulus allows one to identify specific trends or anomalies in the behavior that can provide information about the role of electrolytes in modifying interfacial properties.

The obtained results evidence, independently of the Pluronic F-68 concentration and the ionic strength, a similar qualitative behavior characterized by the increase of the dilational storage modulus with the deformation frequency. This frequency dependence suggests the existence of a relaxation process for a frequency around 10^{-2}-10^{-1} Hz which agrees with previous results by Rivillon et al. [43] for Gibbs monolayers of different Pluronic copolymers, and other similar systems. The emergence of this relaxation process can be ascribed to the diffusion process of the Pluronic F-68 from the bulk to the interface.

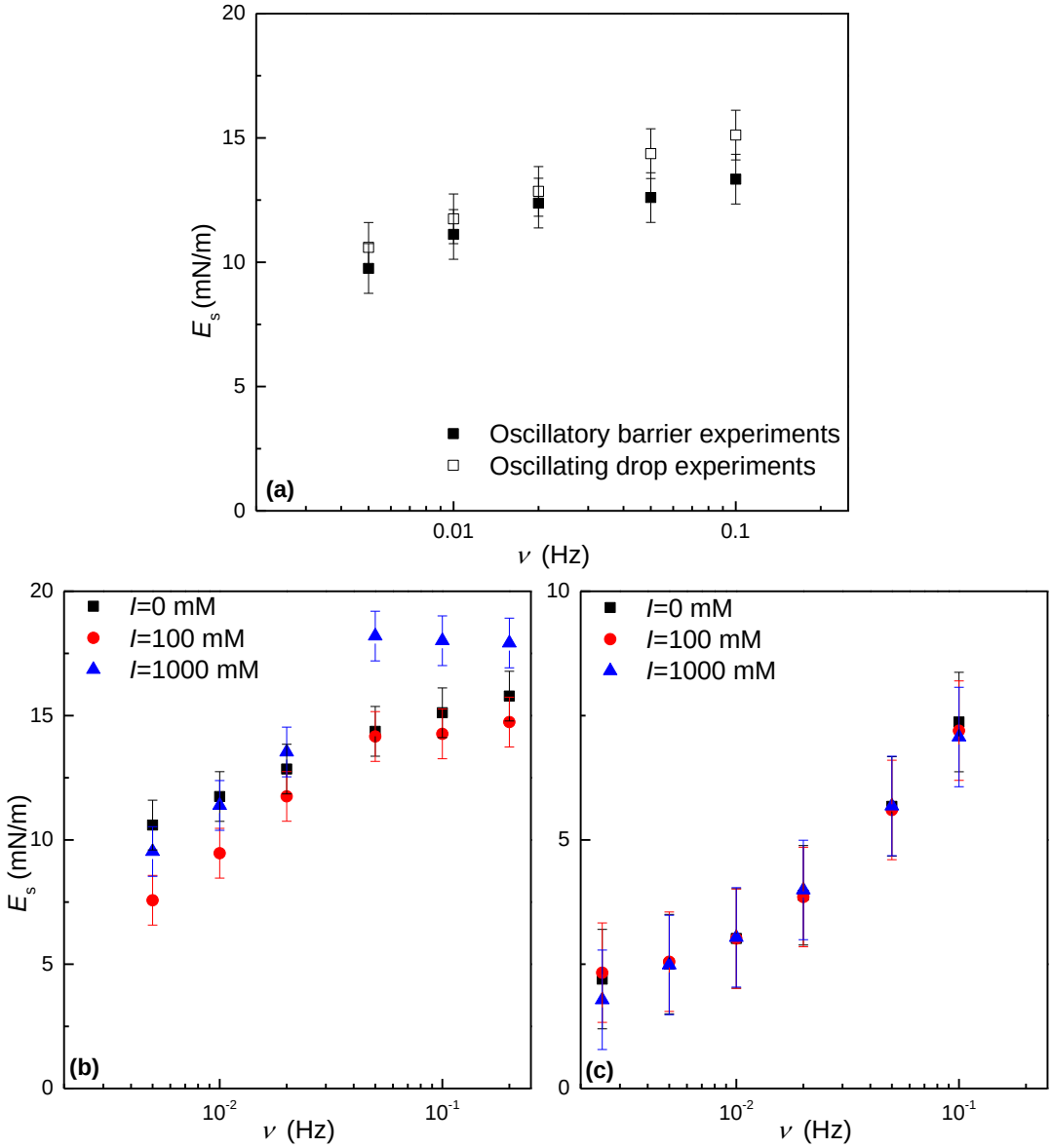

Figure 5.5. (a) Frequency dependence of the storage modulus (E_s) obtained by oscillatory barriers and oscillating drop measurements at 23 °C for Gibbs monolayers obtained for the adsorption of Pluronic F-68 solutions of concentration 10^{-3} mM and a fixed ionic strength of 0 mM. (b) Frequency dependence of the storage modulus (E_s) at 23 °C for Gibbs monolayers obtained for the adsorption of Pluronic F-68 solutions of c=10^{-3} mM, and different ionic strengths at the air/solution interface. (c) Frequency dependence of the storage modulus (E_s) at 23 °C for Gibbs monolayers obtained for the adsorption of Pluronic F-68 solutions of c=10^{-1} mM (b), and different ionic strengths at the air/solution interface.

Deepening in the dilational storage modulus dependences on the concentration of Pluronic F-68 and ionic strength, it can be observed that the variation of the ionic strength within the range 0-1 M does not present a significant impact in the values of the dilational modulus at low frequencies, even though for an ionic strength of 1M and polymer concentration of 10^{-3} mM, a slight increase of the storage modulus can be observed. However, this does not occur for the Gibbs monolayers obtained by the adsorption of solutions of higher concentration (10^{-1} mM) where the dilational storage modulus remains almost unchanged by increasing the ionic strength of the aqueous phase. This is clearer from **Figure 5. 6**(a) where the dependence of the storage modulus on the ionic strength at a fixed frequency of $5x10^{-2}$ Hz is displayed. The explanation for this different effect of the salt depending on the copolymer concentration can be understood from the data shown in **Figure 5.4**. Indeed, for the lowest concentration of Pluronic F-68 (10^{-3} mM) strong change in interfacial tension is observed with the ionic strength, whereas for solutions with a concentration of 10^{-1} mM the change is almost negligible. This suggests a salt-induced conformational change in the former case, which increases the value of the dilatational storage modulus. This agrees with previous studies on the influence of ionic strength on the rheological properties of polymer loaded interfaces [62].

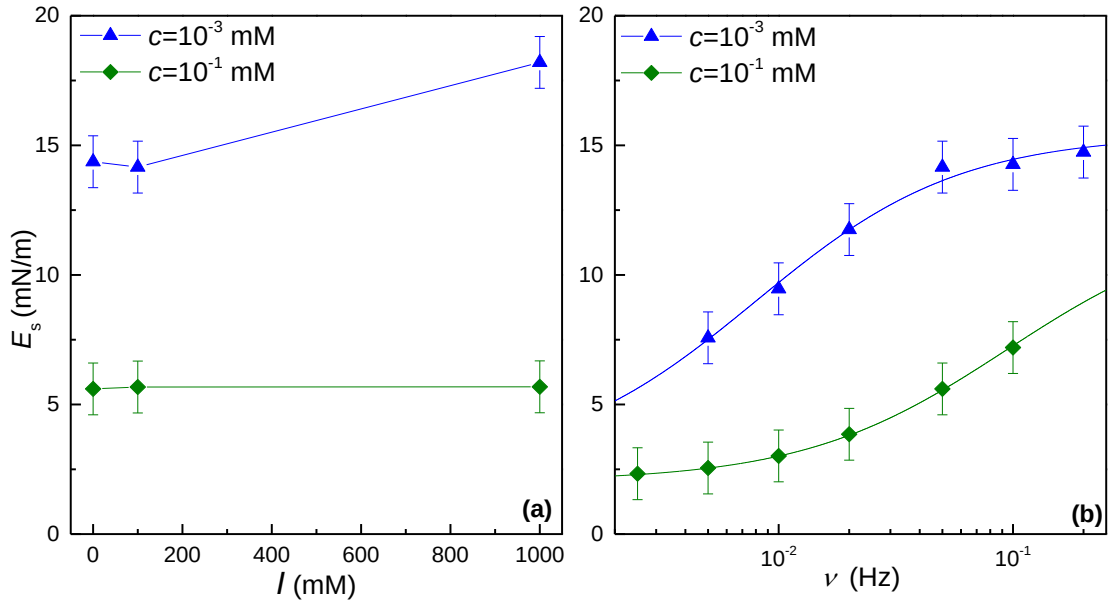

Figure 5. 6. (a) Dependence of the storage modulus at a fixed frequency of $5x10^{-2}$ Hz on the ionic strength for Gibbs monolayers of Pluronic F-68 at two different bulk concentrations. The symbols correspond to the experimental data, and the lines are guides for the eyes. (b) Frequency dependence of the storage modulus (E_s) for Gibbs monolayers obtained for the adsorption of Pluronic F-68 solutions of two different concentrations, c=10^{-3} mM and c=10^{-1} mM, and a fixed ionic strength (100 mM). The symbols correspond to the experimental data, and the lines correspond to the best fit obtained using the Lucassen-Van den Tempel model.

The Pluronic F-68 concentration also affects the relaxation spectrum in the considered frequency range. This is better understood with **Figure 5. 6** (b) where the frequency dependence of the dilational storage modulus at a fixed ionic strength of 100 mM is reported for the two concentrations of Pluronic F-68 studied. The results evidence that the increase in the Pluronic F-68 concentration from 10^{-3} mM to 10^{-1} mM shifts the relaxation process found within the considered frequency range to higher values of the characteristic frequency. This is clearer from the analysis of the experimental data in terms of the Lucassen-Van den Tempel

model given by the following equation [63] (see *Chapter I*, 1.8.2. Interface Dilational Rheology: Theoretical models),

$$E_s^*(\nu) = E_s(\nu) + iE_i(\nu) = E_s(\nu) + i2\pi\nu\kappa_s(\nu) = \varepsilon_0 \frac{1 + \zeta(\nu) + i\zeta(\nu)}{1 + 2\zeta(\nu) + 2\zeta(\nu)^2}, \qquad (5.1)$$

where $E_s^*(\nu)$ is the complex interfacial dilational viscoelastic modulus as a function of the frequency ν (expressed in Hz), with $\kappa_s(\nu)$ defining the interfacial dilational viscosity, ε_0 the Gibbs elasticity and $\zeta = {\nu_D}/{\nu}$ is a parameter defining the exchange of matter between the interface and the adjacent bulk phase, with ν_D being the characteristic frequency of the relaxation process. **Figure 5. 7** reports the best-fit parameters obtained from the analysis of the low frequency dilational results in terms of the Lucassen-Van den Tempel model for the studied Gibbs monolayers.

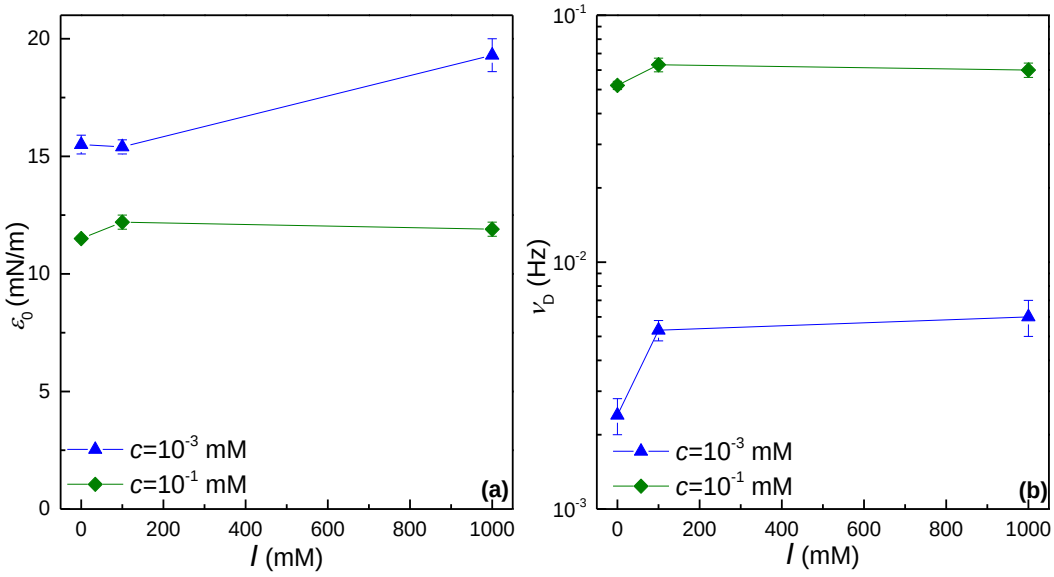

Figure 5. 7. Dependence of the best fit parameters obtained using the Lucassen-Van den Tempel model, ε_0 (a) and ν_D (b), on the ionic strength for Gibbs monolayers of Pluronic F-68 at two different bulk concentrations. The symbols correspond to the experimental data, and the lines are guides by the eyes.

The dependence of ε_0 on the ionic strength of the Pluronic F-68 solutions agrees with the above dependence of the values of E_s. On the other hand, the dependences of the characteristic frequencies of the relaxation process on the ionic strength appears more interesting (see **Figure 5. 7** (b)). Firstly, the results confirm the above discussed scenario related to the increase in the value of the characteristic frequency as the copolymer concentration increase from 10^{-3} mM to 10^{-1} mM. In fact, the results evidence an increase of about 1 order of magnitude for the characteristic relaxation frequency. This may indicate that the exchange process between the bulk and the interface occurs at a higher rate for higher copolymer concentrations, which is the expected result. In addition, independently of the copolymer concentration, the increase in the ionic strength leads to an increase in the characteristic relaxation frequency. This can be again explained by considering the worsening of the solvent quality of the subphase for Pluronic F-68 with the increase in the ionic strength. This is expected to favor the surface adsorption of the copolymer molecules, and a corresponding decrease in the characteristic diffusion time.

5.3.4. High-frequency dilational rheology: electrocapillary wave damping measurements

The evaluation of the damping of electrocapillary waves for Pluronic F-68 Gibbs monolayers at the air/solution interface allows obtaining information of the dilational interfacial rheological response at higher frequencies (above 50 Hz) than typical oscillatory rheology. Therefore, the combination of electrocapillary wave damping measurements with the above discussed results contribute to expand the accessible frequency region of the dilation spectrum. It should be noted that electrocapillary wave experiments were performed in the frequency range of 80-400 Hz. It was not possible to perform experiments over 400 Hz due to the strong decrease in the intensity of the signal that significantly reduces the sensibility of the measurements.

For a capillary wave excited in a point of the interface (xy plane) defined by the coordinate x=0, it is possible to define its spatial profile in terms of a damped cosine according to the following expression (see *Chapter II*, *2.1.4. Electro-Capillary Waves (ECW)*),

$$u_z = u_z^0 e^{-\beta x} cos\left(\frac{2\pi}{\lambda}x + \varphi\right), \tag{5.2}$$

with u_z^0 being the wave amplitude, and β, λ and ϕ the damping coefficient, the characteristic capillary wavelength and the phase lag, respectively. **Figure 5.8** shows the frequency dependence of the parameter β and λ for the two studied Pluronic F-68 concentration and different ionic strengths. The results show that at fixed frequency, the capillary wavelength, λ, slightly decrease as the ionic strength increases, independently of the Pluronic bulk concentration. This is particularly evident when the NaCl concentration overcomes the threshold value of 1M. These results can be rationalize by considering the Kelvin's law ($\lambda = \left(\frac{2\pi\gamma}{\rho}\right)^{\frac{1}{3}} \nu^{-2/3}$, where ρ accounts for the bulk density) [64], although it must be taken into account that this equation is strictly valid for low viscosity simple liquids. The decrease in λ becomes stronger in the region where the variation of γ with the ionic strength is higher (above NaCl concentration around 1M). On the other hand, Gibbs monolayers obtained from solutions of Pluronic F-68 concentration 10^{-1} mM exhibit lower values of λ than when the copolymer concentration is 10^{-3} mM. This may be also rationalized considering the reduction of the interfacial tension with the increase in Pluronic F-68 concentration (see **Figure 5.4**).

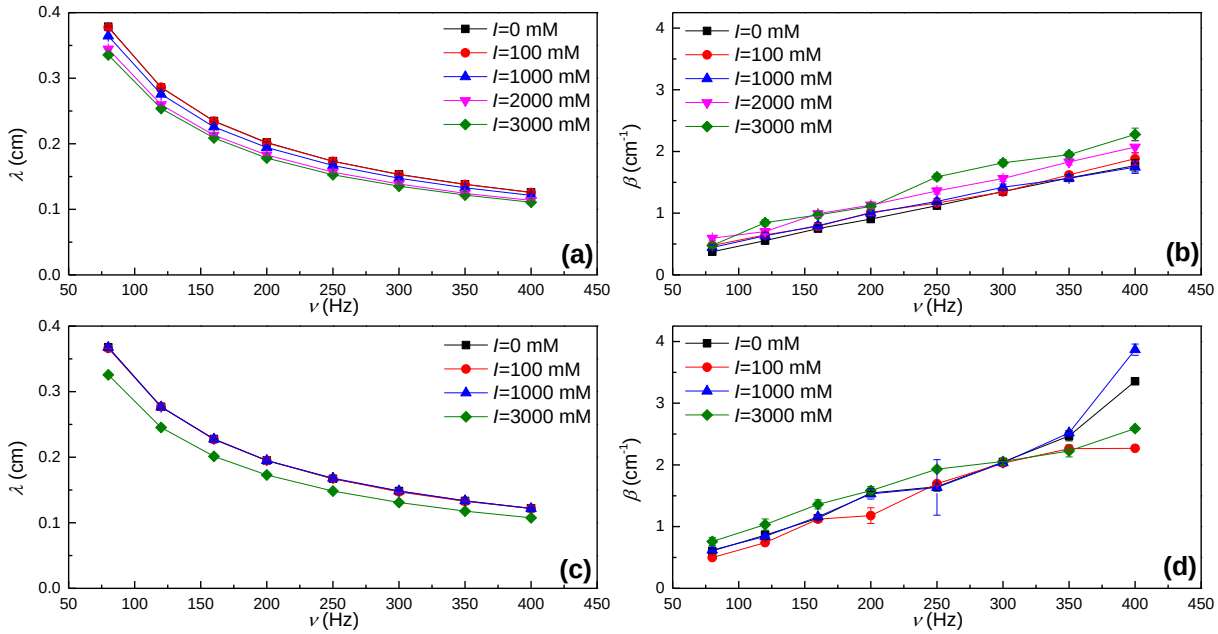

Figure 5.8. Frequency dependences of the wavelength (λ) and damping (β) for monolayers obtained from the adsorption of solutions of two different Pluronic F-68 concentrations at different ionic strengths. (a) and (b) λ and β values, respectively, for Pluronic F-68 solutions with a concentration of 10^{-3} mM, and (c) and (d) λ and β values, respectively, for Pluronic F-68 solutions with a concentration of 10^{-1} mM. The lines are guides by the eyes.

The interpretation of the dependences of the damping coefficient are less straightforward (see **Figure 5.8** (b) and (d)). As occurred for the capillary wavelength, the effect of salt in the damping coefficient is almost negligible when ionic strength is below 1M, whereas the increase of the ionic strength above such threshold slightly increases the damping coefficient values. This can be rationalized as a combination of two different factors. First, the increase of the ionic strength results in an increase in the bulk viscosity of the solution (see **Table 5.1**), which according to the Stokes-like' law must lead to an increase in the damping coefficient [64]. The second factor that influences the increase of β is the increase in the surface excess as a result of the salting-out phenomenon. It should be noted that the increase in the damping coefficient with the concentration of Pluronic F-68 should be ascribed to the higher amount of surfactant adsorbed at the interface, because the viscosity of Pluronic F-68 solutions does not significantly change within the studied concentration range.

A more detailed analysis of the frequency dependences of the capillary wavelength and damping coefficient shows that the experimental data can be described in terms of simple scaling laws $q \sim \omega^a$ and $\beta \sim \omega^b$ (see *Chapter II, 2.1.4. Electro-Capillary Waves (ECW)*), where $\omega = 2\pi\nu$ defines the angular frequency and $q = 2\pi/\lambda$ is the real component of the wavevector. In this study, the value obtained for the exponent a assumes a values of about 0.68, for all the studied conditions, is similar to that predicted from Kelvin's law $q \sim \omega^{2/3}$. On the contrary, the value of the exponent for the scaling law describing the frequency dependence of β differs from the one that can be derived from a Stokes-like law (b=1), and the differences increases with the ionic strength [64]. This suggests the possible existence of viscoelastic loss in the monolayer in agreement with previous studied on Pluronic monolayer in absence of salt [61]. It should be noted that for the highest frequencies evaluated for Gibbs monolayers obtained from solutions with copolymer concentration of 10^{-1} mM, the damping coefficient values diverge from the general tendency which can be ascribed to a worsening of the signal quality.

To obtain information about the dilational response of the monolayer from electrocapillary wave experiments, it is needed to solve numerically the dispersion equation (see *Chapter II*, *2.1.4. Electro-Capillary Waves (ECW)*), $D(q, \omega)=0$, which provides a relation between the characteristics parameter associated with the propagation of the transversal waves (frequency ω, wavelength λ, and damping coefficient β), and the constitutive parameters of the monolayer (interfacial tension γ, dilational storage modulus E_s, and dilational viscosity κ_s) [65,66]. The solution of the dispersion equation provides the complex dilational interfacial modulus,

$$E_s^*(\nu) = E_s(\nu) + i\omega\kappa_s(\nu) = \frac{\dfrac{-\left(\eta\omega(q-m)\right)^2}{\gamma q^2 + i\eta\omega(q+m) - \dfrac{\rho}{q}\omega^2} - i\eta\omega(q+m)}{q^2}, \tag{5.3}$$

where q is the complex wavevector, defined as,

$$q = \frac{2\pi}{\lambda} - i\beta, \tag{5.4}$$

and m is the capillary penetration depth (Re(m) > 0),

$$m = \sqrt{q^2 + i\omega\frac{\rho}{\eta}}. \tag{5.5}$$

According to the above, the determination of the viscoelastic component of the dilational modulus requires to combine the values of surface tension γ reported in **Figure 5.4** with the bulk viscosity and density of Pluronic solutions reported in **Table 5.1**. It should be noted that the extraction of the constitutive parameters of the monolayers from electrocapillary wave measurements is always challenging. This is mainly related to the change of the sensibility of capillary waves to the dilational response of the interface. The resonance condition involves that the frequency of the dilational modes is very close to that corresponding to the capillary ones, providing the highest sensibility of capillary waves for the determination of E_s and $\kappa_s$values. At a first approximation, the resonance occurs for the following interval (see *Chapter II*, *2.1.4. Electro-Capillary Waves (ECW)*),

$$\left(\frac{E_s}{\gamma}\right)_{\mathrm{R}} = \left(\frac{q\eta^2}{\gamma\rho}\right)^{1/4} \approx 0.10 - 0.15, \tag{5.6}$$

where the subindex R indicates the resonance condition. The resonance condition is of a paramount importance for the determination of the dilational parameters from electrocapillary wave experiments. In fact, as the E_s/γ ratio differs from the resonance condition, the dilational parameters extracted from the analysis of the experimental data will

be affected from a higher uncertainty. **Figure 5.9** shows the E_s/γ ratio for all the analyzed samples.

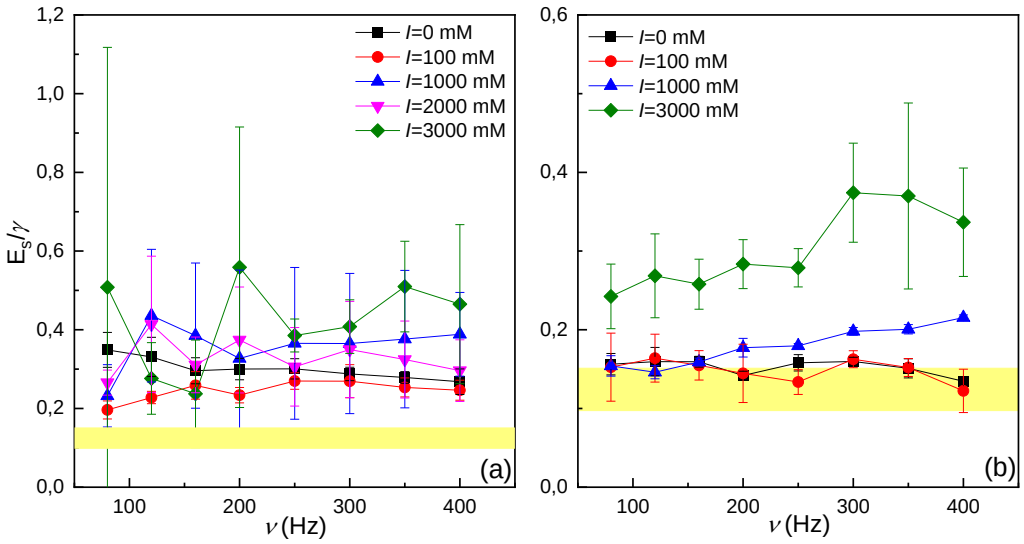

Figure 5.9. Frequency dependences of the E_s/γ ratio for monolayers obtained from the adsorption at the air/solution interface of solutions of two different Pluronic F-68 concentrations at different ionic strengths. (a) Pluronic F-68 solutions with a concentration of 10^{-3} mM, and (b) Pluronic F-68 solutions with a concentration of 10^{-1} mM. The shaded region corresponds to the expected resonance region, and the lines are guides by the eyes.

The results show that for the most diluted solution (concentration 10^{-3} mM), the E_s/γ ratio differs significantly from the resonance condition. This involves that small variations in the input parameters γ and η, as a result of their inaccurate determination, will introduce a high uncertainty in the determination of E_s and κ_s. The situation is better, or at least at the lowest values of the ionic strength, when the concentration of Pluronic F-68 is increased up to 10^{-1} mM. In this case, the values of E_s/γ ratio are closer to the resonance condition. In particular for ionic strength below 1M, the E_s/γ ratios fall into the resonance region. Therefore, the determination of the viscoelastic modulus will be less affected by slight changes in the determination of γ and η. Deepening on the variation of the E_s/γ ratio with the ionic strength, it is clear that an increase in the ionic strength takes the monolayer behavior, independently of the copolymer concentration, far from the resonance condition. This is reflected from the value of the E_s/γ ratio, but also from the increase in the uncertainty of this ratio. Therefore, the results point out that both bulk concentration and surface excess present a critical impact in the applicability of electrocapillary waves in the determination of the dilational properties of monolayers at air/water interface in agreement with previous results by Maestro et al. [52].

Deepening on the effect of the ionic strength on the value of the E_s/γ ratio is clear that the salting-out phenomenon leading to an increase in the surface excess, increases the uncertainty of electrocapillary wave measurements for an accurate determination of the dilational behavior of Pluronic F-68 Gibbs monolayers. In fact, the higher the ionic strength the higher the value of the E_s/γ ratio and the greater the distance from the resonance condition. In

addition, the uncertainty in the determination of the true value of the E_s/γ ratio also increases as evidences the increase in the error bars. However, the increase in the surface excess alone cannot be considered as the only effect worsening the quality of the determination of the dilational properties of the interface by electrocapillary wave measurements as evidenced the better quality of the results obtained for the highest studied concentration (10^{-1} mM).

The combination of rheological experiments allowing assessing the dilational properties of interface in different frequencies range is a very powerful tool for obtaining information of the whole mechanical relaxation spectrum for molecules attached to fluid/fluid interfaces [51,52]. **Figure 5.10** displays the dependence of the storage modulus E_s on the frequency for Gibbs monolayers obtained by adsorption of solutions with two different concentrations of copolymer and different ionic strengths.

The relaxation spectrum obtained by combining oscillatory dilational rheology and electrocapillary wave experiments is in good qualitative agreement with the results obtained only by using the measurements at low frequency, with the storage modulus reducing its value in the whole frequency range as the Pluronic F-127 concentration increases from 10^{-3} mM up to 10^{-1} mM. Deepening on the analysis of the experimental results, it is confirmed that the storage modulus results obtained for conditions far from the resonance situation are affected of higher uncertainty. This is clear from the huge errors bars associated with the results obtained for Gibbs monolayers corresponding to a bulk concentration of 10^{-3} mM. On the contrary, the error bars are less important for experiments obtained from the adsorption of Pluronic F-68 solutions with concentration 10^{-1} mM, where the E_s/γ ratio is closer to that corresponding to the resonance. This is clearer for the storage results obtained for ionic strength below 1000 mM, where it was found an overlapping of the E_s/γ ratio with the resonance region. However, the increase in the ionic strength worsens the accuracy of the determination of the storage modulus as evidence the bigger error bar. However, the latter remains below the uncertainty on the determination of the storage modulus for Gibbs monolayers obtained from Pluronic F-68 solutions of concentration 10^{-3} mM. The above discussion is clearer from the results in **Figure 5. 11**, where the values of the storage modulus obtained from electrocapillary wave experiments in the frequency range of 80-400 Hz are depicted for Gibbs monolayers obtained at two different bulk copolymer concentration and different ionic strengths. The results evidence that in the case of Gibbs monolayers obtained from solutions with concentration 10^{-3} mM, the uncertainty associated with the determination storage modulus values is huge, making difficult to obtain any dependence of the storage modulus on the ionic strength on the subphase. On the other hand, the results obtained by electrocapillary wave experiments do not evidence any dependence of the storage modulus on the frequency for the Gibbs monolayer obtained from solutions at concentration of 10^{-3} mM. The situation changes when the copolymer concentration is increased. In this case, the values of the storage modulus tend to increase with the ionic strength of the solution in agreement with the results reported by Llamas et al. [39] in systems containing lithium salts. In addition, the increase of the ionic strength above 1M introduces a frequency dependence on the storage modulus, which indicates the existence of a relaxation mechanism with a

characteristic frequency in the range of 10^2-10^3 Hz which can be ascribed to the reorganization of the copolymer molecules within the interface.

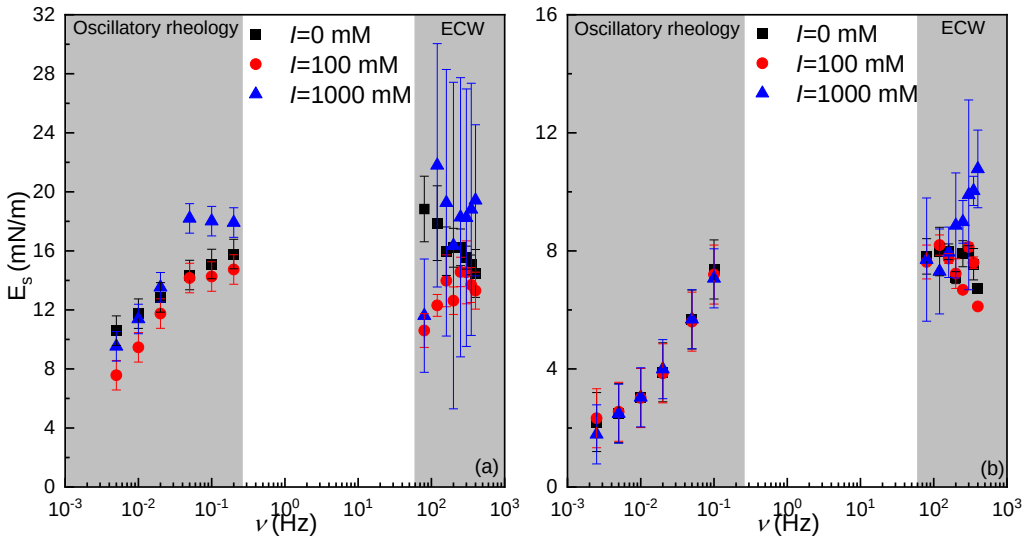

Figure 5.10. Frequency dependence of the storage modulus (E_s) at 23ºC for Gibbs monolayers obtained for the adsorption of Pluronic F-68 solutions of two different concentrations, c=10^{-3} mM (a) and c=10^{-1} mM (b), and different ionic strengths at the air/solution interface. In the panels, the data correspond to oscillatory rheology and electrocapillary wave (ECW) experiments.

Based on the above results, it is clear that the best theoretical representation of the dilational response of Pluronic F-68 Gibbs monolayers at the lowest concentration of copolymer studied in this work (10^{-3} mM) is the Lucassen-Van den Tempel model (see equation (5.1)). This also provides a good representation for the dilation relaxation spectrum of Gibbs monolayers obtained from solutions with concentration 10^{-1} mM, at least at the lowest ionic strengths. However, when the ionic strength reached a value of 1M a second contribution must be included to describe the dilational spectrum [39,51,67,68]. Following the procedure introduced by Ravera et al. [51,67] which provide a description for an interfacial relaxation spectrum characterized by the presence of a diffusion-controlled adsorption and an interfacial relaxation according to the following expression (see *Chapter I*, 1.8.2. Interface Dilational Rheology: Theoretical models),

$$E_s{}^*(\nu) = \frac{1+\zeta(\nu)+i\zeta(\nu)}{1+2\zeta(\nu)+2\zeta(\nu)^2}\left(\varepsilon_0 + (\varepsilon_1-\varepsilon_0)\frac{1+i\chi(\nu)}{1+\chi(\nu)^2}\right), \qquad (5.7)$$

where ε_1 is the high frequency limit of the dilational elasticity and $\chi(\nu) = {}^{\nu_1}/_{\nu}$ a parameter describing the interfacial relaxation process, with ν_1 being their characteristic frequency. **Figure 5. 12** shows the best fits obtained for the dilational spectrum of Gibbs monolayers obtained from the adsorption of Pluronic F-68 solutions with different concentration and at a fixed ionic strength of 1M.

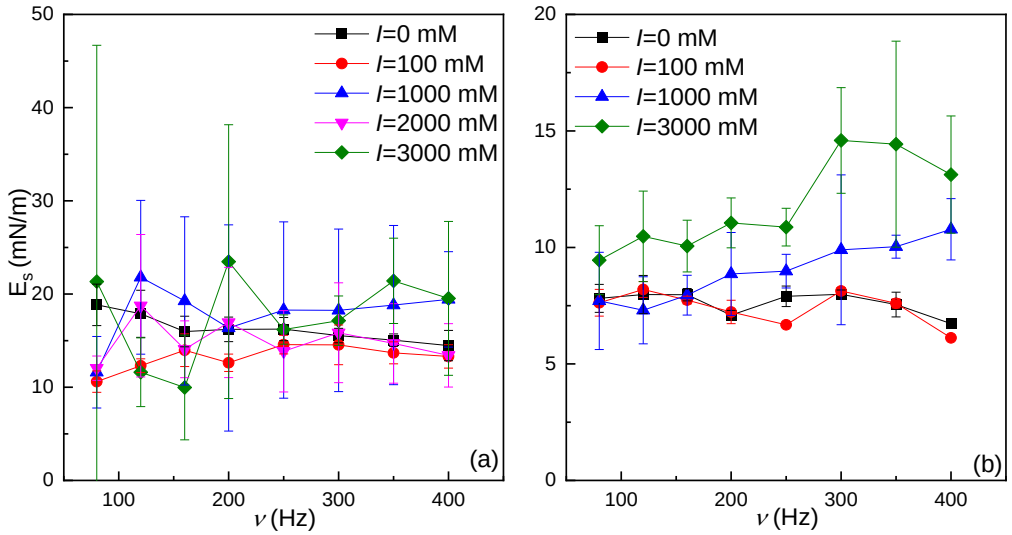

Figure 5. 11. Frequency dependence of the storage modulus (E_s) at 23ºC for Gibbs monolayers obtained by electrocapillary wave experiments for the adsorption of Pluronic F-68 solutions of two different concentrations, c=10^{-3} mM (a) and c=10^{-1} mM (b), and different ionic strengths at the air/solution interface. The lines are guides by the eyes.

The above results evidence that the Lucassen-Van den Tempel model or its combination with an additional relaxation process provide a suitable description of the dilational spectrum of Gibbs monolayers of Pluronic F-68. **Table 5.2** reports the limit elasticities, ε_0 and ε_1, and the characteristic frequencies of the relaxation processes, ν_D and ν_1, obtained from the fitting of the experimental data in the whole frequency range to the Lucassen-Van den Tempel model or to its extension by including an additional process occurring within the interface. Notice that Lucassen-Van den Tempel model accounts for the rheological response of Gibbs monolayers obtained from Pluronic solutions with concentration 10^{-3} mM, independently of the ionic strength, whereas in the case of monolayers obtained from the adsorption of solutions with concentration 10^{-1} mM, it is needed to use the extension of the Lucassen-Van den Tempel model including the additional interfacial process.

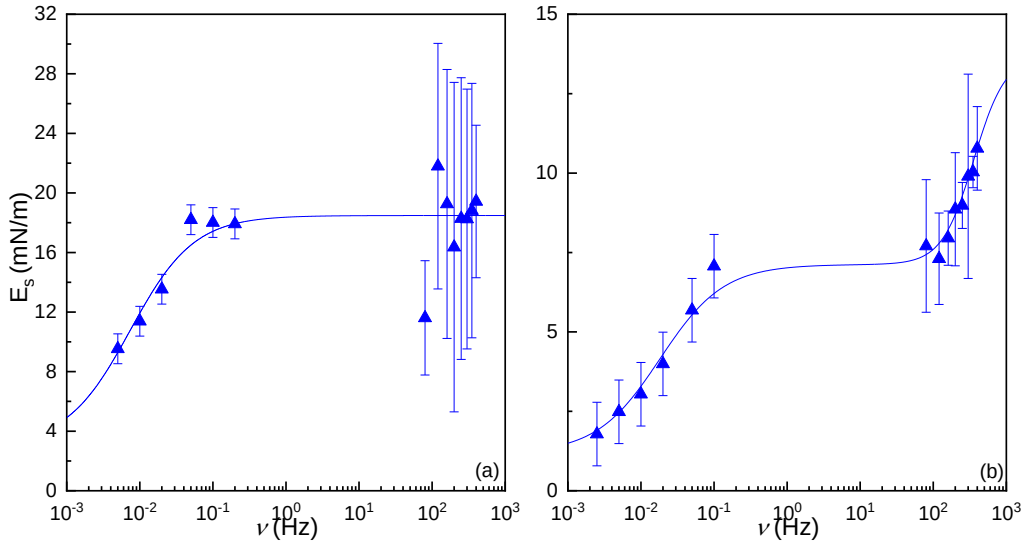

Figure 5. 12. Frequency dependence of the storage modulus (E_s) at 23ºC for Gibbs monolayers obtained for the adsorption of Pluronic F-68 solutions of two different concentrations, C=10^{-3} mM (a) and C=10^{-1} mM (b), and a fixed ionic strength of 1M. In the panels, the symbols correspond to the experimental data obtained by oscillatory rheology and electrocapillary wave (ECW) experiments, and the lines are the best fit to the theoretical model described by equations (5.1) and (5.7).

Table 5.2. Summary of the limit elasticities, ε_0 and ε_1, and the characteristic frequencies of the relaxation processes, ν_D and ν_1, obtained from the fitting of the experimental data in the whole frequency range to the Lucassen-Van den Tempel model or to its extension by including an additional process occurring within the interface.

***c* (mM)**	10^{-3}			10^{-1}		
***I* (mM)**	ε_0 **(mN/m)**	$10^3\nu_D$ **(Hz)**	ε_0 **(mN/m)**	$10^2\nu_D$ **(Hz)**	ε_1 **(mN/m)**	$10^{-2}\nu_1$ **(Hz)**
0	15.6±0.2	2.5±0.4	7.7±0.1	1.5±0.2	-	-
100	14.1±0.2	3.7±0.8	7.4±0.2	1.3±0.3	-	-
1000	18.5±0.4	6±1	7.1±0.3	1.2±0.3	14±1	3.6±0.7

5.4. Conclusions

This work evaluates the effect of the ionic strength on the interfacial tension and dilatational rheology of Gibbs monolayers of Pluronic F-68 solutions with different NaCl concentration. This has been possible by combining several well-established experimental techniques that allow one to evaluate the equilibrium isotherms and the interfacial dilational rheology of the formed Gibbs monolayers. The results have evidenced that the addition of salt significantly affects the interfacial tension while its impact on the dilational rheological response of the Pluronic F-68 Gibbs monolayers appears as less important.

The effect of the ionic strength on the equilibrium isotherm is ascribed to a salting-out phenomenon that reduces the solubility of the hydrophilic blocks of the copolymer in the aqueous phase, enhancing its adsorption at the air/solution interface. This enhances the surface activity of Pluronic F-68, which results in a higher surface excess and stronger ability to lower the interfacial tension. However, this salting-out phenomenon, even though it is independently of the copolymer concentration, appears as a most important contribution to the surface activity of the Pluronic F-68 when the NaCl concentration, i.e., the ionic strength overcomes a threshold value around 1M. The effect of such high concentrations of salt are rarely studied in works dealing with the adsorption of surface-active molecules at fluid/fluid interfaces.

On the contrary to that what was found for the impact of the ionic strength on the equilibrium properties of the Gibbs monolayers, the results obtained by low frequency oscillatory experiments have shown that the ionic strength has only a reduced effect in the modification of the relaxation processes, modifying the characteristic frequencies in such a way that can be interpreted in terms of the enhanced surface activity induced by the addition of salt. However, the extension of the accessible frequency range by including results obtained using measurements based on the evaluation of the damping of interfacial capillary waves excited by the application of an electric field has evidenced that the rheological response of the Gibbs monolayers can be modified by the ionic strength, especially at high copolymer concentrations and high ionic strength. However, most interesting is the fact that the variation of the ionic strength and the copolymer bulk concentration helps on the understanding of the limits of the characterization of interfacial rheology by electrocapillary waves experiments. The results have evidenced that these limits are not only a result of the surface excess and interfacial

tension and deserve a deeper study to exploit the whole potential of electrocapillary wave for evaluating the dilational rheology properties of interfacial films at the air/water interface.

5.5. References

1. Jarak, I.; Varela, C.L.; Tavares Da Silva, E.; Roleira, F.F.M.; Veiga, F.; Figueiras, A. Pluronic-Based Nanovehicles: Recent Advances in Anticancer Therapeutic Applications. *Eur. J. Med. Chem.* **2020**, *206*, 112526, doi:10.1016/j.ejmech.2020.112526.

2. Shamma, R.N.; Sayed, R.H.; Madry, H.; El Sayed, N.S.; Cucchiarini, M. Triblock Copolymer Bioinks in Hydrogel Three-Dimensional Printing for Regenerative Medicine: A Focus on Pluronic F127. *Tissue Eng. Part B Rev.* **2022**, *28*, 451–463, doi:10.1089/ten.teb.2021.0026.

3. Ganguly, R.; Kumar, S.; Kunwar, A.; Nath, S.; Sarma, H.D.; Tripathi, A.; Verma, G.; Chaudhari, D.P.; Aswal, V.K.; Melo, J.S. Structural and Therapeutic Properties of Curcumin Solubilized Pluronic F127 Micellar Solutions and Hydrogels. *J. Mol. Liquids* **2020**, *314*, 113591, doi:10.1016/j.molliq.2020.113591.

4. Singla, P.; Garg, S.; McClements, J.; Jamieson, O.; Peeters, M.; Mahajan, R.K. Advances in the Therapeutic Delivery and Applications of Functionalized Pluronics: A Critical Review. *Adv. Colloid Interface Sci.* **2022**, *299*, 102563, doi:10.1016/j.cis.2021.102563.

5. Lucia, A.; Girard, C.; Fanucce, M.; Coviella, C.; Rubio, R.G.; Ortega, F.; Guzmán, E. Development of an Environmentally Friendly Larvicidal Formulation Based on Essential Oil Compound Blend to Control *Aedes Aegypti* Larvae: Correlations between Physicochemical Properties and Insecticidal Activity. *ACS Sustainable Chem. Eng.* **2020**, *8*, 10995–11006, doi:10.1021/acssuschemeng.0c03778.

6. Kumar, S.S.; Harikrishnan, K.K.; Urmila, S.P.; Gauri, V.; Saritha, A.; Gangopadhyay, M. Comprehensive Review of Pluronic® Polymers of Different Shapes with Prominent Applications in Photodynamic Therapy. *Eur. Polym. J.* **2023**, *200*, 112534, doi:10.1016/j.eurpolymj.2023.112534.

7. Alexandridis, P. Poly(Ethylene Oxide)/Poly(Propylene Oxide) Block Copolymer Surfactants. *Curr. Opin. Colloid Interface Sci.* **1997**, *2*, 478–489, doi:10.1016/S1359-0294(97)80095-7.

8. Li, Z.; Peng, S.; Chen, X.; Zhu, Y.; Zou, L.; Liu, W.; Liu, C. Pluronics Modified Liposomes for Curcumin Encapsulation: Sustained Release, Stability and Bioaccessibility. *Food Res. Int.* **2018**, *108*, 246–253, doi:10.1016/j.foodres.2018.03.048.

9. Braga, G.; Campanholi, K.D.S.S.; Ferreira, S.B.D.S.; Calori, I.R.; De Oliveira, J.H.; Vanzin, D.; Bruschi, M.L.; Pontes, R.M.; Março, P.H.; Tessaro, A.L.; et al. Tautomeric and Aggregational Dynamics of Curcumin-Supersaturated Pluronic Nanocarriers. *ACS Appl. Polym. Mater.* **2020**, *2*, 4493–4511, doi:10.1021/acsapm.0c00589.

10. Shaker, M.A.; Elbadawy, H.M.; Shaker, M.A. Improved Solubility, Dissolution, and Oral Bioavailability for Atorvastatin-Pluronic® Solid Dispersions. *Int. J. Pharm.* **2020**, *574*, 118891, doi:10.1016/j.ijpharm.2019.118891.

11. Carbone, C.; Rubio-Bueno, A.; Ortega, F.; Rubio, R.G.; Guzmán, E. Adsorption of Mixed Dispersions of Silica Nanoparticles and an Amphiphilic Triblock Copolymer at the Water–Vapor Interface. *Appl. Sci.* **2023**, *13*, 10093, doi:10.3390/app131810093.

12. Lucia, A.; Murace, M.; Sartor, G.; Keil, G.; Cámera, R.; Rubio, R.G.; Guzmán, E. Oil in Water Nanoemulsions Loaded with Tebuconazole for Populus Wood Protection against White- and Brown-Rot Fungi. *Forests* **2021**, *12*, 1234, doi:10.3390/f12091234.

13. Lucia, A.; Guzmán, E.; Rubio, R.G.; Ortega, F. Enhanced Solubilization of an Insect Juvenile Hormone (JH) Mimetic (Piryproxyfen) Using Eugenol in Water Nanoemulsions Stabilized by a Triblock Copolymer of Poly(Ethylenglycol) and Poly(Propilenglycol). *Colloids Surf. A* **2020**, *606*, 125513, doi:10.1016/j.colsurfa.2020.125513.

14. Sánchez-Arribas, N.; Guzmán, E.; Lucia, A.; Toloza, A.C.; Velarde, M.G.; Ortega, F.; Rubio, R.G. Environmentally Friendly Platforms for Encapsulation of an Essential Oil: Fabrication, Characterization and Application in Pests Control. *Colloids Surf. A* **2018**, *555*, 473–481, doi:10.1016/j.colsurfa.2018.07.028.

15. Velasco-Rodriguez, B.; Soltero-Martínez, J.F.; Rosales-Rivera, L.C.; Macías-Balleza, E.R.; Landázuri, G.; Larios-Durán, E.R. Adsorption and Interaction of Bovine Serum Albumin and Pluronic P103 Triblock Copolymer on a Gold Electrode: Double-Layer Capacitance Measurements. *ACS Omega* **2020**, *5*, 17347–17355, doi:10.1021/acsomega.0c01704.

16. Yun, K.H.; Sharma, K.; Kim, H.U.; Bae, T.-H. Modification of a PES Microfiltration Membrane to Enhance Sterile Filtration by Inhibiting Protein Adsorption. *J. Ind. Eng. Chem.* **2023**, *123*, 311–319, doi:10.1016/j.jiec.2023.03.048.

17. Pérez-Sánchez, G.; Vicente, F.A.; Schaeffer, N.; Cardoso, I.S.; Ventura, S.P.M.; Jorge, M.; Coutinho, J.A.P. Rationalizing the Phase Behavior of Triblock Copolymers through Experiments and Molecular Simulations. *J. Phys. Chem. C* **2019**, *123*, 21224–21236, doi:10.1021/acs.jpcc.9b04099.

18. Hopkins, C.C.; De Bruyn, J.R. Gelation and Long-Time Relaxation of Aqueous Solutions of Pluronic F127. *J. Rheol.* **2019**, *63*, 191–201, doi:10.1122/1.5054598.

19. Patel, D.; Jana, R.; Lin, M.-H.; Kuperkar, K.; Seth, D.; Chen, L.-J.; Bahadur, P. Revisiting the Salt-Triggered Self-Assembly in Very Hydrophilic Triblock Copolymer Pluronic® F88 Using Multitechnique Approach. *Colloid Polym Sci* **2021**, *299*, 1113–1126, doi:10.1007/s00396-021-04833-6.

20. Da Silva, L.H.M.; Loh, W. Calorimetric Investigation of the Formation of Aqueous Two-Phase Systems in Ternary Mixtures of Water, Poly(Ethylene Oxide) and Electrolytes (Or Dextran). *J. Phys. Chem. B* **2000**, *104*, 10069–10073, doi:10.1021/jp000719t.

21. Suman, K.; Sourav, S.; Joshi, Y.M. Rheological Signatures of Gel–Glass Transition and a Revised Phase Diagram of an Aqueous Triblock Copolymer Solution of Pluronic F127. *Phys. Fluids* **2021**, *33*, 073610, doi:10.1063/5.0057090.

22. Boonrat, O.; Tantishaiyakul, V.; Hirun, N.; Rugmai, S.; Soontaranon, S. Structural Characterization Using SAXS and Rheological Behaviors of Pluronic F127 and Methylcellulose Blends. *Polym. Bull.* **2021**, *78*, 1175–1187, doi:10.1007/s00289-020-03154-y.

23. Zheng, L.; Minamikawa, H.; Harada, K.; Inoue, T.; Chernik, G.G. Effect of Inorganic Salts on the Phase Behavior of an Aqueous Mixture of Heptaethylene Glycol Dodecyl Ether. *Langmuir* **2003**, *19*, 10487–10494, doi:10.1021/la030182l.

24. Pandit, N.; Trygstad, T.; Croy, S.; Bohorquez, M.; Koch, C. Effect of Salts on the Micellization, Clouding, and Solubilization Behavior of Pluronic F127 Solutions. *J. Colloid Interface Sci.* **2000**, *222*, 213–220, doi:10.1006/jcis.1999.6628.

25. Sheelarani, B.; Karunanithi, P.; Dash, S. Effect of Valency of Cation on Micellization Behaviour of Pluronic Mixed Micelle F127 and L64. *Chem. Phys. Lett.* **2020**, *739*, 136956, doi:10.1016/j.cplett.2019.136956.

26. Tripathi, N.; Ray, D.; Aswal, V.K.; Kuperkar, K.; Bahadur, P. Salt Induced Micellization Conduct in PEO–PPO–PEO-Based Block Copolymers: A Thermo-Responsive Approach. *Soft Matter* **2023**, *19*, 7227–7244, doi:10.1039/D3SM00896G.

27. Rudani, B.A.; Sarolia, J.; Rai, R.; Aswal, V.K.; Bahadur, P.; Tiwari, S. Comparative Effect of Physiological Salts upon Micellization of T1304 and T1307. *Langmuir* **2023**, *39*, 9060–9068, doi:10.1021/acs.langmuir.3c00739.

28. Alexandridis, P.; Holzwarth, J.F. Differential Scanning Calorimetry Investigation of the Effect of Salts on Aqueous Solution Properties of an Amphiphilic Block Copolymer (Poloxamer). *Langmuir* **1997**, *13*, 6074–6082, doi:10.1021/la9703712.

29. Ward, C.L.; Cornejo, M.A.; Peli Thanthri, S.H.; Linz, T.H. A Review of Electrophoretic Separations in Temperature-Responsive Pluronic Thermal Gels. *Anal. Chim. Acta* **2023**, *1276*, 341613, doi:10.1016/j.aca.2023.341613.

30. Xu, L.; Li, X.; Zhai, M.; Huang, L.; Peng, J.; Li, J.; Wei, G. Ion-Specific Swelling of Poly(Styrene Sulfonic Acid) Hydrogel. *J. Phys. Chem. B* **2007**, *111*, 3391–3397, doi:10.1021/jp067707d.

31. Loh, W.W.; Lin, Q.; Lim, C.C.; Guo, L.; Tang, Y.K.; Loh, X.J.; Lim, J.Y.C. Hofmeister Effects of Anions on Self-Assembled Thermogels. *Mat. Today Chem.* **2022**, *23*, 100674, doi:10.1016/j.mtchem.2021.100674.

32. Smith, J.D.; Saykally, R.J.; Geissler, P.L. The Effects of Dissolved Halide Anions on Hydrogen Bonding in Liquid Water. *J. Am. Chem. Soc.* **2007**, *129*, 13847–13856, doi:10.1021/ja071933z.

33. Guàrdia, E.; Laria, D.; Martí, J. Hydrogen Bond Structure and Dynamics in Aqueous Electrolytes at Ambient and Supercritical Conditions. *J. Phys. Chem. B* **2006**, *110*, 6332–6338, doi:10.1021/jp056981p.

34. Chen, X.; Flores, S.C.; Lim, S.-M.; Zhang, Y.; Yang, T.; Kherb, J.; Cremer, P.S. Specific Anion Effects on Water Structure Adjacent to Protein Monolayers. *Langmuir* **2010**, *26*, 16447–16454, doi:10.1021/la1015862.

35. Kontogiannis, O.; Selianitis, D.; Lagopati, N.; Pippa, N.; Pispas, S.; Gazouli, M. Surfactant and Block Copolymer Nanostructures: From Design and Development to Nanomedicine Preclinical Studies. *Pharmaceutics* **2023**, *15*, 501, doi:10.3390/pharmaceutics15020501.

36. Li, Y.; Tian, Y.; Jia, X.; Zhang, Z.; Sun, D.; Xie, H.; Zang, D.; Liu, T. Effect of Pharmaceutical Excipients on Micellization of Pluronic and the Application as Drug Carrier to Reverse MDR. *J. Mol. Liquids* **2023**, *383*, 122182, doi:10.1016/j.molliq.2023.122182.

37. Deyerle, B.A.; Zhang, Y. Effects of Hofmeister Anions on the Aggregation Behavior of PEO–PPO–PEO Triblock Copolymers. *Langmuir* **2011**, *27*, 9203–9210, doi:10.1021/la201463g.

38. Ren, C.; Tian, W.; Szleifer, I.; Ma, Y. Specific Salt Effects on Poly(Ethylene Oxide) Electrolyte Solutions. *Macromolecules* **2011**, *44*, 1719–1727, doi:10.1021/ma1027752.

39. Llamas, S.; Mendoza, A.J.; Guzmán, E.; Ortega, F.; Rubio, R.G. Salt Effects on the Air/Solution Interfacial Properties of PEO-Containing Copolymers: Equilibrium, Adsorption Kinetics and Surface Rheological Behavior. *J. Colloid Interface Sci.* **2013**, *400*, 49–58, doi:10.1016/j.jcis.2013.03.015.

40. Muñoz, M.G.; Monroy, F.; Ortega, F.; Rubio, R.G.; Langevin, D. Monolayers of Symmetric Triblock Copolymers at the Air−Water Interface. 1. Equilibrium Properties. *Langmuir* **2000**, *16*, 1083–1093, doi:10.1021/la990142a.

41. Muñoz, M.G.; Monroy, F.; Ortega, F.; Rubio, R.G.; Langevin, D. Monolayers of Symmetric Triblock Copolymers at the Air−Water Interface. 2. Adsorption Kinetics. *Langmuir* **2000**, *16*, 1094–1101, doi:10.1021/la9901433.

42. Noskov, B.A.; Lin, S.-Y.; Loglio, G.; Rubio, R.G.; Miller, R. Dilational Viscoelasticity of PEO−PPO−PEO Triblock Copolymer Films at the Air−Water Interface in the Range of High Surface Pressures. *Langmuir* **2006**, *22*, 2647–2652, doi:10.1021/la052662d.

43. Rivillon, S.; Muñoz, M.G.; Monroy, F.; Ortega, F.; Rubio, R.G. Experimental Study of the Dynamic Properties of Monolayers of PS−PEO Block Copolymers: The Attractive Monomer Surface Case. *Macromolecules* **2003**, *36*, 4068–4077, doi:10.1021/ma021260z.

44. Brinkkötter, M.; Geisler, R.; Großkopf, S.; Hellweg, T.; Schönhoff, M. Influence of Li-Salt on the Mesophases of Pluronic Block Copolymers in Ionic Liquid. *J. Phys. Chem. B* **2020**, *124*, 9464–9474, doi:10.1021/acs.jpcb.0c06664.

45. Kumar, Y.; Hashmi, S.A.; Pandey, G.P. Lithium Ion Transport and Ion–Polymer Interaction in PEO Based Polymer Electrolyte Plasticized with Ionic Liquid. *Solid State Ionics* **2011**, *201*, 73–80, doi:10.1016/j.ssi.2011.08.010.

46. Li, X.; Huang, K.; Xu, Y.; Liu, H. Interaction of Sodium and Potassium Ions with PEO-PPO Copolymer Investigated by FTIR, Raman and NMR. *Vibrational Spectrosc.* **2014**, *75*, 59–64, doi:10.1016/j.vibspec.2014.10.001.

47. Díez-Pascual, A.M.; Monroy, F.; Ortega, F.; Rubio, R.G.; Miller, R.; Noskov, B.A. Adsorption of Water-Soluble Polymers with Surfactant Character. Dilational Viscoelasticity. *Langmuir* **2007**, *23*, 3802–3808, doi:10.1021/la062936c.

48. Cabrerizo-Vílchez, M.A.; Wege, H.A.; Holgado-Terriza, J.A.; Neumann, A.W. Axisymmetric Drop Shape Analysis as Penetration Langmuir Balance. *Rev. Sci. Inst.* **1999**, *70*, 2438–2444, doi:10.1063/1.1149773.

49. Torcello-Gómez, A.; Maldonado-Valderrama, J.; Gálvez-Ruiz, M.J.; Martín-Rodríguez, A.; Cabrerizo-Vílchez, M.A.; De Vicente, J. Surface Rheology of Sorbitan Tristearate and β-Lactoglobulin: Shear and Dilatational Behavior. *J.Non-Newtonian Fluid Mech.* **2011**, *166*, 713–722, doi:10.1016/j.jnnfm.2011.03.008.

50. Berry, J.D.; Neeson, M.J.; Dagastine, R.R.; Chan, D.Y.C.; Tabor, R.F. Measurement of Surface and Interfacial Tension Using Pendant Drop Tensiometry. *J. Colloid Interface Sci.* **2015**, *454*, 226–237, doi:10.1016/j.jcis.2015.05.012.

51. Liggieri, L.; Santini, E.; Guzmán, E.; Maestro, A.; Ravera, F. Wide-Frequency Dilational Rheology Investigation of Mixed Silica Nanoparticle–CTAB Interfacial Layers. *Soft Matter* **2011**, *7*, 7699, doi:10.1039/c1sm05257h.

52. Maestro, A.; Ortega, F.; Rubio, R.G.; Rubio, M.A.; Krägel, J.; Miller, R. Rheology of Poly(Methyl Methacrylate) Langmuir Monolayers: Percolation Transition to a Soft Glasslike System. *J. Chem. Phys.* **2011**, *134*, 104704, doi:10.1063/1.3560612.

53. Monroy, F.; Ortega, F.; Rubio, R.G.; Velarde, M.G. Surface Rheology, Equilibrium and Dynamic Features at Interfaces, with Emphasis on Efficient Tools for Probing Polymer Dynamics at Interfaces. *Adv. Colloid Interface Sci.* **2007**, *134–135*, 175–189, doi:10.1016/j.cis.2007.04.023.

54. Monroy, F.; Ortega, F.; Rubio, R.G. Dilatational Rheology of Insoluble Polymer Monolayers: Poly(Vinylacetate). *Phys. Rev. E* **1998**, *58*, 7629–7641, doi:10.1103/PhysRevE.58.7629.

55. Guzmán, E.; Maestro, A.; Carbone, C.; Ortega, F.; Rubio, R.G. Dilational Rheology of Fluid/Fluid Interfaces: Foundations and Tools. *Fluids* **2022**, *7*, 335, doi:10.3390/fluids7100335.

56. Mendoza, A.J.; Guzmán, E.; Martínez-Pedrero, F.; Ritacco, H.; Rubio, R.G.; Ortega, F.; Starov, V.M.; Miller, R. Particle Laden Fluid Interfaces: Dynamics and Interfacial Rheology. *Adv. Colloid Interface Sci.* **2014**, *206*, 303–319, doi:10.1016/j.cis.2013.10.010.

57. Ramírez, P.; Stocco, A.; Muñoz, J.; Miller, R. Interfacial Rheology and Conformations of Triblock Copolymers Adsorbed onto the Water–Oil Interface. *J. Colloid Interface Sci.* **2012**, *378*, 135–143, doi:10.1016/j.jcis.2012.04.033.

58. Torcello-Gómez, A.; Santander-Ortega, M.J.; Peula-García, J.M.; Maldonado-Valderrama, J.; Gálvez-Ruiz, M.J.; Ortega-Vinuesa, J.L.; Martín-Rodríguez, A. Adsorption of Antibody onto Pluronic F68-Covered Nanoparticles: Link with Surface Properties. *Soft Matter* **2011**, *7*, 8450–8461, doi:10.1039/c1sm05570d.

59. Alexandridis, P.; Athanassiou, V.; Fukuda, S.; Hatton, T.A. Surface Activity of Poly(Ethylene Oxide)-Block-Poly(Propylene Oxide)-Block-Poly(Ethylene Oxide) Copolymers. *Langmuir* **1994**, *10*, 2604–2612, doi:10.1021/la00020a019.

60. Alexandridis, P.; Holzwarth, J.F.; Hatton, T.A. Micellization of Poly(Ethylene Oxide)-Poly(Propylene Oxide)-Poly(Ethylene Oxide) Triblock Copolymers in Aqueous Solutions: Thermodynamics of Copolymer Association. *Macromolecules* **1994**, *27*, 2414–2425, doi:10.1021/ma00087a009.

61. Muñoz, M.G.; Monroy, F.; Hernández, P.; Ortega, F.; Rubio, R.G.; Langevin, D. Anomalous Damping of the Capillary Waves at the Air−Water Interface of a Soluble Triblock Copolymer. *Langmuir* **2003**, *19*, 2147–2154, doi:10.1021/la0206007.

62. Jeworrek, C.; Evers, F.; Howe, J.; Brandenburg, K.; Tolan, M.; Winter, R. Effects of Specific versus Nonspecific Ionic Interactions on the Structure and Lateral Organization of Lipopolysaccharides. *Biophys. J.* **2011**, *100*, 2169–2177, doi:10.1016/j.bpj.2011.03.019.

63. Lucassen, J.; Van Den Tempel, M. Dynamic Measurements of Dilational Properties of a Liquid Interface. *Chem. Eng. Sci.* **1972**, *27*, 1283–1291, doi:10.1016/0009-2509(72)80104-0.

64. Langevin, D. *Light Scattering by Liquid Surfaces and Complementary Techniques*; Surfactant science series; Marcel Dekker: New York, NY, USA, 1992; ISBN 978-0-8247-8607-6.

65. Levich, V.G. *Physicochemical Hydrodynamics*; Prentice-Hall: Englewood Cliffs, NJ, USA, 1962; ISBN 978-0-13-674440-5.

66. Lucassen-Reynders, E.H.; Lucassen, J. Properties of Capillary Waves. *Adv. Colloid Interface Sci.* **1970**, 347–395, doi:10.1016/0001-8686(70)80001-X.

67. Ravera, F.; Ferrari, M.; Santini, E.; Liggieri, L. Influence of Surface Processes on the Dilational Visco-Elasticity of Surfactant Solutions. *Adv. Colloid Interface Sci.* **2005**, *117*, 75–100, doi:10.1016/j.cis.2005.06.002.

68. Maestro, A.; Kotsmar, C.; Javadi, A.; Miller, R.; Ortega, F.; Rubio, R.G. Adsorption of β-Casein–Surfactant Mixed Layers at the Air–Water Interface Evaluated by Interfacial Rheology. *J. Phys. Chem. B* **2012**, *116*, 4898–4907, doi:10.1021/jp301031y.

69. *CRC Handbook of Chemistry and Physics: A Ready-Reference Book of Chemical and Physical Data*; Lide, D.R., Ed.; CRC: Boca Raton, FL, USA, 1998; ISBN 978-0-8493-0479-8.

70. Ozdemir, O.; Karakashev, S.I.; Nguyen, A.V.; Miller, J.D. Adsorption and Surface Tension Analysis of Concentrated Alkali Halide Brine Solutions. *Minerals Eng.* **2009**, *22*, 263–271, doi:10.1016/j.mineng.2008.08.001.

Chapter VI: Interfacial rheology of PtBA/NaCl solutions Langmuir monolayers

6.1. Introduction

The study of polymers confined at interfaces is of paramount importance in many technological applications and for understanding many biological processes [1]. Insoluble monolayers of non-charged flexible homopolymers are the paradigm of quasi-2D model systems because their thickness is usually of the order of the polymer's gyration radius in bulk [2,3]. Poly-(tert-Butyl-Acrylate) (PtBA) is a highly hydrophobic polymer (**Figure 6. 1**), soluble in non-polar solvents such as chloroform which can form Langmuir monolayers at the air-water interface through spreading of the polymer solution in an organic solvent [4]. PtBA has many applications, including its use as a raw material for fiber processing agents, adhesives, coatings, and emulsions. In these applications, the interfacial behavior of the polymer is critically important. Understanding how PtBA behaves at interfaces can inform the design and optimization of these materials for improved performance. Moreover, investigating the interfacial properties of PtBA can provide insights into the fundamental principles governing polymer behavior at interfaces. This knowledge can be extended to other polymers and interfaces, potentially leading to advancements in areas such as drug delivery, where polymeric coatings are used to control the release of active ingredients, and in the development of new materials with tailored interfacial properties [[5]].

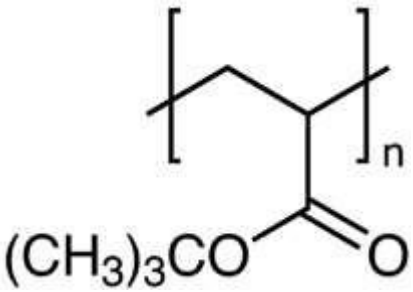

Figure 6. 1. Molecular formula of the Poly-(tert-Butyl Acrylate) (PtBA).

For PtBA Langmuir monolayers, the air-water interface constitutes a good-solvent scenario, where polymer chains are arranged in an extended configuration with most monomers adsorbed at the interface, leading to the entanglement of chains. The relationship between the rheological parameters at a long time and polymer concentration/size is compatible with the existence of diffusional reptation motion controlling the molecular transport in the monolayer [4,6]. The dilational interfacial rheology of PtBA was studied in a previous work [6], with the results evidencing the existence of a reptation-like motion of polymer chains within the interface. In this chapter, the effect of the presence of different NaCl concentrations in the aqueous subphase over the interfacial properties (surface tension and dilational surface rheology) of PtBA Langmuir monolayers will be investigated. The effect of high ionic strength on dilational interfacial rheology of Gibbs monolayers of soluble polymers has been already studied in previous works. For instance, Llamas et al. [7] proved that the presence of Li^+, which interacts with poly(oxyethylene) monomers, affects the interfacial tension and rheology of Gibbs monolayers of Pluronic F-68 (triblock copolymer consisting in two lateral blocks of poly(oxyethylene) and a central one of poly(oxypropylene). Moreover, in *Chapter V* [8], it has

been already discussed that high NaCl concentrations (> 1 M) favor the adsorption of Pluronic F-127 molecules at the air-water interface due to the salting-out effect. This results in a strong decrease in the surface tension and a change in the rheological response of the interface. In the aforementioned systems, the interaction between ions and the polymer occurs in solution and it is reflected at the interface. However, less is known about the potential effect of ionic strength of the subphase over the interfacial properties of a Langmuir monolayer.

In the case of PtBA, which is a non-charged polymer, is not expected that the change in the ionic strength of the subphase introduces any strong interaction between the ions in the subphase and the polymer at the interface. In fact, the presence of salt may lead to a slight increase in the interfacial tension of the water-air interface [9,10], but it is not expected to significantly affect the interfacial properties of the polymer. The interest of this study emerges from the fact that previous studies have shown that the use of dispersion equation for capillary waves (see *Chapter II*, *2.1.4. Electro-Capillary Waves (ECW)*) determine the dilational interfacial modulus may lead to physically unsound results when the ionic strength is increased. Safouane et al. [11] reported negative values of storage and loss dilational interfacial modulus in presence of high concentrations of NaCl (> 3 M); Monroy et al. [12,13] and Stenvot et al. [14] determined the dilational interfacial modulus of cationic surfactant Gibbs monolayers by ECW technique, obtaining negative values of loss modulus at 800 Hz. On the other hand, several authors [13,15-17], performing experiments in cationic surfactant Gibbs monolayers with SQELS technique, obtained also negative values of the loss modulus. Negative values of storage and loss modulus were also reported by Cuenca et al. [18] for experiments on a cationic surfactant performed using the oscillating barriers technique. The authors explain that such negative values, especially those corresponding to the surface viscosities, results from the asymmetry in the adsorption-desorption processes, which makes the usual data analysis procedure unsuitable for the analysis of the system. In summary, many studies in literature have dealt with the potential role of the ionic strength of the determination of the rheological properties of Gibbs monolayers. In contrast, this chapter tries to provide a systematic study of the effect of ionic strength on the interfacial properties of PtBA Langmuir monolayers. Therefore, the effect of the presence of ions in the water subphase was mainly studied to understand how it can affect to the determination of the dilational response, especially at high frequencies obtained by electrocapillary waves measurements (ECW). It is expected that this study can contribute to shed light on the understanding of whether the current models to determine dilational interfacial rheological are still valid in presence of ions that do not interact with the interface. For this purpose, it was studied the effect of the ionic strength on the surface pressure-surface concentration isotherm for PtBA monolayer and the dilatational rheological response obtained in the low frequency region (in the range 10^{-3}-10^{-1} Hz) by the oscillating barriers technique and at higher frequency (in the range 50-500 Hz) by electrocapillary waves technique.

6.2. Materials and methods

6.2.1. Chemicals

Highly monodisperse Poly-tert-Butyl-Acrylate (PtBA) with a weight average molecular weight M_w = 4.6 kDa (M_w/M_n=1.15) purchased at Polymer Source Inc. (Dorvarl, QC, Canada) was dissolved in chloroform stabilized with ethanol (ACS reagent, purity ≥99.8%) supplied by Sigma

Aldrich (Saint Louis, MO, USA) at a concentration of 0.2 g/L. Prior to their use, the solutions were stored, at room temperature, for at least 24 h, in order to ensure a complete dissolution of the PtBA in chloroform. Afterwards, the solutions were stored in a fridge at 4ºC, and they were left to equilibrate at room temperature at least 30 minutes before their use.

NaCl with purity >99.9 % supplied by Sigma-Aldrich (Saint Louis, MO, USA) was dissolved in ultrapure deionized water of Milli-Q grade, with a resistivity higher than 18 MΩ·cm and a total organic content (TOC) of less than 6 ppm. The Milli-Q water was obtained from AquaMAX™-Ultra 370 Series multi-cartridge purification system (Young Lin Instrument Co., Ltd., Gyeonggi-do, Republic of Korea). All solutions were prepared by weight using an analytical balance accurate to ±0.01 mg. Throughout the experiments, temperature was maintained at 23.0ºC with an accuracy of ±0.1 °C.

6.2.2. Experimental methods

The surface pressure $\Pi(\Gamma) = \gamma_0 - \gamma(\Gamma)$, where $\gamma(\Gamma)$ represents the surface tension of the Langmuir monolayer at a defined surface concentration Γ, and γ_0 the surface tension of the bare air-water interface, was measured by using a surface force tensiometer (NIMA PS4, manufactured by Nima Technology, Coventry, UK) fitted with disposable Wilhelmy paper plates (Whatman CHR1 chromatography paper, Merck, Darmstadt) of 20.6 mm of perimeter. A fresh paper plate was used for each measurement to prevent any potential modifications on the plate surface as a result of the material adsorption during previous experiments. The measurements were obtained with an error of ± 1 mN/m. For all the measurements, the temperature was controlled by using a thermostatic bath set at 23.0±0.1 ºC. Each experimental data point reported was an average of at least three independent measurements.

Two experimental techniques were used to determine the dilational rheological response of PtBA Langmuir monolayers in two different frequency (ν) ranges. In the low-frequency range (10^{-3}-10^{-1} Hz), oscillating barrier measurements in a Langmuir balance (model 702 from Nima Technology, Coventry, UK) with a total area of 700 cm^2 (70 cm length x 10 cm width). This method was already described elsewhere [19-21]. In order to minimize the effect of shear on the results obtained using the oscillatory barrier method, the experiments were carried out using a relatively small deformation amplitude (5%). In addition, the paper Wilhelmy plate was placed parallel to the barrier movement in the center of the trough and the barrier oscillations were performed far enough from the contact probe to avoid any possible role of unintended flows in the dilational response. Dilational interfacial rheology at high frequencies (in the range of 80-450 Hz) was evaluated by means of a homemade electrocapillary waves (ECW) device (see *Chapter II*, *2.1.4. Electro-Capillary Waves (ECW)*). This method was also described in previous works [19,21-24].

For the preparation of the monolayer, NaCl solutions of different concentrations (in the range 0-1 M) were poured in the Teflon Langmuir trough, and then PtBA Langmuir monolayers were prepared on their surface by the spreading PtBA solution in chloroform. This was done by uniformly pouring drop-by-drop by means of a Hamilton syringe the required amount of polymeric solution to achieve a specific surface concentration. After, the spreading of the polymer at the air-water interface, it is needed to wait for a complete evaporation of the

chloroform, guaranteeing the correct spreading of the polymer chains at the interface. This was checked by the absence of change in the surface pressure by a period of 10 minutes.

6.3. Results and discussion

6.3.1. Surface pressure isotherms

Figure 6. 2 displays the surface pressure isotherms of PtBA in terms of a surface pressure vs. surface concentration representation as was obtained for monolayers spread on the surfaces of water solutions with different NaCl concentrations, i.e., different ionic strengths (*I*). These isotherms are a true equilibrium representation as were obtained under static conditions, i.e., they were obtained by the sequential addition of small volumes of polymer solution and waiting until the equilibration (point-by-point isotherm), and therefore the nonequilibrium effects associated with the traditional methodology of compression were avoided [2].

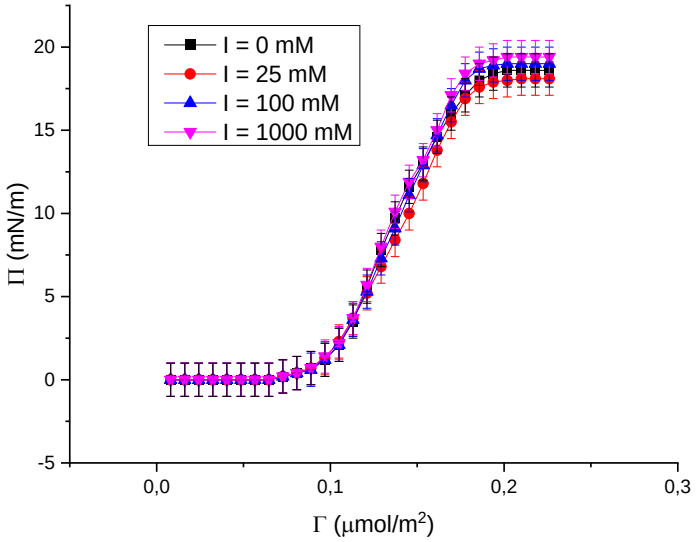

Figure 6. 2. Surface pressure isotherms of PtBA on subphase with different ionic strengths. Notice that the isotherms were obtained point-by-point.

The results show that independently of the ionic strength of the subphase, the surface pressure increases with PtBA surface concentration. Moreover, the results show that within the error bars, there are no changes in the surface pressure isotherm with the variation of the NaCl concentration. This suggests that in the case of PtBA monolayers, the presence of NaCl in the subphase does not affect the behavior of the monolayers. Therefore, the results allow ruling out any interaction of the insoluble monolayer with the Na^+ and Cl^- ions, and therefore this system offers a valuable alternative for evaluating the possible effect of the ionic strength on the reliability of the determination of the rheological properties of Langmuir monolayers. On the other hand, the here obtained isotherm for PtBA on a subphase at $I = 0\ mM$ agrees with the variation of the surface pressure on the molecular weight reported by Maestro et al. [4].

Figure 6. 3 represents for the sake of example, the surface pressure isotherm obtained for monolayers on a subphase without NaCl to elucidate the different possible regime appearing on the monolayer behavior on increasing the surface concentration.

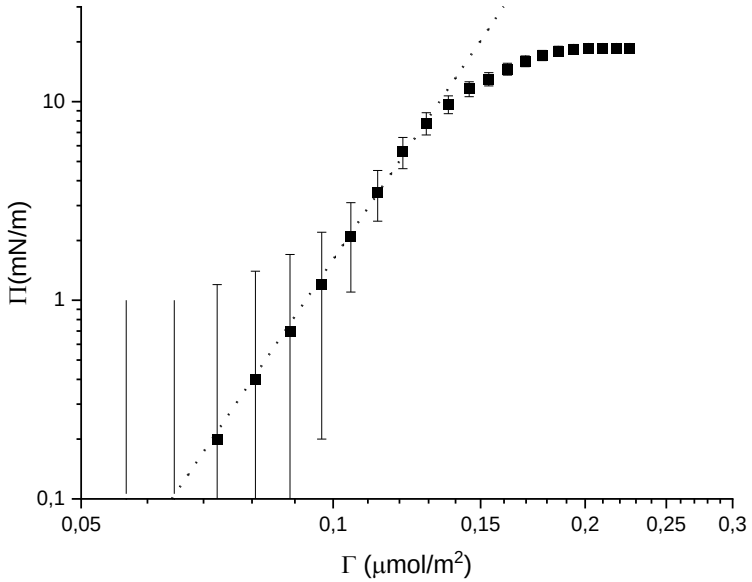

Figure 6. 3. Surface pressure isotherm for PTBA ($M_w = 4.6\ kDa$, $M_w/M_n = 1.15$) on a subphase at $I = 0mM$. The squares correspond to the experimental data and the dashed line to the $\Pi \sim \Gamma^n$ dependence expected for the semidilute regime.

According to the results reported by Maestro et al. [4], PtBA monolayers present, at low surface concentration, a diluted regime, where a small change on the surface pressure occurs as the surface concentration increases, i.e., Π remains close to zero, at the lowest values of the surface concentration. The increase of the surface concentration pushes the system to a regime where the surface pressure changes fast with the surface concentration. This is the so-called the semi-diluted regime, in which the dependence of the surface pressure on the surface concentration can be expressed in terms of a power law relationship between Π and Γ ($\Pi \sim \Gamma^n$). At the highest surface pressures and highest surface concentrations, the system enters in a quasi-plateau region where surface pressure remains almost constant with the increase of the surface concentration, defining the concentrated regime. Unfortunately, with the precision of the obtained experimental data, it was not possible to observe the diluted region in the log-log plot of the obtained isotherms, but it can be assumed that it appears for surface concentrations below 0.07 μmol/m^2.

The analysis of the part of the isotherm corresponding to the semi-dilute regime in terms of $\Pi \sim \Gamma^n$ results in an exponent 6.2±0.2, which is higher than the value $n = 3$ predicted by the theory for good solvent conditions. In fact, it is expected that the scaling exponent fulfills the relationship $n = 2\upsilon/(2\upsilon - 1)$, where υ is the Flory exponent. The Flory exponent in 2D, i.e., monolayers, assumes a value of 0.75 for good solvent conditions, whereas it becomes 0.5 under bad solvent conditions [25]. In the here studied, system υ=0.6. Therefore, it can be expected that the PtBA molecules at the water-air interface assumes a conformation that it is an intermediate state between extended and complete coiled chains.

6.3.2. Equilibrium dilational elasticity

The equilibrium dilational elasticity, E_0 (defined as the dilational storage modulus at zero frequency), is a critical attribute of the monolayer, providing information related to the rigidity

of the monolayer and its capacity to store elastic energy. This property can be obtained from the data of the surface pressure isotherm according to the following equation,

$$E_0(\Gamma) = E_S(\nu = 0, \Gamma) = \Gamma \frac{\partial \Pi(\Gamma)}{\partial \Gamma}. \quad (6.\ 1)$$

Figure 6. 4 shows the dependence of the equilibrium dilational elasticity on the surface concentration for Langmuir monolayers of PtBA on aqueous solutions of different NaCl concentrations. The results show that as it occurs with the surface pressure isotherms, the effect of the ionic strength on the dilational elasticity can be considered almost negligible. In all the cases, the curve of the equilibrium dilational elasticity shows a region where it assumes values close to zero, which corresponds to the quasi-dilute region. Then, the equilibrium elasticity increases with the surface concentration along the semidilute and concentrated regimes. In the latter, the monolayer becomes compact, and the equilibrium dilational elasticity reaches a maximum at a surface concentration in the range $0.15 - 0.16\ \mu mol/m^2$. This maximum is close to the inflection point of the surface pressure isotherms. Once the monolayer reaches the maximum packing, and the elasticity drop to zero with further increases in the surface concentration.

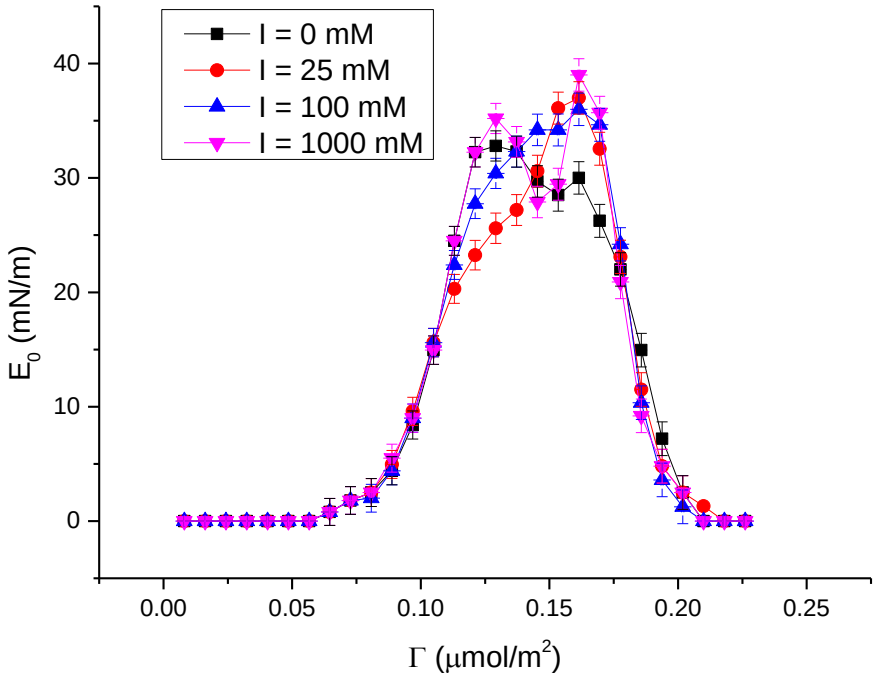

Figure 6. 4. Equilibrium elasticity $E_0(\Gamma)$, as a function of PtBA surface concentration, at different NaCl concentrations (I).

As expected, E_0 depends on Γ, and it shows, at every NaCl concentration, a peak. Since $\Pi(\Gamma)$ does not depend on *I*, $E_0(\Gamma)$ is not affected by NaCl concentration as well.

6.3.3. Low frequency dilational rheology

After evaluating the negligible effect of the ionic strength on the equilibrium properties of PtBA monolayers. The next step is to evaluate how the ionic strength affects the interfacial response

against dilational deformations. For this purpose, a low frequency study was conducted using the oscillatory barrier method in a Langmuir balance. Thus, it was possible to evaluate the surface dilational response at low frequencies (in the frequency range $2.5 \cdot 10^{-3} - 10^{-1}\ Hz$). **Figure 6. 5** shows the frequency (ν) dependence of the storage E_s and loss E_i dilational moduli corresponding to PtBA monolayers spread on water subphases of different ionic strengths I and at a fixed surface concentration $\Gamma = 0.11\ \mu mol/m^2$, which corresponds to the semidilute regime of the monolayer.

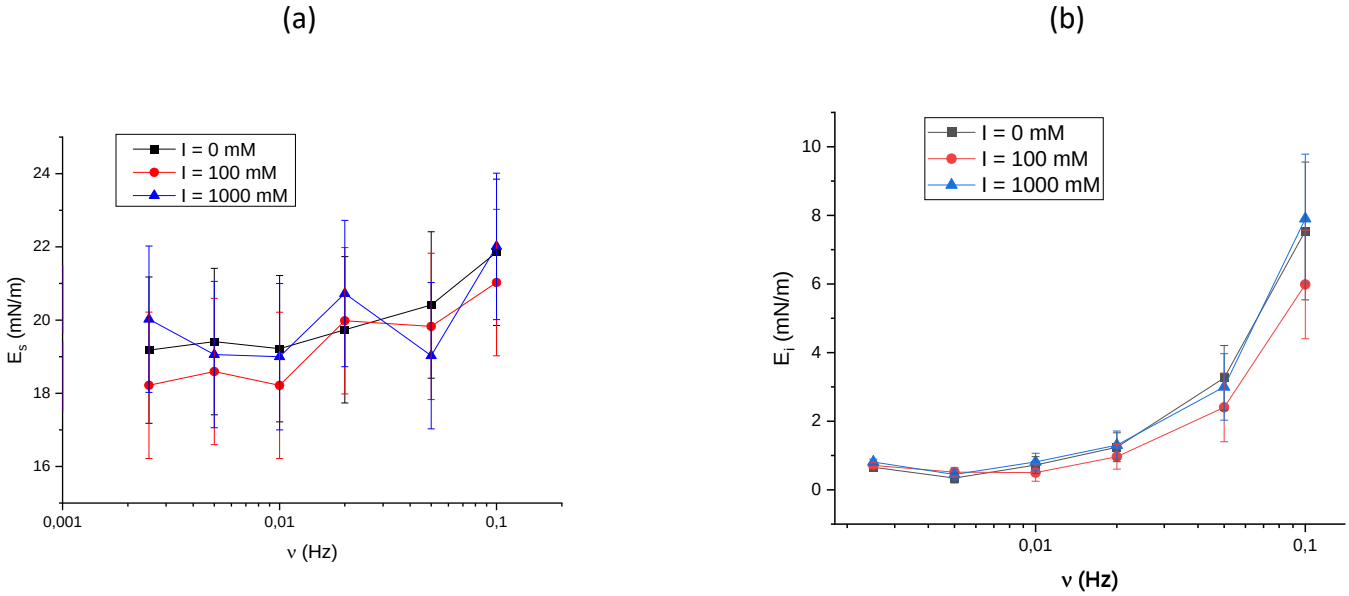

Figure 6. 5. Frequency (ν) dependence of the storage dilational modulus (E_s) and loss dilational modulus (E_i) obtained by oscillatory barriers (at 23 °C), within $2.5 \cdot 10^{-3} - 10^{-1}\ Hz$ frequency range, of PtBA Langmuir monolayers ($\Gamma = 0.11\ \mu mol/m^2$) spread on aqueous subphases with different ionic strengths.

The results show that E_s does not depend on ionic strength within the explored frequency range, and it remains almost constant within the experimental window, even though the results at the highest frequencies suggests a slight increases. On the other hand, the values of $E_s(\nu)$ plotted in **Figure 6. 5** (a) are compatible with the values of E_0. In fact, at the same surface concentration $\Gamma = 0.11\ \mu mol/m^2$, $E_0 \approx 19.5 \pm 2\ mN/m$. According to the plots shown in **Figure 6. 5** (b), neither E_i depends on ionic strength, and it increases at the highest frequencies of the considered frequency range, which suggests the presence of a relaxation process with a characteristic frequency in the range 0.1 Hz. This latter confirm the relaxation process which was suggested from the frequency dependence of the storage modulus.

6.3.3. High-frequency dilational rheology: Electro-Capillary Wave (ECW) measurements

The evaluation of the damping of capillary waves excited by electric fields on PtBA Langmuir monolayers at the air/solution interface makes it possible to determine the dilational interfacial rheological response of the interface in the range of high frequencies (80-450 Hz). In the here discussed study, it was not possible to perform experiments for frequencies higher than 450 Hz due to the strong decrease in the intensity of the signal, which significantly reduced the sensitivity of the measurements.

For a capillary wave excited in a point of the interface (represented by the xy plane), it is possible to define its spatial profile (represented by the vertical displacement along z-

direction, u_z) by the following expression (see *Chapter II, 2.1.4. Electro-Capillary Waves (ECW)*),

$$u_z = u_z^0 e^{-\beta x} \cos\left(\frac{2\pi}{\lambda}x + \varphi\right), \tag{6. 2}$$

with u_z^0 being the wave amplitude, and β, λ and ϕ the damping coefficient, the characteristic capillary wavelength and the phase lag, respectively. **Figure 6. 6** shows the frequency dependences of both β and λ for PtBA monolayers ($\Gamma = 0.11\ \mu mol/m^2$) spread on aqueous solutions with different ionic strengths.

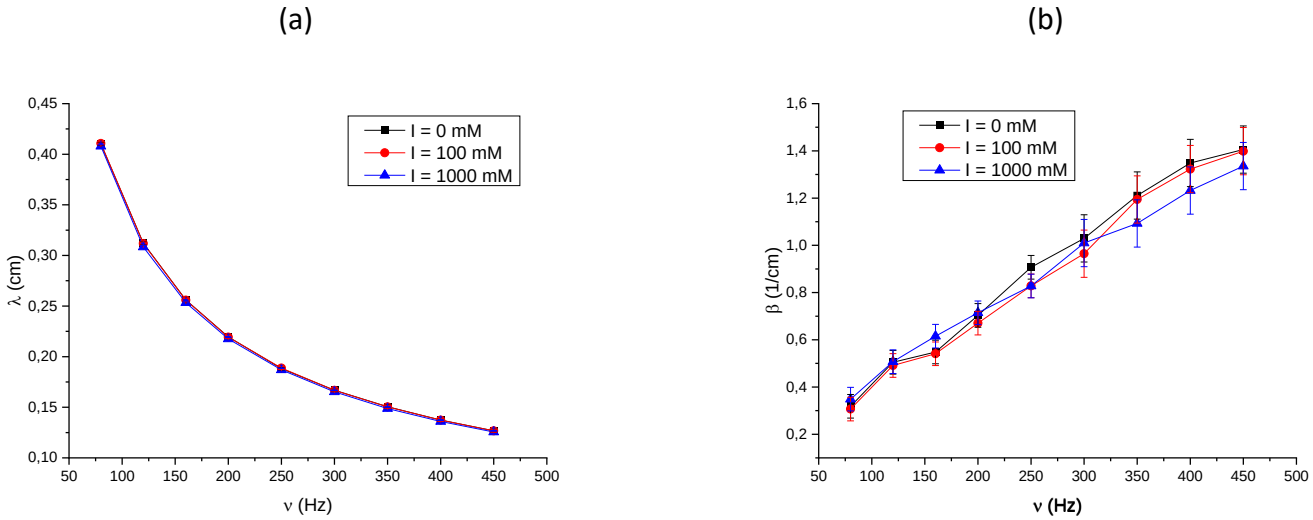

Figure 6. 6. Frequency (ν) dependences of the wavelength λ (a) and damping β (b) of PtBA Langmuir monolayers ($\Gamma = 0.11\ \mu mol/m^2$) spread on aqueous subphases with different ionic strengths.

According to **Figure 6. 6** (a), λ decreases with frequency. Results seem to align with Kelvin's law (see *Chapter II, 2.1.4. Electro-Capillary Waves (ECW)*). The exponent n was found to be around $n \approx 1.47$ (very similar to the value $n = \frac{3}{2}$ predicted by Kelvin law). On the other hand, λ does not seem to vary with *I*, reflecting that NaCl does not change the value of the surface tension γ of PtBA monolayers (in line with the surface pressure isotherms shown in **Figure 6. 2**).

The damping coefficient, as shown in **Figure 6. 6** (b), increases with the frequency, but its trend cannot be interpreted in terms of a Stokes-like law ($\beta \sim \nu^n$, with $n = 1$, see *Chapter II, 2.1.4. Electro-Capillary Waves (ECW)*). In fact, according to the experimental results, $n \approx 0.88$. The diference with respect to Stokes law is due to the viscoelastic behavior of PtBA monolayers. Ionic strength does not affect the values of β. In fact, the bulk viscosity of the aqueous subphase (η) does not change significantly in presence of salt, at least for $I \leq 1M$ [8,11]. Furthermore, as shown in **Figure 6. 2**, salt concentration does not change the surface tension, so, subsequently, the damping properties of the interface remain unchanged.

In order to determine the dilational response of the monolayer from electrocapillary wave experiments, the dispersion equation (a relation between the characteristics parameter associated with the propagation of the transversal waves: the frequency ν, the wavelength λ,

and the damping coefficient β) must be solved with respect to the complex dilational modulus $E_s^*(\nu)$ (see *Chapter II*, *2.1.4. Electro-Capillary Waves (ECW)*). Being $\omega = 2\pi\nu$ the angular frequency, $E_s^*(\nu)$ can be determined as follows,

$$E_s^*(\nu) = E_s(\nu) + i\omega k_s(\nu) = \frac{\dfrac{-\left(\eta\omega(q-m)\right)^2}{\gamma q^2 + i\eta\omega(q+m) - \dfrac{\rho}{q}\omega^2} - i\eta\omega(q+m)}{q^2}, \tag{6. 3}$$

where *q* is the complex wavevector, defined as,

$$q = \frac{2\pi}{\lambda} - i\beta, \tag{6. 4}$$

and *m* is the capillary penetration depth (Re(m) > 0),

$$m = \sqrt{q^2 + i\omega\frac{\rho}{\eta}}, \tag{6. 5}$$

Before to discuss the rheological data obtained from the analysis of the dispersion equation, it will be evaluated the accuracy of the ECW technique to extract information of the dilational response of the interfacial film. In order to guarantee that dilational data obtained by ECW experiments are of good quality, it is needed to take in to consider the resonance condition. According to the resonance condition, the higher accuracy of capillary wave to provide information on the dilational response of the interface occurs when the following condition is satisfied (see *Chapter II*, *2.1.4. Electro-Capillary Waves (ECW)*) [8],

$$\left(\frac{E_s}{\gamma}\right)_R = \left(\frac{q\eta^2}{\gamma\rho}\right)^{1/4} \approx 0.10 - 0.15, \tag{6. 6}$$

where the subindex R indicates the resonance condition. If the E_s/γ ratio, determined by experimental data, is far above the range associated with the resonance condition, the dilational parameters extracted from the analysis of the experimental data will be affected from a big uncertainty. **Figure 6. 7** shows the E_s/γ ratio for all the analyzed samples:

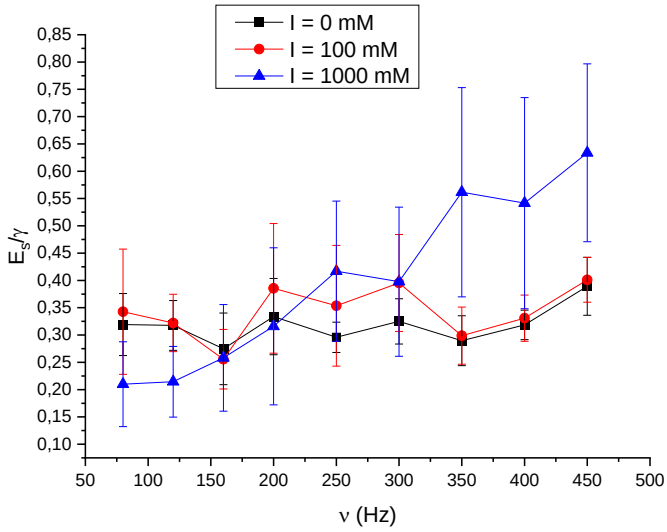

Figure 6. 7. Frequency dependence of $^{E_s}/_{\gamma}$ ratio of PtBA monolayers (at $\Gamma = 0.11\ \mu mol/m^2$) spread on water subphases of different ionic strengths.

The results shows that the values of $^{E_s}/_{\gamma}$ ratio, at all the frequencies probed, and in particular for $\nu > 120Hz$, exceed the values corresponding to the resonance condition. Therefore, it may be expected a high uncertainty in the determination of the dilational properties by ECW. At $I = 1M$, the values of $^{E_s}/_{\gamma}$ clearly stand out, which suggests that both E_s and E_i, at this value of NaCl concentration, will be affected by big error bars. This results aligns with the behavior of Pluronic F-68 Gibbs monolayer studied in *Chapter V* [8] at higher ionic strength, an increase of $^{E_s}/_{\gamma}$ and of E_s error bar was observed as well.

Figure 6. 8 displays the frequency dependences, within the whole experimental window, i.e., combining data of low and high frequencies, of the storage E_s, as well as the loss $E_i = \omega k_s$ dilational moduli for PtBA monolayers (at $\Gamma = 0.11\ \mu mol/m^2$) spread on subphase with different ionic strengths.

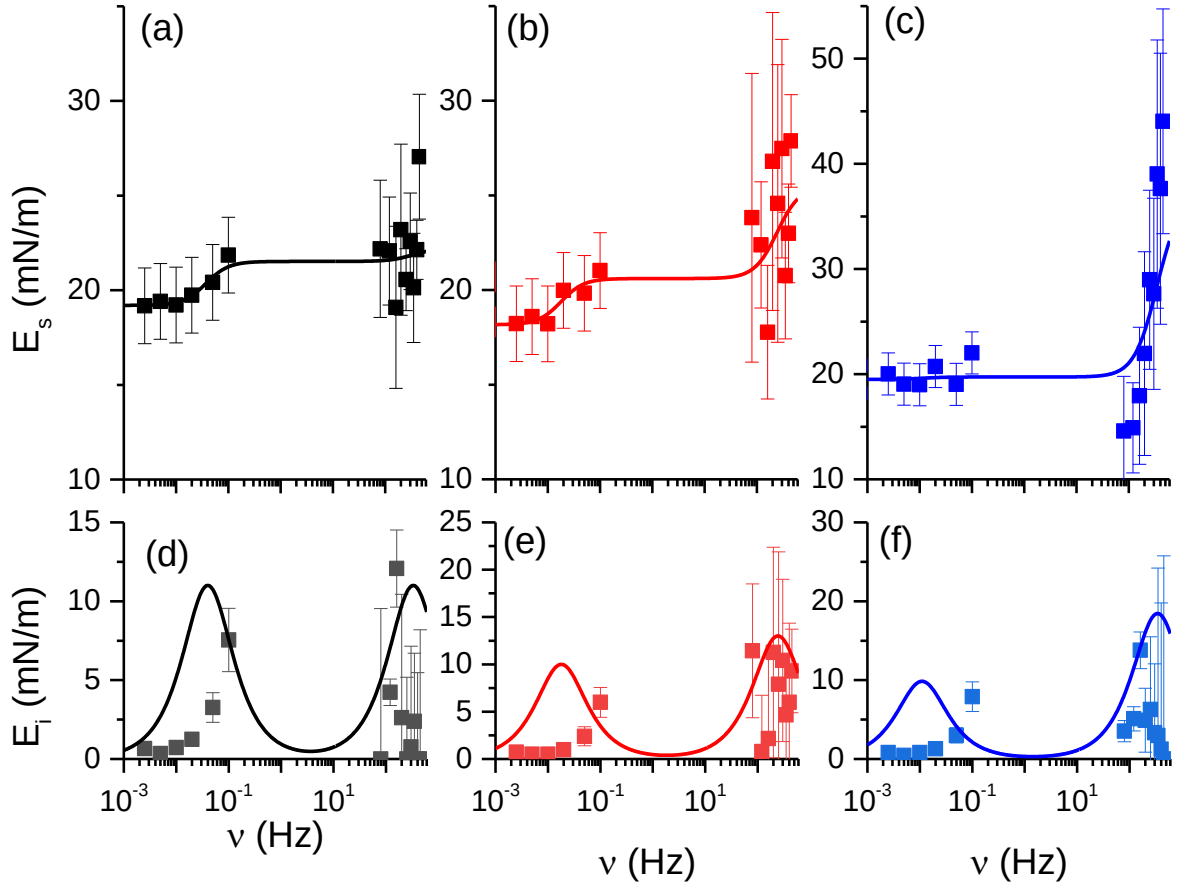

Figure 6. 8. Storage dilational modulus E_s (a, b and c) and loss dilational modulus $E_i = \omega k_s$ (d, e and f) as a function of the frequency ν of PtBA monolayers (at $\Gamma = 0.11\ \mu mol/m^2$) spread on subphases of different ionic strengths. (a and d) 0 mM, (b and e) 100 mM and (c and f) 1M.

The results demonstrated that according with the above discussion related to the resonance condition, dilational results obtained from ECW measurements are affected by a big error bar, especially at the highest ionic strength probed. At $I = 0\ mM$ and at $I = 100\ mM$m the data obtained by ECW appears to match with those obtained by using oscillatory barrier measurements. Conversely, at $I = 1M$, ECW results appear shifted to lower values of the storage modulus than those obtained by oscillatory barrier experiments, which is not reasonable from the physical point of view, and only the big error bars confirm the existence of a physically sound scenario. The poor quality of the results can be understood by considering that under the studied conditions where the system does not comply with the resonance condition, there is a lack of coupling between transversal and longitudinal modes, and, therefore, the determination of the dilational rheological properties by ECW experiments is affected by inaccuracy issues.

In order to analyze the dilational spectrum, two relaxation process were considered, which is summarized in the following expression,

$$E = E_0 + E_1 \frac{1 + i\lambda_1}{1 + \lambda_1^2} + E_2 \frac{1 + i\lambda_2}{1 + \lambda_2^2}, \qquad (6.\ 7)$$

where E_0 refers to the Gibbs elasticity, and E_1 and E_2 correspond to the high frequency elasticity limit for the first and second relaxation processes. $\lambda_j = {}^{\nu_j}/_{\nu}$, where the subindex j can assume values of 1 or 2 depending on the considered relaxation process. **Table 6. 1** summarizes the results obtained by the analysis of the experimental data by considering to relaxation processes.

Table 6. 1. Summary of the characteristics rheological parameters obtained by fitting the experimental results to a model including two relaxation processes.

c_{NaCl} (mM)	E_0 (mN/m)	E_1 (mN/m)	ν_1 (Hz)	E_2 (mN/m)	ν_2 (Hz)
0	19±3	22±6	0.04±0.20	22±4	332±4332
100	19±5	21±5	0.02±0.1	26±4	244±528
1000	19±6	20±4	0.01±0.7	37±10	343±491

Considering the results and the experimental limitations, it can be considered that PtBA films present the same behavior independently on ionic strength, even though the properties of bulk are slightly different with the increase of the ionic strength. In fact, the values of ρ and η are slightly higher [8,11]). A similar behavior was already observed with Pluronic F-68 monolayers, as shown in *Chapter V* [8].

6.4. Conclusions

This chapter was focused on studying the effect of the ionic strength on the interfacial tension and dilatational rheology of PtBA Langmuir monolayers spread on aqueous subphase with different ionic strengths (different NaCl concentration). The dilational rheology studies were performed in two different frequency ranges: $2.5 \cdot 10^{-3} - 10^{-1}\ Hz$ (by means of a Langmuir trough with oscillating barriers) and $80 - 450\ Hz$ (by means of ECW technique). The results have evidenced that the addition of salt ($I \leq 1M$) does not change the properties of the interface. In fact, neither surface pressure nor equilibrium elasticity are affected by ionic strength, which leads to the conclusion that NaCl does not interact with PtBA monolayers. The dilational rheology of PtBA monolayers ($\Gamma = 0.11\ \mu mol/m^2$) at low frequency ($2.5 \cdot 10^{-3} - 10^{-1}\ Hz$) does not change in presence of NaCl in the subphase. The ECW experiments result in a high uncertainty in the determination of the dilational modulus, which can be associated with the fact that the resonance condition is not fulfilled.

In order to fully understand the impact of ionic strength on the dilational rheology of PtBA Langmuir monolayers, other studies may be required, such as the extension of the range of frequency in the study of dilational rheology (possibly in $10^3 - 10^5\ Hz$ frequency range), or the extension the range of polymer surface concentrations and/or ionic strengths.

6.5. References

1. Binder, K. *Classical Statistical Mechanics*; Springer: Dordrecht, Netherlands, 2003; 10.1007/978-94-010-0173-1_1pp. 3-35.
2. Hilles, H.; Maestro, A.; Monroy, F.; Ortega, F.; Rubio, R.G.; Velarde, M.G. Polymer monolayers with a small viscoelastic linear regime: equilibrium and rheology of

poly(octadecyl acrylate) and poly(vinyl stearate). *J Chem Phys* **2007**, *126*, 124904, doi:10.1063/1.2714514.
3. Henderson, J.A.; Richards, R.W.; Penfold, J.; Thomas, R.K. Neutron reflectometry using the kinematic approximation and surface quasi-elastic light scattering from spread films of poly(methyl methacrylate). *Macromolecules* **2002**, *26*, 65-75, doi:10.1021/ma00053a010.
4. Maestro, A.; Hilles, H.M.; Ortega, F.; Rubio, R.G.; Langevin, D.; Monroy, F. Reptation in langmuir polymer monolayers. *Soft Matter* **2010**, *6*, 4407, doi:10.1039/c0sm00250j.
5. Da Rocha Rodrigues, R.; Da Silva, R.; Caseli, L.; Peres, L.O. Conjugated polymers as Langmuir and Langmuir-Blodgett films: Challenges and applications in nanostructured devices. *Adv Colloid Interface Sci* **2020**, *285*, 102277, doi:10.1016/j.cis.2020.102277.
6. Maestro Martín, A. Dymanics of interfacial systems. Universidad Complutense de Madrid, 2010.
7. Llamas, S.; Mendoza, A.J.; Guzman, E.; Ortega, F.; Rubio, R.G. Salt effects on the air/solution interfacial properties of PEO-containing copolymers: equilibrium, adsorption kinetics and surface rheological behavior. *J Colloid Interface Sci* **2013**, *400*, 49-58, doi:10.1016/j.jcis.2013.03.015.
8. Carbone, C.; Guzmán, E.; Maldonado-Valderrama, J.; Rubio, R.G.; Ortega, F. Ionic Strength Effect in the Equilibrium and Rheological Behavior of an Amphiphilic Triblock Copolymer at the Air/Solution Interface. *Colloids and Interfaces* **2024**, *8*, 16, doi:10.3390/colloids8020016.
9. Manciu, M.; Ruckenstein, E. Ions near the air/water interface: I. Compatibility of zeta potential and surface tension experiments. *Colloids and Surfaces A: Physicochemical and Engineering Aspects* **2012**, *400*, 27-35, doi:10.1016/j.colsurfa.2012.02.038.
10. Bahadur, R.; Russell, L.M.; Alavi, S. Surface tensions in NaCl-water-air systems from MD simulations. *J Phys Chem B* **2007**, *111*, 11989-11996, doi:10.1021/jp075356c.
11. Safouane, M.; Langevin, D. Surface viscoelasticity of concentrated salt solutions: specific ion effects. *Chemphyschem* **2009**, *10*, 222-225, doi:10.1002/cphc.200800527.
12. Monroy, F.; Giermanska Kahn, J.; Langevin, D. Dilational viscoelasticity of surfactant monolayers. *Colloids and Surfaces A: Physicochemical and Engineering Aspects* **1998**, *143*, 251-260, doi:10.1016/s0927-7757(98)00373-2.
13. Monroy, F.; Giermanska-Kahn, J.; Langevin, D. Anomalous Damping of Capillary Waves With Surfactant Solutions. *Journal of Non-Equilibrium Thermodynamics* **2001**, *25*, doi:10.1515/jnetdy.2000.019.
14. Stenvot, C.; Langevin, D. Study of viscoelasticity of soluble monolayers using analysis of propagation of excited capillary waves. *Langmuir* **2002**, *4*, 1179-1183, doi:10.1021/la00083a022.
15. Earnshaw, J.C.; McCoo, E. Surface Light-Scattering Studies of Surfactant Solutions. *Langmuir* **2002**, *11*, 1087-1100, doi:10.1021/la00004a011.
16. Sharpe, D.; Eastoe, J. Properties of Surfactant Monolayers Studied by Surface Light Scattering. *Langmuir* **1996**, *12*, 2303-2307, doi:10.1021/la951078+.
17. Monroy, F.; Muñoz, M.G.; Rubio, J.E.F.; Ortega, F.; Rubio, R.G. Capillary Waves in Ionic Surfactant Solutions: Effects of the Electrostatic Adsorption Barrier and Analysis in Terms of a New Dispersion Equation. *The Journal of Physical Chemistry B* **2002**, *106*, 5636-5644, doi:10.1021/jp012044f.
18. Cuenca, V.E.; Ferna Ndez Leyes, M.; Falcone, R.D.O.; Correa, N.M.; Langevin, D.; Ritacco, H.N. Interfacial Dynamics and Its Relations with ?Negative? Surface Viscosities

Measured at Water?Air Interfaces Covered with a Cationic Surfactant. *Langmuir* **2019**, *35*, 8333-8343, doi:10.1021/acs.langmuir.9b00534.
19. Mendoza, A.J.; Guzman, E.; Martinez-Pedrero, F.; Ritacco, H.; Rubio, R.G.; Ortega, F.; Starov, V.M.; Miller, R. Particle laden fluid interfaces: dynamics and interfacial rheology. *Adv Colloid Interface Sci* **2014**, *206*, 303-319, doi:10.1016/j.cis.2013.10.010.
20. Hilles, H.; Monroy, F.; Bonales, L.J.; Ortega, F.; Rubio, R.G. Fourier-transform rheology of polymer Langmuir monolayers: analysis of the non-linear and plastic behaviors. *Adv Colloid Interface Sci* **2006**, *122*, 67-77, doi:10.1016/j.cis.2006.06.013.
21. Monroy, F.; Ortega, F.; Rubio, R.G.; Velarde, M.G. Surface rheology, equilibrium and dynamic features at interfaces, with emphasis on efficient tools for probing polymer dynamics at interfaces. *Adv Colloid Interface Sci* **2007**, *134-135*, 175-189, doi:10.1016/j.cis.2007.04.023.
22. Liggieri, L.; Santini, E.; Guzmán, E.; Maestro, A.; Ravera, F. Wide-frequency dilational rheology investigation of mixed silica nanoparticle–CTAB interfacial layers. *Soft Matter* **2011**, *7*, 7699, doi:10.1039/c1sm05257h.
23. Monroy, F.; Ortega, F.; Rubio, R.G. Dilatational rheology of insoluble polymer monolayers: Poly(vinylacetate). *Physical Review E* **1998**, *58*, 7629-7641, doi:10.1103/PhysRevE.58.7629.
24. Guzmán, E.; Maestro, A.; Carbone, C.; Ortega, F.; Rubio, R.G. Dilational Rheology of Fluid/Fluid Interfaces: Foundations and Tools. *Fluids* **2022**, *7*, 335, doi:10.3390/fluids7100335.
25. Langevin, D.; Monroy, F. Interfacial rheology of polyelectrolytes and polymer monolayers at the air–water interface. *Current Opinion in Colloid & Interface Science* **2010**, *15*, 283-293, doi:10.1016/j.cocis.2010.02.002.

Section 4 Interfacial rheology of covered-silica nanosuspensions

This section is dedicated to the study of the interfacial properties of polymer-capped particles aqueous dispersions to provide a deep understanding on the interaction between particles and surface active molecules, which allows assessing the influence of this nanocomposite dispersion on the liquid/vapor interface stability and properties. This section is divided into two chapters:

- *Chapter VII: Interfacial rheology of Poloxamer-triblock-copolymer/Silica nanosuspensions*

This chapter is aimed at investigating the effect of Pluronic F-127 (an amphiphilic triblock copolymer) on silica nanoparticles adsorption at water/vapor interfaces, as well as on the interfacial rheology (at low frequency, 10^{-3}-10^{-1} Hz) of the formed layers, aimed at understanding the interaction between Pluronic F-127 and silica nanoparticles and the adsorption of complexes at liquid/vapor interface.

- *Chapter VIII: Interfacial Rheology of Chitosan-Silica Nanocomposite Films*

Chapter VIII has the purpose of evaluating the interaction between chitosan (a positively charged polyelectrolyte) and negatively charged silica nanoparticles, the stability of the resulting water dispersions at different pH and concentration condition, the interfacial tension of the dispersions, and the dilational interfacial rheology measured by means of ECW technique.

Chapter VII: Interfacial rheology of Poloxamer-triblock-copolymer/Silica nanosuspensions[††]

7.1. Introduction

The stability of colloidal dispersions can be tuned by physisorption of surfactants or polymers onto their surface through interactions such as electrostatic interactions, hydrogen bonding or van der Waals forces [1-3]. The occurrence of such association results in the formation of complexes that have different properties from the original particles. In fact, the formation of these complexes can modify the interparticle interactions and their ability to adsorb at fluid/fluid interfaces [4,5], which are very important issues for controlling the stability of thin films, emulsions, and foams [6,7]. For example, silica nanoparticles are often extremely hydrophilic and tend to remain dispersed in the bulk, which limits their use in stabilizing emulsions or foams. However, the addition of molecules that can interact with their surface can help to improve their ability to adsorb at fluid/fluid interfaces [8,9]. This has been demonstrated by several authors by using surfactants as modifiers, most of them interacting through electrostatic interactions [10-13] or directly grafted through chemical bonds [14,15].

The enhanced adsorption capacity of modified nanoparticles at fluid/fluid interfaces, in contrast to bare particles, can be ascribed to the surface-active nature of the additives [8]. This effect is particularly noticeable when polymer-capped nanoparticles are used, as they are able to form highly stable emulsions, whereas both unmodified particles and the capping polymer do not exhibit suitable emulsifying properties in solution [14,16]. However, the specific behavior of the polymer responsible for this enhanced efficiency is still poorly understood. Unlike unmodified nanoparticles, which have a limited capability to significantly reduce interfacial tension both at liquid/liquid and liquid/vapor interfaces through spontaneous adsorption, from low-concentration suspensions, capped nanoparticles have the capacity to lower surface tension due to the presence of surface-active molecules bound to their surfaces. This drives the formation of a particle shell at the interface [14], which is relevant to various scientific fields, including physics, chemistry, and materials science, and therefore the motivation to study particle adsorption particles at fluid/fluid interfaces is multifaceted. First, interfacial adsorption plays a central role in several natural and industrial scenarios. In biological systems, the adsorption of proteins and surfactants on cell membranes affects cell function and communication. In industrial applications such as emulsions and foams, adsorption of particles at liquid interfaces affects stability, rheology and overall product quality. In addition, the manipulation of interfacial adsorption has practical implications. Tailoring the adsorption of nanoparticles or molecules can lead to advanced materials with tunable properties, such as enhanced catalytic activity, improved drug delivery systems, and innovative sensors. This knowledge has the potential to revolutionize many industries, from healthcare to energy [16].

The aim of this chapter is to assess the effect of Pluronic F-127, a triblock copolymer composed of two poly(ethylene oxide) terminal segments and a central poly(propylene oxide) segment

[††] This chapter is in part included in the publication: Carbone, C.; Rubio-Bueno, A.; Ortega, F.; Rubio, R.G.; Guzmán, E. Adsorption of Mixed Dispersions of Silica Nanoparticles and an Amphiphilic Triblock Copolymer at the Water–Vapor Interface. Appl. Sci.2023,13, 10093. http://dx.doi.org/10.3390/app131810093

(**Figure 7. 1**), on the modification of the adsorption capabilities of hydrophilic silica nanoparticles at water/vapor interfaces, as well as on the interfacial rheology of the formed layers.

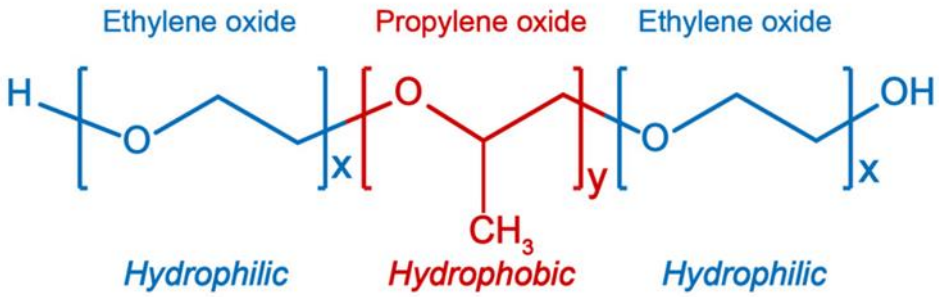

Figure 7. 1. General molecular structure of Poly(ethylene oxide)n–b-poly(propylene oxide)m–b-poly(ethylene oxide)n triblock copolymers. x and y indicate the number of monomers of each type of block that can have a broad range of values.

Several studies have shown that the presence of ether groups in the poly(ethylene oxide) blocks of Pluronic polymers favors their association by hydrogen bonding with hydrophilic silica nanoparticles [17-19], allowing the preparation of decorated particles using a single-step adsorption methodology [20]. This provides an intriguing opportunity to exploit the physico-chemical properties of silica nanoparticles, which have limited affinity for fluid/fluid interfaces, to manipulate and enhance the properties of such interfaces.

7.2. Materials and methods

7.2.1. Chemicals

A triblock copolymer of the Pluronic family, Pluronic F-127, supplied by Merck KGaA (Darmstadt, Germany) was used in this work. Pluronic F-127 consists of two lateral blocks of poly(ethylene oxide) (4.4 kDa) and a central block of poly(propylene oxide) (3.8 kDa). The silica nanoparticles used were Ludox® HS-40 colloidal silica, provided as an aqueous dispersion containing 40%w/w solids, also supplied by Merck KGaA (Darmstadt, Germany).

Milli-Q grade ultrapure deionized water (resistivity≥18 MΩ·cm, total organic content (TOC)<6 ppm) was used to clean all materials and to prepare solutions and dispersions. This water was obtained using an AquaMAXTM-Ultra 370 Series multi-cartridge purification system. (Young Lin Instrument Co., Ltd., Gyeonggi-do, South Korea).

7.2.2. Preparation of Pluronic F-127 solutions and Pluronic F-127-silica nanoparticle mixtures

Solutions and dispersions were prepared by weight using a precision analytical balance with an accuracy of ±0.1 mg. For the Pluronic F-127 solutions, the required amount of solid Pluronic F-127 needed to obtain solutions with concentrations ranging from 0-10 mg/mL was weighed, then poured into a flask and then solubilized with water to obtain the desired solution concentration. For the dispersions containing Pluronic F-127 and silica nanoparticles, the first step was to weigh the appropriate amount of Pluronic F-127 required to obtain mixtures with copolymer concentrations ranging from 0-10 mg/mL. The weighed copolymer was then poured into a flask and the amount of particles required to produce mixed dispersions with two different concentrations of silica nanoparticle (0.1% w/w and 1% w/w) was combined with

the Pluronic F-127 in the same flask. Finally, the water needed to achieve the final composition was added. It should be noted that the solutions and mixed dispersions were kept under stirring at 1000 rpm overnight to ensure their homogeneity. The pH of all dispersions and solutions was in the range 6.2-6.7 as was determined by the means of a pH-meter (model CG842, Schott GmbH, Columbus, OH, USA) fitted with a Blueline 18 pH electrode (SI Analitycs, Mainz Germany).

7.2.3. Experimental methods

Dynamic Light Scattering (DLS) experiments were performed in a quasi-backscattering configuration (scattering angle, θ = 173º) using a Zetasizer Nano ZS instrument from Malvern Instruments Ltd. (Malvern, UK). The DLS experiments were performed using red line radiation emitted by a He-Ne laser at a wavelength (λ) of 632 nm [21]. The DLS experiments allowed us to obtain the apparent diffusion coefficient, D_{app}, at a constant temperature (in our experiments 22ºC) of scatters dispersed in a liquid, assuming their Brownian motion. From the values of the D_{app}, it is possible to evaluate the size of the scatters in terms of the apparent hydrodynamic diameter of the scatters, d_h^{app}, assuming the validity of the Stokes-Einstein equation (see *Chapter II*, 2.3.1. Dynamic Light Scattering (DLS)):

$$d_h^{app} = \frac{k_B T}{3\pi\eta D_{app}} \qquad (7.\ 1)$$

where k_B and T are the Boltzmann constant and the absolute temperature, respectively, and η is the viscosity of the continuous phase. It should be noted that the DLS technique can only be used to analyze transparent dispersions, so multiple scattering phenomena should be avoided.

The effective charge density of Pluronic F-127-decorated silica nanoparticles can be determined by measuring the electrophoretic mobility (u_e) using laser Doppler velocimetry (see *Chapter II*, 2.3.2. Zeta-Potential) with a Zetasizer Nano ZS instrument from Malvern Instrument, Ltd. (Malvern, UK). The electrophoretic mobility is directly proportional to the zeta potential (ζ), which provides a quantification of the effective charge carried by the colloids dispersed in the aqueous medium [22,23].

The dependence of surface tension on Pluronic F-127 concentration was determined for both, F-127 solutions and dispersions of Pluronic F-127-decorated silica nanoparticles. This was carried out using a PS4 surface force tensiometer from Nima Technology (Coventry, UK) equipped with disposable paper Wilhelmy plates (Whatman CHR1 chromatography paper, Whatman, Maidstone, UK). The evolution of the surface tension of the water/vapor interface was measured until equilibrium was reached during a period of at least 30 minutes. Precautions were taken to minimize the influence of evaporation during the measurements. The data reported for each experiment represent the average of three independent measurements. All experiments were carried out at a constant temperature of 22.0 ± 0.1ºC.

Oscillatory barrier experiments [24] were carried out using a NIMA 702 Langmuir balance from Nima Technology (Coventry, UK) equipped with a surface force tensiometer (PS4, Nima Technology, Coventry, UK). This setup allows the time evolution of the surface tension response to sinusoidal changes in surface area to be measured. This makes it possible to determine the dilational viscoelastic moduli of the interfacial layers, defined as $E_s(\nu)^* =$

$E_s(\nu) + iE_i(\nu)$ (where E_s is the dilational elastic modulus and εE_i is the viscous modulus), over a frequency range of 10^{-1} to 10^{-2} Hz, and at a fixed surface deformation amplitude Δu = 0.1. The chosen deformation amplitude was checked to be appropriate to ensure that the results obtained were within the linear response regime of the interface. It should be noted that the imaginary component of the dynamic surface modulus (E_i) remained below 5% of the real component (E_s) in all measurements. Consequently, the detailed discussion of the imaginary part provides limited insight for the clarity of the experimental work and therefore will not be discussed here.

7.3. Results and discussion

7.3.1. Characterization of bare silica nanoparticles and Pluronic F-127

Before studying the association between Pluronic F-127 and silica nanoparticles in aqueous medium, it is important to evaluate the behavior of the unmodified silica nanoparticles and Pluronic F-127 in aqueous medium. The silica nanoparticles used have an average hydrodynamic diameter of about 15±4 nm, as determined by DLS, and an average ζ potential of (-35.7±0.8 mV), which is in agreement with the results previously reported by Liu et al. [25], indicating a negative charge due to the presence of dissociated silanol groups on the nanoparticle surface. This is of paramount importance to ensure the stability of the nanoparticles in aqueous medium. Despite the effective negative charge of the particles, this does not imply complete dissociation of all the silanol groups on the surface of the nanoparticles and therefore it is possible that hydrogen bonding interactions may occur through non-dissociated silanol groups on the surface of the nanoparticles.

The characterization of Pluronic F-127 aqueous solutions has been extensively discussed in previous works [17], and only the most fundamental aspects will be highlighted in this chapter: as the weight fraction of Pluronic F-127 in solution increases, the viscosity of the solution increases progressively. This viscosity increase is particularly noticeable when the copolymer weight fraction reaches about 120 mg/mL, with a sol-gel transition occurring at a copolymer weight fraction of about 200 mg/mL w/w. This sol-gel behavior is consistent with findings from previous studies on various polymers within the Pluronic family [26-29]. This transition limits the range of Pluronic F-127 concentrations that can be effectively used, and we have therefore limited our study to a maximum concentration of 10 mg/mL, where the viscosity of Pluronic F-127 solutions, and their mixtures with silica remain close to that of water.

7.3.2. Characterization of dispersions of Pluronic F-127-decorated silica nanoparticle

The interaction of silica nanoparticles with Pluronic F-127 leads to the formation of copolymer-decorated silica nanoparticles, as demonstrated in a previous work [17] for the combination of Pluronic F-127 and another type of silica nanoparticles (Ludox® TMA). This is consistent with the results reported by Sarkar et al. [18]. They proposed that copolymers belonging to the Pluronic family can adsorb on the silica surface, regardless of whether it is protonated or not, forming a shell that has different conformations depending on the Pluronic concentration considered.

The association between Pluronic F-127 and silica nanoparticles can be rationalized considering the formation of hydrogen bonds between the ether groups present in Pluronic F-127 and the non-dissociated silanol groups on the surface of the silica nanoparticles. It has

been previously reported that the formation of hydrogen bonds between the surface of silica nanoparticles and various polymers is a good alternative to enhance the stability of silica nanoparticle dispersions [30]. In fact, these hydrogen bonds are significantly stronger (about 25-30%) than the interactions between silanol groups and water molecules, which favors the association between Pluronic F-127 and the silica nanoparticles [31]. Consequently, when Pluronic F-127 is introduced into the colloidal dispersion, water molecules on the nanoparticle surface are replaced by copolymer molecules, resulting in the formation of copolymer-decorated silica nanoparticles. It is expected that increasing the number of available silanol groups on the surface of silica nanoparticles by mild acidification of the dispersions may improve the efficiency of silica-Pluronic F-127 association. However, lowering the pH of the dispersion may increase the aggregation of the silica nanoparticles, which will affect both the bulk association and the interfacial properties of the obtained dispersions.

DLS measurements provide empirical support to prove the interaction between copolymer and silica nanoparticles. As an illustrative example, **Figure 7. 2** shows a series of intensity autocorrelation functions ($g^{(2)}(t)$-1) and the resulting distributions of apparent hydrodynamic diameters obtained from their analysis. These results are derived from measurements of mixed dispersions comprising of silica nanoparticles and Pluronic F-127, where the concentration of the copolymer is progressively increased.

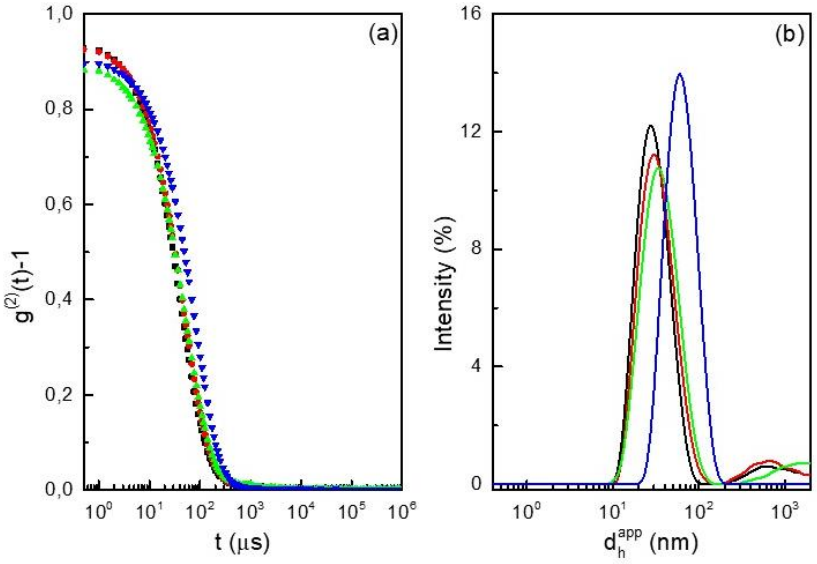

Figure 7. 2. DLS results for mixed dispersions of silica nanoparticles (concentration, 1%w/w) and Pluronic F-127, with increasing concentrations of the latter: (a) intensity autocorrelation functions, and (b) intensity-apparent hydrodynamic diameter distributions obtained from the analysis of the intensity autocorrelation functions in panel (a). The code of color is the same in both panels (concentrations are referred to Pluronic F-127): (■,–) 0.2 mg/mL, (●,–) 1 mg/mL g/L, (▲, –) 3 mg/mL and (▼,–) 10 mg/mL.

The intensity autocorrelation functions obtained from the DLS experiments show a monomodal character regardless of the amount of Pluronic F-127 present in the colloidal dispersions. This indicates the presence of a single population of scatters within the dispersion, as supported by the intensity-apparent hydrodynamic diameter distributions shown in **Figure 7. 2** (b). However, it should be noted that the population appearing at the highest values of apparent hydrodynamic diameter must be considered meaningless, appearing as an artifact in the analysis of the intensity autocorrelation function due to the presence of a reduced number

of aggregates or dust particles in the dispersion. It should be also noted that the scattered intensity increases by a factor of 10^6 with the characteristic dimension of the scatters. Therefore, it is reasonable to expect that the scatter intensity for a significant scatter population in the high apparent hydrodynamic diameter region would be significantly lower than that of the population observed at lower apparent hydrodynamic diameter values. [21,32,33].

A more detailed analysis of the DLS results indicates that the characteristic relaxation time of Pluronic F-127-decorated silica nanoparticles increases progressively with increasing Pluronic F-127 concentration (see **Figure 7. 2** (a)), which can be interpreted as an increase in the characteristic size of the colloidal particles, evaluated in terms of the apparent hydrodynamic diameter, due to the formation of the copolymer layer on their surface (see **Figure 7. 2** (b)). Therefore, based on the DLS results, a very efficient adsorption of Pluronic F-127 on the surface of silica nanoparticles can be assumed which is in agreement with previous results reported by Sánchez-Arribas et al. [17]. It should be noted that average size obtained by DLS for decorated silica nanoparticles is higher than that expected for Pluronic F-127 chains, and that in the case of Pluronic F-127 solutions above the CMC, DLS shows a multimodal system where two different types of species, i.e., single chains and micelles are involved, leading to more complex DLS results [17]. For a deeper understanding of the formation of Pluronic F-127-decorated silica nanoparticles, **Figure 7. 3** shows the dependence on the average apparent hydrodynamic diameter (obtained as the maximum of the intensity-apparent hydrodynamic diameter distribution) on the concentration of the Pluronic F-127 included in the dispersion ($c_{\text{Pluronic F-127}}$) for dispersions with two different concentrations of silica nanoparticles (c_{NP}). It should be noted that the reported apparent hydrodynamic diameter is a concentration dependent quantity, with this dependence resulting from interparticle interactions, and is therefore different from the true hydrodynamic diameter reported in *7.3.1. Characterization of bare silica nanoparticles and Pluronic F-127* subsection [34,35].

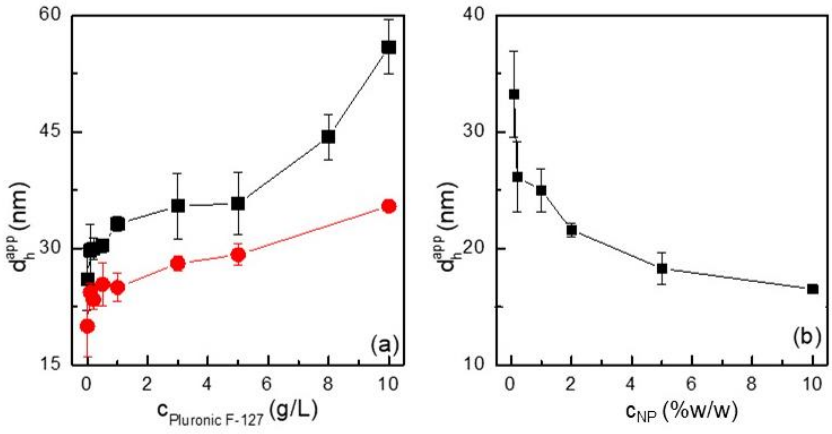

Figure 7. 3. (a) Dependence of the average apparent hydrodynamic diameter on the concentration of Pluronic F-127 for the mixed dispersions. (■) c_{NP}=0.1%w/w and (●) c_{NP}=1%w/w. (b) Dependence of the average apparent hydrodynamic diameter on the nanoparticle concentration for silica nanoparticle dispersions with Pluronic F-127, where the concentration of Pluronic F-127 is fixed at 1 mg/mL. The lines in both panels are guides for the eyes.

The addition of Pluronic F-127 to the silica nanoparticle dispersions results in a significant increase in the apparent hydrodynamic diameter of the nanoparticles when dispersions with a fixed nanoparticle concentration are considered. In fact, the apparent hydrodynamic

diameter (d_h^{app}) increases from approximately 20 nm for the unmodified particles to roughly 60 nm for dispersions containing 0.1%w/w nanoparticle concentration, and up to values of about 30 nm when the concentration of the dispersions is increased by a factor 10 (1%w/w). These observations strongly suggest the adsorption of Pluronic F-127 molecules onto the silica nanoparticle surfaces. At lower Pluronic F-127 concentrations, the copolymer molecules are likely to be adsorbed individually, adopting a flat conformation that becomes increasingly disordered with increasing copolymer concentration, as a result of an increase in the number of polymer segments protruding into the aqueous phase and the consequent increase in d_h^{app}. However, once the critical micelle concentration (CMC) of Pluronic F-127 is overcome, micelles of the copolymer are expected to adsorb directly onto the nanoparticle surfaces. These micelles can be deformed as their number increases to maximize their adsorption on the surface. This is particularly important, at the lowest nanoparticle concentration where the dimension of the Pluronic F-127 capping layer exceeds the average apparent hydrodynamic diameter of Pluronic F-127 micelles (approximately 15-20 nm) [17]. The adsorption of Pluronic F-127 micelles on silica surfaces is consistent with previous reports suggesting that the micellization of Pluronic copolymers on hydrophilic surfaces is preferential compared to the micellization process occurring in bulk aqueous phases [36,37].

Deepening now in the effect of the nanoparticle concentration on the adsorption of Pluronic F-127 on the silica surface. It is important to note that the apparent thickness of the Pluronic F-127 layer is higher as the concentration of nanoparticles is decreased. This can be explained considering the effective area available for the copolymer adsorption. In fact, the lower the nanoparticle concentration the smaller the area available for the adsorption, and therefore it is expected that the existence of a higher competition between the Pluronic F-127 molecules/micelles for occupying the nanoparticle surface, resulting in the formation of more disordered layers with a higher fraction of Pluronic F-127 monomers protruding into the aqueous phase. This demonstrates the complexity of the concentration-dependent adsorption behavior and highlights the importance of understanding surface interactions. In a similar situation to the above, the effect of silica nanoparticle concentration on the adsorption of Pluronic F-127 at constant concentration (1 mg/mL) is examined. As the concentration of silica nanoparticles increases, there is a decrease in the apparent hydrodynamic diameter of the copolymer-nanoparticle complexes. The association of Pluronic F-127 and silica nanoparticles in the aqueous bulk can also be evaluated in terms of the effective charge of the decorated-colloids, evaluated from the ζ-potential (see **Figure 7. 4**).

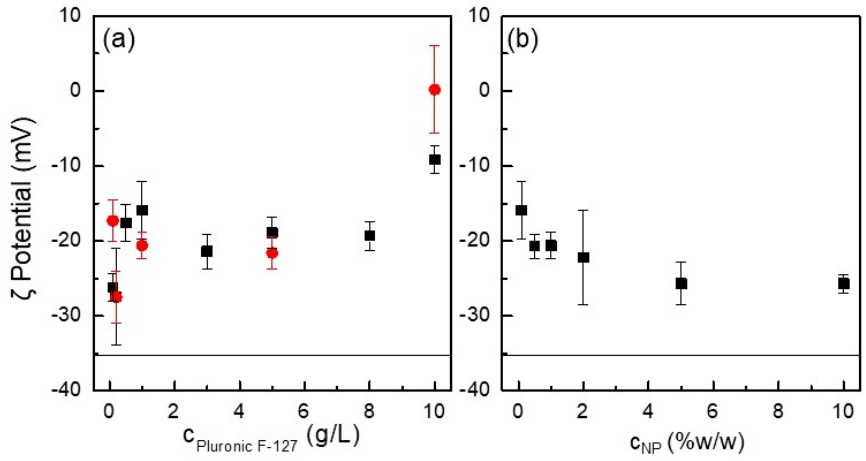

Figure 7. 4. (a) Dependence of the ζ potential on the concentration of Pluronic F-127 for the mixed dispersions. (■) cNP=0.1%w/w and (●) cNP=1%w/w. (b) Dependence of the ζ potential on the nanoparticle concentration for silica nanoparticle dispersions with Pluronic F-127, where the concentration of Pluronic F-127 is fixed at 1 mg/mL. The lines in both panels indicate the ζ potential value corresponding to the bare silica nanoparticles, and the error bars represent the standard deviation of five independent measurements.

The results show a progressive shift of the ζ potential value, moving from that of the unmodified particles to values close to electroneutrality. Based on this result, it can be assumed that the formation of the Pluronic F-127 shell on the silica surface shields the negative charge on the nanoparticle. Consequently, the stability mechanism of the particles in the aqueous medium shifts from electrostatic stabilization to steric stabilization, leading to the formation of core-shell colloids. These colloids consist of an inner core composed of silica nanoparticles, while the outer shell is formed by the capping Pluronic F-127 layer (see references [17,18] for a sketch of the core-shell decorated colloids). In addition, the dependence of the coating density on the number of nanoparticles dispersed in the aqueous medium is supported by the observed reduction in the effective charge of the copolymer-decorated nanoparticles with increasing nanoparticle concentration. As mentioned earlier, a higher particle concentration results in a limited availability of Pluronic F-127 to coat each individual particle.

7.3.3. Adsorption of Pluronic F-127-decorated silica nanoparticles at the water/vapor interface

The study of the adsorption of Pluronic F-127-decorated silica nanoparticles at the water/vapor interface requires a careful investigation of the equilibrium interfacial tension of both the Pluronic F-127- and particle-laden water/vapor interfaces. In addition, it is interesting to investigate the interfacial dilatational response of the formed layers once equilibrium is achieved. Understanding these aspects is of paramount importance when using interfacial layers to stabilize dispersed systems, and considering that in the system studied here, a water/vapor interface is considered. The information obtained may be relevant to improve the stability of foams [39-41].

Before discussing the adsorption of Pluronic F-127 and copolymer-decorated silica nanoparticles at the water/vapor interface, it is important to highlight that the bare silica nanoparticles exhibit minimal interfacial activity when considering their interaction with water/vapor interfaces. This observation is consistent with previous results reported in the literature [14,38,39]. The lack of significant interfacial activity may be attributed to the

reluctance of the nanoparticle to spontaneously adsorb at the water/vapor interface. However, it is also possible that they do adsorb to some extent but exert weak dipolar repulsive forces at the interfaces [40]. In contrast, the interfacial tension of the bare water/vapor interface is significantly affected by both Pluronic F-127 and copolymer-decorated nanoparticles. **Figure 7. 5** shows the relationship between Pluronic F-127 concentration and interfacial tension observed at the water/vapor interface after adsorption of either Pluronic F-127 or copolymer coated nanoparticles.

In the case of the interaction of Pluronic F-127 with the liquid/vapor interface, the behavior is consistent with that expected for the adsorption of an amphiphilic copolymer with surfactant character. In fact, the ability of Pluronic F-127 to reorganize at the interface with its most hydrophobic blocks, i.e., the poly(propylene oxide) ones, protruding towards the vapor phase, while the poly(ethylene oxide) blocks ensure the attachment of the copolymer to the liquid interface. Considering the investigated concentration range of Pluronic F-127, it is expected that the Pluronic F-127 is attached to the interface in a mushroom or brush conformation [41-44]. It is more interesting to evaluate the change in water/vapor interfacial tension with the Pluronic F-127 concentration when dispersions of Pluronic F-127-decorated silica nanoparticles are considered. The results show that for a fixed concentration of Pluronic F-127, the interfacial tension increases with the concentration of silica nanoparticles. This is similar to the effect observed by Ravera et al. [38] in their study of the adsorption of surfactant-decorated particles at the water/vapor interface. This type of phenomenon is different from that observed in other colloidal systems, such as polymer-surfactant mixtures, where the association process is accompanied by an enhanced decrease in the surface tension of the fluid/fluid interface [45].

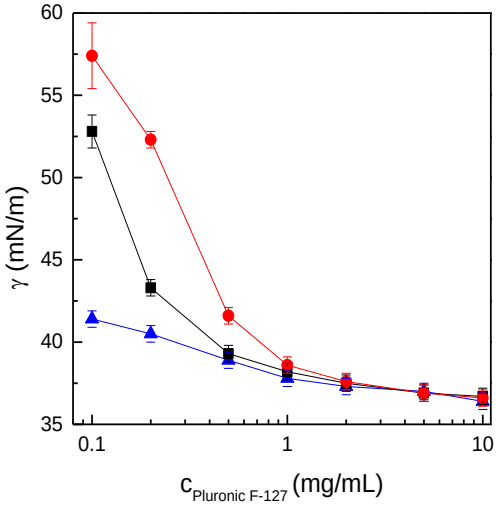

Figure 7. 5. Pluronic F-127 concentration dependence of the interfacial tension of the bare water/vapor interface upon the adsorption of Pluronic F-127 or copolymer-decorated silica nanoparticles. (▲) c_{NP}=0 %w/w (Pluronic F-127 solutions), (■) c_{NP}=0.1%w/w and (●) c_{NP}=1%w/w. The lines are guides for the eyes, and the error bars are obtained as the standard deviation of three replica for each sample.

For the case of Pluronic F-127 solutions in the investigated copolymer concentration range the interfacial tension is on a plateau region related to the maximum coverage of the interface, or closer to such a situation (at the lowest Pluronic F-127 concentrations), for copolymer-decorated particles the results show higher values of the interfacial tension than for the

copolymer solutions at low Pluronic F-127 concentration, and then as the Pluronic F-127 concentration increases, the interfacial tension decreases to values similar to those found for bare Pluronic F-127 solutions. These results can be explained by considering two different frameworks. The first assumes that the introduction of silica nanoparticles causes a depletion of Pluronic F-127 molecules from the aqueous phase to the surface of the silica nanoparticles, thereby reducing the effective concentration of free copolymer in solution. This results in a situation characterized by the adsorption of the Pluronic F-127 in solution, leaving the copolymer-decorated particles dispersed in the aqueous phase. This reduction in the available concentration of Pluronic F-127 will result in higher interfacial tension values. The second scenario assumes that the adsorption of Pluronic F-127 onto the surface of the particles reduces their ability to reorganize at the interface, and thus reduces the ability of the decorated particles to reduce the interfacial tension associated with the Pluronic F-127 shell compared to Pluronic F-127 solutions of the same concentration. Both scenarios are consistent with the dependence of the interfacial tension on the silica nanoparticle concentration. In fact, at low nanoparticle concentrations, the available area for Pluronic F-127 is small, and therefore both the depletion and the reduction in the degree of freedom of the attached Pluronic F-127 molecules will be very limited. Therefore, the effect of the particles on the interfacial tension of the water/vapor interface appears to be similar to bare Pluronic F-127 than when the particle concentration is increased. In the latter case, both the depletion and the reduction in the degrees of freedom of Pluronic F-127 during adsorption will be greater. However, based on the results obtained for the bulk characterization of the dispersions, it can be assumed that the most important effect on the modification of the interfacial tension is related to the adsorption of the decorated particles at the water/vapor interface. Based on the above results, it is not expected that the formation of a densely packed particle-laden interface mediated by the adsorption of Pluronic F-127 on the particle surface can be the responsible for the reduction of the interfacial tension. This is directly mediated by the Pluronic F-127 chains adsorbed on the particle surface penetrating the interface and exerting long-range repulsions between the particles.

The interfacial dilational elastic modulus (E_s) of the particle-laden interfaces was determined upon the equilibration of the adsorption process, i.e., when the interfacial tension reaches its equilibrium value. The frequency dependence of the interfacial dilational elastic modulus for Pluronic F-127 and copolymer-decorated silica nanoparticles with different concentrations of Pluronic F-127 is shown in **Figure 7. 6**.

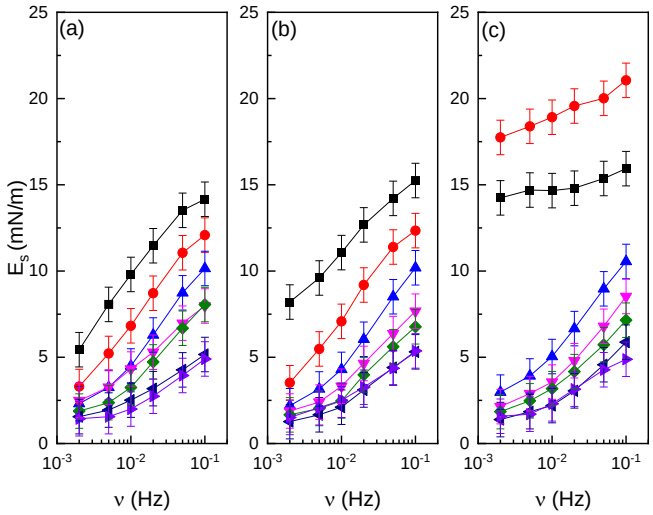

Figure 7. 6. Dependence of the interfacial dilational elastic modulus on the frequency of the sinusoidal deformation (the amplitude of deformation was maintained in 10% for all the experiments) for equilibrated layers of Pluronic F-127 and copolymer-decorated silica nanoparticles. (a) c_{NP}=0 %w/w (Pluronic F-127 solutions), (b) c_{NP}=0.1%w/w and (c) c_{NP}=1%w/w. The use of symbols with different colors indicates the different concentration of Pluronic F-127 in the studied samples: (■) 0.1 mg/mL, (●) 0.2 mg/mL, (▲) 0.5 mg/mL, (▼) 1 mg/mL, (◆) 2 mg/mL, (◀) 5 mg/mL and (▶) 10 mg/mL. The lines are guides for the eyes, and the error bars are obtained as the standard deviation of three replica for each experiment.

As expected, in almost all experiments, as the strain frequency increases the value of the interfacial dilational elastic modulus also increases. However, for the lowest Pluronic F-127 concentrations, and the highest particle concentration, the interfacial dilational elastic modulus appears to be weakly dependent on the frequency, which may indicate the formation of a solid-like particle-laden interface in agreement with Zhang et al. [46]. On the other hand, the copolymer concentration dependence of the interfacial dilational elastic modulus is not the same for all the particles concentrations. At low particle concentration, i.e., for layers formed only by Pluronic F-127 and layers formed when the particle concentration is 0.1%w/w, the interfacial dilational elastic modulus decreases with increasing concentration. This situation changes as particle concentration increases (1%w/w), where ε' initially increases with the Pluronic F-127 concentration and then, after reaching a threshold, the interfacial dilational elastic modulus begins to decrease with increasing concentration. The above behavior is easily seen in the plot of the interfacial dilational modulus versus Pluronic F-127 concentration for experiments performed at a fixed frequency of 10^{-1} Hz (see **Figure 7. 7**). It should be noted that the existence of a peak for the adsorption of colloids from dispersions where the particle concentration is 1% w/w has a real physical origin. In fact, considering the state of the monolayer at the lowest concentration range, an increase in the dilational elasticity with Pluronic F-127 concentration is consistent with the sharp decrease in surface tension observed in the isotherm shown in **Figure 7. 5**. It is expected that a similar dependence may appear for Pluronic F-127 solutions and dispersions with a particle concentration of 0.1% w/w by decreasing the Pluronic F-127 concentration below the range studied.

The analysis of the frequency dependence of the interfacial dilational elastic modulus shows the presence of a relaxation mechanism in the investigated frequency range, as evidenced by the inflection point in the curves. Considering the analyzed frequency range and its shift to higher values of frequency with the copolymer concentration, it can be assumed that the observed relaxation may correspond to the diffusion transfer of the copolymer, or copolymer-

decorated particles to the interface [10,38]. The results do not exclude the presence of additional relaxation process occurring at the interface [10,47]. However, the limitation of the accessible frequency range analyzed by oscillatory barrier experiments does not allow to evaluate their role in the stabilization of the liquid/vapor interfaces.

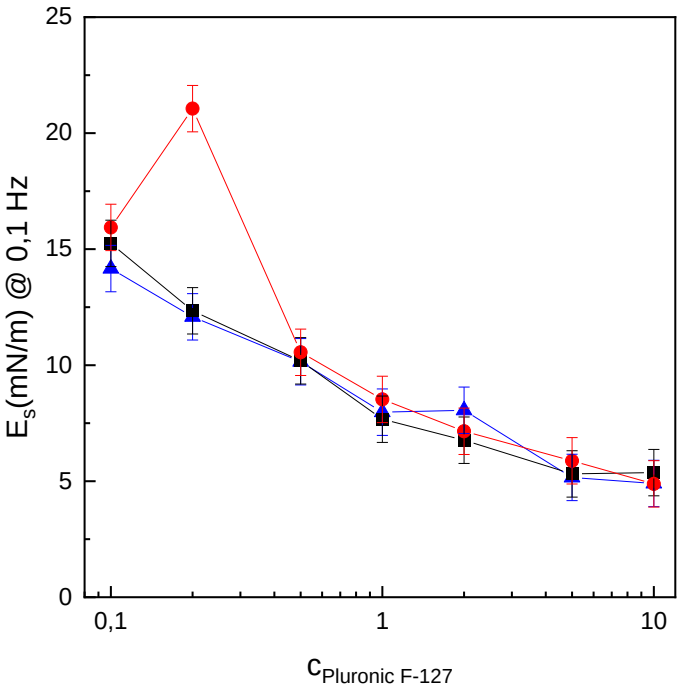

Figure 7. 7. Dependence of the interfacial dilational elastic modulus on the Pluronic F-127 for sinusoidal deformations (the amplitude of deformation was maintained in 10% for all the experiments) with a fixed frequency of 10-1 Hz for equilibrated layers of Pluronic F-127 and copolymer-decorated silica nanoparticles. (▲) cNP=0 %w/w (Pluronic F-127 solutions), (■) cNP=0.1%w/w and (●) cNP=1%w/w. The lines are guides for the eyes, and the error bars are obtained as the standard deviation of three replica for each experiment.

The dependence of the interfacial dilational elastic modulus on the copolymer concentration, shown in **Figure 7. 7**, shows differences consistent with the different states of the interface according to the interfacial tension measurements. In fact, for Pluronic F-127 layers and those containing a low concentration of particles (0.1% w/w), the system is close to an interfacial tension plateau, i.e., the saturation of the interface, which explains the decrease in the dilatational modulus with the copolymer concentration. However, for the samples containing a particle concentration of 1% w/w, the interfacial tension isotherm for the lowest Pluronic F-127 concentration is in a region of steepest decrease, and this is consistent with the initial increase in the elastic modulus followed by a decrease when the interfacial state is close to the maximum adsorption, as evidenced by the interfacial tension plateau. In addition, the rheological measurements show values for the interfacial dilational elastic modulus that are very similar, shifted only by the presence of particles. In fact, this appears to be controlled solely by the presence of Pluronic F-127, again indicating the negligible role of the particles in controlling the interfacial properties of the interface. Therefore, the mechanical response of the interface suggests that the ability of Pluronic F-127 to reorganize at the water/vapor interface is essential in controlling the properties of the layers obtained, independently of the presence of particles. This can be understood by considering that the association of particles with Pluronic F-127 limits the ability of the latter to undergo its characteristic reorganizations

at the interface, which is reasonable considering that some segments are attached to the surface of the particles, and therefore limit the ability of Pluronic F-127 to reach its equilibrium conformation. Thus, considering the above scenario, the silica nanoparticles at the liquid/vapor interface act as obstacles to the reconfiguration of the copolymer chains. Once, the Pluronic F-127 density is high enough to overcome the hindrance associated with the nanoparticles, the interfacial behavior of the decorated nanoparticles becomes reminiscent of what is expected for the bare copolymer.

7.4. Conclusions

The interaction between Pluronic F-127 and hydrophilic silica nanoparticles leads to the formation of stable complexes (copolymer-decorated nanoparticles) through hydrogen bonding between the oxyethylene groups of the copolymer and the non-dissociated silanol groups on the surface of the silica nanoparticles. The formation of these complexes favors the transport of the silica nanoparticles, which have poor interfacial activity, to the water-vapor interface and aids in their attachment.

The results obtained have indicated that the adsorption of copolymer-decorated nanoparticles at the water/vapor interface does not lead to noticeable differences from the interfacial properties of Pluronic F-127 in the same concentration range and only a shift in them is found depending on the particle concentration. In fact, the density of the Pluronic F-127 shell determines the interfacial tension due to its effect on the reorganization of the Pluronic F-127 molecules at the interface. The same idea can explain the dependence of the interfacial dilational elastic modulus on the concentration Pluronic F-127 and silica nanoparticles. In fact, particles at the liquid/vapor interface behave as simple obstacles, and when the concentration of Pluronic F-127 becomes high enough to overcome the hindrance induced by the particles, the interfacial behavior becomes reminiscent of that corresponding to bare Pluronic F-127 solutions. This means that the modification of particles with Pluronic F-127 opens interesting avenues for tuning the mechanical performance of liquid/vapor interfaces which impact decisively on the interfacial stability, and for applications of particle-laden interfaces in the stabilization of dispersed systems. In particular, since this chapter has been focused on water/vapor interfaces, the results can be used to understand the most fundamental physicochemical principles underlying the stabilization of particle-stabilized foams.

7.5. References

1. Santini, E.; Guzmán, E.; Ravera, F.; Ferrari, M.; Liggieri, L. Properties and structure of interfacial layers formed by hydrophilic silica dispersions and palmitic acid. *Phys. Chem. Chem. Phys.* **2012**, *14*, 607-615, doi:10.1039/C1CP22552A.
2. Shao, X.; Duan, F.; Hou, Y.; Zhong, X. Role of surfactant in controlling the deposition pattern of a particle-laden droplet: Fundamentals and strategies. *Adv. Colloid Interface Sci.* **2020**, *275*, 102049, doi:10.1016/j.cis.2019.102049.
3. Li-Destri, G.; Ruffino, R.; Tuccitto, N.; Marletta, G. In situ structure and force characterization of 2D nano-colloids at the air/water interface. *Soft Matter* **2019**, *15*, 8475-8482, doi:10.1039/C9SM01476D.
4. Maestro, A. Tailoring the interfacial assembly of colloidal particles by engineering the mechanical properties of the interface. *Curr. Opin. Colloid Interface Sci.* **2019**, *39*, 232-250, doi:10.1016/j.cocis.2019.02.013.

5. Garbin, V.; Crocker, J.C.; Stebe, K.J. Nanoparticles at fluid interfaces: Exploiting capping ligands to control adsorption, stability and dynamics. *J. Colloid Interface Sci.* **2012**, *387*, 1-11, doi:10.1016/j.jcis.2012.07.047.
6. Santini, E.; Guzmán, E.; Ferrari, M.; Liggieri, L. Emulsions stabilized by the interaction of silica nanoparticles and palmitic acid at the water–hexane interface. *Colloids Surf. A* **2014**, *460*, 333-341, doi:10.1016/j.colsurfa.2014.02.054.
7. González-González, A.; Sánchez-Arribas, N.; Santini, E.; Rodríguez-Villafuerte, J.L.; Carbone, C.; Ravera, F.; Ortega, F.; Liggieri, L.; Rubio, R.G.; Guzmán, E. Effects of Oil Phase on the Inversion of Pickering Emulsions Stabilized by Palmitic Acid Decorated Silica Nanoparticles. *Colloids Interfaces* **2022**, *6*, 27, doi:10.3390/colloids6020027.
8. Vialetto, J.; Anyfantakis, M. Exploiting Additives for Directing the Adsorption and Organization of Colloid Particles at Fluid Interfaces. *Langmuir* **2021**, *37*, 9302-9335, doi:10.1021/acs.langmuir.1c01029.
9. Milyaeva, O.Y.; Campbell, R.A.; Gochev, G.; Loglio, G.; Lin, S.-Y.; Miller, R.; Noskov, B.A. Dynamic Surface Properties of Mixed Dispersions of Silica Nanoparticles and Lysozyme. *J. Phys. Chem. B* **2019**, *123*, 4803-4812, doi:10.1021/acs.jpcb.9b03352.
10. Ravera, F.; Ferrari, M.; Liggieri, L.; Loglio, G.; Santini, E.; Zanobini, A. Liquid–liquid interfacial properties of mixed nanoparticle–surfactant systems. *Colloids Surf. A* **2008**, *323*, 99-108, doi:10.1016/j.colsurfa.2007.10.017.
11. Santini, E.; Krägel, J.; Ravera, F.; Liggieri, L.; Miller, R. Study of the monolayer structure and wettability properties of silica nanoparticles and CTAB using the Langmuir trough technique. *Colloids Surf. A* **2011**, *382*, 186-191, doi:10.1016/j.colsurfa.2010.11.042.
12. Maestro, A.; Rio, E.; Drenckhan, W.; Langevin, D.; Salonen, A. Foams stabilised by mixtures of nanoparticles and oppositely charged surfactants: relationship between bubble shrinkage and foam coarsening. *Soft Matter* **2014**, *10*, 6975-6983, doi:10.1039/C4SM00047A.
13. Maestro, A.; Deshmukh, O.S.; Mugele, F.; Langevin, D. Interfacial Assembly of Surfactant-Decorated Nanoparticles: On the Rheological Description of a Colloidal 2D Glass. *Langmuir* **2015**, *31*, 6289-6297, doi:10.1021/acs.langmuir.5b00632.
14. Alvarez, N.J.; Anna, S.L.; Saigal, T.; Tilton, R.D.; Walker, L.M. Interfacial dynamics and rheology of polymer-grafted nanoparticles at air-water and xylene-water interfaces. *Langmuir* **2012**, *28*, 8052-8063, doi:10.1021/la300737p.
15. Yong, X. Modeling the Assembly of Polymer-Grafted Nanoparticles at Oil–Water Interfaces. *Langmuir* **2015**, *31*, 11458-11469, doi:10.1021/acs.langmuir.5b03405.
16. Guzmán, E.; Martínez-Pedrero, F.; Calero, C.; Maestro, A.; Ortega, F.; Rubio, R.G. A broad perspective to particle-laden fluid interfaces systems: from chemically homogeneous particles to active colloids. *Adv. Colloid Interface Sci.* **2022**, *302*, 102620, doi:10.1016/j.cis.2022.102620.
17. Sánchez-Arribas, N.; Guzmán, E.; Lucia, A.; Toloza, A.C.; Velarde, M.G.; Ortega, F.; Rubio, R.G. Environmentally friendly platforms for encapsulation of an essential oil: Fabrication, characterization and application in pests control. *Colloids Surf. A* **2018**, *555*, 473-481, doi:10.1016/j.colsurfa.2018.07.028.
18. Sarkar, B.; Venugopal, V.; Tsianou, M.; Alexandridis, P. Adsorption of Pluronic block copolymers on silica nanoparticles. *Colloids Surf. A* **2013**, *422*, 155-164, doi:10.1016/j.colsurfa.2013.01.010.
19. Kumar, S.; Ganguly, R.; Nath, S.; Aswal, V.K. Pluronic Induced Interparticle Attraction and Re-entrant Liquid–Liquid Phase Separation in Charged Silica Nanoparticle Suspensions. *Langmuir* **2023**, *39*, 8109-8119, doi:10.1021/acs.langmuir.3c00491.

20. Yu, K.; Zhang, H.; Biggs, S.; Xu, Z.; Cayre, O.J.; Harbottle, D. The rheology of polyvinylpyrrolidone-coated silica nanoparticles positioned at an air-aqueous interface. *J Colloid Interface Sci* **2018**, *527*, 346-355, doi:10.1016/j.jcis.2018.05.035.
21. Berne, B.J.; Pecora, R. *Dynamic Light Scattering: With Applications to Chemistry, Biology, and Physics*; Dover Publications, Inc.: Mineola, NY, USA, 1976.
22. Hunter, R.J. *Zeta potential in colloid science: principles and applications*; Academic Press: London, UK, 1998.
23. Smoluchowski, M. *Handbuch der Electrizität und des Magnetismus (Graetz)*; Barth: Leipzig, Germany, 1921; Vol. 2.
24. Guzmán, E.; Maestro, A.; Carbone, C.; Ortega, F.; Rubio, R.G. Dilational Rheology of Fluid/Fluid Interfaces: Foundations and Tools. *Fluids* **2022**, *7*, 335, doi:10.3390/fluids7100335.
25. Liu, Z.; Bode, V.; Hadayati, P.; Onay, H.; Sudhölter, E.J.R. Understanding the stability mechanism of silica nanoparticles: The effect of cations and EOR chemicals. *Fuel* **2020**, *280*, 118650, doi:10.1016/j.fuel.2020.118650.
26. Malmsten, M. Soft drug delivery systems. *Soft Matter* **2006**, *2*, 760-769, doi:10.1039/B608348J.
27. Bohorquez, M.; Koch, C.; Trygstad, T.; Pandit, N. A Study of the Temperature-Dependent Micellization of Pluronic F127. *J. Colloid Interface Sci.* **1999**, *216*, 34-40, doi:10.1006/jcis.1999.6273.
28. Vandenhaute, M.; Schelfhout, J.; Van Vlierberghe, S.; Mendes, E.; Dubruel, P. Cross-linkable, thermo-responsive Pluronic® building blocks for biomedical applications: Synthesis and physico-chemical evaluation. *Eur. Polym. J.* **2014**, *53*, 126-138, doi:10.1016/j.eurpolymj.2014.01.016.
29. Dehghan Kelishady, P.; Saadat, E.; Ravar, F.; Akbari, H.; Dorkoosh, F. Pluronic F127 polymeric micelles for co-delivery of paclitaxel and lapatinib against metastatic breast cancer: preparation, optimization and in vitro evaluation. *Pharm. Dev. Technol.* **2015**, *20*, 1009-1017, doi:10.3109/10837450.2014.965323.
30. Tang, C.; Li, X.; Li, Z.; Hao, J. Interfacial Hydrogen Bonds and Their Influence Mechanism on Increasing the Thermal Stability of Nano-SiO_2-Modified Meta-Aramid Fibres. *Polymers* **2017**, *9*, 504, doi:10.3390/polym9100504.
31. Voronin, E.F.; Gun'ko, V.M.; Guzenko, N.V.; Pakhlov, E.M.; Nosach, L.V.; Leboda, R.; Skubiszewska-Zieba, J.; Malysheva, M.L.; Borysenko, M.V.; Chuiko, A.A. Interaction of poly(ethylene oxide) with fumed silica. *J. Colloid Interface Sci.* **2004**, *279*, 326-340, doi:10.1016/j.jcis.2004.06.073.
32. Segudovic, N.; Dezelic, G. Light Scattering in Binary Liquid Mixtures. I. Isotropic Scattering. *Croat. Chem. Acta* **1973**, *45*, 385-406.
33. Johnson, B.L.; J. Smith. *Light scattering from polymer solutions*; Huglin, M.B., Ed. Academic Press: New York, NY, USA, 1972.
34. Hackley, V.A.; Clogston, J.D. Measuring the Hydrodynamic Size of Nanoparticles in Aqueous Media Using Batch-Mode Dynamic Light Scattering. In *Characterization of Nanoparticles Intended for Drug Delivery*, McNeil, S.E., Ed. Humana Press: Totowa, NJ, USA, 2011; 10.1007/978-1-60327-198-1_4pp. 35-52.
35. Manh Thang, N.; Geckeis, H.; Kim, J.I.; Beck, H.P. Application of the flow field flow fractionation (FFFF) to the characterization of aquatic humic colloids: evaluation and optimization of the method. *Colloids Surf. A* **2001**, *181*, 289-301, doi:10.1016/S0927-7757(00)00803-7.

36. He, L.; Zhang, L.; Liang, H. The Effects of Nanoparticles on the Lamellar Phase Separation of Diblock Copolymers. *J. Chem. Phys. B* **2008**, *112*, 4194-4203, doi:10.1021/jp0757412.
37. Levitz, P. Aggregative adsorption of nonionic surfactants onto hydrophilic solid/water interface. Relation with bulk micellization. *Langmuir* **1991**, *7*, 1595-1608, doi:10.1021/la00056a010.
38. Ravera, F.; Santini, E.; Loglio, G.; Ferrari, M.; Liggieri, L. Effect of Nanoparticles on the Interfacial Properties of Liquid/Liquid and Liquid/Air Surface Layers. *J. Phys. Chem. B* **2006**, *110*, 19543-19551, doi:10.1021/jp0636468.
39. Guzmán, E.; Liggieri, L.; Santini, E.; Ferrari, M.; Ravera, F. DPPC–DOPC Langmuir monolayers modified by hydrophilic silica nanoparticles: Phase behaviour, structure and rheology. *Colloids Surf. A* **2012**, *413*, 174-183, doi:10.1016/j.colsurfa.2011.12.059.
40. Guzmán, E.; Ortega, F.; Rubio, R.G. Forces Controlling the Assembly of Particles at Fluid Interfaces. *Langmuir* **2022**, *38*, 13313-13321, doi:10.1021/acs.langmuir.2c02038.
41. Pérez-Mosqueda, L.M.; Maldonado-Valderrama, J.; Ramírez, P.; Cabrerizo-Vílchez, M.A.; Muñoz, J. Interfacial characterization of Pluronic PE9400 at biocompatible (air–water and limonene–water) interfaces. *Colloids Surf. B* **2013**, *111*, 171-178, doi:10.1016/j.colsurfb.2013.05.029.
42. Ramírez, P.; Muñoz, J.; Fainerman, V.B.; Aksenenko, E.V.; Mucic, N.; Miller, R. Dynamic interfacial tension of triblock copolymers solutions at the water–hexane interface. *Colloids Surf. A* **2011**, *391*, 119-124, doi:10.1016/j.colsurfa.2011.04.019.
43. Ramírez, P.; Stocco, A.; Muñoz, J.; Miller, R. Interfacial rheology and conformations of triblock copolymers adsorbed onto the water–oil interface. *J. Colloid Interface Sci.* **2012**, *378*, 135-143, doi:10.1016/j.jcis.2012.04.033.
44. Llamas, S.; Mendoza, A.J.; Guzmán, E.; Ortega, F.; Rubio, R.G. Salt effects on the air/solution interfacial properties of PEO-containing copolymers: Equilibrium, adsorption kinetics and surface rheological behavior. *J Colloid Interface Sci* **2013**, *400*, 49-58, doi:10.1016/j.jcis.2013.03.015.
45. Llamas, S.; Fernández-Peña, L.; Akanno, A.; Guzmán, E.; Ortega, V.; Ortega, F.; Csaky, A.G.; Campbell, R.A.; Rubio, R.G. Towards understanding the behavior of polyelectrolyte - surfactant mixtures at the water / vapor interface closer to technologically-relevant conditions. *Phys. Chem. Chem. Phys.* **2018**, *20*, 1395-1407. doi: 1310.1039/c1397cp05528e.
46. Zhang, H.; Zhou, M.; Guo, Z.; Lan, X.; Zhang, L.; Zhang, L. Effect of hydrophobicity on the interfacial rheological behaviors of nanoparticles at decane-water interface. *J. Mol. Liquids* **2019**, *294*, 111618, doi:10.1016/j.molliq.2019.111618.
47. Ravera, F.; Ferrari, M.; Santini, E.; Liggieri, L. Influence of surface processes on the dilational visco-elasticity of surfactant solutions. *Adv. Colloid Interface Sci.* **2005**, *117*, 75-100, doi:10.1016/j.cis.2005.06.002.

Chapter VIII: Interfacial Rheology of Chitosan-Silica Nanocomposite Films[‡‡]

8.1. Introduction

Particle-laden liquid/fluid interfaces are widely studied systems in academia and industry. This is partly due to their important role in the stabilization of dispersed systems such as foams, Pickering emulsions and thin films [1-4]. However, even though particle trapping at liquid/liquid or liquid/vapor interfaces can be considered nearly irreversible, in most cases with a trapping energy exceeding the thermal energy [5,6] the formation of particle-laden films is not always trivial because the transport and trapping of particles at the interface depends on several variables, including the particle density, which can force particle sedimentation. This hydrophilic/hydrophobic balance is defined by their wettability, which determines their penetration at the interface [6-8]. The latter is accounted for by the particle three phase contact angle at the fluid interface, which strongly influences the equilibrium situation of the particle-laden interface [8-10]. Unfortunately, many particles exhibit extreme wettability, such as silica nanoparticles, and prefer to remain dispersed in one of the continuous phases rather than adsorb at the fluid interface [7,11-14]. This requires their surface modification to provide optimal wettability for adsorption at the fluid interface [9,14].

The surface modification of colloidal particles is often based on the binding of ligands to the particles to confer a new functionality [14,15]. There is a wide range of ligands that have been used to modify the surface properties of colloidal particles. These can be bound to the particle surface by a true chemical bond, i.e., covalently, as in the case of silanization of silica surfaces or thiolation of noble metals [16,17], or they can be bound by weaker molecule-particle interactions, such as electrostatic interactions, hydrogen bonding, or van der Waals forces [18-20]. In the particular case of silica nanoparticles, the electrostatic interaction of dissociated silanol groups with cationic surfactant or polymers, or the interaction through hydrogen bonding between the non-dissociated silanol group on the silica surface and the agent used to modify the silica surface can help to modify the wettability of silica surfaces [20-27]. In the last two decades, health and environmental issues have become more and more important, hence companies are looking for using particles and polymer of natural origin [28-30].

Allison et al. [27] proposed the use of chitosan to modify the wettability of silica nanoparticles as a tool for stabilization of edible Pickering emulsions. They found that the electrostatic interaction between cationic chitosan and silica nanoparticles contributes to increase the hydrophobicity of silica nanoparticles and their adsorption to oil/water interfaces. This former agrees with the modification of the zeta potential (ζ potential) reported by Heidari et al. [31]. Moreover, chitosan-capped silica nanoparticles can organize with different structures at the oil/water interface, resulting in viscoelastic films or agglomerated particle networks depending on the chitosan concentration. This has a significant effect on the rheological properties of the particle-laden fluid/fluid interface. In a more recent work, Allison et al. [26] demonstrated that the stabilization of Pickering emulsions stabilized by chitosan-capped particles can be tuned

[‡‡] This chapter is in part included in the publication: Carbone, C.; Navarro-Arrebola, I.; Ortega, F.; Liggieri, L.; Rubio, R.G.; Guzmán, E. Interfacial Rheology of Chitosan-Silica Nanocomposite Films at the Aqueous Dispersion/Air Interface. Particle (SUBMITTED July 2024)

by pH changes, allowing modulation of the chitosan-silica interaction, and thus the adsorption of the modified particles at the water/oil interface. It should be noted that although the ability of chitosan-capped particles to adsorb at fluid/fluid interfaces is well recognized, particularly in the context of Pickering emulsion stabilization [26,27,31-34], there is a lack of knowledge related to the interaction of this type of colloidal systems with water/air interfaces. In addition to their application on the stabilization of interface dominated systems, chitosan-capped silica nanoparticles can find applications as drug carriers by exploiting their pH-responsiveness [35].

Here, the adsorption of chitosan-modified hydrophilic silica nanoparticles at the aqueous dispersion/air interface is investigated. For this purpose, silica nanoparticles are modified by direct electrostatic interactions with chitosan chains. This requires the evaluation of the optimal conditions under which chitosan and silica can interact to form stable dispersions, which can be influenced by the strong pH-responsiveness of chitosan. In fact, the solubility of chitosan in water is very limited, requiring acidic conditions for its solubilization, and increasing the pH to values close to neutrality leads to a reduction of the quality of water as a solvent for chitosan [36]. On the other hand, silica nanoparticles maintain a negative charge over a pH range of 4 to 9 due to deprotonation of their surface silanol groups. Based on the above discussion, we first evaluate the interaction between chitosan and silica nanoparticles, and the stability of the resulting dispersions at different pH conditions, and then, once the optimal conditions are selected, we study the adsorption of the chitosan-capped particles at the aqueous dispersion/air interface and the high-frequency dilatational rheological response of the formed layers by using electrocapillary wave damping measurements. This systematic study can pave the way for the use of chitosan-capped particles to modify the properties of water/air interfaces, which can impact decisively in the stabilization of liquid and solid foams.

8.2. Materials and methods

8.2.1. Chemicals

Chitosan (low molecular weight, deacetylation degree 75-85%) was purchased from Merck (Darmstadt, Germany). Silicon dioxide nanoparticles (Levasil® CS30-316P) was supplied by Nouryon (Amsterdam, The Netherlands) as an aqueous dispersion of negatively charged colloidal particles (concentration 30%w/w). Acetic glacial acid and sodium hydroxide (purity >99.9%) for adjusting pH were purchased from Fisher Scientific (Hampton, NH, USA).

Ultrapure deionized water of Milli-Q quality, with resistivity >18 MΩ·cm, and a total organic content of <6 ppm, obtained using a AquaMAX™-Ultra 370 Series multi-cartridge purification system (Young Lin Instrument Co., Ltd., Gyeonggi-do, South Korea) was used for cleaning and solution preparation.

8.2.2. Chitosan-Silica dispersion preparation

A stock solution of chitosan with a concentration of 20 mM was prepared. The required amount of chitosan was weighed and poured into a flask, which was then partially filled with water. Then, 100 µL of glacial acetic acid was added to the flask to lower the pH and ensure complete dissolution of the chitosan. The pH of the resulting aqueous chitosan solution was then adjusted to 4.5 by dropwise addition of 10^{-2} mM sodium hydroxide solution. Finally, the volume of the solution was brought to the desired final value by adding the required amount of dilute aqueous acetic acid solution at pH=4.5.

The mixed chitosan-silica dispersion was prepared by a 1:1 dilution according to the procedure described by Ravera et al [37]. Briefly, a chitosan solution (pH=4.5) at twice the concentration of the final mixed dispersion was added dropwise to a stirred suspension of silica nanoparticles at twice the concentration of the final mixed dispersion. This method minimizes potential concentration gradients that could drive the system out of equilibrium [38,39]. Once the mixed dispersion is prepared, the pH is adjusted to 4.5 by adding acetic acid or sodium hydroxide. The dispersion obtained is stirred at 1000 rpm for 30 minutes to ensure thorough homogenization and then allowed to stand overnight. The single-phase or phase-separated character of the dispersions was then assessed by the absence or presence of a sedimented solid phase at the bottom of the container together with a dilute aqueous phase. For the purpose of the present study, only single-phase dispersions were considered.

8.2.3. Experimental methods

The effective charge density of the chitosan-capped silica particles was determined from electrophoretic mobility (u_e) measurements using laser Doppler velocimetry. These measurements were performed using a Nanosizer ZS (Malvern Instruments, Malvern, UK). According to the Henry's equation, the electrophoretic mobility is directly related to the zeta potential (ζ) (see *Chapter II*, 2.3.2. Zeta-Potential) [40].

The bulk viscosity of the samples was measured using an Ubbelohde viscometer (see *Chapter II*, 2.2.1. Capillary Viscometers). The liquid samples were placed in a glass viscometer maintained at 23°C. The liquid was then drawn up through a capillary and a measuring bulb, and the time taken for the liquid to fall through the bulb was recorded. The viscometer was calibrated using filtered Milli-Q water, and each sample was filtered prior to testing. The determination of viscosity is based on the principle that the flow time is directly proportional to the viscosity and inversely proportional to the density of the solution.

The interfacial tension at the air/dispersion interface was determined using a K10T Digital Tensiometer (KRÜSS GmbH, Hamburg, Germany) equipped with a platinum Wilhelmy plate contact probe (contact area of 40.5 mm). Prior to each measurement, the platinum plate was cleaned with ethanol and Milli-Q water, followed by burning with an ethanol torch to remove any residual organic matter. Samples were placed in a glass cuvette that was cleaned with ethanol and Milli-Q water prior to use. The temperature was maintained at 23°C using a thermostatic bath for all measurements. Each data point reported represents the average of at least three independent measurements. Experiments were run long enough to ensure that a steady state interfacial tension was reached.

A home-built electrocapillary waves (ECW) device was used to determine the dilational rheological properties of the particle-laden fluid/fluid interface at high frequencies (in the range of 10-10^3 Hz). Further details on this technique can be found in previous works [41,42], and in *Chapter II* (*2.1.4. Electro-Capillary Waves (ECW)*).

8.3. Results and discussion

8.3.1. Chitosan Adsorption on Silica Nanoparticles

The adsorption of chitosan on silica nanoparticles modifies the hydrophobicity of the nanoparticles. This is strongly dependent on the pH value which modulates the charge of the chitosan capping layer. In fact, the decrease in the pH from values close to 9 down to 4 leads

to an increase in the cationic charge of the chitosan, i.e., the degree of positive charge, as a result of the protonation of the amine groups. Therefore, a good alternative to explore the chitosan binding to silica nanoparticles is to work at a pH below the pK_a of the amine groups of chitosan (5.5) where chitosan is strongly positively charged and soluble in water, whereas silica nanoparticles are negatively charged in the pH range of 4-9 [26]. Based on the above discussion, a pH=4.5 was chosen to evaluate the adsorption of chitosan on silica nanoparticles, and the stability of the obtained dispersions. Thus, it is possible to select the optimal compositions that result in stable dispersions of particles that can adsorb at the fluid/fluid interface. It should be noted that maximum chitosan adsorption on silica surfaces is expected to occur in the pH range 4-pK_a [26]. **Figure 8. 1** shows the compositional maps as a chitosan concentration (C_{CHI})-silica nanoparticle concentration (C_{NPs}) diagram for dispersions of chitosan-capped silica nanoparticles at pH=4.5. Both stable and two-phase systems remain in the same state at least for a 7-week period.

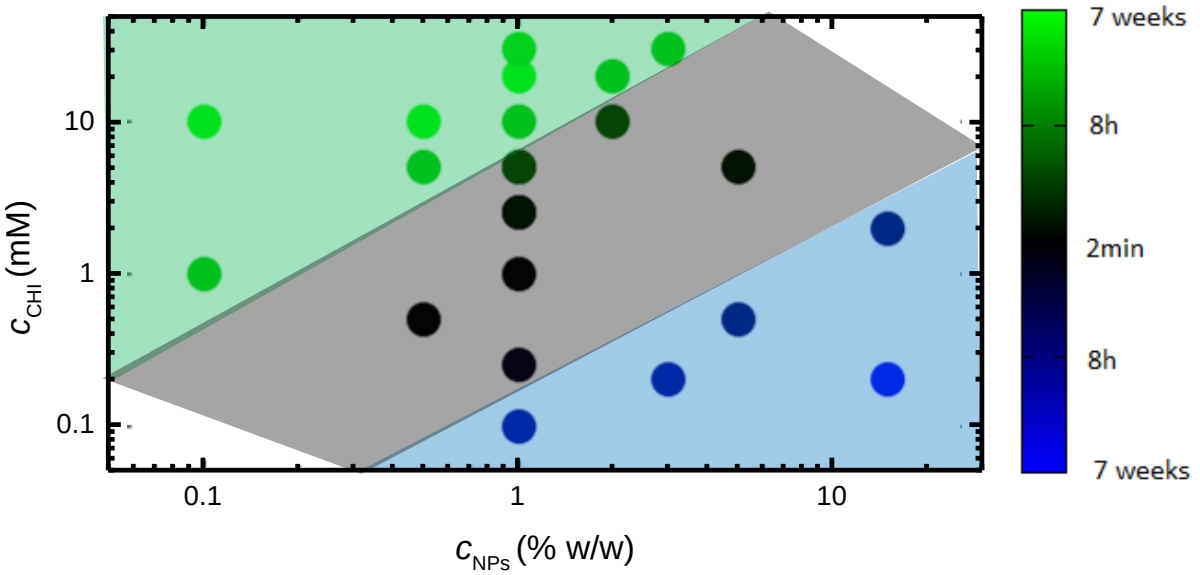

Figure 8. 1. C_{CHI}-C_{NPs} compositional maps where the stable or instable characters of mixed dispersions including chitosan and silica nanoparticles at pH=4.5 are shown. Green and blue symbols correspond to single-phase mixtures and grey symbols correspond to phase-separated mixtures. The shadowed regions indicate the different stability/instability regions in the compositional map, the color code is the same that for the symbols. Note that the defined timescale represents the maximum stability observed for the samples when considering unstable dispersions. For stable samples, it indicates the longest experimental observation period, after which the samples remain stable.

A better understanding of the characteristics of the chitosan-capped nanoparticles can be obtained by studying their surface charge. This is possible through measurements of electrophoretic mobility that give information on the ζ-potential of the particles. **Figure 8. 2** shows the dependence of the ζ-potential on the silica nanoparticles concentration for dispersions with different chitosan concentrations.

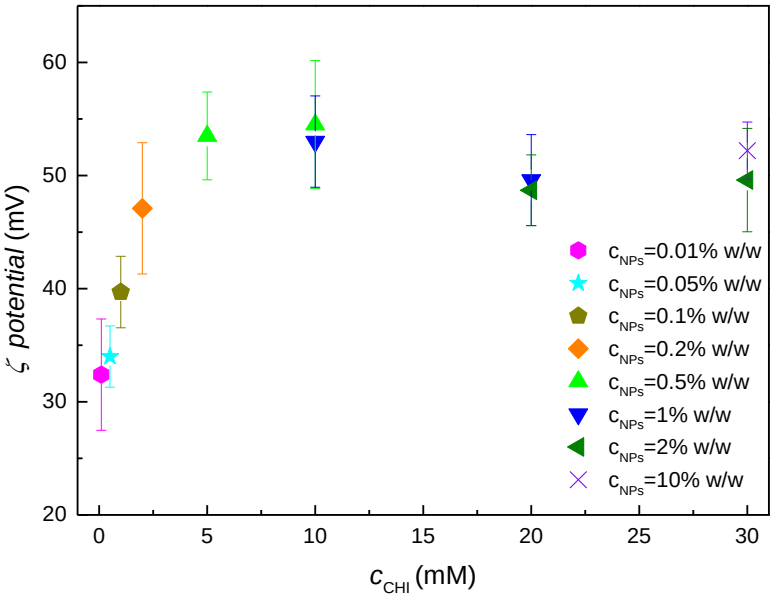

Figure 8. 2. Dependence of the ζ-potential on the chitosan concentration for dispersions with different silica nanoparticles concentrations at pH=4.5.

A deeper analysis of the compositional map on the light of the ζ-potential results suggests that the binding of chitosan to silica nanoparticles is mediated by a charge neutralization process. In fact, considering that pristine silica nanoparticles have a negative charge, as evidences the value of the ζ-potential around (-42±5) mV, and the positive values of the ζ-potential for the dispersions of the mixed systems, it is demonstrated clearly the adsorption of chitosan on the surface of the negatively charged silica nanoparticles. Thus, for a fixed particle concentration, as the chitosan concentration increases, the adsorption of chitosan on the silica surface leads to a neutralization of the negative charge of the nanoparticle surface up to the state of zero net charge, i.e., the isoelectric point, where the nanoparticles lack colloidal stability and therefore the chitosan-capped particles forms aggregates that sediment as a solid phase, leaving a dilute liquid phase, mainly containing chitosan as supernatant [26]. Further increase of the chitosan concentration beyond the isoelectric point results in a charge inversion process leading to the production of overcharged chitosan-capped particles characterized by their positive charge. This scenario explains the phase behavior of aqueous dispersions of chitosan-capped silica nanoparticles at pH=4.5. It should be noted that similar behavior have been reported for a broad range of colloidal systems assembled through electrostatic interactions, e.g., polyelectrolyte multilayers, oppositely charged polyelectrolyte-surfactant mixtures and interpolyelectrolyte complexes, among others [38,43-45].

8.3.2. Adsorption on chitosan-capped silica nanoparticles at the dispersion/air interface

The characterization of the adsorption of chitosan-capped silica nanoparticles at the aqueous dispersion/air interface was performed in terms of measurements of the equilibrium interfacial tension and the dilational properties of the particle-laden interface obtained by evaluating the interfacial damping of electrocapillary waves. **Figure 8. 3** shows the dependence of the interfacial tension of the aqueous dispersion/air interface on the silica nanoparticles concentration for dispersions with different chitosan concentrations. It is worth noting that bare silica nanoparticles are extremely hydrophilic, and their surface activity is almost negligible.

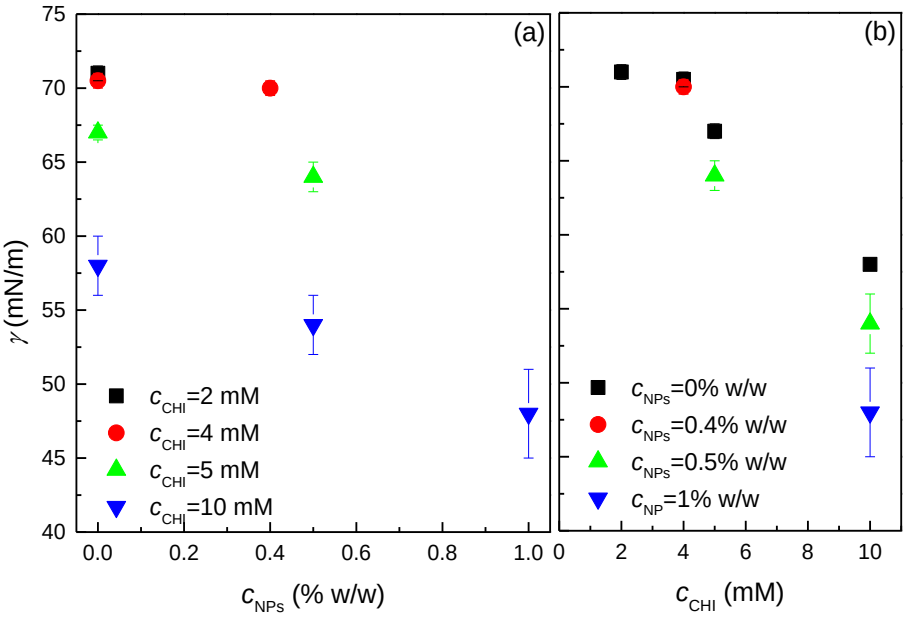

Figure 8. 3. (a) Dependence of the interfacial tension of the aqueous dispersion/air interface on the silica nanoparticles concentration for dispersions at pH=4.5 with different chitosan concentrations. (b) Dependence of the interfacial tension of the aqueous dispersion/air interface on the chitosan concentration for dispersions at pH=4.5 with different silica nanoparticles concentrations.

In contrast to the aforementioned phenomenon for silica nanoparticle adsorption, chitosan exhibits a concentration-dependent surface activity. Its adsorption at the aqueous solution/air interface results in a decrease in the interfacial tension, which varies from values close to those corresponding to a pure water/vapor interface (~72 mN/m) for the lowest chitosan concentrations to values below 60 mN/m for the highest concentration studied (10 mM). This can be understood by considering that chitosan presents a certain degree of amphiphilicity as a result of the two types of monomers existing within the chains. The chitosan used in this study is a random copolymer combining, in a molar ratio of 80:20, hydrophilic 2-amino-2-deoxy-β-D-glucose monomers, which are positively charged at the pH of this study, and a series of more hydrophobic N-acetyl-2-amino-2-deoxy-β-D-glucose monomers, which do not present a charge. The latter plays a central role on the control of the chitosan adsorption to the aqueous solution/air interface [46]. The findings concerning the adsorption of chitosan at the water/vapor interface are in agreement with those previously reported by Babak et al. [47]. Their results indicated minimal adsorption at highly dilute concentrations and a notable increase in adsorption as the concentration exceeded 10^{-2} mM.

Deepening of the adsorption of chitosan capped-particles at the aqueous dispersion/air interface, it is clear from the results that the increase in both the concentration of particles at fixed chitosan concentration and the later at fixed particle concentration leads to an enhancement on the ability of the dispersions to lower the interfacial tension. Moreover, the results show a strong synergistic effect of the interaction of chitosan and silica nanoparticles in decrease of the interfacial tension. This means that the adsorption of the mixed dispersions leads to a stronger decrease in the interfacial tension of the liquid/air interface than the individual components itself. This synergistic adsorption is similar to that reported by Maestro et al. [48] for the adsorption at the water/vapor interface of silica nanoparticles decorated by an alkyltrimethylammonium bromide surfactant.

At low chitosan concentration and fixed nanoparticle concentration, chitosan-capped silica nanoparticles shows a very reduced surface activity, and therefore a reduced interfacial coverage can be expected. This leads to an almost negligible reduction of the interfacial tension in relation to that of the pristine water/vapor interface. However, the increase of the chitosan concentration in dispersion with a fixed silica concentration leads to a strong enhancement of the surface activity of the capped-silica nanoparticles. This can be understood by considering that as the chitosan concentration increases, the hydrophobization of the nanoparticles is enough to increase their surface activity and promote their adsorption to the aqueous dispersion/vapor interface [27].

8.3.3. Surface dilational response of chitosan-capped silica nanoparticle layers at the dispersion/air interface

The study of the damping of capillary waves induced by electric fields, due to the presence of chitosan-capped nanoparticle layers at the dispersion/air interface, provides insights into the dilatational interfacial rheological response at frequencies above 50 Hz. Thus, it is possible to obtain information about kinetic processes occurring within the adsorbed layer, e.g., redistribution processes of chitosan molecules between the particles and the fluid/fluid interface, or some reorganization of the adsorbed layer [41]. To evaluate this type of phenomena, ECW experiments were performed in the range of 60-450 Hz. It should be noted that it was not possible to perform experiments at frequencies above 450 Hz, because the signal intensity decreased significantly, which significantly reduced the sensitivity of the measurements.

When a capillary wave is generated at an arbitrary point of a fluid/fluid interface (xy plane) defined as coordinate x = 0, its spatial profile can be described as a damped cosine wave given by the following expression (see *Chapter II*, *2.1.4. Electro-Capillary Waves (ECW)*):

$$u_z = u_z^0 e^{-\beta x} \cos\left(\frac{2\pi}{\lambda} x + \varphi\right) \quad (8.\ 1)$$

where u_z^0 is the wave amplitude, and β and λ are the damping coefficient and the characteristic wavelength of the capillary wave, respectively. ϕ accounts for the phase lag. **Figure 8. 4** shows the frequency (ν) dependences of the damping coefficients and the characteristic wavelengths corresponding to layers of chitosan-capped silica nanoparticles adsorbed at the dispersion/air interface.

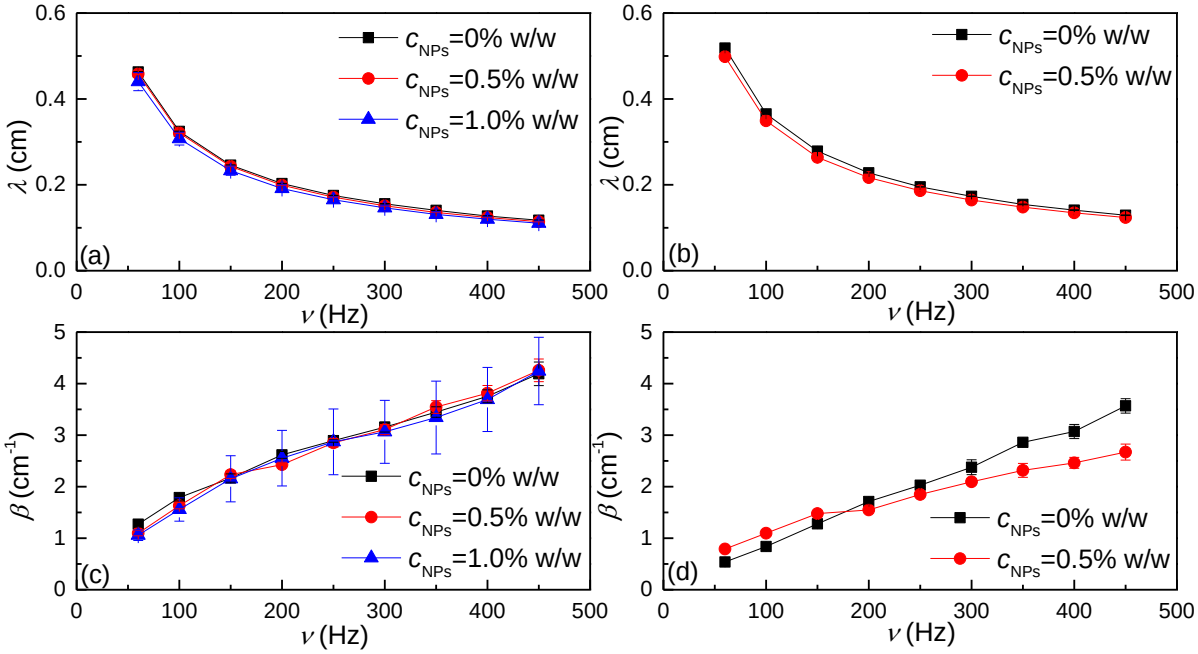

Figure 8. 4. Frequency dependences of the wavelength (λ) and damping (β) for layers obtained from the adsorption of dispersions of chitosan-capped silica nanoparticles, with different chitosan and silica nanoparticles concentrations, at the dispersion/air interface (pH=4.5). (a,b) λ values for layers obtained from the adsorption of dispersions with chitosan concentrations 10 mM and 5 mM, respectively, and (c,d) β values for layers obtained from the adsorption of dispersions with chitosan concentrations 10 mM and 5 mM, respectively. The lines are guides for the eyes.

The results indicate that at constant frequency, the capillary wavelength, λ, slightly change with increasing particle concentration, regardless of the chitosan concentration. As a first approach these observations can be explained in terms of Kelvin's law (see *Chapter II*, *2.1.4. Electro-Capillary Waves (ECW)*): $\lambda = \left(\frac{2\pi\gamma}{\nu^2\rho}\right)^{\frac{1}{3}}$ (where ρ represents the bulk density), which is a first order approximation strictly valid only for the surface of low-viscosity simple liquids [49]. In fact, the higher the particle concentration the lower the interfacial tension and consequently the lower the value of the capillary wavelength. On the other hand, the layers obtained from dispersion with lower values of C_{CHI}=5 mM have higher values of λ than when the chitosan concentration is higher (C_{CHI}=10 mM). This can also be understood by considering that for a fixed nanoparticle concentration, the interfacial tension assumes higher values as the polymer concentration decreases (see **Figure 8. 3**).

The interpretation of the frequency dependencies found for the damping coefficient is less straightforward (see **Figure 8. 4** (c) and (d)). For the damping coefficient at the highest chitosan concentration studied (C_{CHI}=10 mM), there are no effect of the particle concentration. On the contrary, for dispersions with a chitosan concentration of 5 mM, the damping coefficient decreases as the particle concentration increases. Moreover, the increase in polymer concentration results in an increase in the value of the damping coefficient for a fixed silica nanoparticles concentration. The latter can be understood by considering a derivation of Stokes's law ($\beta = \frac{4\eta\omega}{3\gamma}$, where η represents the solution viscosity, see *Chapter II*, *2.1.4. Electro-Capillary Waves (ECW)*) which predicts, for the surface of low viscosity pure liquids, an increase in the damping coefficient proportional to an increase in bulk shear viscosity (viscosity data for

chitosan solutions and chitosan-capped silica nanoparticle dispersions are reported in **Table 8. 1**). In addition, the decrease in the interfacial tension due to the increase in the polymer concentration, should lead to an increase in the damping coefficient. Also, it must be expected that the increase in the surface concentration should also contribute to the increase in the damping coefficient due to the viscoelasticity of the monolayer.

Table 8. 1. Viscosity data for chitosan solutions and chitosan-capped particle dispersions at pH=4.5 as were obtained by using a Ubbelohde viscometer. Notice that only stable chitosan-capped particle dispersions were measured.

c_{CHI} (mM)	η (mPa.s) c_{NPs}=0%w/w	η (mPa.s) c_{NPs}=0.4%w/w	η (mPa.s) c_{NPs}=0.5%w/w	η (mPa.s) c_{NPs}=1.0%w/w
2	1.5±0.1	-	-	-
4	3.04±0.2	2.01±0.1	-	-
5	3.5±0.3	-	2.4±0.2	-
10	5.1±0.5	-	4.5±0.5	4.1±0.5

Paying attention now to the modification of the damping coefficient with the particle concentration, two different regimes can be observed from the results. At high chitosan concentration (C_{CHI}=10 mM), the damping coefficient is almost the same independently of the silica nanoparticles concentration. This can be understood by considering that at such high chitosan concentration, the variation of the solution viscosity is very small with the increase in the particle concentration. On the contrary, when the concentration of chitosan is reduced to 5 mM, the viscosity decreases more markedly with the increase in the particle concentration, and this therefore leads to a decrease in the damping coefficient with the particle concentration.

A more detailed study of the frequency dependence of the capillary wavelength and the damping coefficient shows that the experimental data are consistent with simple scaling laws: $q \sim \omega^a$ and $\beta \sim \omega^b$, where $\omega=2\pi\nu$ represents the angular frequency and $q=2\pi/\lambda$ is the real part of the capillary wavevector. In this analysis, the exponent "*a*" was found to be in the range 0.67-0.69 under all conditions studied, which is close to the prediction of Kelvin's law: $q \sim \omega^{2/3}$. Conversely, the exponent for the scaling law describing the frequency dependence of β disagrees with the expected value derived from the Stokes-like law (b=1) [49]. This is undoubtedly related to viscoelastic character of the interfacial layer.

To extract information about the dilational response of the monolayer from ECW experiments, it is necessary to solve numerically the dispersion equation, $D(q,\omega)=0$. This equation establishes a relationship between the key parameters of transverse wave propagation (frequency ω, wavelength λ, and damping coefficient β) and the constitutive parameters of the monolayer, such as interfacial tension (γ), dilational storage modulus (E_s), and dilational viscosity (κ_s) [50,51].

$$D(q,\omega)=T(q,\omega,\gamma)L(q,\omega,{E_s}^*)+C(q,\omega)=0 \qquad (8.\ 2)$$

This assumes that the dilational rheological behavior of layers at the water/air interface is characterized by the interaction between the transverse or capillary term $T(q,\omega,\gamma)$ and the longitudinal or dilational term $L(q,\omega,E_s^*)$ whereas $C(q,\omega)$ is a term accounting for the coupling between transverse or capillary and longitudinal or dilational waves [52]. Solving the dispersion equation is possible to obtain the dilational viscoelastic modulus as (see *Chapter II*, *2.1.4. Electro-Capillary Waves (ECW)*):

$$E_s^*(\nu) = E_s(\nu) + iE_i(\nu) = \frac{\dfrac{-\left(\eta\omega(q-m)\right)^2}{\gamma q^2 + i\eta\omega(q+m) - \dfrac{\rho}{q}\omega^2} - i\eta\omega(q+m)}{q^2} \quad (8.\ 3)$$

where *q* is the complex capillary wavevector, defined as:

$$q = \frac{2\pi}{\lambda} - i\beta \quad (8.\ 4)$$

and *m* is the capillary penetration depth (Re(m) > 0):

$$m = \sqrt{q^2 + i\omega\frac{\rho}{\eta}} \quad (8.\ 5)$$

Figure 8. 5 shows the frequency dependencies of the interfacial dilational elastic (E_s) and viscous (E_i) moduli corresponding to layers of chitosan-capped silica nanoparticles at the dispersion/air interface obtained for the adsorption of dispersions with increasing concentrations of silica nanoparticles and a fixed of chitosan (10 mM).

The experimental data shows that except for chitosan solutions (C_{NPs}=0%w/w) the storage component of the dilational viscoelastic response, i.e., the elastic modulus, of the nanocomposite layer is higher than the viscous modulus. Moreover, the storage contribution for nanocomposite layers is higher than that found for chitosan (see **Figure 8. 5** (a)), while the opposite is true for the viscous modulus. This can be assumed to be result of the different structure of the layers, whereas pure chitosan layers at the solution/air dispersion present certain ability to reorganize at the interface and dissipate the energy associated with the interfacial deformation through the reorganization of the polymer chains. This situation is more limited when the nanocomposite layers are considered, here most of chitosan is expected to be attached to the particles, and therefore its reorganization within the interface is very limited. In addition, the dilational deformation of the interface is expected to contribute to the packing of the particles at the interface, which presents a more limited capacity to reorganize. This, in turn, contribute to the increase of the importance of the elastic component of the dilational response.

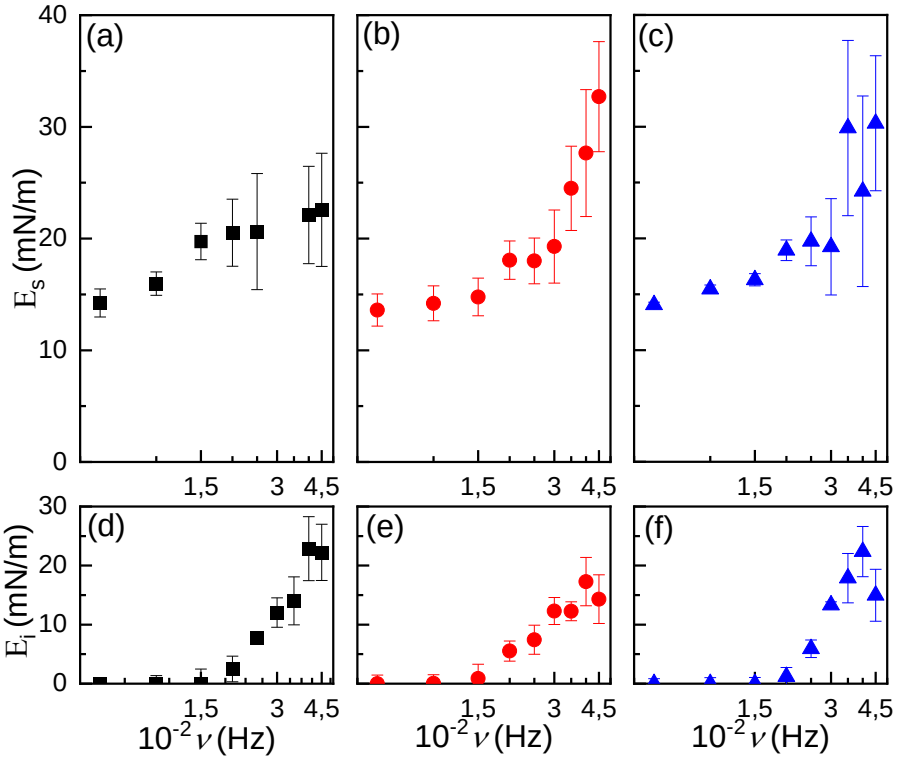

Figure 8. 5. Frequency dependences of the interfacial elastic (E_s) and viscous (E_i) moduli obtained from ECW experiments for layers obtained from the adsorption of dispersions of chitosan-capped silica nanoparticles, with different silica nanoparticles concentrations and a fixed chitosan concentration (10 mM), at the dispersion/air interface (pH=4.5). (a,b,c) E_s values for layers obtained from the adsorption of dispersions with silica nanoparticle concentrations 0%w/w, 0.5%w/w and 1.0%w/w, respectively, and (d,e,f) E_s values for layers obtained from the adsorption of dispersions with silica nanoparticles concentrations 0%w/w, 0.5%w/w and 1.0%w/w, respectively.

The above situation changes when chitosan concentration is reduced to 5 mM (see **Figure 8. 6**). In fact, in these conditions, chitosan layer shows a mainly elastic behavior ($E_i \approx 0$), independently of the frequency explored), whereas in the case of the chitosan-silica nanoparticle composite layer, elastic and viscous moduli present similar values. This can be understood considering that in the case of chitosan layer, the low chitosan concentration allows the chitosan to attach at the interface in an extended conformation. Therefore, the viscous dissipation as result of the presence of segments protruding to the air phase is strongly hindered. On the other hand, the different behavior on the viscoelastic response of the composite layer in relation to layers with higher chitosan concentration can be interpreted considering that the higher the chitosan concentration in the mixed dispersion the higher the packing of the particles at the interface as a result of the cross-linking between the chitosan-capping layers. This leads to an increase of the importance of the elastic contribution with the increase in the chitosan concentration in the mixed dispersion.

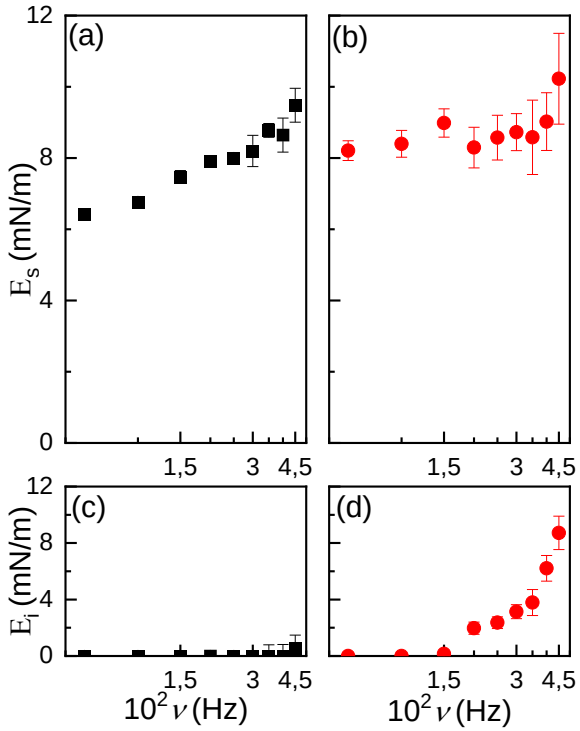

Figure 8. 6. Frequency dependences of the interfacial elastic (E_s) and viscous (E_i) moduli obtained from electrocapillary wave experiments for layers obtained from the adsorption of dispersions of chitosan-capped silica nanoparticles, with different silica nanoparticles concentrations and a fixed chitosan concentration (5 mM), at the dispersion/air interface (pH=4.5). (a,b) E_s values for layers obtained from the adsorption of dispersions with silica nanoparticles concentrations 0%w/w and 0.5%w/w, respectively, and (c,d) E_i values for layers obtained from the adsorption of dispersions with silica nanoparticles concentrations 0%w/w and 0.5%w/w respectively.

A more detailed analysis of the dilational viscoelastic moduli shows the presence of a relaxation process with a characteristic frequency in the range of 10^2 Hz for the particle-laden films. According to the frequency range in which appears this relaxation process, this process cannot be ascribed to a diffusion-controlled adsorption of the particles at the interface, which should appear in the frequency region below 1 Hz [41]. Therefore, the relaxation appearing in the dilational response should be related to a kinetics process occurring within the interface. This may be a result of the reorganization of the chitosan chains attached to the particles, or even to free chitosan molecules co-adsorbed at the interface together with the chitosan capped particles. It is not probable that this kinetics process at the interface can be associated with a time-dependent reorganization of the particles at the interface which may appears at frequencies closer to that corresponding to the diffusion from the bulk to the interface [41]. (44) Unfortunately, the limited accessible experimental window provided by the ECW measurements performed in this work does not allow a more detailed analysis of the relaxation process occurring within the interfacial films.

8.4. Conclusions

The adsorption of chitosan on silica nanoparticles has a significant impact on their hydrophobicity and charge properties. At pH 4.5, optimal adsorption occurs due to the strong positive charge of chitosan and the negative charge of silica nanoparticles, facilitating electrostatic interactions. This optimal pH was selected to evaluate stability of chitosan-silica nanoparticle dispersions and their ability to adsorb at the water/air interface. The compositional map at pH 4.5 indicated two distinct stable regions for these dispersions,

separated by an unstable region prone to rapid phase separation. This instability is attributed to the neutralization of the silica nanoparticle surface charge by adsorbed chitosan, reaching an isoelectric point where colloidal stability is lost, and particles sediment. Beyond this point, further increase in chitosan concentration results in charge inversion and the formation of positively charged chitosan-capped nanoparticles as demonstrated in the electrophoretic mobility measurements. In fact, pristine silica nanoparticles exhibited a negative ζ potential, whereas chitosan-capped nanoparticles showed positive values, affirming the adsorption and resulting charge changes.

Adsorption studies at the aqueous dispersion/air interface showed that chitosan significantly reduces interfacial tension, contrasting with the negligible surface activity of bare silica nanoparticles. The interfacial tension decreased with increasing chitosan concentration, illustrating chitosan's amphiphilic nature and its role in enhancing the surface activity of the nanoparticles. This synergistic effect leads to a stronger reduction in interfacial tension in comparison to the individual components.

The damping of ECW experiments offered insight into the interfacial rheology of chitosan-capped nanoparticle layers. The presence of these nanoparticles resulted in alterations to both the capillary wavelength and the damping coefficient. At higher particle concentrations, a reduction in interfacial tension and capillary wavelength was observed. The damping coefficient exhibited a dependence on both particle and chitosan concentrations. At elevated chitosan concentrations, the viscosity of the dispersions increased, leading to enhanced damping. Additionally, the surface excess of the layer formed was expected to be higher, contributing to the observed increase in damping. The frequency dependence of the interfacial dilatational elastic and viscous moduli demonstrated that nanocomposite layers exhibited a higher elastic modulus in comparison to pure chitosan layers. This can be attributed to the restricted capacity of composite layers at the interface for reorganization, which consequently increases the importance of the elastic response. Overall, the study highlights the critical role of pH in modulating chitosan adsorption on silica nanoparticles, the resulting phase behavior, surface charge modifications, and enhanced interfacial properties of the composites. These findings provide a deeper understanding of the interaction mechanisms and potential applications of chitosan-silica nanoparticle systems in various fields.

8.5. References

1. Binks, B.P. Colloidal Particles at a Range of Fluid-Fluid Interfaces. *Langmuir* **2017**, *33*, 6947-6963, doi:10.1021/acs.langmuir.7b00860.
2. Guzman, E.; Martinez-Pedrero, F.; Calero, C.; Maestro, A.; Ortega, F.; Rubio, R.G. A broad perspective to particle-laden fluid interfaces systems: from chemically homogeneous particles to active colloids. *Adv Colloid Interface Sci* **2022**, *302*, 102620, doi:10.1016/j.cis.2022.102620.
3. Maestro, A.; Santini, E.; Guzman, E. Physico-chemical foundations of particle-laden fluid interfaces. *Eur Phys J E Soft Matter* **2018**, *41*, 97, doi:10.1140/epje/i2018-11708-6.
4. Guzman, E.; Abelenda-Nunez, I.; Maestro, A.; Ortega, F.; Santamaria, A.; Rubio, R.G. Particle-laden fluid/fluid interfaces: physico-chemical foundations. *J Phys Condens Matter* **2021**, *33*, doi:10.1088/1361-648X/ac0938.

5. Zanini, M.; Isa, L. Particle contact angles at fluid interfaces: pushing the boundary beyond hard uniform spherical colloids. *J Phys Condens Matter* **2016**, *28*, 313002, doi:10.1088/0953-8984/28/31/313002.
6. Bayles, A.V.; Vermant, J. Divide, Conquer, and Stabilize: Engineering Strong Fluid-Fluid Interfaces. *Langmuir* **2022**, *38*, 6499-6505, doi:10.1021/acs.langmuir.2c00948.
7. Vialetto, J.; Anyfantakis, M. Exploiting Additives for Directing the Adsorption and Organization of Colloid Particles at Fluid Interfaces. *Langmuir* **2021**, *37*, 9302-9335, doi:10.1021/acs.langmuir.1c01029.
8. Ballard, N.; Law, A.D.; Bon, S.A.F. Colloidal particles at fluid interfaces: behaviour of isolated particles. *Soft Matter* **2019**, *15*, 1186-1199, doi:10.1039/c8sm02048e.
9. Maestro, A. Tailoring the interfacial assembly of colloidal particles by engineering the mechanical properties of the interface. *Current Opinion in Colloid & Interface Science* **2019**, *39*, 232-250, doi:10.1016/j.cocis.2019.02.013.
10. Maestro, A.; Guzmán, E.; Ortega, F.; Rubio, R.G. Contact angle of micro- and nanoparticles at fluid interfaces. *Current Opinion in Colloid & Interface Science* **2014**, *19*, 355-367, doi:10.1016/j.cocis.2014.04.008.
11. Lin, Y.; Skaff, H.; Emrick, T.; Dinsmore, A.D.; Russell, T.P. Nanoparticle assembly and transport at liquid-liquid interfaces. *Science* **2003**, *299*, 226-229, doi:10.1126/science.1078616.
12. Forth, J.; Kim, P.Y.; Xie, G.; Liu, X.; Helms, B.A.; Russell, T.P. Building Reconfigurable Devices Using Complex Liquid-Fluid Interfaces. *Adv Mater* **2019**, *31*, e1806370, doi:10.1002/adma.201806370.
13. Garbin, V. Colloidal particles: Surfactants with a difference. *Physics Today* **2013**, *66*, 68-69, doi:10.1063/pt.3.2158.
14. Garbin, V.; Crocker, J.C.; Stebe, K.J. Nanoparticles at fluid interfaces: exploiting capping ligands to control adsorption, stability and dynamics. *J Colloid Interface Sci* **2012**, *387*, 1-11, doi:10.1016/j.jcis.2012.07.047.
15. Yan, Y.L.; Cai, Y.X.; Liu, X.C.; Ma, G.W.; Lv, W.; Wang, M.X. Hydrophobic Modification on the Surface of SiO(2) Nanoparticle: Wettability Control. *Langmuir* **2020**, *36*, 14924-14932, doi:10.1021/acs.langmuir.0c02118.
16. Starvaggi, N.C.; Bradford, B.J.; Taylor, C.D.L.; Pentzer, E.B. Wettability-tuned silica particles for emulsion-templated microcapsules. *Soft Matter* **2023**, *19*, 7635-7643, doi:10.1039/d3sm00860f.
17. Rong, H.-T.; Frey, S.; Yang, Y.-J.; Zharnikov, M.; Buck, M.; Wühn, M.; Wöll, C.; Helmchen, G. On the Importance of the Headgroup Substrate Bond in Thiol Monolayers: A Study of Biphenyl-Based Thiols on Gold and Silver. *Langmuir* **2001**, *17*, 1582-1593, doi:10.1021/la0014050.
18. Songolzadeh, R.; Moghadasi, J. Stabilizing silica nanoparticles in high saline water by using ionic surfactants for wettability alteration application. *Colloid and Polymer Science* **2016**, *295*, 145-155, doi:10.1007/s00396-016-3987-3.
19. Santini, E.; Guzmán, E.; Ferrari, M.; Liggieri, L. Emulsions stabilized by the interaction of silica nanoparticles and palmitic acid at the water–hexane interface. *Colloids and Surfaces A: Physicochemical and Engineering Aspects* **2014**, *460*, 333-341, doi:10.1016/j.colsurfa.2014.02.054.
20. González-González, A.; Sánchez-Arribas, N.; Santini, E.; Rodríguez-Villafuerte, J.L.; Carbone, C.; Ravera, F.; Ortega, F.; Liggieri, L.; Rubio, R.G.; Guzmán, E. Effects of Oil Phase on the Inversion of Pickering Emulsions Stabilized by Palmitic Acid Decorated Silica Nanoparticles. *Colloids and Interfaces* **2022**, *6*, 27, doi:10.3390/colloids6020027.

21. Sun, G.; Guo, T.; Luo, J.; Liu, R.; Ngai, T.; Binks, B.P. Phase Inversion of Pickering Emulsions Induced by Interfacial Electrostatic Attraction. *Langmuir* **2023**, *39*, 1386-1393, doi:10.1021/acs.langmuir.2c02048.
22. Anyfantakis, M.; Vialetto, J.; Best, A.; Auernhammer, G.K.; Butt, H.J.; Binks, B.P.; Baigl, D. Adsorption and Crystallization of Particles at the Air-Water Interface Induced by Minute Amounts of Surfactant. *Langmuir* **2018**, *34*, 15526-15536, doi:10.1021/acs.langmuir.8b03233.
23. Jiang, J.; Zhu, Y.; Cui, Z.; Binks, B.P. Switchable pickering emulsions stabilized by silica nanoparticles hydrophobized in situ with a switchable surfactant. *Angew Chem Int Ed Engl* **2013**, *52*, 12373-12376, doi:10.1002/anie.201305947.
24. Binks, B.P.; Isa, L.; Tyowua, A.T. Direct measurement of contact angles of silica particles in relation to double inversion of pickering emulsions. *Langmuir* **2013**, *29*, 4923-4927, doi:10.1021/la4006899.
25. Maestro, A.; Guzmán, E.; Santini, E.; Ravera, F.; Liggieri, L.; Ortega, F.; Rubio, R.G. Wettability of silicananoparticle–surfactant nanocomposite interfacial layers. *Soft Matter* **2012**, *8*, 837-843, doi:10.1039/c1sm06421e.
26. Alison, L.; Demirors, A.F.; Tervoort, E.; Teleki, A.; Vermant, J.; Studart, A.R. Emulsions Stabilized by Chitosan-Modified Silica Nanoparticles: pH Control of Structure-Property Relations. *Langmuir* **2018**, *34*, 6147-6160, doi:10.1021/acs.langmuir.8b00622.
27. Alison, L.; Ruhs, P.A.; Tervoort, E.; Teleki, A.; Zanini, M.; Isa, L.; Studart, A.R. Pickering and Network Stabilization of Biocompatible Emulsions Using Chitosan-Modified Silica Nanoparticles. *Langmuir* **2016**, *32*, 13446-13457, doi:10.1021/acs.langmuir.6b03439.
28. Luengo, G.S.; Fameau, A.L.; Leonforte, F.; Greaves, A.J. Surface science of cosmetic substrates, cleansing actives and formulations. *Adv Colloid Interface Sci* **2021**, *290*, 102383, doi:10.1016/j.cis.2021.102383.
29. Luengo, G.S.; Leonforte, F.; Greaves, A.; Rubio, R.G.; Guzman, E. Physico-chemical challenges on the self-assembly of natural and bio-based ingredients on hair surfaces: towards sustainable haircare formulations. *Green Chemistry* **2023**, *25*, 7863-7882, doi:10.1039/d3gc02763e.
30. Fernandez-Pena, L.; Guzman, E.; Leonforte, F.; Serrano-Pueyo, A.; Regulski, K.; Tournier-Couturier, L.; Ortega, F.; Rubio, R.G.; Luengo, G.S. Effect of molecular structure of eco-friendly glycolipid biosurfactants on the adsorption of hair-care conditioning polymers. *Colloids Surf B Biointerfaces* **2020**, *185*, 110578, doi:10.1016/j.colsurfb.2019.110578.
31. Heidari, F.; Jafari, S.M.; Ziaiifar, A.M.; Anton, N. Surface modification of silica nanoparticles by chitosan for stabilization of water-in-oil Pickering emulsions. *Carbohydrate Polymer Technologies and Applications* **2023**, *6*, 100381, doi:10.1016/j.carpta.2023.100381.
32. Nan, F.; Wu, J.; Qi, F.; Liu, Y.; Ngai, T.; Ma, G. Uniform chitosan-coated alginate particles as emulsifiers for preparation of stable Pickering emulsions with stimulus dependence. *Colloids and Surfaces A: Physicochemical and Engineering Aspects* **2014**, *456*, 246-252, doi:10.1016/j.colsurfa.2014.05.017.
33. Wongkongkatep, P.; Manopwisedjaroen, K.; Tiposoth, P.; Archakunakorn, S.; Pongtharangkul, T.; Suphantharika, M.; Honda, K.; Hamachi, I.; Wongkongkatep, J. Bacteria interface pickering emulsions stabilized by self-assembled bacteria-chitosan network. *Langmuir* **2012**, *28*, 5729-5736, doi:10.1021/la300660x.
34. An, J.; Zhang, X.; Guo, Q.; Zhao, Y.; Wu, Z.; Li, C. Glycopolymer modified magnetic mesoporous silica nanoparticles for MR imaging and targeted drug delivery. *Colloids*

and Surfaces A: Physicochemical and Engineering Aspects **2015**, *482*, 98-108, doi:10.1016/j.colsurfa.2015.04.035.
35. Hu, X.; Wang, Y.; Peng, B. Chitosan-capped mesoporous silica nanoparticles as pH-responsive nanocarriers for controlled drug release. *Chem Asian J* **2014**, *9*, 319-327, doi:10.1002/asia.201301105.
36. Sogias, I.A.; Khutoryanskiy, V.V.; Williams, A.C. Exploring the Factors Affecting the Solubility of Chitosan in Water. *Macromolecular Chemistry and Physics* **2010**, *211*, 426-433, doi:10.1002/macp.200900385.
37. Ravera, F.; Santini, E.; Loglio, G.; Ferrari, M.; Liggieri, L. Effect of nanoparticles on the interfacial properties of liquid/liquid and liquid/air surface layers. *J Phys Chem B* **2006**, *110*, 19543-19551, doi:10.1021/jp0636468.
38. Varga, I.; Campbell, R.A. General Physical Description of the Behavior of Oppositely Charged Polyelectrolyte/Surfactant Mixtures at the Air/Water Interface. *Langmuir* **2017**, *33*, 5915-5924, doi:10.1021/acs.langmuir.7b01288.
39. Puente-Santamaría, A.; Ortega, F.; Maestro, A.; Rubio, R.G.; Guzmán, E. Non-equilibrium states in polyelectrolyte-surfactant systems at fluid interfaces: A critical review. *Current Opinion in Colloid & Interface Science* **2024**, *71*, 101804, doi:10.1016/j.cocis.2024.101804.
40. Smoluchowski, M. *Handbuch der Elektrizität und des Magnetismus*; Graetz, L., Ed. J.A. Barth: Leipzig, Germany, 1921.
41. Liggieri, L.; Santini, E.; Guzmán, E.; Maestro, A.; Ravera, F. Wide-frequency dilational rheology investigation of mixed silica nanoparticle–CTAB interfacial layers. *Soft Matter* **2011**, *7*, 7699, doi:10.1039/c1sm05257h.
42. Maestro, A.; Ortega, F.; Rubio, R.G.; Rubio, M.A.; Kragel, J.; Miller, R. Rheology of poly(methyl methacrylate) Langmuir monolayers: percolation transition to a soft glasslike system. *J Chem Phys* **2011**, *134*, 104704, doi:10.1063/1.3560612.
43. Van Tassel, P.R. Polyelectrolyte adsorption and layer-by-layer assembly: Electrochemical control. *Current Opinion in Colloid & Interface Science* **2012**, *17*, 106-113, doi:10.1016/j.cocis.2011.08.008.
44. Fares, H.M.; Schlenoff, J.B. Equilibrium Overcompensation in Polyelectrolyte Complexes. *Macromolecules* **2017**, *50*, 3968-3978, doi:10.1021/acs.macromol.7b00665.
45. He, R.; Chen, J.; Zhang, C.; Lu, D.; Zhang, L.; He, T. Quantification of overcompensated cations in layer-by-layer membrane by Orange yellow II. *Separation and Purification Technology* **2024**, *331*, 125637, doi:10.1016/j.seppur.2023.125637.
46. Nilsen-Nygaard, J.; Strand, S.; Vårum, K.; Draget, K.; Nordgård, C. Chitosan: Gels and Interfacial Properties. *Polymers* **2015**, *7*, 552-579, doi:10.3390/polym7030552.
47. Babak, V.; Lukina, I.; Vikhoreva, G.; Desbrières, J.; Rinaudo, M. Interfacial properties of dynamic association between chitin derivatives and surfactants. *Colloids and Surfaces A: Physicochemical and Engineering Aspects* **1999**, *147*, 139-148, doi:10.1016/s0927-7757(98)00752-3.
48. Maestro, A.; Rio, E.; Drenckhan, W.; Langevin, D.; Salonen, A. Foams stabilised by mixtures of nanoparticles and oppositely charged surfactants: relationship between bubble shrinkage and foam coarsening. *Soft Matter* **2014**, *10*, 6975-6983, doi:10.1039/c4sm00047a.
49. Langevin, D. *Light Scattering by Liquid Surfaces and Complementary Techniques.* ; CRC Press: New York, US, 1992; Vol. 41.

50. Levich, V.G. *Physicochemical Hydrodynamics* Prentice-Hall: Englewood Cliffs, New Jersey, US, 1962.
51. Lucassen-Reynders, E.H.; Lucassen, J. Properties of capillary waves. *Advances in Colloid and Interface Science* **1970**, *2*, 347-395, doi:10.1016/0001-8686(70)80001-x.
52. Ravera, F.; Ferrari, M.; Santini, E.; Liggieri, L. Influence of surface processes on the dilational visco-elasticity of surfactant solutions. *Adv Colloid Interface Sci* **2005**, *117*, 75-100, doi:10.1016/j.cis.2005.06.002.

Section 5 Interfacial rheology of viscoelastic polymer solutions

- *Chapter IX: Interfacial rheology of PVA/Borax viscoelastic solutions.*

Section 5 consists in a single chapter, which is focused on the dilational interfacial response of a system exhibiting a non-negligible shear bulk viscoelasticity in the subphase. This issue is not taken into account by the classical hydrodynamic models used to determine the dilational interfacial modulus by surface wave damping propagation parameters. For the aim of this study, Poly(vinyl alcohol) (PVA, a water-soluble polymer) was mixed with a crosslinker (BORAX). PVA/BORAX solutions were chosen as potential candidates for this study, because they exhibit bulk viscoelasticity within ECW frequency range, and their bulk shear viscosity does not exceed ECW operative limits. The study compares the dilational interfacial modulus calculated with the classical hydrodynamic models with the one calculated with a dispersion equation taking into account the bulk viscoelasticity of the subphase.

Chapter IX: Interfacial rheology of PVA/Borax viscoelastic solutions

9.1. Introduction

In the previous chapters of this PhD thesis, the dilational interfacial rheological response was determined by means of the analysis of the propagation parameters of damped capillary waves on the surface of complex liquids. The hydrodynamic models that were employed to determine the dilational interfacial modulus of the films were based on the assumption that the liquids exhibit a mainly viscous character. This means that their bulk shear viscosity does not depend on the frequency of the mechanical perturbations, and the contribution of the shear elasticity to their rheological behavior can be neglected. However, many complex fluids, such as polymer gels and polymer solutions above the overlapping concentration contain entangled polymers [1]. This results in the emergence of viscoelastic behavior in the bulk. This viscoelastic character of the bulk subphase is not included in the dispersion equation for capillary waves proposed by Lucassen [2,3].

The study of surface capillary modes in viscoelastic fluids is crucial not only in determining the dilational interfacial response of complex fluids, but also finds many technological applications, especially in polymer lubricants (affecting energy dissipation), coatings, biotechnology and tribology, where the interfacial behavior, as well as bulk viscoelasticity, play a key role in the performance of the products [4-6]. There is evidence, for example, proving that the flow of liquids in polymer gel coated pipes is different with respect to the one occurring in uncoated pipes [6,7].

The first hydrodynamic model for describing surface modes of viscoelastic fluids was proposed by Harden, Pleiner and Pincus, who derived a dispersion equation assuming the presence of viscoelasticity in the bulk, but without taking into account any surface dilational contribution [6,8]. This is known as “HPP Theory”, and it will be briefly described in the following. There are several studies were the validity of HPP theory was proved [9-12]. However, there is also evidence that the description of such theory is not able to provide an accurate description under any condition. For instance, the Surface Laser Light Scattering (SLLS) spectrum of the poly-N-vinyl-2-pyrrolidone water solutions deviates significantly from the prediction of the HPP theory [4,13]. To solve this issue, Wang and Huang [4] introduced a new hydrodynamicl model describing the surface modes of both capillary waves and elastic waves, including the effect of the surface dilational contribution, as a consequence of the polymer adsorption at the interface, phenomena that were ignored by the HPP theory.

Similarly to that what was already shown in *Chapter II* (*2.1.4. Electro-Capillary Waves (ECW)*), in order to derive the dispersion relation of capillary surface waves in a viscoelastic fluid, the first step is to determine the velocity field components along x-axis (direction of propagation) and z-axis (transversal direction) (see **Figure 9. 1**).

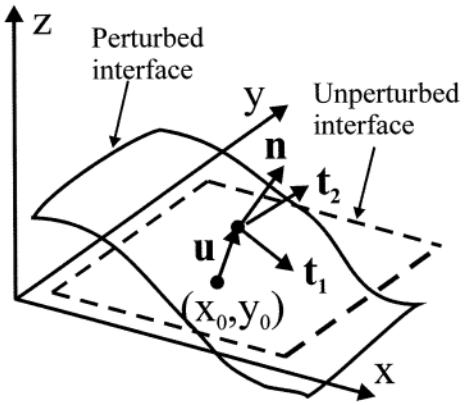

Figure 9. 1. Surface geometry of fluid/fluid interface and reference system. Adapted from ref. [14].

The velocity components ($\boldsymbol{v}(x,z,t) = [v_x(x,z,t), v_z(x,z,t)]$) can be obtained by solving the Navier-Stokes equation of an incompressible and viscoelastic fluid [4,15],

$$\rho \frac{\partial \boldsymbol{v}(x,z,t)}{\partial t} = -\nabla P(x,z,t) + \int_0^t G(t-\tau)\nabla^2 \boldsymbol{v}(x,z,\tau)d\tau, \tag{9. 1}$$

where $P(x,z,t)$ is the pressure field, ρ is the density of the fluid and $G(t)$ is the time dependent bulk shear modulus. For simplicity, since the phase above the interface is less dense and less viscous, its presence can be neglected in solving the hydrodynamic problem. The boundary conditions at the interface ($z = 0$), similarly to what described in see *Chapter II* (*2.1.4. Electro-Capillary Waves (ECW)*) (as reported, for example, in ref. [3,4]) can be defined as,

$$-P + \sigma_{zz} = \gamma \frac{\partial^2 u_z}{\partial x^2}, \tag{9. 2}$$

And

$$\sigma_{xz} = E_s^* \frac{\partial^2 u_x}{\partial x^2}, \tag{9. 3}$$

where γ is the surface tension, E_s^* is the complex dilational interfacial modulus, u_z and u_x are the vertical and the horizontal displacements of the interface, respectively,

$$u_z = \int_0^t v_z(x,0,\tau)d\tau, \tag{9. 4}$$

and

$$u_x = \int_0^t v_x(x,0,\tau)d\tau. \tag{9. 5}$$

σ_{jk} is the bulk shear stress at the interface, defined as,

$$\sigma_{jk} = \int_0^t G(t-\tau)\left(\frac{\partial v_j}{\partial k} + \frac{\partial v_k}{\partial j}\right)d\tau. \tag{9. 6}$$

It is useful to define some quantities that will be useful to define some ancillary variables to solve the hydrodynamic problem. First of all, the Fourier transform, with respect to x-variable, of the j-component ($j = x, z$) of the velocity ($v_{j,q}(t)$) for the surface vertical displacement ($u_{z,q}(t)$) and for the pressure ($P_q(t)$),

$$v_{j,q}(z,t) = \int_{-\infty}^{+\infty} v_j(x,z,t)e^{iqx}dx, \tag{9. 7}$$

$$u_{z,q}(t) = \int_{-\infty}^{+\infty} u_z(x,t)e^{iqx}dx, \tag{9. 8}$$

and

$$P_q(t) = \int_{-\infty}^{+\infty} P(x,t)e^{iqx}dx, \tag{9. 9}$$

where *q* is the complex capillary wavevector,

$$q = \frac{2\pi}{\lambda} - \beta, \tag{9. 10}$$

with λ being the capillary wavelength and β the spatial damping coefficient of the capillary wave. The general solution of the hydrodynamic problem ($v_{z,q}$) can be written as follows,

$$v_{q,z}(z,t) = f(t)e^{qz} + g(t)e^{mz}, \tag{9. 11}$$

where $f(t)$ and $g(t)$ are two time-dependent functions that can be determined by setting boundary conditions, i.e., equations (9. 2) and (9. 3) to the hydrodynamic problem, and m is the capillary penetration depth defined in a viscoelastic fluid,

$$m = \sqrt{q^2 + \frac{i\omega\rho}{\eta^*(\omega)}}, \tag{9. 12}$$

where $\omega = 2\pi\nu$ is the angular frequency (and ν the frequency). Equation (9. 12) is formally equivalent to the capillary penetration depth defined in see *Chapter II* (*2.1.4. Electro-Capillary Waves (ECW)*), but, in a viscoelastic fluid, the bulk shear viscosity is a frequency dependent complex magnitude. As previously explained (see *Chapter I*, *1.3. Bulk Shear Rheology*) the complex shear viscosity is given by the Laplace transform of $G(t)$ with respect to the Laplace variable $s = i\omega$,

$$\eta^*(\omega) = \eta'(\omega) - i\eta''(\omega) = \int_0^{+\infty} G(t)e^{-i\omega t}dt. \tag{9. 13}$$

$\eta^*(\omega)$ is related to the complex shear modulus $G^*(\omega)$:

$$G^*(\omega) = i\omega\eta^*(\omega) = i\omega\eta'(\omega) + \omega\eta''(\omega) = G'(\omega) + iG''(\omega). \tag{9. 14}$$

The real part of the complex viscosity ($\eta'(\omega)$) is associated to the loss modulus $G''(\omega)$, and represents the bulk shear viscosity of the fluid, while the imaginary part ($\eta''(\omega)$) is related to the storage modulus $G'(\omega)$, thus it is related to the bulk shear elasticity of the fluid.

By combining equation (9. 1) with the boundary conditions (equations (9. 4) and (9. 5)), after carrying out some mathematical transformation (see reference [4]), the following linear system of two equations in 2 unknowns ($\hat{f}$ and $\hat{g}$) can be obtained,

$$\begin{bmatrix}\hat{f}\\ \hat{g}\end{bmatrix}\cdot \boldsymbol{M} = \begin{bmatrix}-Bu_{z,q}(0)\\ -\dfrac{iE_s^* q^3 u_{z,q}(0)}{i\omega\eta^*(\omega)}\end{bmatrix}, \tag{9. 15}$$

where $\hat{f}$ and $\hat{g}$ are the Laplace transforms with respect to the Laplace variable $s = i\omega$ of $f(t)$ and $g(t)$, and $\boldsymbol{M}$ is the matrix of the coefficients:

$$\boldsymbol{M} = \begin{bmatrix} b + B + \dfrac{\eta^*(\omega)q}{\rho}(1+q) & 2q^2 + \dfrac{E_s^* q^3}{i\omega\eta^*(\omega)} \\ b + B + \dfrac{\eta^*(\omega)m}{\rho}(1+m) & q^2 + m^2 + \dfrac{E_s^* q^2 m}{i\omega\eta^*(\omega)} \end{bmatrix}, \tag{9. 16}$$

where $b = i\omega + \frac{\eta^*(\omega)q^2}{\rho}$ and $B = \frac{\gamma q^3}{i\omega\rho}$. By setting that $\det(\boldsymbol{M}) = 0$, which means that the solution of the linear system exists and it is unique, the dispersion equation can be easily obtained,

$$\left[(1+2M)^{\frac{1}{2}} - (1+M)^2 - \frac{BM}{V}\right] + \frac{E_s^* q}{2G^*(\omega)}\left[\frac{B}{V} - (1+2M)^{\frac{1}{2}}\left(\frac{B}{V} + M\right)\right] = 0, \tag{9. 17}$$

where $M = \frac{1}{2}\left(\frac{m^2}{q^2} - 1\right)$ and $V = \frac{2q^2\eta^*(\omega)}{\rho}$. Equation (9. 17) can be also expressed in the following form,

$$\left[\gamma q^2 + i\eta^*(\omega)\omega(q+m) - \frac{\rho\omega^2}{q}\right]\left[{E_s}^*(\omega)q^2 + i\eta^*(\omega)\omega(q+m)\right] + \left[\eta^*(\omega)\omega(q-m)\right]^2 = 0. \tag{9. 18}$$

Equation (9. 18) reduces to the dispersion equation derived by Lucassen [2,3] (previously described in see *Chapter II*, *2.1.4. Electro-Capillary Waves (ECW)*), in case of purely viscous liquids (hence, in case of negligible bulk elasticity ($\eta''(\omega) \approx 0$ and $\eta'(\omega) = \eta$ does not depend on frequency),

$$\left[\gamma q^2 + i\eta\omega(q+m) - \frac{\rho\omega^2}{q}\right]\left[{E_s}^*(\omega)q^2 + i\eta\omega(q+m)\right] + \left[\eta\omega(q-m)\right]^2 = 0. \tag{9. 19}$$

In case of a viscoelastic fluid, but with negligible surface interfacial dilational contribution (${E_s}^* = 0$), equation (9. 18) reduces to the dispersion equation derived by Harden, Pleiner-and Pincus (HPP theory) [6,8],

$$\left[i\omega + \frac{2\eta^*(\omega)}{\rho}q^2\right]^2 - 4\left(\frac{\eta^*(\omega)}{\rho}\right)^2 q^4\left[1 + \frac{i\omega\rho}{\eta^*(\omega)q^2}\right]^{\frac{1}{2}} + \frac{\gamma q^3}{\rho} = 0. \tag{9. 20}$$

The aim of this chapter is to study the effect of bulk viscoelasticity on the dilational surface modulus ${E_s}^*$ determined in the range of frequency of electrocapillary waves (ECW) technique. ECW measurements on gels or extremely concentrated polymer solutions are practically unfeasible due to the high viscosity, which would produce a huge damping in the propagating

capillary waves. Thus, solutions with $\eta'(\omega) > 2 \cdot 10^{-2}\ Pa \cdot s$ would not allow a systematic study within ECW frequency range due to the high contribution of the damping to the response. This threshold value was determined as a rule of thumb, according to the usual experimental limits of ECW technique, and it may vary also according to the surface adsorption, which also affects damping. Furthermore, in order to appreciate the effect of bulk elasticity, the imaginary part of the complex viscosity should be comparable to the real part: this happens when $G'(\omega)$ and $G''(\omega)$ are in the same order of magnitude.

Poly-Vinil-Alcohol (PVA, **Figure 9. 2**) is a water-soluble partially amphiphilic polymer that can form hydrogen bonds, which can lead, in water solutions, to the formation of gels when the solution concentration is high enough. Thus, the physico-chemical properties of PVA make it a good candidate to evaluate the role of the bulk viscoelasticity in the damping of capillary waves. On the other hand, PVA finds many biomedical applications, especially in drug delivery, tissue engineering, cosmetics, scaffolds… [1,16], but it can also be used in other industrial applications, e.g., oil industry, food packaging… [17-19].

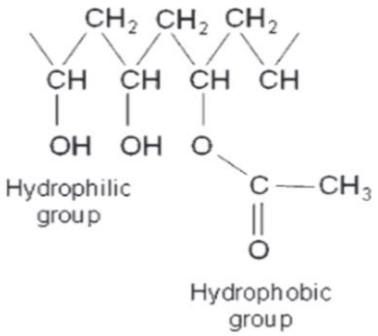

Figure 9. 2. General chemical formula of Poly-Vinil-Alcohol (PVA), containing hydrophilic groups (-OH) and hydrophobic residual groups (Acetyl groups, -CH3COO-). Adapted from ref. [20].

The degree of acetylation of PVA , i.e., the presence of acetyl groups, affects the hydrophobicity/hydrophilicity of the polymer chains [21]. This parameter allows to control the interfacial properties of PVA Gibbs monolayers. Bhattacharya et al. proved that PVA adsorbs at liquid/air interface, slightly changing the surface tension of water solutions [22] while Liu et al. studied PVA water/oil interfacial rheology by means of pendant drop technique [21].

When PVA is dissolved together with sodium tetraborate ($Na_2B_4O_7$, commonly known as Borax) can form gels, by diol complexation using borate ions (see **Figure 9. 3**) [18,23].

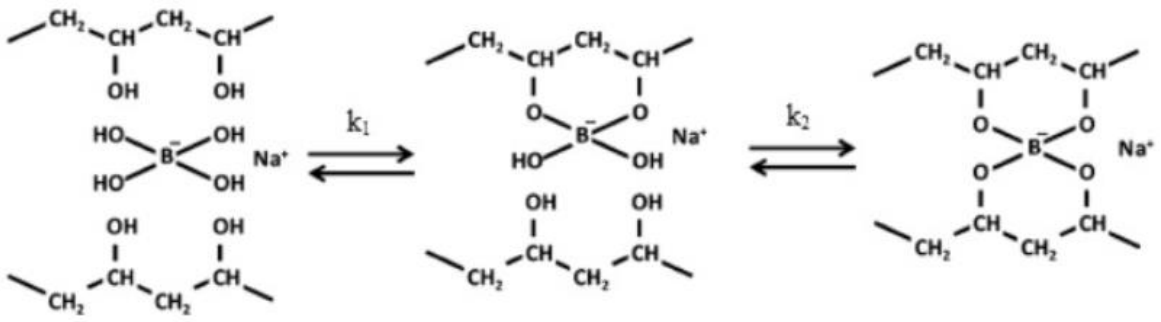

Figure 9. 3. Dissociation of sodium tetraborate decahydrate (Borax) in water and physical crosslinking process and equilibrium of complexation between PVA chains and borate ions. Adapted from [23])

The rheological properties of PVA/Borax solutions make them suitable for this study. In fact, the presence of Borax, increases the elastic component ($G'(\omega)$), without increasing too much the viscosity, in such a way that, at a certain PVA/Borax ratio, $G'(\omega)$ and $G''(\omega)$ will be comparable one to each other, in the $70 - 600$ Hz frequency range.

9.2. Materials and methods

9.2.1. Materials and solution preparation

Poly Vinyl Alcohol (PVA) $M_w = 146000 - 186000\ Da$, 99+% hydrolyzed, supplied by Sigma Aldrich (Saint Louis, MO, USA) was used to prepare polymeric solutions, at 3 different concentrations (5, 9 and 10 g/l). Borax Anhydrous (sodium tetraborate, $Na_2B_4O_7$, $M_w = 201.22\ Da$) BioUltra (99%), supplied by Sigma Aldrich (Germany), was mixed with PVA, to obtain PVA solutions with 0.2 M final Borax concentration.

Ultrapure deionized water of Milli-Q grade, with a resistivity higher than 18 MΩ·cm and a total organic content (TOC) of less than 6 ppm, was used for preparing the solutions and for material cleaning purposes. To achieve this level of purity, an AquaMAX™-Ultra 370 Series multi-cartridge purification system (Young Lin Instrument Co., Ltd., Gyeonggi-do, Republic of Korea) was used.

PVA/Borax solutions were prepared by weighing the correspondent quantities by means of an analytical balance (0.01 mg accuracy), in 1 L of Milli-Q grade water. Then, the mixture is maintained in sealed bottle, where the solution was kept stirring for 12 hours, at 700 rpm, at constant temperature (80-90 °C, in a thermostatic bath).

9.2.2. Experimental methods

The vapor/liquid interfacial tension was measured by means of a surface force tensiometer (model K10T Digital Tensiometer, KRÜSS GmbH, Hamburg, Germany), fitted with a platinum Wilhelmy plate contact probe of 40.5 mm of perimeter. Each experimental data point was obtained as an average of at least 3 measurements, which were carried out until adsorption equilibrium was reached, i.e., a constant surface tension in time, during at least 10 minutes. Temperature was kept constant at 23.0ºC (with an accuracy of ±0.1 °C), by means of a thermostatic bath.

Dilational interfacial rheology measurements at high frequency (in the range of 70-600 Hz) were performed by using a homemade electrocapillary wave (ECW) device, described elsewhere [24-29] (see *Chapter II*, *2.1.4. Electro-Capillary Waves (ECW)*, for detailed description). Experiments were done at 23 °C (the temperature of the Langmuir Trough was maintained constant by means of a thermostatic bath). The accessible range of frequencies depend on the viscosity of the samples, the most viscous samples allowed measurements only until 400 Hz due to large damping coefficients of capillary waves that did not allow to scan the profile of the wave with enough resolution, while less viscous samples allowed to perform measurements until 600 Hz. Any measurement was carried out 4 hours after being poured in the Langmuir trough, during this time, surface tension was monitored, in order to make sure that the system reached adsorption equilibrium.

Bulk shear viscosity measurements were carried out by means of diffuse wave spectroscopy (DWS, see *Chapter II*, 2.2.3. Diffusing Wave Spectroscopy (DWS), for detailed description)

technique (DWS-ResearchLab from LS instruments, Switzerland). Latex sulfate Poly-Styrene (PS) colloidal dispersion (8% w/v, 0.74 µm, supplied by Invitrogen, Thermo Fisher Scientific, USA) were used as tracker particles. The average diameter of the tracker particles was previously measured by means of Dynamic Light Scattering technique (Zetasizer Nano ZS instrument from Malvern Instrument, Ltd., Malvern UK), and it was estimated to be around 0.84 µm, comparable to the one indicated by the supplier. Every sample was mixed with tracker particles colloidal dispersion according to the following ratio: 0.0757 g of latex PS colloidal dispersion every 1 g of sample solution (7.57%w/w). The sample is poured in a quartz cuvette (5 mm path length L), and experiments are carried out at 23°C (temperature is kept constant by means of a Peltier system). Calibration was carried out in Milli-Q grade water, in order to determine the mean free path (l^*) of tracker particles, in such a way that $L > 10l^*$.

9.3. Results and discussion

9.3.1. Bulk Shear Rheology

The frequency dependences, ν, of G' and G'' as were obtained by DWS measurements for PVA and PVA/borax solutions are shown in **Figure 9. 4**:

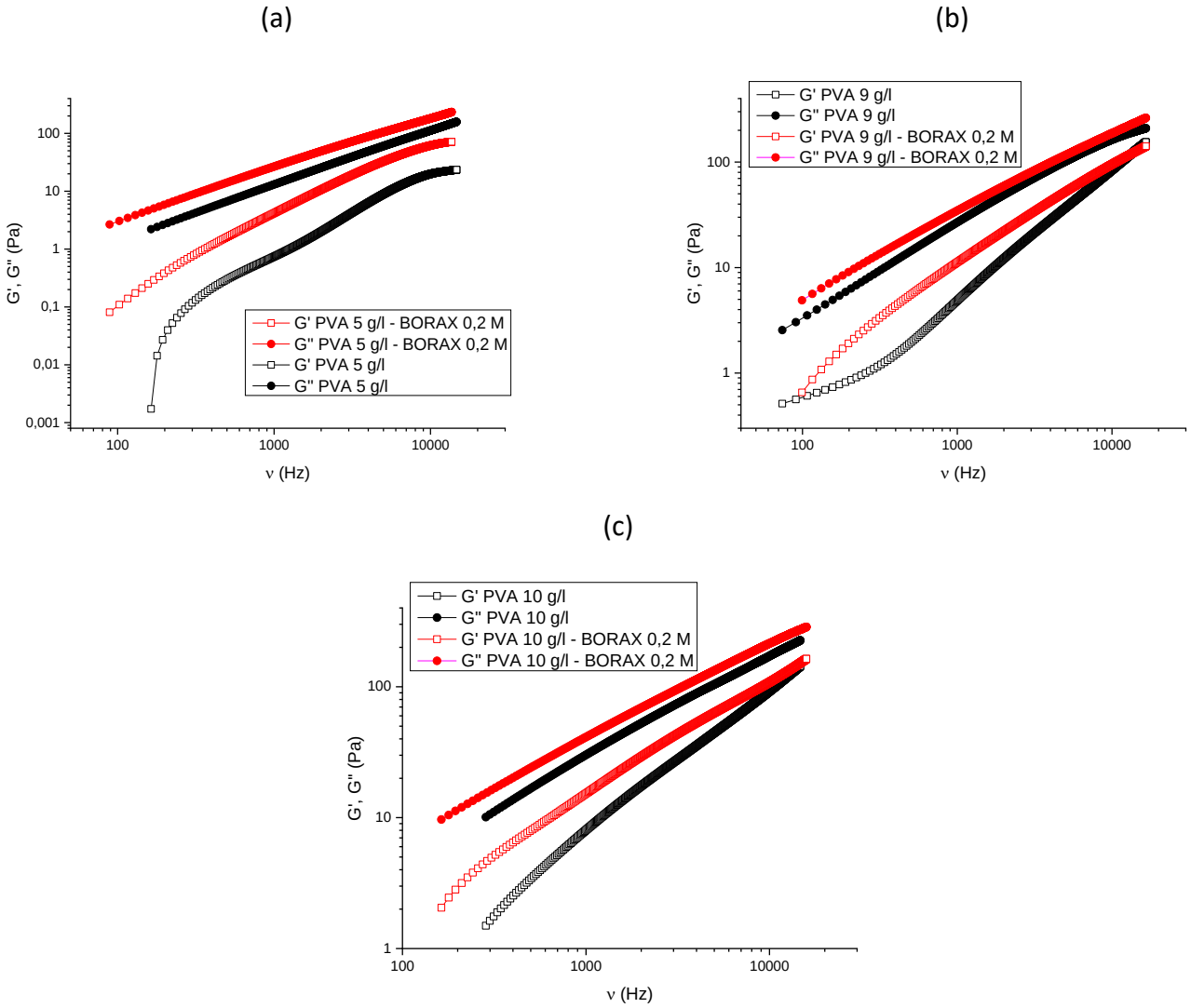

Figure 9. 4. Storage shear modulus G' and loss shear modulus G'', versus frequency ν, of PVA and PVA/Borax(0.2 mol/l) solutions, at 3 different PVA concentrations: $C_{PVA} = 5g/l$ (a), $C_{PVA} = 9g/l$ (b) and $C_{PVA} = 10g/l$ (c).

As expected, G', as well as G'', increase with PVA concentration, and the presence of Borax (0.2 mol/l) provokes a further increase of both shear moduli (at every PVA concentration). Actually, in those solutions containing Borax, polymer content is not enough to reach the gel point, but the difference between $G'$and G'' is slightly reduced, with both moduli showing similar values. However, at $C_{PVA} = 5g/l$, independently on the presence of Borax, the storage modulus G' is always 1 order of magnitude below G'' (at least, within 100-600 Hz frequency range), which means that, in the considered frequency range, elasticity contribution is almost negligible, G'' linearly increases with ν (in log-log scale), the viscosity is almost frequency independent, and the fluid can be considered as a purely viscous system. The same occurs, in absence of Borax, for PVA solutions with concentration in the range $9 - 10$ g/l. On the other hand, when Borax (0.2 M) is added, the coexistence of viscous and elastic response can be appreciated in a frequency range compatible with ECW experiments. In this case, G' and G'' present values in the same order of magnitude.

In order to estimate data between 70 Hz and 100 Hz, since DWS did not allow to obtain data below 100 Hz, an extrapolation was carried out, by fitting G' and G'' experimental data with equation (9. 21) and (9. 22) [18] and determining the values of G' and G'' at the desired value of ν,

$$\log[G'(\omega)] = b' + a' \log(\omega), \tag{9. 21}$$

and

$$log[G''(\omega)] = b'' + a'' lo\, g(\omega). \tag{9. 22}$$

The values of a' range between 0.80 and 1.40, while the values of a'' are between 0.70 and 1. These values are slightly different with respect to the ones reported in ref. [18], which are $a' \approx 2$ and $a'' \approx 1$, corresponding to the values predicted by Maxwell model (see *Chapter I*, *1.3. Bulk Shear Rheology*) in the limit of $\nu \to 0$. This discrepancy may be due to the fact that the fitting of the data plotted in **Figure 9. 4** is not in the same frequency range as ref. [18] (where the data are collected at $\nu < 100\ Hz$), and therefore the frequency range considered in this chapter is not close enough to the limit value of 0 Hz.

The complex viscosity $\eta^*(\omega)$ can be easily calculated by means of the following formula,

$$\eta^*(\omega) = \frac{G^*(\omega)}{i\omega} = \eta'(\omega) - i\eta''(\omega). \tag{9. 23}$$

$\eta'(\omega)$ and $\eta''(\omega)$ were determined, by interpolation and extrapolation, using equations (9. 21)-(9. 23), in ECW range of frequency (70-600 Hz). The results are plotted in **Figure 9. 5**.

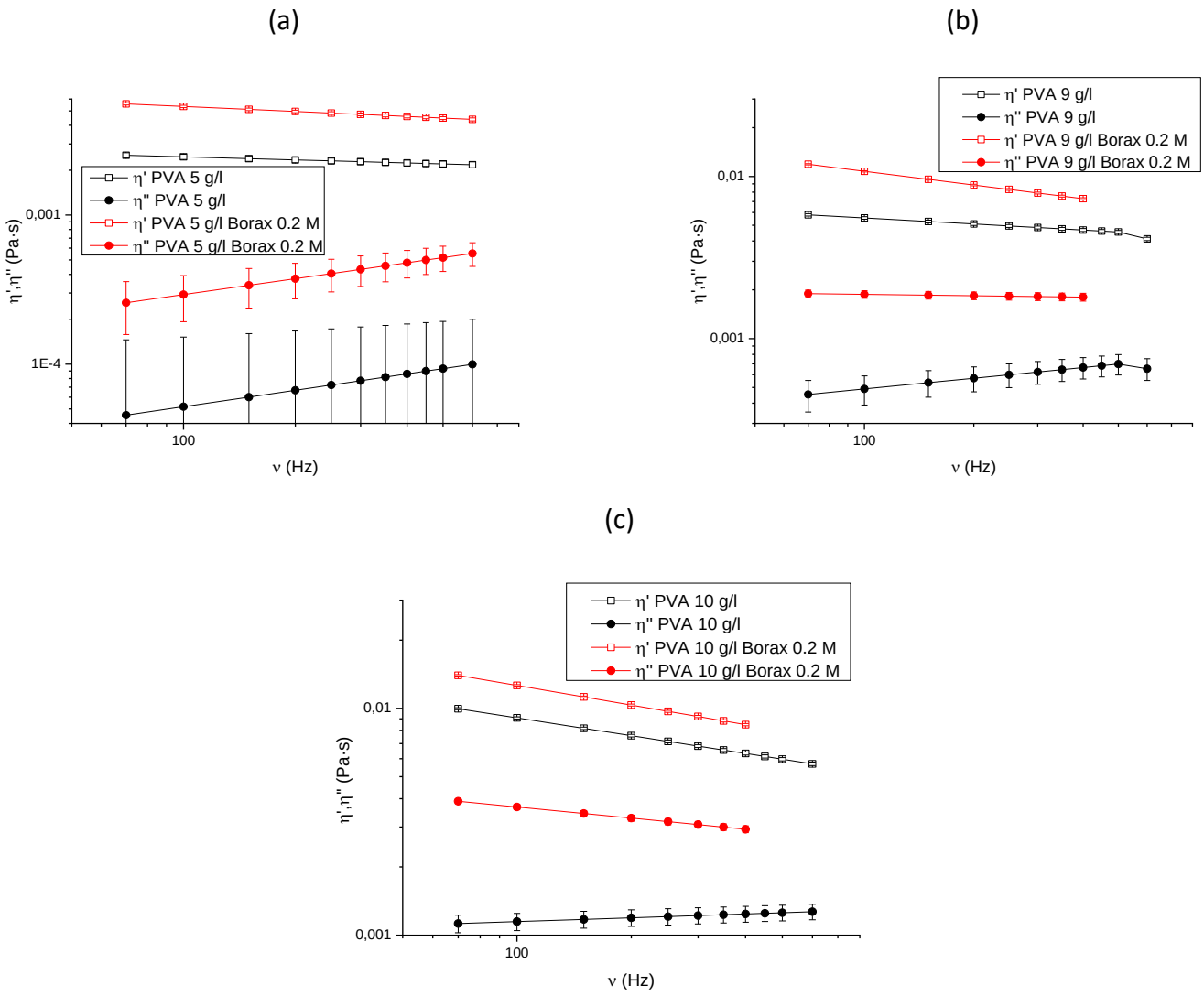

Figure 9. 5. Real part $\eta'(\omega)$and imaginary part $\eta''(\omega)$ of complex viscosity, versus frequency ν, of PVA and PVA/Borax(0.2 mol/l) solutions, at 3 different PVA concentrations: $C_{PVA} = 5g/l$ (a), $C_{PVA} = 9g/l$ (b) and $C_{PVA} = 10g/l$ (c).

It is worth to notice that the real part of the complex viscosity ($\eta'(\omega)$) is always below the critical threshold of $2 \cdot 10^{-2}\ Pa \cdot s$, which means that measurements with ECW technique can be done with enough resolution in the aforementioned frequency range. The effect of bulk elasticity is almost negligible in 5 g/l PVA samples, while in 9 g/l and 10 g/l PVA samples (with Borax), the value of $\eta''(\omega)$ is comparable to $\eta'(\omega)$. In fact, the presence of borax, reduces the gap between the imaginary and the real part of complex viscosity. These samples are the ones where bulk viscoelasticity was observed, and η' decreases with frequency (while, in the other samples, except for the one with 10 g/l PVA without Borax, η' is almost constant with frequency).

9.3.2. Interfacial tension

Once the viscoelasticity of the bulk solutions was evaluated, the second step is to evaluate the ability of the PVA to adsorb at the air/water interface in absence and presence of borax was evaluated by interfacial tension measurement. The surface tension of PVA solution, in absence and presence of Borax, as a function of C_{PVA} is plotted in **Figure 9. 6**:

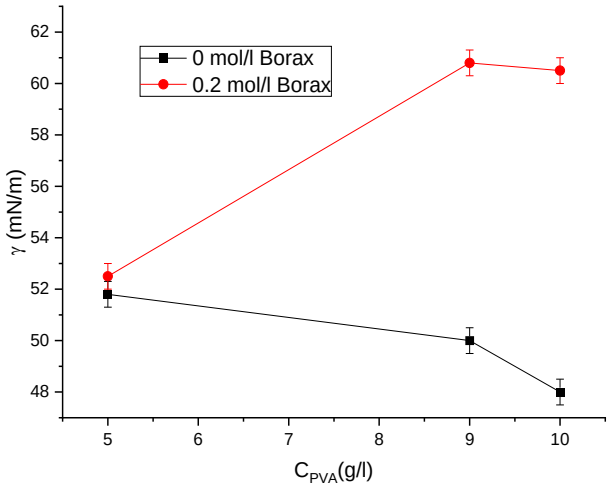

Figure 9. 6. Surface tension γ of PVA solutions in absence and presence Borax as a function of PVA concentration (C_{PVA}).

PVA chains, being amphiphilic, tend to adsorb at liquid/vapor interface, decreasing the surface tension of pure water. This aligns with the results reported by Bhattacharya et al. [22]. The molecular weight of PVA also affects its capability of decreasing γ. In this chapter, the molecular weight of the PVA used was higher than the one studied in [22]. This is compatible with the higher decrease in the surface tension observed in this study.

The surface tension of PVA solutions with 5 g/l of polymer content does not seem to be hugely affected by Borax content, due to the fact that the polymer concentration is not high enough to give raise to chemical crosslink. Therefore, the Borax concentration is not enough at low polymer concentration to produce a considerable change of polymer chains arrangement, neither in the bulk nor at the interface. Conversely, when $C_{PVA} = 9 - 10\ g/l$, the tendency is reversed. In presence of Borax (0.2 mol/l), an increase in PVA concentration produces in turn an increase of γ. This is similar to the behavior observed by Ichinose et al. [30] in other gelling system (agarose-water solutions). This behavior can be explained considering that the cross-linking occurring as a result of the sol-gel transition hinders the mobility of the polymer chains, limiting their adsorption to the fluid interface, which results in an increase in surface tension. This increase can take the surface tension values up to values higher than the ones of pure water. This occurs in PVA/Borax solutions where γ increases as a result of the onset in the gelation region, and hence the increase of surface tension is associated to a sol-gel transition. This behavior is consistent with the bulk shear rheology results reported in the previous subsection. In fact, at $C_{PVA} = 9 - 10\ g/l$, Borax changes the viscosity and the elasticity of the bulk, while at $C_{PVA} = 5\ g/l$ it has little impact.

Another phenomenon that contributes to the surface tension growth is the presence of residual Borax that did not form diol bonds with PVA and remains dissolved into the solution: as reported by Granneman et al. [31]. Borax, if dissolved in water as occurs with other salts, tends to slightly increase the surface tension of aqueous solutions.

Another aspect to take into account is that the measurement of the surface tension of a viscoelastic polymeric solution, by means of a surface force tensiometer fitted with a Wilhelmy plate, may be quite challenging. In fact, the plate, exerting a force on liquid surface, produces a deformation, but, since the viscosity of the liquid varies with frequency (hence, with time), the mechanical response detected by the tensiometer may be time-dependent, which may generate artefacts in the measurement of the surface tension: this can be partially solved by keeping the plate immersed in the solution for enough time (1.5 hours), waiting until surface tension stabilizes. Furthermore, the elastic behavior of the solution, may affect its deformability, provoking distortion of liquid meniscus. Other methods, that are not based on the use of external forces, can be used, like capillary rise method, based on the trade-off between gravity and capillarity in a capillary tube [32].

9.3.3. Damping and capillary wavelength

For a capillary wave excited in a point of the interface (xy plane) defined by the coordinate x=0, it is possible to define its spatial profile in terms of a damped cosine according to the following expression (see *Chapter II*, *2.1.4. Electro-Capillary Waves (ECW)*),

$$u_z = u_z^0 e^{-\beta x} cos\left(\frac{2\pi}{\lambda}x + \varphi\right), \tag{9. 24}$$

with u_z^0 being the wave amplitude, and β, λ and φ the damping coefficient, the characteristic capillary wavelength and the phase lag, respectively. **Figure 9. 7** shows the frequency dependence of β and λ, of PVA solutions in absence and presence of Borax.

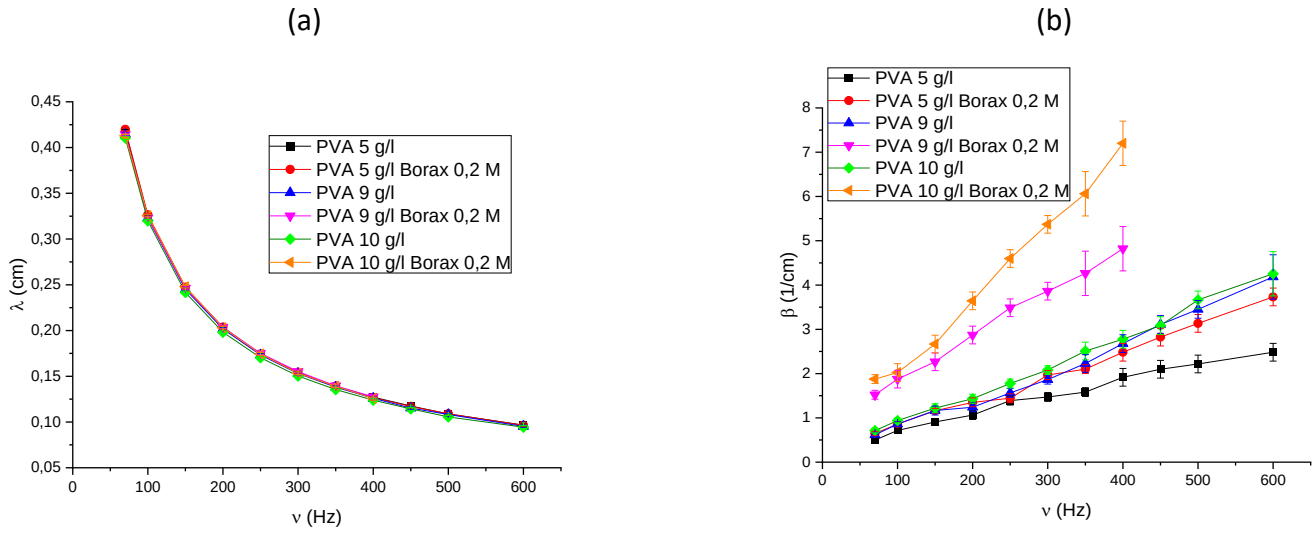

Figure 9. 7. λ (a) and β (b), versus frequency (ν), of PVA and PVA/Borax (0.2 M) solutions, at different PVA content (5 g/l, 9 g/l and 10 g/l).

The result shows that the values of λ are rather independent on the PVA concentration and the presence of Borax. This behavior can be explained by recalling Kelvin's law [33] (see *Chapter II*, *2.1.4. Electro-Capillary Waves (ECW)*) which is defined as,

$$\lambda = \left(\frac{2\pi\gamma}{\rho}\right)^{\frac{1}{3}} \nu^{-2/3}. \tag{9. 25}$$

Kelvin's law is strictly valid in low viscosity pure liquids, but it can be used in this system as a first approximation to qualitatively explain the trend of λ with γ and ρ. According to Kelvin's law, λ increases with surface tension and decreases with density. Depending on both PVA and Borax concentration, γ ranges between $48 - 61\ mN/m$, while $\rho \approx 1 - 1.05\ kg/l$. Samples with $C_{PVA} = 9 - 10\ g/l$ (and with $0.2\ mol/l$ of Borax) are the ones characterized by the highest value of γ, but are simultaneously those with the highest value of the density. In fact, the presence of Borax increases the density of the solution. Thus, in this situation the effect associated with the increase in γ competes with the increase in ρ, and therefore the value of λ almost remains unchanged. In fact, the experimental resolution of ECW set-up does not allow to separate the values of λ of each solution.

Kelvin's law can be expressed as a power law,

$$\lambda = A\nu^{-a}. \tag{9. 26}$$

All of the samples qualitatively follow the trend predicted equation (9. 26), and a ranges between 0.67 and 0.68, which agrees with the prediction of Kelvin's law (exponent of $2/3$ in equation (9. 25)). On the other hand, when the damping coefficient β is analyzed, the values plotted in **Figure 9. 7** (b) seem to qualitatively align with the prediction given by a derivation of the Stokes law [33] (see *Chapter II*, *2.1.4. Electro-Capillary Waves (ECW)*), which is also valid for low viscosity pure liquids,

$$\beta = \frac{8\eta\pi\nu}{3\gamma}. \tag{9. 27}$$

In fact, in every sample, β monotonically increases with frequency, and the most viscous samples, especially those with $C_{PVA} = 9 - 10\ g/l$ and $0.2\ mol/l$ Borax, at fixed ν, are characterized by the highest values of β. This trend is more evident at the highest frequencies probed. On the other hand, samples having similar viscosity, like the ones with $C_{PVA} = 9\ g/l$ and $C_{PVA} = 10\ g/l$ (without Borax), also have similar damping behavior. It should be pointed out that β also depends on γ, but the variation of surface tension between each sample is not enough to produce considerable variation of the damping coefficient, with its value being mainly dependent on the bulk viscosity of the samples. As occurred with Kelvin's law, also Stokes law can be expressed as a power law,

$$\beta = B\nu^{b}. \tag{9. 28}$$

By fitting the data plotted in **Figure 9. 7** (b) with eq. (9. 28), the values of b range between $0.65 - 0.86$ (depending on the sample), lower than 1 (the value given by eq. (9. 27)). The reason why none of the samples obeys to derived Stokes law is given by the fact that there might be viscous dissipation at the interface, but it is also due to the fact that bulk shear viscosity, in some samples, also strongly depends on frequency, so the dependence of β on ν may not be straightforward.

9.3.4. Dilational interfacial rheology

Based on the bulk rheology, the surface tension and the capillary wavelength/damping data discussed in the previous subsections, the dilational interfacial modulus ($E_s{}^*(\omega) = E_s(\omega) + iE_i(\omega)$) of PVA solutions in absence and presence of Borax was computed by means of two different hydrodynamic models:

- The model proposed by Lucassen, in which the dilational properties of the interface are determined by solving equation (9. 19) (Lucassen dispersion equation [2,3]). In this approach, only the real part of the complex viscosity ($\eta'(\omega)$) and its dependence on frequency are considered,

$$E_s{}^*(\omega) = \frac{\dfrac{-\left(\eta'(\omega)\omega(q-m)\right)^2}{\gamma q^2 + i\eta'(\omega)\omega(q+m) - \dfrac{\rho}{q}\omega^2} - i\eta'(\omega)\omega(q+m)}{q^2}, \tag{9. 29}$$

where the capillary penetration depth m is defined as $m = \left(q^2 + \frac{i\omega\rho}{\eta'(\omega)}\right)^{0.5}$.

- The second approach is to use the model proposed by Wang defined by equation (9. 18) (Wang-Huang dispersion equation [4]). This equation is structurally similar to equation (9. 19), with the only difference that the complex viscosity $\eta^*(\omega) = \eta'(\omega) - i\eta''(\omega)$ replaces $\eta'(\omega)$, taking into account also the effects of bulk shear elasticity,

$$E_s{}^*(\omega) = \frac{\dfrac{-\left(\eta^*(\omega)\omega(q-m)\right)^2}{\gamma q^2 + i\eta^*(\omega)\omega(q+m) - \dfrac{\rho}{q}\omega^2} - i\eta^*(\omega)\omega(q+m)}{q^2}, \tag{9. 30}$$

where the capillary penetration depth m is here defined as $m = \left(q^2 + \frac{i\omega\rho}{\eta^*(\omega)}\right)^{0.5}$.

The interfacial dilational modulus determined by Lucassen and Wang model are compared, one to each other, in **Figure 9. 8** (E_s) and **Figure 9. 9** (E_i):

(a) (b)

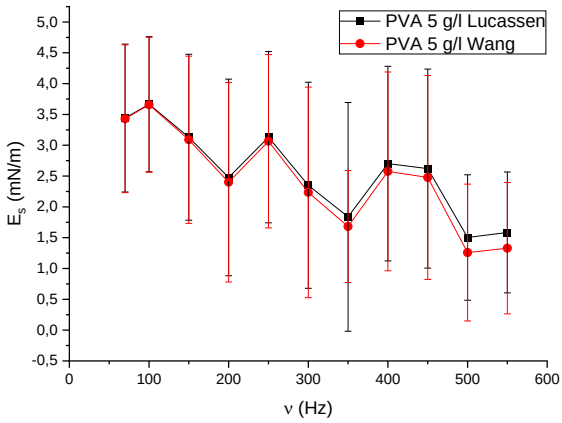

(c)

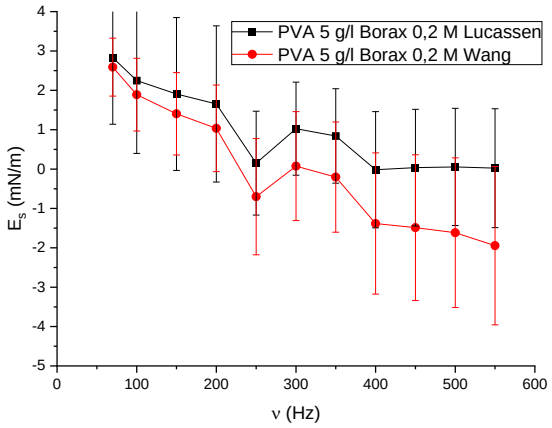

(d)

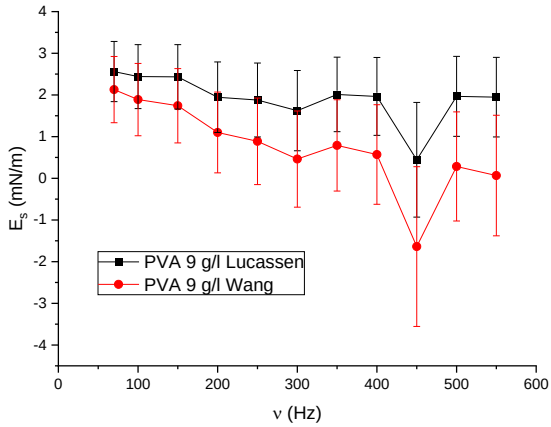

(e)

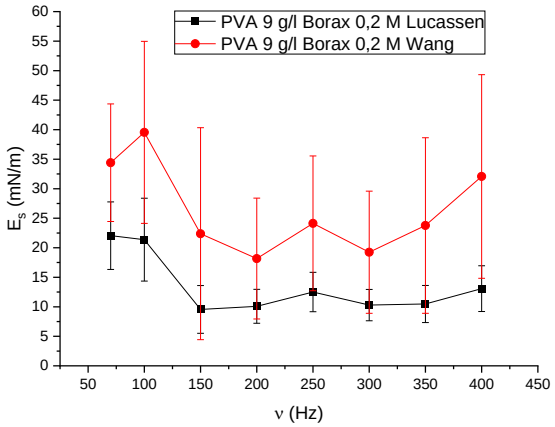

(f)

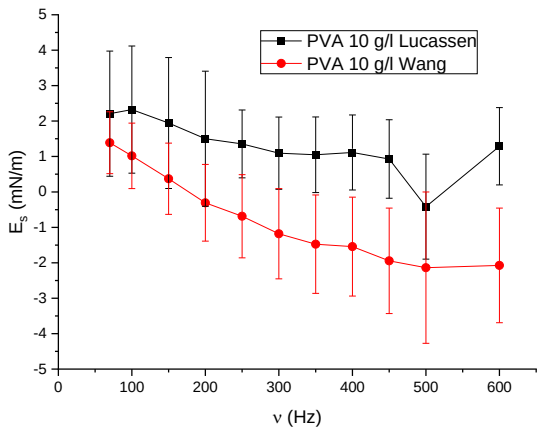

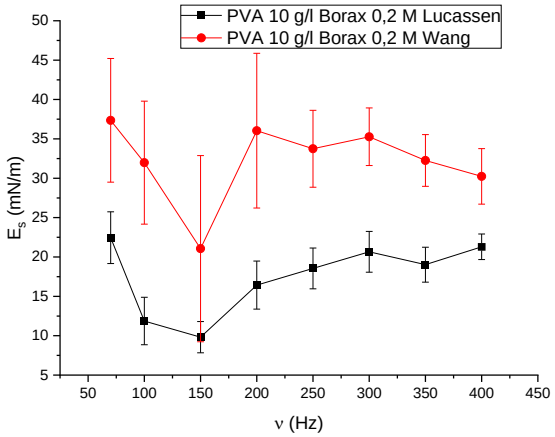

Figure 9. 8. Storage interfacial dilational modulus E_s versus frequency ν, determined both by Lucassen and Wang dispersion equation, of PVA/Borax solutions: (a) $C_{PVA} = 5g/l$, (b) $C_{PVA} = 5g/l$ and 0.2 mol/l Borax, (c) $C_{PVA} = 9g/l$, (d), $C_{PVA} = 9g/l$ and 0.2 mol/l Borax, (e) $C_{PVA} = 10g/l$, (f) $C_{PVA} = 10g/l$ and 0.2 mol/l Borax.

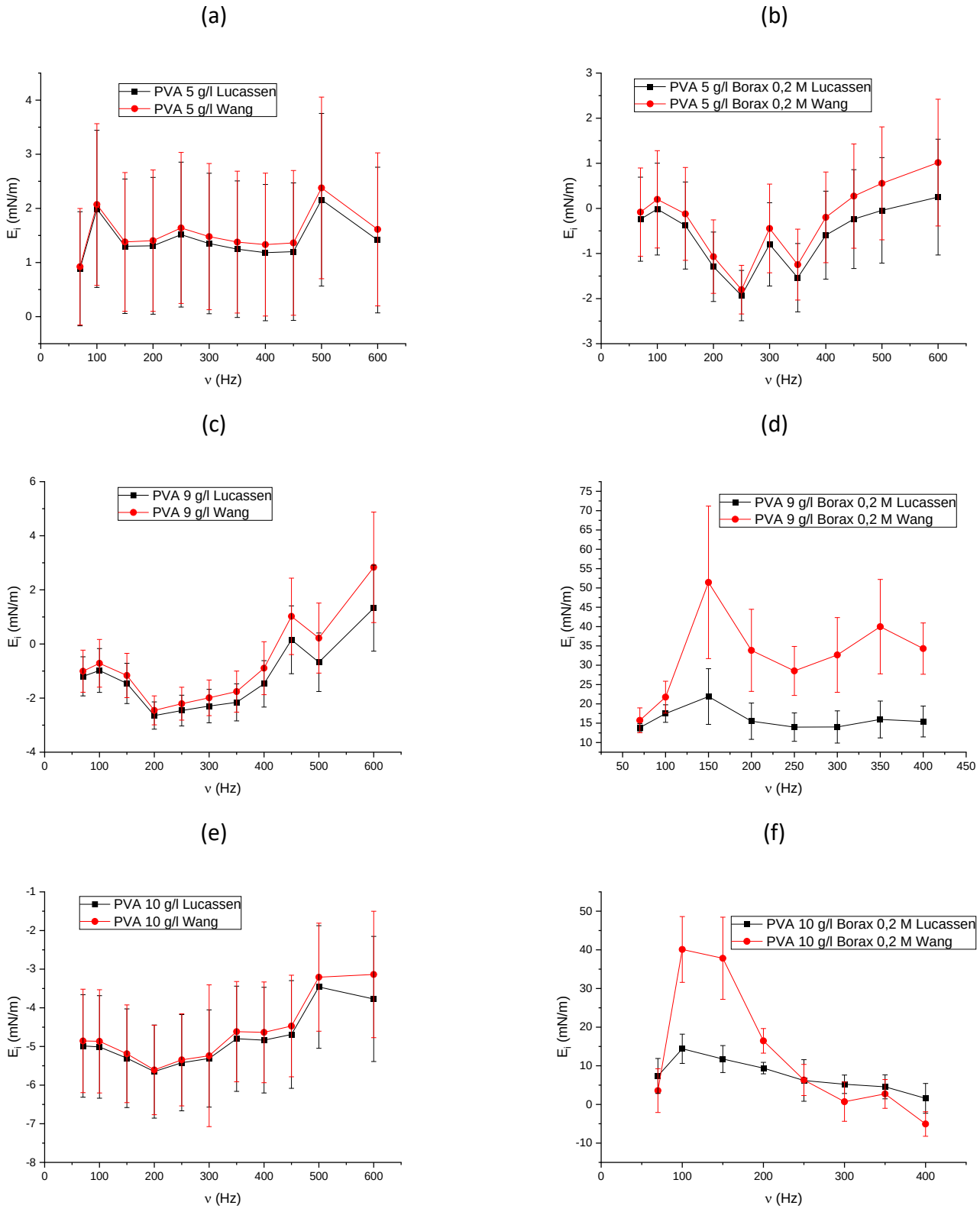

Figure 9. 9. Loss interfacial dilational modulus (E_i) versus frequency ν, determined both by Lucassen and Wang dispersion equation, of PVA/Borax solutions: (a) $C_{PVA} = 5g/l$, (b) $C_{PVA} = 5g/l$ and 0.2 mol/l Borax, (c) $C_{PVA} = 9g/l$, (d), $C_{PVA} = 9g/l$ and 0.2 mol/l Borax, (e) $C_{PVA} = 10g/l$, (f) $C_{PVA} = 10g/l$ and 0.2 mol/l Borax.

Concerning the storage modulus E_s, the first outcome is that in every sample characterized by low bulk elasticity (low $\eta''(\omega)$), also exhibits low values of E_s. In fact, as shown in **Figure 9. 8** (a), (c) and (e) (PVA solutions without Borax), surface dilational contribution is almost

negligible. The only sample containing Borax that also presents zero E_s is the one in **Figure 9. 8** (b) ($C_{PVA} = 5\ g/l$ and $0.2\ mol/l$ Borax). In the aforementioned samples, polymer chains do not arrange at the interface to form ordered structures, so interfacial elasticity does not play a key role in interface stabilization. The behavior is similar in relation to the loss dilational interfacial modulus. As observed in **Figure 9. 9** (a), (b), (c), (e), in the same samples with negligible surface elasticity, E_i is negligible as well. This can be explained considering that polymer chains adsorbed at liquid/vapor interface do not overlap one to each other, so no surface viscosity effect is observed. Furthermore, as expected, no difference is perceived between Wang and Lucassen model, due to the negligible bulk elasticity contribution. In fact, when $\eta''(\omega) \ll \eta'(\omega)$, the two dispersion equations are equivalent one to each other.

On the other hand, in those samples in which coexistence of bulk viscosity and elasticity was observed within ECW frequency range ($C_{PVA} = 9 - 10\ g/l$ and $0.2\ mol/l$ Borax, **Figure 9. 8** (d) and (f)), E_s is much higher, with values ranging between $30 - 40\ mN/m$ (determined by Wang equation) and $10 - 20\ mN/m$ (determined by Lucassen model). In these samples, since $\eta''(\omega)$ and $\eta'(\omega)$ are comparable, the difference between the two hydrodynamic models is more remarkable, and apparently, Lucassen equation, leads to an underestimation of E_s. The difference between the two models is more evident in $C_{PVA} = 10\ g/l$ and $0.2\ mol/l$ Borax, which is the sample characterized by the highest bulk viscous and elastic contribution. On the other hand, in the sample with Borax and in $C_{PVA} = 9\ g/l$ which is characterized by a limited bulk elastic contribution, the values of E_s determined by the two models tend to overlap within their error bar. The same considerations apply also to E_i. The loss dilational modulus of samples with $C_{PVA} = 9 - 10\ g/l$ and $0.2\ mol/l$ Borax samples stand out, reaching peaks of $40 - 45\ mN/m$ (determined by Wang dispersion equation) and of $15 - 20\ mN/m$ (with Lucassen dispersion equation).

In polymeric solutions with $C_{PVA} = 9 - 10\ g/l$, since Borax induced partial gelation, the effect of sol-gel transition is observed also at the interface. This can be understood considering that PVA-Borax complexes can arrange in ordered structures at the liquid/vapor interface, which turns the interface stiffer. The overlapping of the polymer chains confer a viscous behavior to the interface, with non-zero loss dilational modulus. It goes without saying that the onset of surface elasticity is not controlled by surface adsorption, but rather by the intrinsic stiffness of the interface due to the structures formed by PVA/Borax complexes. It is important to note that no relaxation dynamic can be observed in the analyzed frequency range.

In order to understand the reason why E_s error bars in $C_{PVA} = 9 - 10\ g/l$ and $0.2\ mol/l$ Borax samples are so huge, it is worth to determine their E_s/γ and compare it to the value associated to the resonance condition [33] (see *Chapter II*, *2.1.4. Electro-Capillary Waves (ECW)*),

$$\left(\frac{E_s}{\gamma}\right)_R = \left(\frac{q\eta'^2}{\gamma\rho}\right)^{1/4} \approx 0.25 - 0.30, \tag{9. 31}$$

where the subindex R indicates the resonance condition. $\left(\frac{E_S}{\gamma}\right)_R$ is defined only in purely viscous fluids ($\eta'' = 0$), so in its calculation the influence of bulk elasticity is not taken into account: by including the effect of the imaginary part of the complex viscosity (η''), $\left(\frac{E_S}{\gamma}\right)_R$ ratio would be a complex number, which has no physical meaning. An alternative idea would be to replace η' by the complex viscosity (η^*) in equation (9. 31). Thus, it will be possible to compute the "complex $\left(\frac{E_S}{\gamma}\right)_R^*$ ratio", and only consider its real part. In this case, the results are very similar, because $Re\left[\left(\frac{E_S}{\gamma}\right)_R^*\right] \approx 0.26 - 0.32$. Or, otherwise, instead of η^*, another option may be considering its modulus ($|\eta^*|$), but also in this case the estimation of $\left(\frac{E_S}{\gamma}\right)_R$ would lead to similar results. It is interesting to notice that the estimated values of $\left(\frac{E_S}{\gamma}\right)_R$ in this system ($0.25 - 0.30$) are larger than the ones determined in the previous chapters ($0.10 - 0.15$), due to the higher viscosity of the medium.

In **Figure 9. 10**, the E_s/γ ratio, determined from the experimental data, is compared to $\left(\frac{E_S}{\gamma}\right)_R$ of $C_{PVA} = 9 - 10\ g/l$ and $0.2\ mol/l$ Borax samples (in all of the other samples, E_s/γ ratio is almost zero, due to the extremely low values of E_s). Whenever E_s/γ does not match with the resonance value ($0.25 - 0.30$), then dilational and capillary modes are not coupled, and the value of E_s will be strongly affected by any perturbation to the value of γ, which implies, in turn, that the error bar of E_s will be huge.

(a) (b)

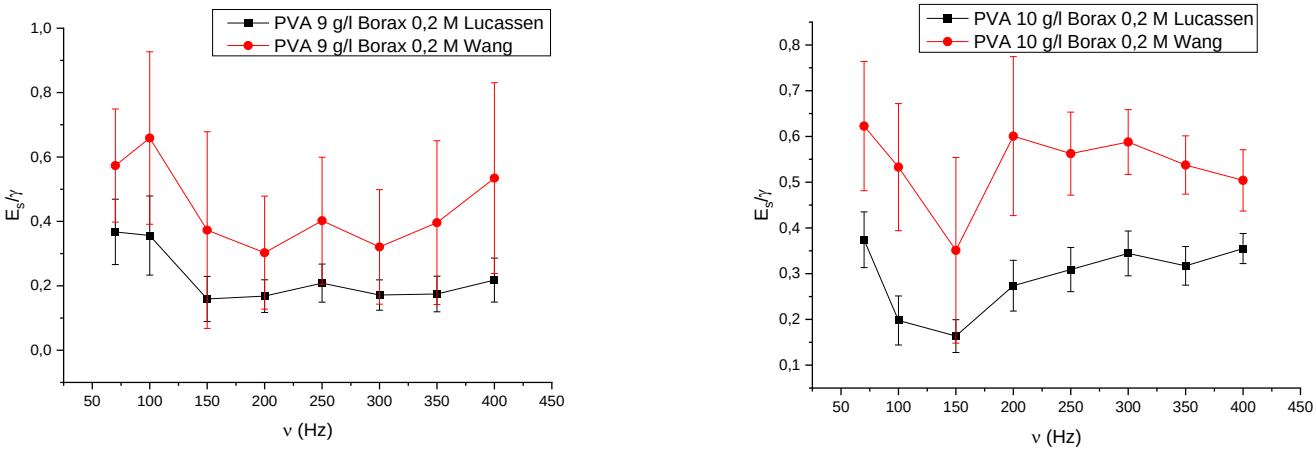

Figure 9. 10. E_s/γ ratio of PVA/Borax solutions: (a) $C_{PVA} = 9g/l$ - 0.2 mol/l Borax, (b) C_{PVA}10 g/l - 0.2 mol/l Borax.

In general, the E_s/γ ratios determined by Lucassen equation are comparable to the one associated to resonance condition, which aligns with the smaller error bars of E_s observed in **Figure 9. 8** (d) and (f). On the other hand, E_s/γ ratios calculated with E_s data determined by means of Wang dispersion equation, are larger than $\left(\frac{E_S}{\gamma}\right)_R$, which is coherent with the fact that E_s error bars are higher than those calculated using the Lucassen model. Apparently, there is

no physical reason why experimental E_s/γ ratios are higher in Wang model case. The reason is purely numerical, the same perturbation in the value of γ, leads to larger E_s variation in case of Wang dispersion equation.

9.4. Conclusions

The study of dilational interfacial rheology of viscoelastic fluids deserves particular attention, due to the necessity of experimental validation of the hydrodynamic models providing information on the surface modes that are already present in literature. In this chapter, the dilational interfacial response in Electro-Capillary Waves frequency range (70-600 Hz) of PVA/Borax solutions was studied, underlining the difference between the values calculated by means of Lucassen and Wang dispersion equation. Thus, it has been possible to understand the impact of bulk shear elasticity contribution on the damping of capillary waves.

First of all, bulk shear rheology of PVA/Borax solution was characterized by DWS. The only samples that exhibit a non-negligible shear elasticity were the ones with $C_{PVA} = 9 - 10\ g/l$ and $0.2\ mol/l$ Borax: in such systems, $G'(\omega)$ was of the same order of magnitude of $G''(\omega)$, and $\eta'(\omega)$ was comparable to $\eta''(\omega)$. Furthermore, the values of $\eta'(\omega)$ were below the critical operative threshold of ECW technique ($< 2 \cdot 10^{-3} Pa \cdot s$).

The surface tension of PVA decreases with polymer concentration, but, in presence of Borax ($0.2\ mol/l$) the trend is inverted: in fact, in $C_{PVA} = 9 - 10\ g/l$ solutions, the presence of Borax induces an abrupt surface tension growth, which might be associated to the onset of a sol-gel transition (although, in these conditions, gelation did not completely occur).

The capillary wavelength measured by ECW technique remains unchanged between all of the samples: surface tension variation is always compensated by density change, and the resolution of the set-up does not allow to distinguish between the values of λ measured in every condition. The damping coefficient varies coherently with the viscosity of each samples: solutions with the highest bulk viscosity, also exhibits the highest values of β. Due to the presence of either bulk or surface viscoelasticity, the trend of β versus ν does not follow the one predicted by Stokes law.

A correlation between bulk viscoelasticity and surface viscoelasticity was observed. In fact, in the same samples with $C_{PVA} = 9 - 10\ g/l$ and $0.2\ mol/l$ Borax, in which the coexistence of shear viscosity and elasticity was observed in the bulk, viscoelastic behavior also appears on the surface: these are the only samples where considerably high values of both E_s and E_i were detected, while in the other samples the dilational interfacial contribution is almost nil. A plausible hypothesis might be that partial gelation occurs both in the bulk and on the surface, in such a way that at polymer chains form highly ordered arrangements and, thus, a stiffer interface. The dilational interfacial modulus (both its real and imaginary part) computed by means of Wang equation always results higher (almost the double) than the one calculated by means of Lucassen equation: this happens only in partially gelled samples ($C_{PVA} = 9 - 10\ g/l$ and $0.2\ mol/l$ Borax), while in the other samples no difference between Wang and Lucassen model can be perceived.

An estimation of the resonance value of $\left(\frac{E_s}{\gamma}\right)_R$ was proposed, only considering the real part of complex viscosity (η'): the values are a bit higher than the ones observed for aqueous solutions

previously studied: $\left(\frac{E_s}{\gamma}\right)_R$ ranges between $0.25 - 0.30$. The error bars associated to the values of E_s calculated by means of Wang equation result to be huger than the ones determined by Lucassen model, due to the fact that E_s/γ ratios are higher and deviate from the resonance value.

The issue of surface modes on viscoelastic liquids deserves further experimental work. For instance, the study of surface dilational response of viscoelastic PVA/Borax solutions may be extended up to higher frequencies, by means, for example, of Surface Quasi-Elastic Light Scattering (SQELS), that allows to determine dilational interfacial rheology up to 10^5-10^6 Hz (where the bulk elasticity contribution is even higher). The study may be extended to other systems, like micellar dispersions or other polymers, such as micellar solutions that tend to form rod-like structures (like alkyl quaternary ammonium salts with organic counterions or high salt concentration), higher molecular weight water soluble biopolymers (like proteins or Polysaccharides), in order to provide more experimental validation to Wang model.

9.5. References

1. Norton, A.B.; Hancocks, R.D.; Grover, L.M. Poly (vinyl alcohol) modification of low acyl gellan hydrogels for applications in tissue regeneration. *Food Hydrocolloids* **2014**, *42*, 373-377, doi:10.1016/j.foodhyd.2014.05.001.
2. Lucassen-Reynders, E.H.; Lucassen, J. Properties of capillary waves. *Advances in Colloid and Interface Science* **1970**, *2*, 347-395, doi:10.1016/0001-8686(70)80001-x.
3. Lucassen, J. Longitudinal capillary waves. Part 1.—Theory. *Trans. Faraday Soc.* **1968**, *64*, 2221-2229, doi:10.1039/tf9686402221.
4. Wang, C.H.; Huang, Q.R. Hydrodynamic surface waves in concentrated polymer solutions in the presence of surface adsorption. *J. Chem. Phys.* **1997**, *107*, 5898–5906 doi:doi.org/10.1063/1.474315.
5. Krindel, P.; Silberberg, A. Flow through gel-walled tubes. *Journal of Colloid and Interface Science* **1979**, *71*, 39-50, doi:10.1016/0021-9797(79)90219-4.
6. Harden, J.L.; Pleiner, H.; Pincus, P.A. Hydrodynamic surface modes on concentrated polymer solutions and gels. *The Journal of Chemical Physics* **1991**, *94*, 5208-5221, doi:10.1063/1.460525.
7. Silberberg, A. Physicochemical hydrodynamics in turbulent flows close to the interface. *Physicochemical Hydrodynamics* **1987** *9*, 419-426.
8. Pleiner, H.; Harden, J.L.; Pincus, P. Surface Modes on a Viscoelastic Medium. *Europhysics Letters (EPL)* **1988**, *7*, 383-387, doi:10.1209/0295-5075/7/5/001.
9. Cao, B.H.; Kim, M.W.; Cummins, H.Z. Surface waves on polymer solutions: Complete capillary wave–elastic wave crossover. *The Journal of Chemical Physics* **1995**, *102*, 9375-9379, doi:10.1063/1.468805.
10. Dorshow, R.B.; Turkevich, L.A. First observation of capillary to Rayleigh mode crossover on the surface of polymer solutions. *Phys Rev Lett* **1993**, *70*, 2439-2442, doi:10.1103/PhysRevLett.70.2439.
11. Dorshow, R.B.; Turkevich, L.A. Comment on: Surface modes on polymer solutions by surface light-scattering techniques. *The Journal of Chemical Physics* **1993**, *98*, 8349-8350, doi:10.1063/1.464543.
12. Huang, Q.R.; Wang, C.H.; Deng, N.J. Clear-cut experimental observation of the capillary wave to elastic wave crossover in concentrated polymer solutions. *The Journal of Chemical Physics* **1998**, *108*, 3827-3834, doi:10.1063/1.475771.

13. Huang, Q.R.; Wang, C.H. Surface laser light scattering studies of the air/poly(N-vinyl-2-pyrrolidone)-water solution interface. *The Journal of Chemical Physics* **1996**, *105*, 6546-6552, doi:10.1063/1.472463.
14. Buzza, D.M.A. General Theory for Capillary Waves and Surface Light Scattering. *Langmuir* **2002**, *18*, 8418-8435, doi:10.1021/la011713d.
15. Landau, L.D.; Lifshitz, E.M. *Fluid Mechanics*; Pergamon Press: Elmsford, New York, USA, 1987; Vol. 6.
16. Teodorescu, M.; Bercea, M.; Morariu, S. Biomaterials of PVA and PVP in medical and pharmaceutical applications: Perspectives and challenges. *Biotechnol Adv* **2019**, *37*, 109-131, doi:10.1016/j.biotechadv.2018.11.008.
17. Conway, M.W.; Almond, S.W.; Briscoe, J.E.; Harris, L.E. Chemical Model for the Rheological Behavior of Crosslinked Fluid Systems. *Journal of Petroleum Technology* **1983**, *35*, 315-320, doi:10.2118/9334-pa.
18. Lin, H.-L.; Liu, Y.-F.; Yu, T.L.; Liu, W.-H.; Rwei, S.-P. Light scattering and viscoelasticity study of poly(vinyl alcohol)–borax aqueous solutions and gels. *Polymer* **2005**, *46*, 5541-5549, doi:10.1016/j.polymer.2005.04.074.
19. Oun, A.A.; Shin, G.H.; Rhim, J.-W.; Kim, J.T. Recent advances in polyvinyl alcohol-based composite films and their applications in food packaging. *Food Packaging and Shelf Life* **2022**, *34*, 100991, doi:10.1016/j.fpsl.2022.100991.
20. Lamminmäki, T.; Kettle, J.; Puukko, P.; Ketoja, J.; Gane, P.A.C. Printing: The role of binder type in determining inkjet print quality. *Nordic Pulp & Paper Research Journal* **2010**, *25*, 380-390, doi:10.3183/npprj-2010-25-03-p380-390.
21. Liu, M.; Zheng, Y.; Liu, Y.; Zhang, Z.; Wang, Y.; Li, J.; Chen, Q.; Li, J.; Huang, Y.; Yin, Q. Effects of poly(vinyl alcohol) and poly(acrylic acid) on interfacial properties and stability of compound droplets. *International Journal of Hydrogen Energy* **2020**, *45*, 2925-2935, doi:10.1016/j.ijhydene.2019.11.129.
22. Bhattacharya, A.; Ray, P. Studies on surface tension of poly(vinyl alcohol): Effect of concentration, temperature, and addition of chaotropic agents. *Journal of Applied Polymer Science* **2004**, *93*, 122-130, doi:10.1002/app.20436.
23. Mahjoub, H.F.; Zammali, M.; Abbes, C.; Othman, T. Microrheological study of PVA/borax physical gels: Effect of chain length and elastic reinforcement by sodium hydroxide addition. *Journal of Molecular Liquids* **2019**, *291*, 111272, doi:10.1016/j.molliq.2019.111272.
24. Liggieri, L.; Santini, E.; Guzmán, E.; Maestro, A.; Ravera, F. Wide-frequency dilational rheology investigation of mixed silica nanoparticle–CTAB interfacial layers. *Soft Matter* **2011**, *7*, 7699, doi:10.1039/c1sm05257h.
25. Maestro, A.; Ortega, F.; Rubio, R.G.; Rubio, M.A.; Kragel, J.; Miller, R. Rheology of poly(methyl methacrylate) Langmuir monolayers: percolation transition to a soft glasslike system. *J Chem Phys* **2011**, *134*, 104704, doi:10.1063/1.3560612.
26. Monroy, F.; Ortega, F.; Rubio, R.G.; Velarde, M.G. Surface rheology, equilibrium and dynamic features at interfaces, with emphasis on efficient tools for probing polymer dynamics at interfaces. *Adv Colloid Interface Sci* **2007**, *134-135*, 175-189, doi:10.1016/j.cis.2007.04.023.
27. Monroy, F.; Ortega, F.; Rubio, R.G. Dilatational rheology of insoluble polymer monolayers: Poly(vinylacetate). *Physical Review E* **1998**, *58*, 7629-7641, doi:10.1103/PhysRevE.58.7629.

28. Guzmán, E.; Maestro, A.; Carbone, C.; Ortega, F.; Rubio, R.G. Dilational Rheology of Fluid/Fluid Interfaces: Foundations and Tools. *Fluids* **2022**, *7*, 335, doi:10.3390/fluids7100335.
29. Mendoza, A.J.; Guzman, E.; Martinez-Pedrero, F.; Ritacco, H.; Rubio, R.G.; Ortega, F.; Starov, V.M.; Miller, R. Particle laden fluid interfaces: dynamics and interfacial rheology. *Adv Colloid Interface Sci* **2014**, *206*, 303-319, doi:10.1016/j.cis.2013.10.010.
30. Ichinose, N.; Ura, H. Concentration dependence of the sol-gel phase behavior of agarose-water system observed by the optical bubble pressure tensiometry. *Sci Rep* **2020**, *10*, 2620, doi:10.1038/s41598-020-58905-8.
31. Granneman, S.J.C.; Shahidzadeh, N.; Lubelli, B.; Van Hees, R.P.J. Effect of borax on the wetting properties and crystallization behavior of sodium sulfate. *CrystEngComm* **2017**, *19*, 1106-1114, doi:10.1039/c6ce02163h.
32. Cao, J.K.; Zhou, D.F.; Zhang, Y.B. Improvements in the surface tension measurement using the capillary rise method and its application to water under external magnetic fields. *Journal of Molecular Liquids* **2023**, *382*, 121988, doi:10.1016/j.molliq.2023.121988.
33. Langevin, D. *Light Scattering by Liquid Surfaces and Complementary Techniques.* ; CRC Press: New York, US, 1992; Vol. 41.

Concluding remarks

This PhD thesis has been focused on the interfacial properties of a wide range of complex fluids, paying special attention to the interfacial dilational rheology of this type of systems. In particular, this PhD Thesis has exploited the interfacial dilational rheology as a powerful tool to probe the behavior of liquid/vapor interface, which has allowed obtaining some indirect information about the stability and microscopic phenomena occurring within the interface in complex fluids. The research presented here does not only provide some advances in the knowledge of how these fluids respond to mechanical perturbations at interfaces, but also critically evaluates the current hydrodynamic models that are employed to interpret dilational interfacial responses. In this PhD Thesis, interfacial dilational rheology experiments were carried out in different ranges of frequency, with different experimental set-ups: at low frequency (10^{-3}-10^{-1} Hz) and at high frequency (10-10^{3} Hz). The latter range of frequency was probed by means of Electro-Capillary Waves (ECW) technique, which focus a key part of the experimental work contained in this PhD Thesis.

In relation to the main aims and scopes of the present PhD Thesis, one of the achieved milestones was the optimization of an ECW set-up optimization. The original device available in the laboratory requires to obtain results with good quality of a long optical pathway, and in the present PhD Thesis, it has been possible to design a more compact devices by modifying the design of the optical pathway. However, the experimental results has demonstrated that to improve the sensitivity of the signal and the quality of raw data, it is worth to further increase the optical pathway for the detection and introduce further strategies to limit the external noise.

Part of the work was dedicated to further investigation of the hydrodynamic models that are used to relate the dilational interfacial response of fluids with the propagation parameters of capillary waves generated on their interfaces, underlining their theoretical limits and achieving a better comprehension of them. A deeper study of the dispersion equation of capillary waves led to understand the optimal experimental conditions where this model better works. Being E_s the dilational interfacial elasticity and γ the surface tension, the optimal E_s/γ ratio was estimated to be around 0.1-0.15 (in most of the liquid/vapor interfaces). This ratio corresponds to the one associated to the resonance condition, where capillary and dilational modes are coupled. If the system fulfills this condition, the dispersion equation fully predicts the behavior of the interface, and the dilational interfacial modulus values will be characterized with a high precision, because they will not be largely affected by experimental uncertainty of raw data (such as capillary waves propagation parameters and surface tension).

The issue of resonance condition is the point of departure to explain the occurrence of non-physically sound results in the determination of the dilational interfacial modulus, as well as the presence of huge error bars. For instance, as discussed in Section 3 (Chapter V-VI), the fact that many authors report negative values of both elastic and loss modulus, is not directly connected to the presence of ionic strength, but it is rather due to the non-accomplishment of the resonance condition, which in some cases may happen in presence of high ionic strength. Or, in other chapters (e.g., Chapter IV) the negative results of dilational interfacial

viscosity and the huge error bars of dilational elasticity are associated to high E_s/γ ratios, directly related to the non-fulfillment of resonance condition.

Another theoretical limitation of many hydrodynamic models of capillary waves was given by the presence of shear viscoelasticity in the bulk, as discussed in Chapter IX. The experimental results pointed out that bulk shear viscoelasticity effects can have a huge impact in dilational interfacial modulus, and this effect must be taken into account into the dispersion equation.

Apart from the experimental and theoretical issues associated with data collection and analysis, ECW technique (accompanied by other set-ups used to characterize interfacial dilational rheology and other bulk/interfacial properties) helped to achieve a better comprehension of the behavior of many complex fluids. For example, in Chapter IV, ECW data were used as an instrument to investigate in detail the spreading and drop impact phenomena of trisiloxane surfactants solutions, leading to the conclusion that sessile drop oscillation is ruled by capillarity and spreading is not ruled by interfacial dilation rheology. Chapter V data led to conclude that the mechanical behavior of interfaces can change in presence of high ionic strength. In Chapter VIII, the dilational interfacial response allowed to obtain information about interfacial microscopic phenomena (such as molecular reorganization, steric hindrance, etc...) and the stability of foams. In Chapter IX, dilational interfacial rheology helped understanding that crosslinking phenomena in the bulk can also occur at the interface, affecting its mechanical properties.

Future perspectives of this study may be extending the frequency range of dilational interfacial rheology characterization of these systems, possibly up to 10^5 (with SQELS technique), in order to assess the validity of the hydrodynamic models at higher frequencies and possibly obtain other kind of information about the behavior of complex fluids. This work may be complemented by shear interfacial rheology experimental works, as well as studying other kind of complex fluids, such as surfactant/polymers solutions, micellar dispersions, other polymer- or surfactant-decorated nanoparticle dispersions, other biopolymers, etc…

It is crucial to underscore that by meticulously identifying the shortcomings and deficiencies within the existing hydrodynamic models, this research paves the way for future advancements in the field. The insights gained from this work provide crucial pathways for the refinement and enhancement of theoretical frameworks, which have the potential to significantly improve the precision and scope of hydrodynamic predictions. It is anticipated that these advancements will enhance the predictive capabilities of hydrodynamic models, thereby facilitating more effective control and manipulation of interfacial phenomena in both industrial processes and biological systems. Consequently, this PhD Thesis not only contributes to our understanding of interfacial rheology but also serves as a catalyst for future breakthroughs in the study and practical application of complex fluids, fostering innovation across multiple domains.

List of publications

This page contains all the publications (submitted or published) that gave rise to some chapters of the thesis:

- Guzmán, E.; Maestro, A.; Carbone, C.; Ortega, F.; Rubio, R.G. Dilational Rheology of Fluid/Fluid Interfaces: Foundations and Tools. Fluids 2022, 7, 335. https://doi.org/10.3390/fluids7100335
- Carbone, C.; Guzmán, E.; Maldonado-Valderrama, J.; Rubio, R.G.; Ortega, F. Ionic Strength Effect in the Equilibrium and Rheological Behavior of an Amphiphilic Triblock Copolymer at the Air/Solution Interface. Colloids Interfaces 2024, 8, 16. https://doi.org/10.3390/colloids8020016
- Carbone, C.; Rubio-Bueno, A.; Ortega, F.; Rubio, R.G.; Guzmán, E. Adsorption of Mixed Dispersions of Silica Nanoparticles and an Amphiphilic Triblock Copolymer at the Water–Vapor Interface. Appl. Sci.2023,13, 10093. http://dx.doi.org/10.3390/app131810093
- Carbone, C.; Navarro-Arrebola, I.; Ortega, F.; Liggieri, L.; Rubio, R.G.; Guzmán, E. Interfacial Rheology of Chitosan-Silica Nanocomposite Films at the Aqueous Dispersion/Air Interface. Particle (SUBMITTED July 2024)